Linear Stability of Rotating Stellar Clusters

Simon Rozier

Sorbonne Université

École Doctorale 127 - Astronomie et Astrophysique d'Ile de France

Institut d'Astrophysique de Paris

Linear Stability of Rotating Stellar Clusters

présentée par

Simon ROZIER

Thèse de doctorat d'Astronomie & Astrophysique

Dirigée par M. Christophe Pichon
M. Jean-Baptiste Fouvry

Présentée et soutenue publiquement le 17 septembre 2020

Devant un jury composé de

M.	Benoît Semelin	Président du jury
M.	Christophe Pichon	Directeur de thèse
M.	Jean-Baptiste Fouvry	Co-directeur de thèse
M.	Eugene Vasiliev	Rapporteur
M.	Dominique Aubert	Rapporteur
Mme	Anna Lisa Varri	Examinatrice
M.	Sven De Rijcke	Examinateur
M.	Benoit Famaey	Examinateur

Plagiarism disclaimer

I hereby declare that I am the author of all of the following, except when stated explicitly.

Section 3.2 is inspired from Palmer et al. (1989) and Palmer (1994).

Section 4.2 builds upon Palmer (1994).

Many results of Chapter 4 are reproduced from Rozier et al. (2019).

Part of the work I present in Chapter 5 comes from the submitted paper Breen et al. (2020).

SR

Acknowledgements

Let me thank the people and institutions which took part in my PhD work.

I thank the École polytechnique for financing my PhD, as well as administrative staff at Sorbonne Université who worked to register me smoothly.

I thank the people at École doctorale 127 who acted to make sure that my PhD was going well.

I am also grateful to people at IAP, research and administrative staff, IT people, maintenance and cleaning personnel, who acted so that I could work in a sound and scientifically vivid environment, with fine facilities and equipment, as well as many occasions to take part in seminars and workshops.

I thank the organisers of all the scientific events I attended during my PhD, which were particular occasions to discover new topics of today's astrophysics, and learn more about my own subject. I also thank the people and institutions who made it possible for me to attend these events, by financing, filing and billing.

Some researchers had an important influence on the content of the present manuscript. I warmly thank the members of my jury, and in particular the referees E. Vasiliev and D. Aubert, for their challenging comments and questions which added precisions and perspective to my production.

In a variety of places, the content of this manuscript is impacted by my Scottish collaborators, D. Heggie, P. Breen and A. L. Varri. Not only did they bring a tremendous insight on stellar cluster theory, but they also brought their expertise and taught me a lot on N-body simulations' science.

Of course, I will never thank enough my supervisors, C. Pichon and J.-B. Fouvry. Throughout the PhD, they were able to set the right level of supervision, so that I could enjoy a certain independence in my everyday research, while making sure I did not get lost in naive or hopeless developments. Towards the end, their support during the difficult months of confinement was decisive in my ability to write this manuscript, as well as the large amount of work they provided in commenting consecutive versions of the manuscript and of the defense. Without their help, I would not have been as proud as I am of this manuscript and the presentation.

During my PhD, I was also able to discover what it means to be a teacher to a class of undergraduates. I enjoyed this experience a lot, and would like to thank the course organisers for making it possible. I hope I will be able to reproduce this experience frequently during my career.

For their presence, the fun and the always renewed interest for cold warfare, I am grateful to my office mates, Shweta and Amael. I will surely never forget these three years in their company. I also thank all the other PhD students who came and went during my time at IAP, the atmosphere they all created was really loveable.

Finally, I want to thank all the non-academics who had a role in the success of my PhD. This includes my friends and relatives, who stubbornly asked about my research and pushed me to always rephrase the problems in new interesting ways. I also thank all those who supported me during the hardest months of writing, in particular the friends who welcomed me on working retreats. And of course, I thank my partner Léa, who was a support at every moment.

Table of contents

Résumé

Ces dernières décennies, des preuves observationnelles ont montré que les systèmes stellaires sphéroïdaux présentent une importante diversité cinématique. Des plus grandes galaxies aux plus petits amas stellaires, la distribution de vitesse des étoiles présente de l'anisotropie dans différentes directions (une préférence pour les orbites plutôt allongées ou plutôt circulaires), ainsi que de la rotation globale (une direction préférentielle de la vitesse azimutale). Il a aussi été montré que cette diversité varie au cours de l'histoire de l'Univers, par des changements brutaux ou des perturbations régulières. Ces observations ont ainsi récemment renouvelé l'intérêt de la modélisation de systèmes stellaires sphériques présentant des profils d'anisotropie et de rotation divers. Cependant, la stabilité et l'évolution des systèmes sphéroïdaux anisotropes en rotation a été peu étudiée. À quel degré d'anisotropie et de rotation s'attend-on après la formation de ces structures, et à différentes époques de leur évolution ? Comment évoluent-elles lorsqu'elles sont isolées ? Comment leur environnement influe-t-il sur leur cinématique ? La réponse linéaire de ces objets joue un rôle central dans leur destin. D'une part, la compréhension de leur stabilité est nécessaire à une modélisation cohérente. En effet, on peut alors identifier l'ensemble des états autorisés dans lesquels les amas stellaires peuvent être lorsqu'on les observe. D'autre part, l'identification des attracteurs parmi l'ensemble des équilibres stables est critique pour analyser la manière dont ils évoluent et interagissent avec leur environnement, ce qui permet de contraindre leurs scénarios de formation et d'évolution. Dans cette thèse, j'utilise la méthode de la matrice de réponse, complémentée par des simulations à N corps, pour évaluer la stabilité linéaire d'équilibres sphériques. J'étends cette méthode des matrices aux amas en rotation, ce qui lui donne un degré de liberté supplémentaire, et je développe des méthodes numériques qui optimisent son évaluation. Ces nouvelles méthodes me permettent d'effectuer de nombreuses analyses de stabilité, sur de nombreux amas présentant de l'anisotropie à des degrés et saveurs divers, ainsi qu'une variété dans l'amplitude et la distribution du moment angulaire net. Comme les amas stellaires sont des systèmes intrinsèquement résonants, j'interprète la stabilité des amas stellaires anisotropes en rotation par le biais de trois processus résonnants de déstabilisation connus : l'instabilité d'orbite radiale (ROI) dans les systèmes radialement anisotropes, l'instabilité d'orbite circulaire (COI) dans les systèmes tangentiellement anisotropes, et l'instabilité d'alignement (TI) dans les systèmes tournants. Je montre que les systèmes sans rotation présentant un haut degré d'anisotropie sont instables, autant dans le régime radial (ROI) que dans le régime tangentiel (COI). La rotation entraîne la déstabilisation des systèmes anisotropes (via la TI), ce qui réduit d'autant le domaine de stabilité autour des systèmes isotropes. Cela signifie que les amas sphériques stables ne peuvent pas avoir une anisotropie ou une rotation importantes, et à l'inverse que des systèmes fortement anisotropes ou en rotation rapide ne peuvent pas être sphériques. À partir d'une étude détaillée des processus de déstabilisation, d'une part en termes de résonances avec la méthode des matrices, d'autre part en termes de position dans l'amas grâce à des simulations à N corps, je présente un critère de stabilité pour les sphères tangentiellement anisotropes en rotation et avec fort cisaillement, en accord avec la limite de stabilité d'un large échantillon de simulations. Ces résultats montrent que les processus résonnants et les modes auto-maintenus peuvent être des sources importantes de l'évolution séculaire des amas stellaires sphéroïdaux à haute complexité cinématique. Ces résultats ont une importance particulière à une époque où les simulations cosmologiques atteignent une résolution suffisante pour analyser leur dynamique, afin de mieux comprendre comment ils évoluent au cours de l'histoire de l'Univers.

Abstract

In the last few decades, observational evidence showed that spheroidal stellar systems display large kinematic diversity. From the largest galaxies to the smallest star clusters, the velocity distribution of stars displays both various flavours of anisotropy (preference for more elongated or more circular orbits), as well as net angular momentum (preferred direction of the azimuthal velocity). This diversity was also shown to vary with cosmic time, through brutal changes and steady perturbations. These observations recently triggered a revived interest for the modelling of spheroidal stellar systems with various anisotropy and rotation profiles. Meanwhile, the stability and evolution of anisotropic, rotating spheroidal systems were scarcely studied. What degree of anisotropy and rotation is expected at the formation of these structures, and at various epochs of their evolution? How do they evolve, in isolation? How does the environment impact their kinematics? In all these prospects, the linear response of stellar clusters is central to their fate. On the one hand, understanding how stable they are is necessary for their consistent modelling. Indeed, it identifies the ensemble of authorised states in which star clusters can be at the time of their observation. On the other hand, identifying the attractors among the stable equilibria is critical to analyse the way they can evolve and interact with their environment, therefore putting constraints on their scenarios of formation and evolution. Here, I use the response matrix method to evaluate the linear response of spherical equilibria, and complement it with N-body simulations. I extend the matrix method to rotating clusters, where the matrix has an extra degree of freedom, and develop numerical techniques leading to its fast computation. This allows me to perform numerous stability analyses, on many clusters with various degrees and flavours in their velocity anisotropy, and different degrees and distributions of net angular momentum. Since star clusters are intrinsically resonant systems, I interpret the stability of rotating, anisotropic star clusters using three known resonant destabilising processes: the radial orbit instability (ROI) in radially anisotropic systems, the circular orbits instability (COI) in tangentially anisotropic systems, and the tumbling instability (TI) in rotating systems. I find that non-rotating clusters with sufficient velocity anisotropy are unstable, both in the radial (ROI) and in the tangential regime (COI). Rotation further enhances the destabilisation of anisotropic systems (through the TI), hence it narrows down the authorised stability domain around isotropic systems. This means that stable spherical clusters can only have a low amount of anisotropy and rotation, and conversely that highly anisotropic or fast rotating clusters cannot be spherical. From a detailed study of destabilising processes, both in terms of resonances via linear theory, and in terms of location in the cluster via N-body simulations, I develop a stability criterion for tangentially anisotropic, rotating spheres with high shear, which reproduces the stability boundary of a large sample of simulations. These results show that resonant processes and self-sustained modes can be important drivers of the secular evolution of spheroidal star clusters with intricate kinematics. It will prove of prime importance at a time when ab initio cosmological simulations reach sufficient resolution to resolve their dynamics, to best make sense of how they evolve over a Hubble time.

Chapter 1

Introduction

In today's astronomy, self-gravitating systems can be broadly classified in two kinds of shapes. On the one hand are disks, where one dimension of the structure is smaller than the other two. The largest of these are the disk galaxies, composed of hundreds of billions of stars. Also in this category fall smaller disk-like systems, such as proto-planetary structures around new-born stars, accretion disks feeding black holes, and dust disks and rings orbiting around planets. On the other hand are structures which display significant vertical extension, which are called triaxial because their three axes are of similar sizes. On the largest scales are galaxy clusters made of some 10^{2-4} galaxies. A variety of galaxies also fall in that category, from the large elliptical galaxies, made of up to 10^{13} stars and usually found in the most crowded regions of galaxy clusters, down to small dwarf ellipticals, made of as few as 10^7 stars. At even lower scales are triaxial systems inside galaxies, such as galactic bulges with up to 10^{11} stars, or globular clusters (GCs) of about 10^5 stars. Then, at the very centre of galaxies, nuclear star clusters (NSCs) are the stellar systems orbiting around the galaxies' central black holes, with e.g. about 10^6 for that of the Milky Way. Finally, the smallest systems are self-gravitating fluid bodies, such as stars and planets. For the largest systems, i.e. the galaxies and galaxy clusters, the current cosmological ΛCDM paradigm (Blumenthal et al., 1984) predicts that they are embedded within even larger massive triaxial components, the dark matter (DM) halos.

A critical characteristic, which affects the system's nature in both categories, is the the role played by dissipative processes. In fluid-dominated systems made of gas, shocks play a determinant role in setting up the initial dynamics. Indeed, it ensures that the trajectory of neighbouring elements of the system remains similar, since intersecting orbits would lead to shocks which, when isothermal, radiate away some of the system's energy. In star clusters, however, the lack of collisions makes it possible for the constituents of the system to have completely different trajectories, even if they are physically close at times. The present manuscript focuses on theoretical questions related to the formation and evolution of such triaxial collisionless stellar systems.

A simple closed box scenario for the formation and evolution of these systems can be summarised as follows. First, on a few dynamical times (i.e. the time taken by an element of the system to rotate around the centre), as a result of strong potential fluctuations, the proto-cluster undergoes a violent relaxation (Lynden-Bell, 1967), allowing it to reach a dynamically steady state. The motion of the stars is then dominated by the mean field. On longer timescales, the cluster will slowly explore subsequent thermodynamical equilibria, as a result of relaxation sourced by finite-N fluctuations or external potential perturbations (Binney & Tremaine, 2008). During the first stage of evolution, the system is insensitive to its finite number of constituents (stars in stellar systems, DM particles or substructures in DM halos), but sensitive to the time-varying average potential created by the ensemble of all other particles. It can therefore be treated as a collisionless system. It is also during this stage that the system may develop linear instabilities, that significantly rearrange the system's orbital structure, should the violent relaxation stage have left it close to an unlikely (low entropy) configuration (which is typically the case when baryonic processes have dominated the dynamics pre-star formation). At some later stage, secular evolution will also slowly draw the system closer to marginal stability (see, e.g., Fouvry et al., 2015a; De Rijcke et al., 2019b).

The outcome of violent relaxation is a quasi-stationary state with typically high (cylindrical or triaxial) symmetry. In this configuration, which involves anisotropy and rotation, the mean-field is dynamically locked by its symmetries in configuration space, which allows for the existence of a dynamical equilibrium by preventing any torques between different parts of the system. If in isolation, it is then

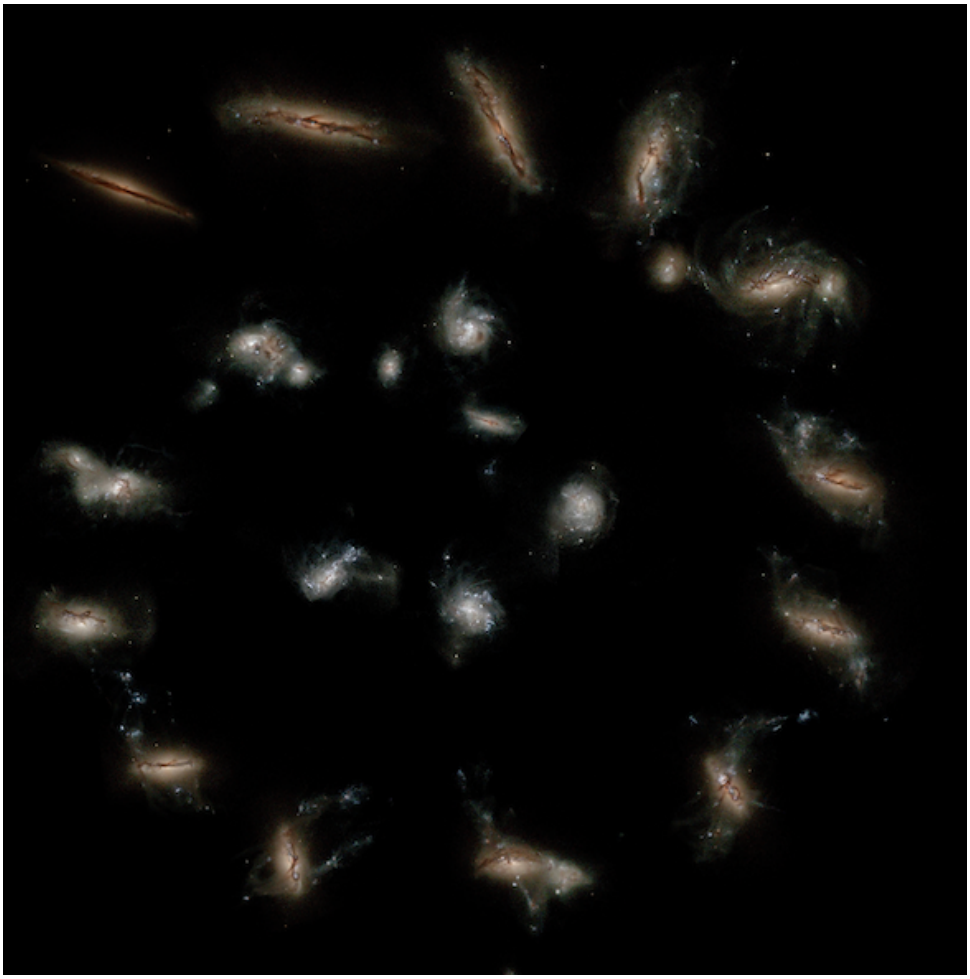

Figure 1.1: Evolution of a typical galaxy over cosmic times. Snapshots from the NewHorizon simulation (Park et al., 2019). The galaxy is regularly perturbed by its environment, and therefore alternates between periods of violent transformations, of steady perturbations and of self-induced relaxation.

only through resonant interactions between individual stars that the system can subsequently evolve (in particular through energy and angular momentum exchanges between resonant stars, see Lynden-Bell & Kalnajs, 1972; Tremaine & Weinberg, 1984), via linear instabilities or orbital diffusion, towards more probable equilibria (i.e. with more isotropy and a different distribution of rotation).

The present discussion, while appealing, has neglected a key ingredient for the evolution of self-gravitating systems: they do not evolve in isolation. The closed box paradigm must therefore be amended to account for their interaction with their environment both in terms of infall and of gravitational perturbations (see Figs. 1.1 and 1.3). If the system is open, the resonant interactions between the system's particles and external correlated perturbations, possibly amplified by the system's self-gravity, will also drive its secular evolution. Hence, the linear response of the system is a critical component of its evolution, since it describes how the system responds to internal and external perturbations.

For galaxies, modern cosmological simulations (see, e.g., Park et al., 2019) suggest for instance that the cosmic appearance of thin galactic disks is driven by a fine-tuning between cooling mechanisms (e.g., coplanar infall of gas), and heating processes (merging of small virialised objects, turbulence, deflection on molecular clouds, etc.). Cosmic evolution seems to conspire to promote a redshift-dependent transition mass between cosmic-driven morphology on the one hand (through mergers, strong feedback and turbulence), to secularly-driven morphology on the other hand (which promotes self-regulation around marginal stability with an effective Toomre Q number (Toomre, 1964) close to one, see Fig. 1.2). Understanding what drives the marginal stability of galaxies is therefore all the more important that *it corresponds to an attraction point of galactic evolution.* Identifying marginal stability criteria that would be the equivalent of Toomre's number in the context of rotating stellar clusters should prove as valuable in the context of spheroids, e.g. in elliptical galaxies. More generally, linear response theory is of interest even when the spheroids are stable, since it quantifies the amplitude of their (strong) response to exter-

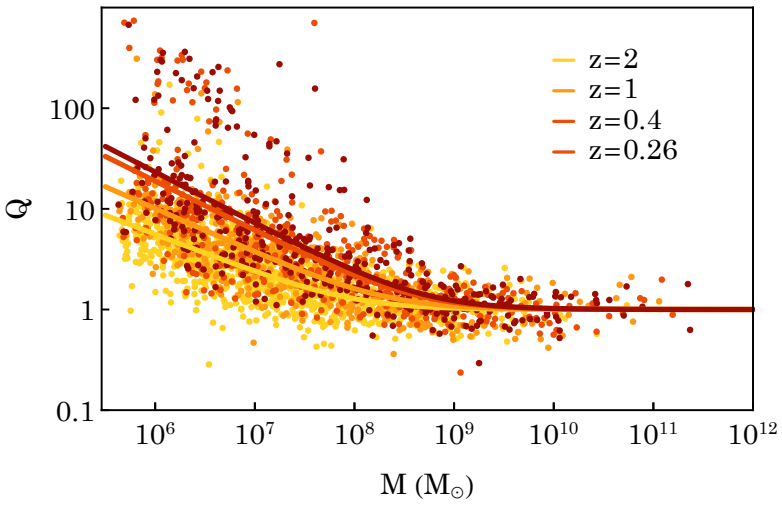

Figure 1.2: $\log Q$ versus $\log M$ for different redshifts, as measured from galaxies in the NewHorizon simulation (Park et al., 2019). The different curves correspond to fits for redshifts $z = 2$, 1, 0.4, and 0.26 fitted by $(1 + M_0(z)/M)^{\alpha(z)}$. The transition mass $M_0(z)$ scales like the mass of non-linearity, which defines the local dynamical clock, reflecting the idea that, for more massive discs (in units of that mass), secular processes can operate more swiftly and efficiently. The measured Toomre number is the effective one (see Romeo & Falstad, 2013), taking into account both the stellar and the gas component. Remarkably, marginal stability is an attractor.

Figure 1.3: HST image of the Abell 370 galaxy cluster. Elliptical galaxies (in yellow) are usually embedded within a rich environment. A few gravitational arcs are also visible on this image.

nal stimuli. Indeed, our current understanding of galaxy formation for instance decisively suggests that through its lifetime, a given galaxy will experience a sequence of re-formation of its disc and spheroid, as it acquires gas, and sub-components with inconsistent kinematics. Depending on its stability threshold and the intensity of the perturbation, it will also reshuffle its orbital structure. Hence, the above-mentioned closed box scenario only applies to recurrent stages of its lifespan. Such reasoning still holds for nuclear and globular clusters, as they are also subject to gas rich infall or strong tidal interactions. All in all, it is essential to understand the linear response of self gravitating systems with arbitrary level of rotation and kinematic diversity.

Let me insist on the importance of gas dynamics in the context of this thesis. While the gas is sub-dominant in mass in the inner region of most stellar clusters, it does play a very important role in the recurrent regeneration of its (statistically unlikely from a purely stellar point of view) kinematic complexity. Indeed, in many astrophysically relevant settings, the cold gas (from which stars emerge) can and will radiate away most of its entropy, and therefore launch new stars on dynamically cold and possibly counter rotating orbits. These new kinematic components are fairly unlikely from a collisionless dynamics perspective, and will significantly impact the response of the stellar system. Hence, the environment of cosmic structures operates at two levels: (i) directly, as a source of potential perturbations, and (ii) secularly, via adiabatic infall, which changes the responsiveness of the underlying equilibrium, lowering its entropy. My thesis will mostly focus on the latter, while exploring the stability threshold of a given sphere as one parametrically changes its kinematic properties. But keep in mind that the linear response theory applies to both processes.

The theory for the formation and evolution of triaxial collisionless structures historically focused on spherical systems (but see, e.g., Robijn, 1995, for an application in the context of triaxial systems). Indeed, their high degree of symmetry (in particular straightforwardly integrable orbits) makes it easier to develop analytical techniques, as I will show in Section 1.3.2. Furthermore, it is likely (and has been investigated by, e.g., Antonini et al., 2009) that some of the concepts coming from the study of spherical structures can be generalised to triaxial systems, where the three axes all have different (yet similar) values.

Historical theoretical studies on spherical stellar systems have primarily focused on structures where the velocity distribution is isotropic (Antonov, 1961; Doremus et al., 1971). Then, it was extended to non-rotating structures, where the velocity distribution is independent of the orientation inside the cluster (Kandrup & Sygnet, 1985; Perez & Aly, 1996; Polyachenko & Shukhman, 1981). Yet, recent evidence from observations and cosmological simulations showed that these systems usually present complex kinematics, with anisotropy in the velocity distribution, differential rotation, and stellar populations with different kinematic characteristics (see, e.g., Emsellem et al., 2011; Cordoni et al., 2020). These features reflect both the recurrent re-formation of the cluster (since the end of the violent relaxation phase locks it in a possibly low-entropy equilibrium) or its secular evolution driven by correlated perturbations (mergers, gas infall, tidal interactions with the environment). In both cases, the linear response of the system determines which equilibria it can explore and how strongly it reacts to these perturbations. Therefore, studying the linear response of star clusters helps disentangling the influence of different perturbers on the system. Hence, it is an important tool in the context of the so-called cosmic archeology, which aims to understand the origin of our Milky Way by studying its kinematic structures. Finally, since the modelling of these complex systems is sometimes carried out independently of their linear stability, it is also of interest to provide the techniques to remedy this. *One of the goals of my PhD is therefore to investigate the impact of kinematic diversity (e.g., velocity anisotropy and rotation) on the onset of dynamical instabilities in self-gravitating spherical stellar clusters.* In the coming sections, I will summarise some evidence of anisotropy and rotation in spheroidal star clusters, and briefly describe some methods generically used to model them. I will then set the mathematical apparatus which I will use to study their dynamics. Finally, I will briefly present previous results on the linear stability of spherical systems.

1.1 Kinematic richness in spheroidal systems

While cosmological simulations suggest that kinematic diversity appears as a natural recurrent state over the lifetime of spheroidal clusters, the interest for these features is also currently driven by recent observations and simulations of a variety of stellar clusters, using different observational techniques. Here, I present some evidence for complex kinematics in these different systems, from the largest to the smallest scale.

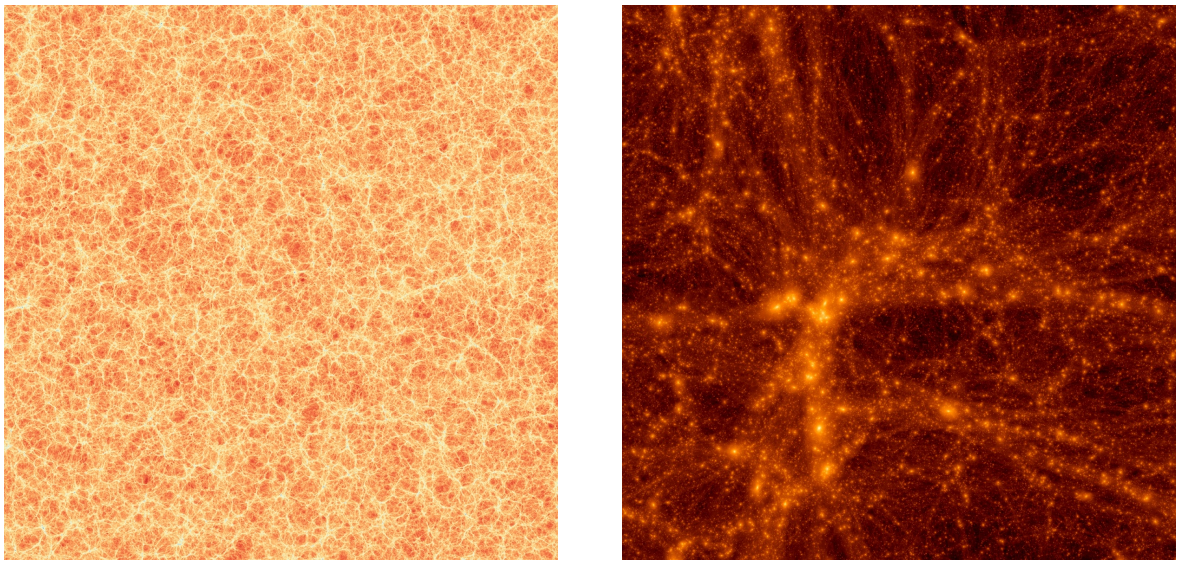

(a) Full (b) Zoom

Figure 1.4: (a) A slice through the dark matter density on scales of hundreds of Mpc in a dark matter ΛCDM simulation, displaying the large scale structure of the density field. (b) Dark matter density on smaller scales $(20\,\mathrm{Mpc})^3$. Many dark matter halos are present in the box. This picture shows how intricate it may be to disentangle a single DM halo from its environment, as well as the variety in shapes and substructures that these halos may display. DM haloes are definitely not isolated islands, and the cosmic environment plays a fundamental role in the definition of their orbital structure.

1.1.1 Dark matter halos

The kinematics of DM halos is usually studied by means of isolated N-body or cosmological simulations. In this field, the detection of anisotropy is often reduced to determining whether a halo is relaxed (hence rather isotropic) or not, in order to put constraints on the collisional properties of DM particles. Generally, simulated halos display an isotropic centre and an intermediate region where the anisotropy is progressively growing in the radial direction (Lemze et al., 2012). In the outer region, the triaxiality of the halo requires using other indicators of the velocity distribution (Wojtak et al., 2013). Relying on the assumption that DM and hot gas have the same specific energy, Host et al. (2009) were able to indirectly constrain the anisotropy of the DM halo of observed galaxy clusters. Their results are in agreement with previous results from simulations.

Since the derivation of a phenomenological universal density profile for simulated DM halos in Navarro et al. (1997), other relations were derived by similar phenomenological means to relate their density to their velocity dispersions. These include, e.g., the phase space density profile (Taylor & Navarro, 2001), and the anisotropy-density slope relation (Hansen & Moore, 2006). However, there is not yet a consensus for the specific origin of velocity anisotropy in DM halos (Hansen, 2009, but see below).

The hierarchical structure formation scenario produced by the ΛCDM paradigm (Blumenthal et al., 1984) naturally forms DM halos with an initial angular momentum. Indeed, Peebles (1969) showed that, at the time of gravitational collapse, the tidal torques applied by forming DM halos to each other were leading to the development of angular momentum in the newly-formed structures (see also Codis et al., 2015). Later, numerical cosmological simulations such as the ones illustrated in Fig. 1.4 provided statistical measurements of the global angular momentum in DM halos, summarised in what is now called the spin parameter distribution (Bullock et al., 2001; Aubert et al., 2004; Bett et al., 2007). More recently, the evolution of halo spin over cosmic age and loci within the large scale structures was investigated (Codis et al., 2012), focusing either on the interaction with the environment (see, e.g., Vitvitska et al., 2002) or with the inner baryonic content (Bryan et al., 2013). Similarly, cosmic tides from filaments were shown to impact the velocity anisotropy of dark halos (Borzyszkowski et al., 2017).

These different evolutionary patterns lead to a variety in rotation curves. Even if the initial structure formation, or a period of isolated evolution, were producing a smooth rotation profile, the interaction with the baryons would modify the central part of the curve in a variety of ways (e.g., trough AGN or supernova feedbacks), and the same would go in the outskirts through the interaction of the halo with its environment (e.g., through cold gas accretion). These processes undoubtedly produce an intricate structure in the halo, e.g. with a core, intermediate shell and outer shell rotating around three different

axes.

The shapes of DM halos also reflect the diversity of cosmic environments in which they form. Indeed, they often display important triaxiality (prolateness, mainly; see, e.g. Jeeson-Daniel et al., 2011), and it is therefore complex to properly define a rotation curve. Naively, one could fear that they are too far from sphericity to be concerned by the results of the present manuscript. Fortunately, Antonini et al. (2009) showed that triaxial systems could display the same dynamical instabilities as those present in spherical systems (the radial orbit instability in that case, see Section 1.4). Furthermore, the triaxiality of the DM halos could precisely be due to early dynamical destabilisation, leading to a triaxial endstate. Linear stability studies can then be used to constrain the past history of these structures.

1.1.2 Elliptical and spheroidal galaxies

We now have numerous observational evidence for anisotropy and rotation in elliptical and spheroidal galaxies. Indeed, the recent development of integral field spectroscopy, which measures spatially resolved spectra on the field of view of distant objects, allowed for important advancements in the description of their internal kinematics. Earth-based instruments provided kinematic surveys of these objects, such as SAURON (Bacon et al., 2001; Kuntschner et al., 2006), ATLAS3D (Cappellari et al., 2011; Emsellem et al., 2011) and KMOS3D (Wisnioski et al., 2015, 2019). These surveys revealed that elliptical galaxies are generally rotating, as exemplified by Figs. 1.5 and 1.6. The systematic detection of global angular momentum in elliptical galaxies led to the discovery that two classes of galaxies co-exist, now coined slow- and fast-rotators (Emsellem et al., 2011). Unfortunately, such spectroscopic data typically give access to moments of the stellar velocity distribution, such as the mean line-of-sight velocity (via the shift in emission lines) and the line-of-sight velocity dispersion (via the line widths). As such, as discussed in Section 1.2, the constraints they provide on the anisotropy profile always suffer from the mass-anisotropy degeneracy.

At smaller scales, astrometric measurements were performed on nearby dwarf satellites of the Milky Way. Combining data from space-based missions such as the Hubble Space Telescope (HST) and Gaia, it is becoming possible to gather accurate 3D kinematic data for individual stars in Milky Way satellites. Such measurements in the Sculptor dwarf (Massari et al., 2018), the Draco dwarf (Massari et al., 2020) and other ultra faint dwarfs (Massari & Helmi, 2018) tend to confirm the universality of asymmetric kinematics, in particular anisotropy. Astrometric measurements in the Large Magellanic Cloud in Vasiliev (2018) also showed that this nearby dwarf is rotating. It is likely that upcoming observations, among which the next Gaia Data Releases, will improve our knowledge of the stellar kinematics in these galaxies. These measurements are informative, since they give access to the velocity distribution of galaxies independently of their mass. However, there still remains degeneracies from uncertainties in the line-of-sight distance of the stars, which somewhat makes the theoretical interpretations harder.

The kinematic structure of spheroidal galaxies appears to be mainly driven by secular processes and their interaction with their cosmic environment. On the largest scales, it is believed that massive elliptical galaxies are produced by major mergers. During their formation, super massive black holes are formed, and the efficiency of the corresponding AGN feedback prevents the reformation of massive discs by quenching cold gas infall. More generally, in the favoured hierarchical clustering scenario, most galaxies build up through minor mergers and gas inflow. The dynamical endstate therefore depends on the characteristics of the progenitors, as well as on the geometrical characteristics of the merger. Hence, the steady occurrence of minor mergers driven by the geometry of the large scale structure also impacts the system's phase space (Welker et al., 2014). In parallel, cool gas accumulates in the centre to reform a slowly growing stellar component. In particular, there are indications that fast- and slow-rotators can also be distinguished by the presence or not of such a flattened component (Krajnović et al., 2008; Emsellem et al., 2011). This impacts the dynamical temperature of the system. Indeed, later perturbations may disrupt these stars into the spheroid, as a kinematically distinct component, which may push the cluster towards linear instabilities. On smaller scales, other kinematic features can be attributed to stellar feedback, or emerge from the tidal interaction with larger galaxies.

1.1.3 Globular Clusters

Globular clusters (GCs) are star clusters orbiting inside galaxies (see Fig. 1.7). They have certainly regained great interest in stellar dynamics today. Indeed, we stand at a time of two simultaneous major improvements. On the one hand, astrometry is now approaching a complete 6D reconstruction of the inner kinematics of galactic GCs (Bianchini et al., 2018). On the other hand, N-body methods are

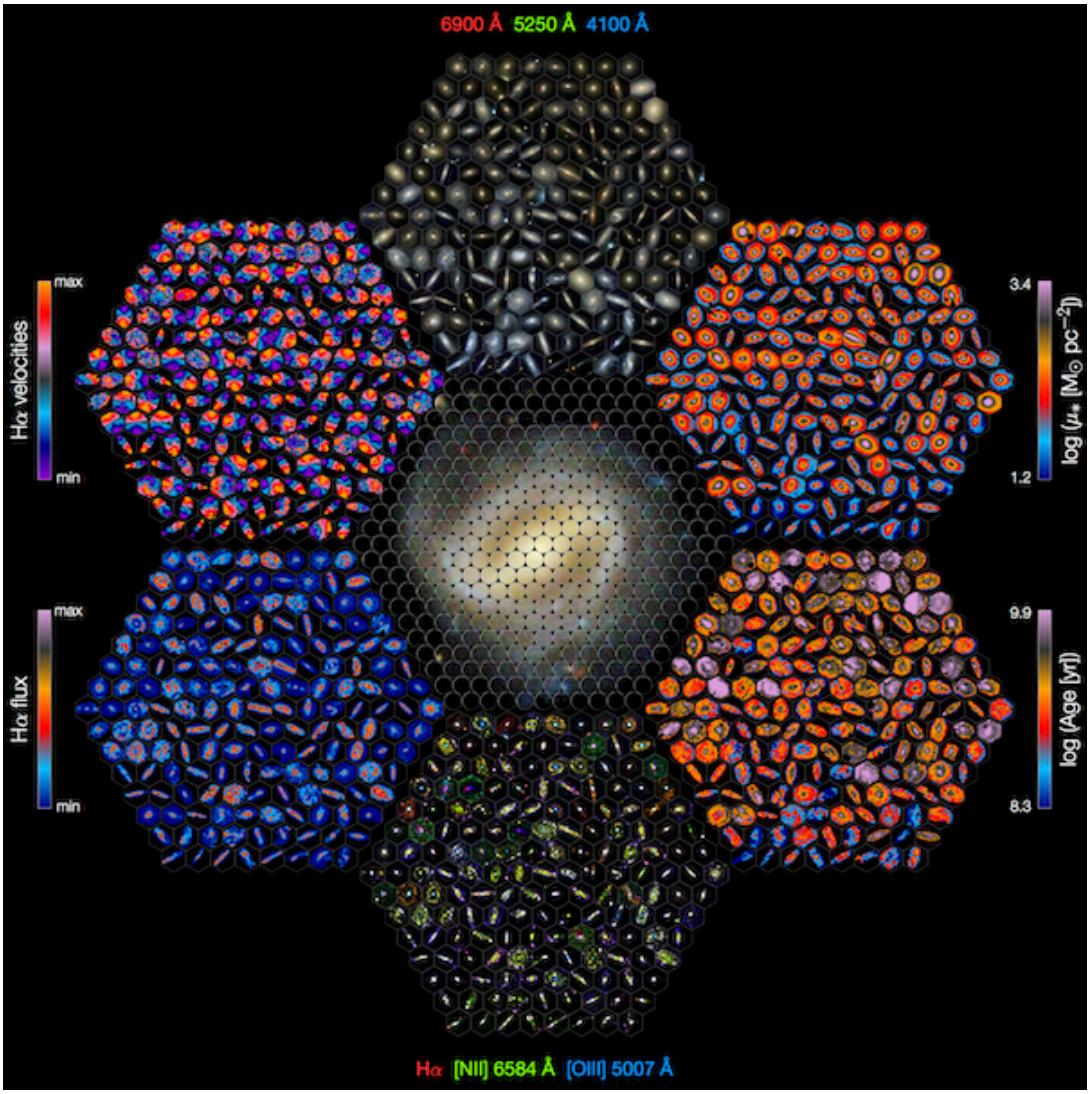

Figure 1.5: Summary representation of the CALIFA survey (Husemann et al., 2013). The kinematics are represented by Hα velocities. One can note great kinematic diversities among all the sampled galaxies.

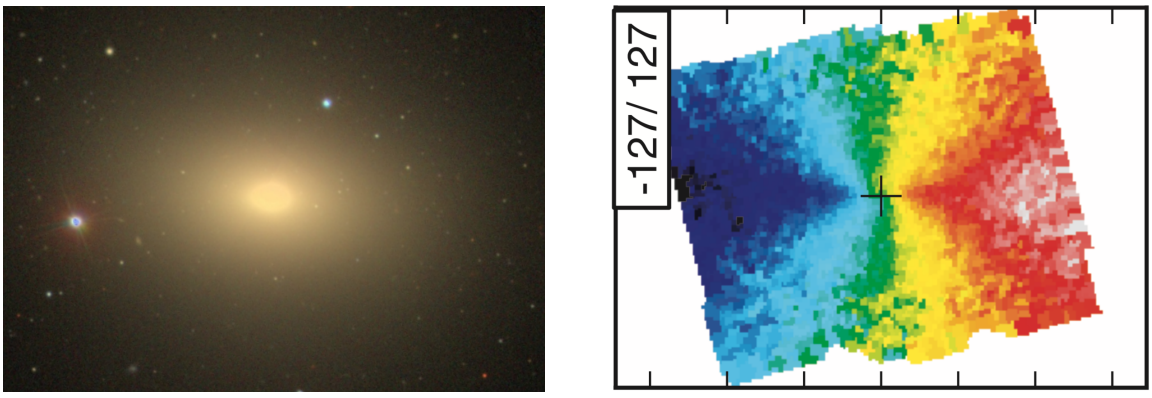

(a) SDSS image

(b) Line-of-sight velocity map

Figure 1.6: (a) Image of the elliptical galaxy NGC 4621 from the Sloan Digital Sky Survey, on a field of view of ~ 15 arcmin corresponding to a size of ~ 50 kpc. (b) From Emsellem et al. (2011). Velocity field from the integral field spectroscopic survey Atlas3D, on a field of view of ~ 30 arcsec (~ 2 kpc) at the centre of the galaxy. The colour levels indicate line-of-sight velocities, from $-127\,\mathrm{km.s^{-1}}$ (black) to $127\,\mathrm{km.s^{-1}}$ (white). The dipolar structure of the velocity field is a clear indication of rotation.

Figure 1.7: HST image of the GC M10, which is composed of $\sim 10^5$ stars. This field encompasses the central region, of about 4 pc across. Despite their seemingly spherical shape, recent observations have highlighted the kinematic diversity of GCs.

reaching a state where GCs can now be simulated in full, for their full lifetime (Wang et al., 2016).

Astrometric measurements of galactic globular clusters now cover a variety of objects. In general, line-of-sight velocities are easier to observe, because they are based on spectroscopic observations of individual stars. In the last 60 years, such measurements were complemented by proper motions, using stellar position measurements at time intervals of tens of years (see, e.g., van Leeuwen et al., 2000, and references therein). With the advances in precision positioning, it later became possible to measure proper motions of GC stars with much lower time bases. Using HST data, Anderson & King (2003) measured proper motions of stars in 47 Tuc, complementing the radial velocity measurements from Meylan & Mayor (1986), in order to confirm rotation in that GC and constrain the rotation axis. Recent measurements incorporate a much larger number of stars, especially using HST and Gaia data. These regularly detect rotation (see, e.g., Ferraro et al., 2018; Bianchini et al., 2018; Vasiliev, 2019; Sollima et al., 2019), anisotropy in the radial direction, and also mild anisotropy in the tangential direction in some cases (Watkins et al., 2015; Jindal et al., 2019).

The kinematic measurements of galactic GCs also allow for the separation of the different stellar populations. Indeed, it is now known (yet still unexplained) that GCs are composed of different stellar populations, characterised by their metallic abundances (see, e.g., Carretta et al., 2009). Several kinematic surveys were performed on these different populations, exhibiting evidence for different density distributions, velocity dispersion profiles and rotation patterns, in each population (Milone et al., 2018; Kamann et al., 2020; Cordoni et al., 2020).

The origin of anisotropy and rotation in GCs is an active subject of research, and my work should hopefully provide some context in which to frame part of it. It has been known for a while (Binney & Tremaine, 2008) that the collisional evolution of GCs leads to a phase of core collapse (Lynden-Bell & Wood, 1968), when part of the stars end up in a dense core, and the other part in an extended halo. In a GC with a distribution of masses, collisional processes also lead to the equipartition of energy, with the most massive stars in the centre and the lightest in the outskirts. Energy equipartition can now be observed in GCs (see, e.g., Bellini et al., 2018), and can be used to characterise the dynamical state of GCs. These processes may also modify the velocity distribution of isolated spherical clusters.

Indeed, Giersz & Heggie (1994) showed, using direct N-body simulations, that the migration of stars from the centre was driving them preferentially along radial orbits, creating radial anisotropy in the outer parts of the cluster. Later on, Baumgardt & Makino (2003) (see also Takahashi et al., 1997; Giersz & Heggie, 1997; Hurley & Shara, 2012) simulated GCs embedded in a tidal field. They showed that the

population of radial orbits formed at core collapse progressively escapes due to the interaction with the tidal field, which has the effect of restoring isotropy in the outer part of the GCs, and even creating a mild tangential anisotropy. More recently, Tiongco et al. (2016b) showed that the flavour and distribution of this evolutionary anisotropy depends on the tidal force applied to the GC.

In the same vein, rotation can also emerge from evolutionary aspects of the GC. Indeed, Tiongco et al. (2016a) showed that rotation naturally appears in GCs rotating in a galactic tidal field. The GC starts rotating through mainly two process, the preferential loss of prograde orbits and the transition of highly elongated orbits from prograde to retrograde rotation.

Another line of work focuses on the processes leading to anisotropy and rotation at the formation of GCs. van Albada (1982) showed that strong radial anisotropy emerges in spheroidal stellar systems from the early phase of violent relaxation. Similar experiments were performed with forming clusters orbiting in a galactic tidal field by Vesperini et al. (2014). It is shown there that the Coriolis force depletes the eccentricity of the elongated orbits, diminishing the radial anisotropy of the newly-formed cluster (even creating a mild tangential anisotropy in the outskirts). This effect also imprints a rotation profile to the cluster. The presence of angular momentum in young GCs was indeed observed by Hénault-Brunet et al. (2012). An alternative explanation for the early rotation of GCs is based on the direct transfer of angular momentum from the molecular gas during star formation, and is backed by recent hydrodynamical simulations (Ballone et al., 2020). The gas itself rotates, presumably because of large scale tidal torques during gravitational collapse (Mapelli, 2017).

Recent studies also focused on the role of primordial anisotropy and rotation in the dynamics and evolution of GCs. Breen et al. (2017) showed for instance that initially radially anisotropic GCs undergo a slower collisional evolution than isotropic GCs, and that tangentially anisotropic GCs are evolving faster. Tiongco et al. (2018) showed that rotating GCs orbiting in a galactic tidal field are undergoing a variety of phenomena, such as complex oscillation of the rotation axis, variation of the internal rotation profile, or variation of the internal density.

1.1.4 Nuclear Star Clusters

Let me more briefly present some properties of nuclear star clusters (NSCs). Their observation is more challenging, because they are very small (usually a few pc) and located in crowded regions of their host galaxies. Hence, only those of the Milky Way and other nearby galaxies can be resolved by integral field spectroscopy. That of our own Milky Way was observed, e.g., by Feldmeier et al. (2014) (see also Fig. 1.8). It appears to be rotating relatively fast, with ratios of line-of-sight velocity to velocity dispersion $V/\sigma \sim 1$. In Feldmeier-Krause et al. (2017), it was modelled through Schwarzschild's orbit superposition technique (see Section 1.2), and its anisotropy was estimated to be significantly tangential. There are also indications of multiple dynamical components, namely a halo of old stars (see also, e.g., Schödel et al., 2009), and a disk of young stars (see, e.g., Tanner et al., 2006). Details and references can also be found in Genzel et al. (2010).

Another example of an NSC observed using an integral field unit is given in Seth et al. (2008), which looked at NGC 4244. In that case too, the NSC appears as a fast rotator, with $V/\sigma \sim 1$ in some regions. Later, dynamical modelling of the NSC with a made-to-measure model (see Section 1.2) estimated that it has a complex anisotropy structure, with evolving anisotropies both in the azimuthal and the polar directions (De Lorenzi et al., 2013).

Several competing scenarios have been proposed for the formation of NSCs and the build-up of their angular momentum. On the one hand, they may form by episodic in-situ star formation, from gas which falls into the centre of the galaxy (Loose et al., 1982; Milosavljević, 2004). In this scenario, the angular momentum is naturally transferred from the gas to the newly formed stars. On the other hand, NSCs could be formed by the accretion of GCs to the centre of the galaxy (Tremaine et al., 1975). Recently, Tsatsi et al. (2017) showed using direct N-body simulations that this scenario can also account for a significant angular momentum. In both scenarios, the NSCs can never be fully considered as isolated. The study of their linear stability may therefore inform us on the influence of the perturbations (either from in-situ star formation or from cluster accretion) on the kinematic structure of these objects. In these clusters, the dynamics is however dominated by the central massive black hole, which has an important impact on the system's frequency structure. NSCs should therefore be the systems to which my results apply the least straightforwardly.

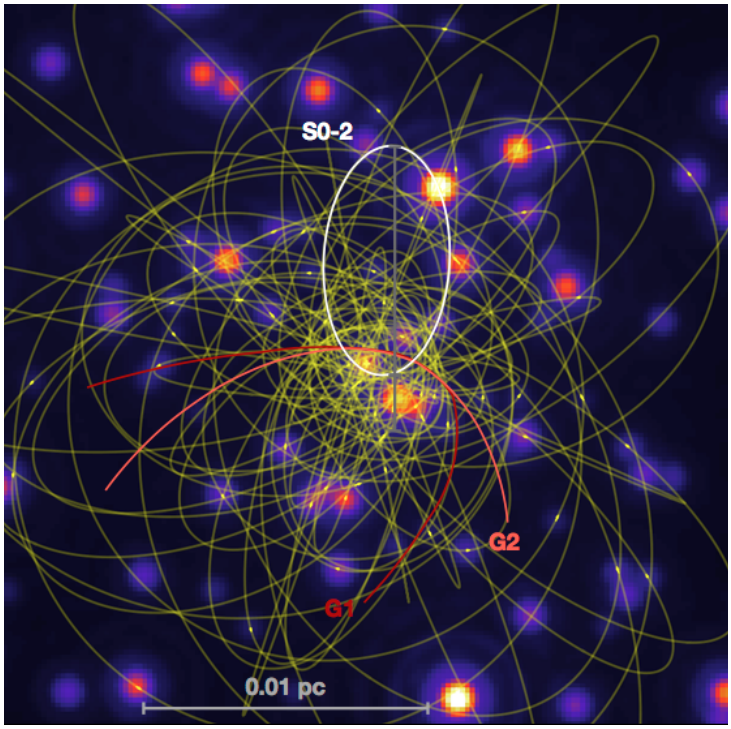

Figure 1.8: Simulated image of the S cluster in the Galactic center as it will be seen by the TMT in a couple of years (see Do et al., 2019). Note that the orbits are quasi-Keplerian owing to the presence of the cantral super massive black hole.

1.2 Modelling methods for stellar and galactic clusters

The methods used to model stellar clusters are all imprinted by the particular purposes they serve. The modelling of DM halos is either used in relation to the inner baryonic structures, or to infer the properties of dark matter particles. In galactic dynamics, one usually tries to infer information on the DM halo, in particular its density profile and its shape. In GC science, the goal is usually to link the kinematics of the cluster to its formation and evolution scenario, as well as the possible identification of intermediate mass black holes. This is also of interest to NSC modelling, where the goal is usually to link the kinematics of the cluster to its central black hole (mass, growth, formation, evolution, ...). I briefly present here four broadly used methods, their advantages and the different issues they face.

The first and oldest of these methods is based on the Jeans equations (Jeans, 1919). These equations correspond to moments of the collisionless Boltzmann equation (see eq. (1.11)), via integrating over the cluster's phase space distribution. They can be seen as equations relating the physical space density to the first moments of the velocity distribution. Usually, this method is used to produce a dynamical prediction for the spatial density of a stellar system, e.g. for black hole mass estimates in GCs and NSCs. When applied to incomplete data (e.g., line-of-sight velocity moments only), one can constrain the missing information (e.g., the density) using these equations. Since the set of equations is not closed, this problem cannot be solved without using extra assumptions, in particular that the system is in dynamical equilibrium, or regarding the shape of the system and of its velocity ellipsoid (i.e. the ratios between velocity dispersions in the three directions of space). The latter problem is known as the mass-anisotropy degeneracy. Indeed, one can always produce a different result for the model's density by assuming a different shape of the velocity ellipsoid. State-of-the-art techniques in this domain (see, e.g., Cappellari, 2008) still suffer from important biases, coming from the assumptions on the shape of the system and the velocity ellipsoid (Bonnivard et al., 2015). Furthermore, the models produced by this method only concern the first moments of the spatial and velocity distributions. As such, they do not provide a full description of the system's phase space, nor do they warrant that the underlying distribution function (DF) is positive. Hence, the results produced by Jeans modelling on a single object may cover a variety of phase space structures, including dynamically stable and unstable ones. Linear stability analyses, such as the ones that I will present in this manuscript, can then provide extra constraints on the models produced by this method.

A second class of modelling methods is called the orbit superposition method, and was introduced in Schwarzschild (1979). It is based on the reconstruction of a set of observables (surface brightness, line of

sight velocity moments) from the superposition of pre-computed orbits in an initially assumed potential. This method yields self-consistent DFs for the system (Vasiliev & Athanassoula, 2015), however it makes a strong assumption on the shape of the underlying potential (it is fixed a priori). Furthermore, there is no guarantee that the resulting distribution is an equilibrium, and even if it is so, a stability analysis is still required to determine if such a distribution is stable. Analytical methods to determine their stability may suffer from the fact that the produced distributions are not analytical.

In order to produce an analytical phase space DF for a given object, some studies relied on exhibiting such distributions, with possibly parametrical fitting. With a single DF, or a superposition of several DFs corresponding to the same potential, the result is by design self-consistent. Multi-component modelling of stellar systems can also be performed with such a method (Kuijken & Dubinski, 1995), yet the produced model is not necessarily at equilibrium, or linearly stable. Assuming isotropy in the velocity space, it is also possible to rely on Eddington's inversion formula (Eddington, 1916) and its generalisation (Magorrian, 1995; Evans et al., 1997), once a density distribution was assumed (see, e.g., Lacroix et al., 2018). In the same vein, it is possible to produce anisotropic Osipkov-Merritt DFs (Osipkov, 1979; Merritt, 1985) for certain classes of systems from, again, an assumed density distribution. Some other particular forms of anisotropic DFs can also be produced by separating the E and L components (see Binney & Tremaine, 2008). The interest of this method relies on the fact that the produced models are easier to study with analytical tools (e.g., linear stability analyses with the methods presented throughout the present manuscript), since they produce analytical DFs for the observed systems. However, they crucially rely on the assumption made on the density distribution in the system, and require a certain degree of symmetry. Furthermore, the class of existing analytical distributions is far from encompassing the complexity of phase space distributions in actual stellar systems.

The final class of modelling methods was first proposed in Syer & Tremaine (1996), and is known as made-to-measure (M2M) models. It is based on the N-body integration of a set of particles, slowly varying their mass in order to fit some observables (density, velocity distribution, ...). As the method also includes a way to adapt the potential, it produces self-consistent equilibria for stellar systems. However, as for orbit-based methods, the phase space distributions produced are also numerical, and generally unfit for use with analytical methods.

Other modelling methods for stellar systems, adapted or not from these four, can be used (see, e.g., Vasiliev & Athanassoula, 2015). The application of many of these methods is now much facilitated thanks to efficient, publicly available softwares, such as AGAMA (Vasiliev, 2019).

1.3 Hamiltonian dynamics

In my thesis, I study analytically the linear response of star clusters. I therefore rely on mathematical tools which allow for their dynamical modelling. The Hamiltonian framework describes the dynamics of a self-gravitating system made of a large number of particles. In this formalism, the dynamics in a long-range force such as gravity is better described using angle-action coordinates. I will now present this framework, as well as the statistical tools describing the ensemble of particles.

1.3.1 Mean field hypothesis

Here and throughout this manuscript, I will consider that gravity is a long-range interaction, and that the system is composed of a large number of particles. As a consequence, I can make the assumption that *a single particle effectively feels the mean potential from the accumulation of all other particles, independently of the precise position of each of these particles.* All particles in the system therefore interact with each other only through the mean potential that they self-consistently generate together. It is then equivalent to assuming that the system is collisionless, i.e. that the particles do not actually interact with one another. Of course, to be effective, this approximation requires that the background potential be a good representation of the distribution of stars in the system.

1.3.2 Hamilton's equations and angle-action coordinates

To describe the dynamics of a test particle in a gravitational potential, I will rely on the Hamiltonian framework. Noting $\mathbf{x}$ and $\mathbf{v}$ the vectors of 3-dimensional positions and velocities of that particle, I can define a scalar function, the Hamiltonian $H(\mathbf{x}, \mathbf{v}, t)$, which describes the full dynamics of that particle.

The evolution equations are then given by Hamilton's equations

$$\dot{\mathbf{x}} = \frac{\partial H}{\partial \mathbf{v}} \quad ; \quad \dot{\mathbf{v}} = -\frac{\partial H}{\partial \mathbf{x}}, \tag{1.1}$$

where dots denote the time derivative along the motion of the particle. Together with the initial conditions $\mathbf{x}_0, \mathbf{v}_0$, Hamilton's equations fully describe the particle's dynamics.

A particularly useful feature of Hamiltonian dynamics is the possibility to change the phase space coordinates in which the problem is expressed. Let me define the Poisson bracket applying to two scalar functions of phase space $f_1(\mathbf{x}, \mathbf{v}), f_2(\mathbf{x}, \mathbf{v})$ as

$$[f_1, f_2] = \frac{\partial f_1}{\partial \mathbf{x}} \cdot \frac{\partial f_2}{\partial \mathbf{v}} - \frac{\partial f_1}{\partial \mathbf{v}} \cdot \frac{\partial f_2}{\partial \mathbf{x}}. \tag{1.2}$$

In this notation, Hamilton's equations can be rewritten

$$\dot{\mathbf{w}} = [\mathbf{w}, H], \tag{1.3}$$

where I noted $\mathbf{w}$ the 6-dimensional vector $\mathbf{w} = (\mathbf{x}, \mathbf{v})$. Now let me consider a new set of phase space coordinates $\mathbf{u} = (\mathbf{q}, \mathbf{p})$. Let me also assume that these new coordinates are canonical, i.e. they satisfy, whatever i, j,

$$[u_i, u_j] = \mathbf{J}_{ij}, \tag{1.4}$$

where $\mathbf{J}$ is the symplectic matrix

$$\mathbf{J} = \begin{pmatrix} \mathbf{0} & \mathbf{I} \\ -\mathbf{I} & \mathbf{0} \end{pmatrix}, \tag{1.5}$$

with $\mathbf{I}$ the 3×3 identity matrix. Then, it can be shown that these new coordinates satisfy Hamilton's equations with the same Hamiltonian as $(\mathbf{x}, \mathbf{v})$, i.e.

$$\dot{\mathbf{u}} = [\mathbf{u}, H]. \tag{1.6}$$

Furthermore, the definition of the Poisson bracket is independent of the set of canonical coordinates chosen. Finally, different phase space coordinates define the same phase space volumes, i.e. $\mathrm{d}\mathbf{w} = \mathrm{d}\mathbf{u}$.

In star cluster dynamics, it can be interesting to reduce the complexity of Hamilton's equations by a suitable choice of canonical coordinates. For example, if the coordinates are chosen so that one of the $\partial H / \partial w_i$ vanishes (i.e. H is independent of w_i), then the dynamics of the conjugate momentum is straightforward (it is constant, see eq. (1.1)).

This is the case of an integral of the motion $I(\mathbf{w})$. It is defined by a function of phase space which is constant along the orbits. Denoting $\mathrm{d}/\mathrm{d}t$ the time derivative following the trajectory (i.e. the total derivative w.r.t. time), one has $\mathrm{d}I/\mathrm{d}t = 0$. If $I(\mathbf{w})$ is an isolating integral, it is then enlightening to try and use it as one of the phase space coordinates. This property is defined by the fact that for any value I_0 in the image of $I(\mathbf{w})$, the level set of I_0 (i.e. the part of phase space where $I(\mathbf{w}) = I_0$) is a smooth manifold of dimension 5. Now suppose that there are 3 independent isolating integrals (i.e. each integral is isolating, and their differentials are linearly independent in all points). Such systems, where the phase space can be completely described by integrals of the motion, are called integrable systems. In integrable systems, it is possible to build a set of canonical coordinates, called the angle-action coordinates and noted $(\boldsymbol{\theta}, \mathbf{J})$, where the actions $\mathbf{J}$ are independent isolating integrals of the motion. Consequently, Hamilton's equations written in action-angles coordinates impose that the Hamiltonian be independent of the angles $\boldsymbol{\theta}$, i.e. $H = H(\mathbf{J}, t)$. Then, the motion of the angles is much simplified, as given by the remaining set of Hamilton's equations

$$\dot{\boldsymbol{\theta}} = \frac{\partial H}{\partial \mathbf{J}} = \boldsymbol{\Omega}(\mathbf{J}, t), \tag{1.7}$$

where I defined the orbital frequencies $\boldsymbol{\Omega}$ as the rate of change of the angles $\boldsymbol{\theta}$ along the trajectory. Note that these frequencies may change in time, reflecting changes in the background potential. However, in a stationary state, the angles undergo a uniform quasi-periodic motion. In a stationary state, the interest of the angle-action coordinates is therefore to describe the complex kinematics of the system by a set of constant actions and of angles which are correspondingly linearly growing in time. Figure 1.9 illustrates the angle-action coordinates of a unidimensional harmonic oscillator. The use of this set of canonical coordinates allows us to describe its dynamics by $(\theta(t), J)$, where J is constant and θ is linearly growing in time. This greatly simplifies the description by positions and velocities $(x(t), v(t))$,

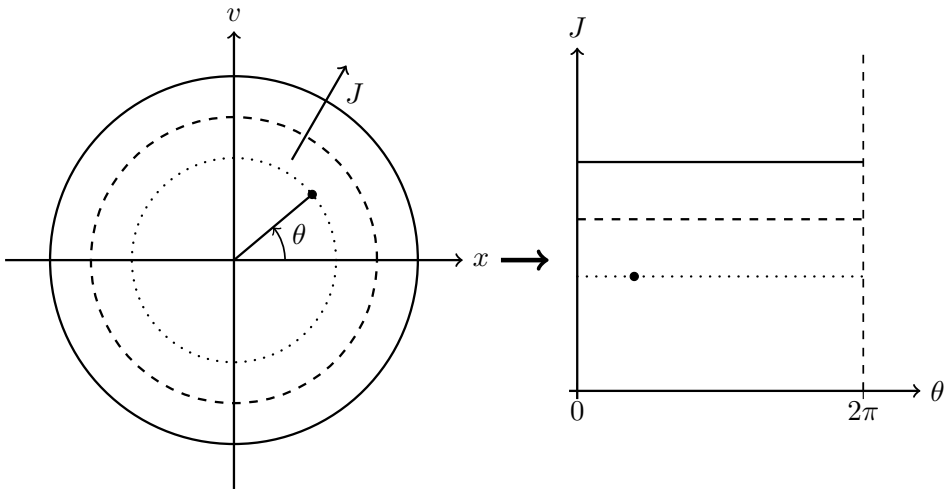

Figure 1.9: Extracted from Fouvry (2016). Phase space diagrams of a unidimensional harmonic oscillator. *Left panel:* Particle's trajectories in (x, v) coordinates (position and velocity). In these coordinates, the dynamics is described in terms of trigonometric functions of time. The action (essentially the energy), however, is related to the size of the phase space circle, and is a constant of the motion. The angle runs over the circle. *Right panel:* Same phase space diagrams in the (θ, J) plane. The angle being 2π-periodic, this plane is homeomorphic to a cylinder. In higher dimensions, the angle-action space is therefore homeomorphic to a torus.

which are trigonometric functions of time. Angle-action coordinates therefore reveal the fundamental orbital structure of that dynamics.

In a stationary spherical system, one can easily show that the energy, the norm of the angular momentum and the projection of the angular momentum along a fixed cartesian axis are conserved. From these three conserved quantities, one can derive a set of canonical variables where three of them are independent isolating integrals of the motion. This set is composed of the radial action J_r, i.e. the radial integral of the radial velocity between peri- and apocentre (see eq. 2.58), the norm L of the angular momentum, and its projection along the z direction, L_z. As a consequence, *spherically symmetric systems are generally integrable*[1].

1.3.3 Statistical description of an N-body system

Due to the large number of particles, statistical methods can be used to describe the state of an N-body system. Let me define a mesoscopic element of phase space, as an element small enough that it essentially follows a single trajectory, but large enough that there is a sufficient number of particles in the region to compute average physical quantities. I can then define the phase space density F as the average mass of stars in a phase space element, divided by the volume of the element. In that expression, F is known as the phase space distribution function (DF). As such, it satisfies the normalisation convention

$$\int \mathrm{d}\mathbf{w}\, F = M_{\rm tot}, \tag{1.8}$$

with $M_{\rm tot}$ the total active mass. Since all particles are assumed to be identical, F can also be considered as the probability DF of a single particle evolving in the mean-field potential. It is therefore a function of $(\mathbf{x}, \mathbf{v}, t)$ of a single particle. To ensure the self-consistency of this DF, it can be integrated to reproduce the spatial structure of the cluster, so that

$$\rho_0(\mathbf{x}, t) = \int \mathrm{d}\mathbf{v}\, F(\mathbf{x}, \mathbf{v}, t), \qquad \psi_0(\mathbf{x}, t) = -G \int \mathrm{d}\mathbf{x}'\, \mathrm{d}\mathbf{v}'\, \frac{F(\mathbf{x}', \mathbf{v}', t)}{|\mathbf{x}' - \mathbf{x}|}, \tag{1.9}$$

where ρ_0 is the spatial density of the cluster and ψ_0 its potential. Here, the potential and density are equivalently related by the Poisson equation

$$\Delta \psi_0 = 4\pi G \rho_0. \tag{1.10}$$

[1] In practice, orbits in a spherically symmetric system present a fourth integral of the motion, the third angle θ_3, conjugate variable of $J_3 = L_z$. This fourth integral reflects the fact that orbits are confined to a plane, which does not precess around the vertical axis. In the following, I will consider it as any other angle, but with a frequency $\Omega_3 = 0$.

Since F represents the density of stars in phase space, it satisfies the continuity equation

$$\frac{\partial F}{\partial t} + \frac{\partial}{\partial \mathbf{w}} \cdot (F\,\dot{\mathbf{w}}) = 0, \tag{1.11}$$

where $\dot{\mathbf{w}}$ follows the individual equation of motion given by eq. (1.3). Equation (1.11) is the collisionless Boltzmann equation (CBE). It describes the conservation of the phase space mass distribution along the trajectories. The quantity $F(\mathbf{w})\,\mathrm{d}\mathbf{w}$ can be interpreted as the mass in a volume $\mathrm{d}\mathbf{w}$ around the phase space position $\mathbf{w}$.

The interest of the angle-action coordinates becomes obvious when used in the CBE. Indeed, applying Hamilton's equations, the CBE can be rewritten

$$\frac{\partial F}{\partial t} + [F, H(F)] = 0. \tag{1.12}$$

Using angle-action coordinates, one gets

$$\boxed{\frac{\partial F}{\partial t} + \boldsymbol{\Omega}(\mathbf{J}) \cdot \frac{\partial F}{\partial \boldsymbol{\theta}} = 0.} \tag{1.13}$$

Note that this equation is non-linear, because the definition of the angle-action coordinates, and therefore also of the frequencies, depends of the phase space DF via the background potential, ψ_0. From the CBE in this form, one sees that its steady-state solutions (i.e. $\partial F/\partial t = 0$) are systems in which $F = F(\mathbf{J})$. This is known as the Jeans theorem (Jeans, 1915). In this manuscript, DFs corresponding to steady-state solutions of the CBE are called equilibria. This notion of equilibrium has the following meaning. If the system has so many particles (an infinite number, each of infinitesimal mass) that it is exactly described by the background potential, then its phase space distribution remains constant. In real cases, only quasi-equilibria can be reached by a stellar system, because it will always evolve due to its finite number of constituents (see the kinetic theory of self-gravitating systems, e.g., Jeans, 1929; Chandrasekhar, 1942, 1943a,b, 1949; Hamilton et al., 2018), and as importantly because it does not evolve in isolation.

1.3.4 Linearising the collisionless Boltzmann equation

My work extensively relies on the ability to build self-consistent equilibrium distributions for spherical systems, i.e. where the DF is associated with the right potential. Indeed, I am mainly interested in how spherical equilibria respond to perturbations in the background potential. To deal with this question, I assume that the perturbing potential is small, and rely on a linear expansion of the CBE. Hence, I consider an equilibrium DF, F, corresponding to a background potential ψ_0, which verifies (from eq. (1.13))

$$\boldsymbol{\Omega}(\mathbf{J}) \cdot \frac{\partial F}{\partial \boldsymbol{\theta}} = 0. \tag{1.14}$$

Note that the information on the background potential impacts several elements of that equation: the definition of the angle-action variables, and the frequency $\boldsymbol{\Omega}(\mathbf{J})$ (see eq. (1.7)). Let me now assume that this equilibrium is perturbed by an external potential, $\psi^{\mathrm{e}} \ll \psi_0$. The system reshuffles under the effect of this perturbation, so that overall, its own self-generated potential is now $\psi_0 + \psi^{\mathrm{s}}$, with $\psi^{\mathrm{s}} \ll \psi_0$. This rearrangement in the system corresponds to the change of the DF into $F + f$, with $f \ll F$. Owing to self-consistency, the perturbations in the potential and in the DF are related by

$$\psi^{\mathrm{s}}(\mathbf{x}, t) = -G \int \mathrm{d}\mathbf{x}'\,\mathrm{d}\mathbf{v}'\,\frac{f(\mathbf{x}', \mathbf{v}', t)}{|\mathbf{x}' - \mathbf{x}|}. \tag{1.15}$$

Note that the dynamics can still be described by the angle-action variables of the equilibrium distribution, so this DF perturbation accounts for perturbations to the angles and actions due to the perturbation of the potential. However, in these variables, the perturbed Hamiltonian is no more a function of the actions only. It is now given by

$$H(\mathbf{J}, \boldsymbol{\theta}) = H_0(\mathbf{J}) + (\psi^{\mathrm{e}}(\mathbf{J}, \boldsymbol{\theta}, t) + \psi^{\mathrm{s}}(\mathbf{J}, \boldsymbol{\theta}, t)), \tag{1.16}$$

where H_0 is the Hamiltonian of the equilibrium potential,

$$H_0(\mathbf{J}) = \frac{v^2}{2} + \psi_0(\mathbf{x}). \tag{1.17}$$

Since the perturbed system is assumed to be also collisionless, it verifies the CBE, so that

$$\frac{\partial F}{\partial t} + \frac{\partial f}{\partial t} + [F + f, H_0 + (\psi^{\rm e} + \psi^{\rm s})] = 0. \tag{1.18}$$

Developing the Poisson bracket and simplifying with the equilibrium CBE, and the facts that $F = F(\mathbf{J})$ and $H_0 = H_0(\mathbf{J})$, one gets

$$\frac{\partial f}{\partial t} + \boldsymbol{\Omega}(\mathbf{J}) \cdot \frac{\partial f}{\partial \boldsymbol{\theta}} - \frac{\partial F}{\partial \mathbf{J}} \cdot \frac{\partial(\psi^{\rm e} + \psi^{\rm s})}{\partial \boldsymbol{\theta}} - \frac{\partial f}{\partial \mathbf{J}} \cdot \frac{\partial(\psi^{\rm e} + \psi^{\rm s})}{\partial \boldsymbol{\theta}} = 0. \tag{1.19}$$

The linearised CBE is obtained by keeping only first order terms in the perturbations, giving

$$\boxed{\frac{\partial f}{\partial t} + \boldsymbol{\Omega}(\mathbf{J}) \cdot \frac{\partial f}{\partial \boldsymbol{\theta}} - \frac{\partial F}{\partial \mathbf{J}} \cdot \frac{\partial(\psi^{\rm e} + \psi^{\rm s})}{\partial \boldsymbol{\theta}} = 0.} \tag{1.20}$$

This equation shows that, following the unperturbed orbits, the rate of change of the perturbed distribution is directly proportional to the $\boldsymbol{\theta}$-gradient of the perturbed potential. Throughout the manuscript, I use this equation together with the Poisson equation to describe the linear response of spheroidal stellar systems. Since the Poisson equation (eq. (1.10)) is linear, it can be straightforwardly expressed in the perturbations as

$$\boxed{\Delta\psi^{\rm s} = 4\pi G\rho^{\rm s}.} \tag{1.21}$$

The linearised collisionless Boltzmann – Poisson system is the fundamental equation on which the linear response of self-gravitating, collisionless systems is built. The analytical methods I use are all derived from this system. Studying the linear response of a system usually amounts to solving for the self-consistent potential and DF perturbations (resp., $\psi^{\rm s}$ and f) generated by a given external potential $\psi^{\rm e}$.

1.4 Linear stability of spherical star clusters

Three main approaches are generically used to study the linear stability of spherical star clusters: analytical methods based on variational principles, analytical methods based on the resolution of the linearised collisionless Boltzmann - Poisson system, and numerical N-body methods.

Variational principles typically involve an argument based on the sign of the energy which can be extracted from the system. The theorems derived by variational principles led to general constraints on the phase space structure of stable equilibria. Antonov's second law (Antonov, 1961; Gillon, 1980) states that a stellar system with an ergodic DF (i.e. $F = F(E)$, with E the energy of a particle), where the DF satisfies $\mathrm{d}F/\mathrm{d}E < 0$, is stable to any non-spherically symmetric perturbation. Conversely, the Doremus-Feix-Baumann theorem (Doremus et al., 1971) states that the same DFs are also stable to spherically symmetric perturbations, so that such spheres are linearly stable overall. Together, these results constrain the density profile that a stable ergodic (therefore isotropic) equilibrium can have.

A peculiar class of models are studied for their resemblance with NSCs: those with a central mass representing a significant fraction of the total mass. In these cases, the frequency structure differs a lot from that of a cuspy or cored smooth potential. Tremaine (2005) exhibits unstable and neutral modes in such systems. Polyachenko et al. (2008) investigate the role of angular momentum distribution in these clusters, showing that non-monotonic distributions may lead to an instability.

For anisotropic equilibria, fewer general analytical results exist, although I should mention those of Kandrup & Sygnet (1985); Perez & Aly (1996), who prove the stability of a large class of non-rotating and rotating spherical equilibria to spherically symmetric perturbations. In this regime, linear stability results mostly rely on N-body simulations, and methods based on the resolution of the linearised CBE. This is particularly true in the radially anisotropic regime, where a destabilising process occurs, called the radial orbit instability (ROI). Since the first analytical and numerical results on the ROI by Antonov (1973) and Henon (1973), two main processes have been proposed as the source of this instability in radially biased systems. On the one hand, Barnes et al. (1986) show that the dispersion in the tangential velocities of radial orbits is too low to overcome the gravitational force. This identifies the ROI as a Jeans-like process. On the other hand, the analytical model by Palmer & Papaloizou (1987) associates the ROI with the spherical counterpart of the tumbling process in stellar disks, first proposed by Lynden-Bell (1979). According to this process, the torque imposed by a weak bar-like perturbation on radial orbits leads to a change in their precession rates. This change acts so that the bar and the orbit are

more aligned. As a consequence, any weak bar-like perturbation can grow, and hence be the basis of an instability. Figure 1.10a sketches the alignment of highly elongated orbits, which is the basis of the ROI.

Even though the identification of the instability is about 50 years old, there still is no consensus. While Merritt (1987) favours the tumbling-like instability by arguing that the particles move too fast on their orbits for the Jeans-like process to occur, Polyachenko & Shukhman (2015, 2017) recently showed that the tumbling-like process could not account for all instabilities in radially anisotropic systems (especially when they have a high pattern speed, or an odd degree of symmetry). Still, this instability is thought to have an important role in the formation of galaxies and DM halos (van Albada, 1982; Merritt & Aguilar, 1985). A comprehensive review on the ROI can be found in Maréchal & Perez (2011).

The analytical methods I will use derive from the matrix method of Kalnajs (1977). Similar methods were previously used to study the ROI, e.g. by Polyachenko & Shukhman (1981) (who were the first to derive the matrix method for spherical systems), Saha (1991), Weinberg (1991a) and Polyachenko & Shukhman (2015). I will present this method in detail in Chapter 2. In Section 2.3.3, I compare results from my own implementation to those from Saha (1991).

1.5 Overview

This manuscript is dedicated to the linear stability of spherical star clusters with a smooth cored potential and a velocity distribution presenting anisotropy, rotation and shear. The methods I will use are mainly analytical, relying on the response matrix, and are often complemented by results from N-body simulations. *Through this study, I will try to answer the following questions: By which processes can an anisotropic rotating star cluster reshuffle its orbital structure and access the free energy encoded in its kinematic anisotropy and rotation? What specific role do resonances play in the process? Which resonance matters most, and how do they operate? How anisotropic and rotating can a stable system be? Can one design simple stability criteria for anisotropic rotating clusters? Can the analytical matrix method be made more efficient than direct N-body explorations?*

Note that my work will mainly focus on $\ell = 2$ (i.e. quadrupolar, or two-armed) instabilities. Indeed, modes with larger multipolar numbers involve smaller physical scales, and it is therefore likely that self-gravity is dampened in those cases. Conversely, $\ell = 1$ modes may be important to the dynamics of star clusters (see, e.g., Weinberg, 1994), however I chose not to consider them. Indeed, I will show that already many instabilities in spherical clusters develop with $\ell = 2$, and N-body simulations confirm that these are the main ones.

In Chapter 2, I will derive the response matrix for spherical systems, from the linearised collisionless Boltzmann – Poisson system of equations. I will explain in detail the specific numerical methods I developed for the computation of the response matrix. These new techniques largely improve the computational time, and bring this analytical method to a state where systematic parameters explorations are possible, with performances sometimes better than those reached by numerical simulations. To validate my new implementation, I will reproduce results from Saha (1991) on the radial orbit instability.

Chapter 3 focuses on a scarcely explored regime in non-rotating spherical star clusters presenting kinematic anisotropy: tangentially anisotropic systems. For context, I will build upon the analytical derivation from Palmer et al. (1989) for the existence of a circular orbit instability (COI), and perform a thorough exploration of this regime with different versions of the response matrix. The COI involves the resonant interaction of nearly circular orbits at a particular frequency. It is sketched in Fig. 1.10b. Using my new implementation, I will explore the parameter space of increasing tangential anisotropy, detect a slowly growing instability in that regime, and confirm, using a new method with a restricted matrix, that this instability is indeed the COI. Finally, I will report on attempts to detect it in the regime of extreme tangential anisotropy, where orbits are all circular.

In Chapter 4, I will examine rotating spheres with various anisotropies. I will first recall an analytical derivation from Allen et al. (1992), giving the argument for a possible instability driven by the rotation of the cluster, the tumbling instability (TI). The origin of this process will be developed in Chapters 4 and 5. It is related to oscillations in the orientation of orbital planes, as sketched in Fig. 1.10c. In order to perform a parameter space exploration of anisotropic, rotating spheres, I will derive the response matrix for rotating spherical star clusters, which is significantly more costly given the loss of symmetry. Using the matrix and N-body methods, I will then show that a large fraction of anisotropic, rotating clusters are indeed linearly unstable, displaying violent instabilities in some cases. I will identify a phenomenological stability criterion from this parameter exploration. I will finally focus on the radially anisotropic regime, trying to disentangle the relative role of the ROI and the TI. In this regime, it seems that the TI never exists on its own, and rather enhances the ROI.

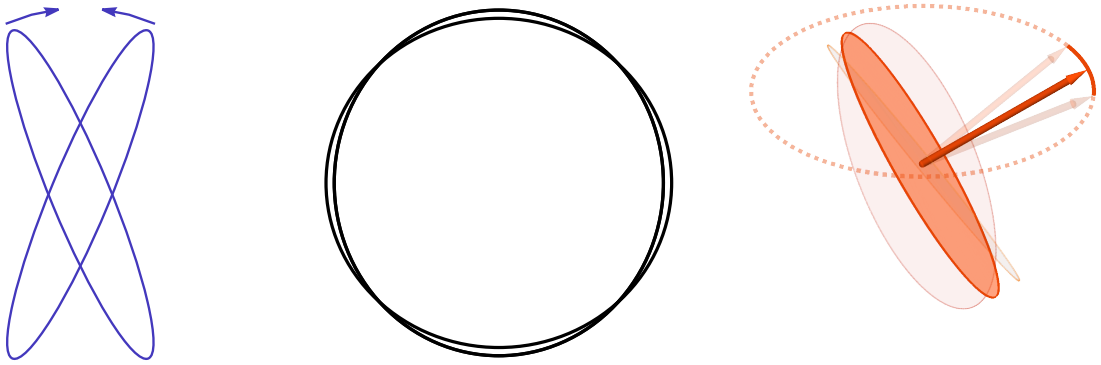

(a) ROI (b) COI (c) TI

Figure 1.10: Sketches representing the three types of instabilities discussed in my manuscript. (a) The radial orbit instability (ROI) relies on the alignment of elongated orbits. (b) The circular orbit instability (COI) occurs in systems composed of many nearly circular orbits. (c) The tumbling instability (TI) involves the precession of orbital planes around the cluster's rotation axis, as well as an oscillation of their inclination.

Chapter 5 further elaborates on the construction of a stability criterion, especially in the regime of tangentially anisotropic, rotating spheres, with intricate rotation patterns. I will discuss stability results stemming from both the matrix method and N-body simulations, with an interest on the particular positions in the cluster which are determinant to the instabilities. To analyse the destabilising processes in more details, I will present orbital frequency measurements in N-body simulations, complementing results from the restricted matrix method. These results enlighten the role of different parts of the cluster in the instability, in relation with the COI and tumbling processes. I will show that, in tangentially anisotropic systems too, the TI enhances the COI, and does not seem to develop its own instability.

Finally, in Chapter 6, I will conclude and discuss the implications of my work on various current subjects of interest in astrophysics. I will also present some possible future advancements, as well as new questions that my work triggered.

Chapter 2

Matrix methods for spheres

2.1 Introduction

The stability of a given equilibrium to a small perturbation can be roughly addressed while making the following distinction: if the response of the system tends to absorb the perturbation, so that the final state is essentially the same as the initial equilibrium, then the system is stable; otherwise, if the system's response is much larger than the initial amplitude of the perturbation, and leads it to a completely different state, then the system is unstable. Although simplistic in general[1], this definition gives at least an accurate idea of what an *instability* is. In some areas of physics, including the cases of stellar and fluid equilibria, the definition of an instability is sometimes more restrictive: the response of the system should have an *exponential* growth in time. This restriction is allowed by the linear structure of the equations governing the dynamics of these systems, and yields dispersion relations, linking the shape of a perturbation to typical frequencies, i.e. growth and oscillation.

Here, my focus will be on so called linear stability: the physical systems will be assumed to be in an equilibrium configuration, i.e. a configuration which should be a steady state. On top of this background equilibrium, I will consider small perturbations, and evaluate their effect on the system at linear order in the phase space perturbations. In self-gravitating systems, the perturber can take the form of a small gravitational potential that is added to the background equilibrium configuration. Depending on what is defined as the system, another example of perturbation can be another small system that comes to interact with that of interest, such as a minor merger in the case of galaxies and dark matter halos in general. As the background mean potential is the result of smoothing individual stars or particles, its actual graininess must also be considered as a perturbation. As a consequence, any N-body realisation of a stellar system intrinsically presents some internal Poisson perturbation, even if the initial conditions are drawn from the isolated equilibrium of interest.

In self-gravitating systems, instabilities emerge as modes of the system, i.e. self-sustained patterns that grow exponentially in time. The general framework to study the linear stability of self-gravitating systems is based on the search for exponentially growing global modes, hence it follows the steps illustrated in Fig. 2.1:

- Consider an external perturbing potential of some form.
- Use the linearised CBE (eq. (1.20)), which describes the system's dynamical evolution, to compute the perturbation to the system's phase space DF entailed by the external perturber.
- From the DF perturbation, compute the density perturbation entailed by the external perturber.
- Using the Poisson equation, compute the potential perturbation associated with the density perturbation.
- Loop the process so that the system also responds to the subsequent perturbations, at every step. At this point, one is able to describe the dressed linear response of the system to any external perturber.

[1] In particular, this distinction does not incorporate systems in which a perturbation can have a large but transient effect, leading to an equilibrium somewhat close to the initial state of the system. This is the case of the swing amplification in disks (Toomre, 1981), or of weakly damped $\ell = 1$ modes in spherical clusters (Weinberg, 1994).

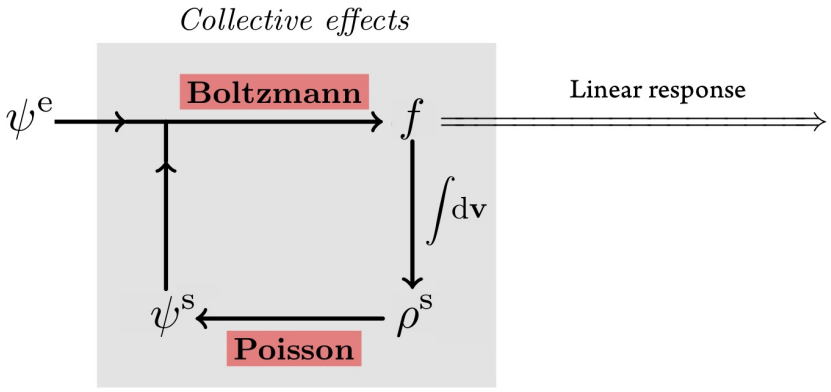

Figure 2.1: Sketch of the procedure for computing the linear response of a self-gravitating system. Here, ψ^{e} is the external perturbing potential. It creates the wake f in the system's DF. This wake is self-consistently integrated to ρ^{s}, the self-generated density perturbation in the system. Through the Poisson equation, this density perturbation corresponds to the potential perturbation ψ^{s}. Finally, the system also responds to this polarisation, so the potential perturbation retroactively acts on the system again.

- Look for external perturbers for which the response is equal to the forcing, in which case the mode is self-sustained. If one such self-sustained mode exists with a positive value of the growth rate, then the system is unstable to this particular perturber. Note that if the growth rate is too low, secular effects, such as orbital diffusion, might affect the system before the linear instability grows significantly, swamping the effect of the instability.

Once a mode with sufficiently large growth rate has been found (compared to, say, a fraction of a Hubble time), one can usually consider the system as unstable, i.e. one can consider that the mode will necessarily grow. Indeed, the particle noise has in general some initial amplitude in every possible perturber's shape, so that a system which is unstable to a particular perturber will usually be destabilised by the corresponding shot noise.

In some cases, the proof of stability or instability does not require looking for particular modes of the system, but only describing the properties of the operator that links a general external perturber to the perturbation it creates in the system. For example, it is sometimes possible to derive general properties of the system, while relying on the evolution of its energy when exposed to any kind of perturbation. Historically, this path was taken by Antonov (1961) to prove what is now called Antonov's second law, and by Doremus et al. (1971) to prove the Doremus-Feix-Baumann theorem (see Section 1.4). Similar arguments are given in Palmer et al. (1989) and Allen et al. (1992) to prove the existence of the circular orbit and tumbling instabilities, and detailed reference to these demonstrations will be made in Sections 3.2 and 4.2. Conversely, Mikhaĭlovskiĭ et al. (1971) and Synakh et al. (1971) (see also Fridman et al., 1984a) use particular test functions to prove the stability of homogeneous spherical systems made of circular orbits, resp. without and with net angular momentum.

A major breakthrough in the characterisation of linear modes in collisionless systems was made in Kalnajs (1977), reframing the previously integro-differential problem into a matrix eigenvalue problem while relying on functional bases in potential and density. This framework, called the matrix method, is what I will mainly use in my thesis to characterise instabilities in spherical systems. Since its first formulation, it inspired a number of stability studies of various self-gravitating systems. These include studies of disk systems (Zang, 1976; Kalnajs, 1978; Sawamura, 1988; Palmer & Papaloizou, 1990; Vauterin & Dejonghe, 1996; Pichon & Cannon, 1997; Evans & Read, 1998a,b; Jalali & Hunter, 2005; Jalali, 2007, 2008; Dury et al., 2008; De Rijcke & Voulis, 2016; De Rijcke et al., 2019a,b), axisymmetric structures (Palmer et al., 1990; Weinberg, 1991b) and spherical systems (Polyachenko & Shukhman, 1981; Tremaine & Weinberg, 1984; Palmer & Papaloizou, 1987, 1988; Saha, 1991; Weinberg, 1991a, 1994; Bertin et al., 1994; Tremaine, 2005; Polyachenko et al., 2012; Polyachenko & Shukhman, 2015; Rozier et al., 2019; Breen et al., 2020). The upcoming sections are devoted to the derivation of the response matrix for general self-gravitating collisionless spherical systems. I particularly insist on new features I developed in the numerical implementation of the response matrix, which considerably improve the computation speed (by a factor of about 1000), and a validation of the implementation based on recovering previously published instabilities.

In the literature, different denominations are sometimes used for modes which oscillate (the frequency

has a non-zero real part) in addition to their exponential growth, which are usually called *overstabilities*, while their non-oscillating counterparts are called instabilities. In this manuscript, I will sometimes refer to the latter as *purely growing* instabilities. Notice that for modes with multipolar number $m \neq 0$, oscillation is equivalent to the rotation of the pattern. Among other modes that a system can exhibit are the *neutral* modes (with a growth rate equal to 0) and the *damped* modes (with negative growth rate).

2.2 The response matrix

The purpose of this section is to develop the expression of the response matrix from the general equations that rule the dynamics of collisionless systems, and to show how this tool can be used to detect instabilities in stellar clusters.

2.2.1 The linearised collisionless Boltzmann equation

As I underlined in Section 1.3.3, the present study of the linear stability of stellar systems relies on the linearisation of the collisionless Boltzmann – Poisson system in angle-action coordinates. Noting $\psi^{\rm e}$ the external potential perturbation and $\psi^{\rm s}$ the subsequent potential wake in the system, F the equilibrium DF and f its perturbation, the linearised collisionless Boltzmann equation (CBE) is

$$\frac{\partial f}{\partial t} + \boldsymbol{\Omega}\cdot\frac{\partial f}{\partial \boldsymbol{\theta}} - \frac{\partial F}{\partial \mathbf{J}}\cdot\frac{\partial [\psi^{\rm e}+\psi^{\rm s}]}{\partial \boldsymbol{\theta}} = 0, \tag{2.1}$$

where I recall that $\boldsymbol{\Omega}(\mathbf{J})$ are the orbital frequencies of motion. My goal is to find modes of the system that have a time evolution proportional to $\mathrm{e}^{-\mathrm{i}\omega t}$, where $\omega = \omega_0 + \mathrm{i}\,\eta$ is the complex frequency of the mode. The real part ω_0 of the frequency is the oscillation frequency. It represents the rate at which a particular point in the system sees the mode oscillating, and is related to the *pattern speed* $\Omega_{\rm p}$ of the mode through the relation $\omega_0 = m\,\Omega_{\rm p}$, where m is the degree of symmetry of the mode (e.g., $m = 1$ for seiche modes, $m = 2$ for bars and 2-armed spirals, ...). The pattern speed is the angular rate at which the mode rotates around its rotation axis. The imaginary part η of the frequency is the growth rate of the mode. It characterises the rate with which the amplitude of the mode grows in time, and in the present convention it is positive for instabilities and negative for damped modes.

In eq. (2.1), any function of the phase space coordinates must be 2π-periodic in the angles, as the phase space coordinates themselves are. As a consequence, f and $\psi = \psi^{\rm e} + \psi^{\rm s}$ can be expanded in Fourier series of the angles as

$$\begin{aligned} f(\boldsymbol{\theta},\mathbf{J},t) &= \sum_{\mathbf{n}} f_{\mathbf{n}}(\mathbf{J},t)\,\mathrm{e}^{\mathrm{i}\mathbf{n}\cdot\boldsymbol{\theta}} \quad , \quad f_{\mathbf{n}}(\mathbf{J},t) = \int \frac{\mathrm{d}\boldsymbol{\theta}}{(2\pi)^3}\, f(\mathbf{J},\boldsymbol{\theta},t)\,\mathrm{e}^{-\mathrm{i}\mathbf{n}\cdot\boldsymbol{\theta}}, \\ \psi(\boldsymbol{\theta},\mathbf{J},t) &= \sum_{\mathbf{n}} \psi_{\mathbf{n}}(\mathbf{J},t)\,\mathrm{e}^{\mathrm{i}\mathbf{n}\cdot\boldsymbol{\theta}} \quad , \quad \psi_{\mathbf{n}}(\mathbf{J},t) = \int \frac{\mathrm{d}\boldsymbol{\theta}}{(2\pi)^3}\, \psi(\mathbf{J},\boldsymbol{\theta},t)\,\mathrm{e}^{-\mathrm{i}\mathbf{n}\cdot\boldsymbol{\theta}}, \end{aligned} \tag{2.2}$$

where $\mathbf{n} \in \mathbb{Z}^3$ is the triplet of Fourier coefficients associated with the angles. Multiplying eq. (2.1) by $\mathrm{e}^{-\mathrm{i}\,\mathbf{n}\cdot\boldsymbol{\theta}}$ and integrating over angles, each Fourier component separately satisfies

$$\frac{\partial f_{\mathbf{n}}}{\partial t} + \mathrm{i}\,\mathbf{n}\cdot\boldsymbol{\Omega}\, f_{\mathbf{n}} - \mathrm{i}\,\mathbf{n}\cdot\frac{\partial F}{\partial \mathbf{J}}\,\psi_{\mathbf{n}} = 0. \tag{2.3}$$

If the Laplace transform of time-varying quantities is now defined as

$$\widehat{X}(\omega) = \int_0^\infty \mathrm{d}t\, X(t)\,\mathrm{e}^{\mathrm{i}\omega t}, \tag{2.4}$$

the Laplace-transformed quantities verify

$$\left[f_{\mathbf{n}}\,\mathrm{e}^{\mathrm{i}\omega t}\right]_0^\infty + \mathrm{i}\,(\mathbf{n}\cdot\boldsymbol{\Omega} - \omega)\,\widehat{f}_{\mathbf{n}} - \mathrm{i}\,\mathbf{n}\cdot\frac{\partial F}{\partial \mathbf{J}}\,\widehat{\psi}_{\mathbf{n}} = 0. \tag{2.5}$$

Here, I made the assumption that the system is in its equilibrium state at $t = 0$, so that $f_{\mathbf{n}}(t = 0) = 0$. Furthermore, I assumed that $\mathrm{Im}(\omega) \geq \gamma$, where $\gamma > 0$ is large enough to ensure that $f_{\mathbf{n}}\,\mathrm{e}^{\mathrm{i}\omega t} \to 0$ as $t \to \infty$. Under these assumptions, the first term drops in eq. (2.5) and

$$\boxed{\widehat{f}_{\mathbf{n}}(\mathbf{J},\omega) = -\mathbf{n}\cdot\frac{\partial F}{\partial \mathbf{J}}\,\frac{\widehat{\psi}_{\mathbf{n}}(\mathbf{J},\omega)}{\omega - \mathbf{n}\cdot\boldsymbol{\Omega}}.} \tag{2.6}$$

Through a linearisation of the collisionless Boltzmann equation, it is therefore possible, at every given Fourier mode $\mathbf{n}$ in angles and every time frequency ω, to establish a proportionality relation between the perturbing potential ψ, corresponding to the sum of the external perturber ψ^{e} and the wake in the system ψ^{s}, and the perturbation in the DF f. Interestingly enough, the amplitude of the DF perturbation depends on the variations of the equilibrium DF around the given actions, but more importantly the denominator in eq. (2.6) is resonant. At certain sets of actions $\mathbf{J}$ and angular Fourier numbers $\mathbf{n}$, the denominator $\omega - \mathbf{n}\cdot\boldsymbol{\Omega}$ can take very small values, which may dramatically amplify the DF perturbation. This observation will lead me to refer to the set of angular Fourier numbers $\mathbf{n}$ as the *resonance vector*.

Similar equations were used in the coordinate system of positions and velocities (see, e.g., Fridman et al., 1984a; Palmer, 1994; Vauterin & Dejonghe, 1996), but the present form in orbital space better highlights the properties of the response in orbital space. In order to produce an actual dispersion relation, it is necessary to make use of an independent relation linking the DF perturbation and the potential perturbation: the Poisson equation.

2.2.2 Bi-orthogonal potential-density bases

As advertised, the closing of the problem requires using the Poisson equation

$$\Delta\psi_0 = 4\pi G\rho_0, \tag{2.7}$$

which relates the potential to the density. This equation is linear, and as it is both satisfied by the equilibrium $(\psi_0,\ \rho_0)$ and total $(\psi_0+\psi,\ \rho_0+\rho)$ quantities, I immediately obtain for the linearised quantities

$$\Delta\psi = 4\pi G\rho. \tag{2.8}$$

The problem in the resolution of the system is that the Poisson equation only depends on the shape of the system in physical space. As a consequence, this equation is naturally described in $(\mathbf{x},\mathbf{v})$, but harder to represent in $(\boldsymbol{\theta},\mathbf{J})$ (but see Pichon & Cannon, 1997, for such a form). Furthermore, the Poisson equation is representative of the unscreened, long-range property of the gravitational force. Consequently, in general, it is not possible to restrict the perturbations locally in physical space. Results were produced in particular cases where either of these restrictions did not apply (for example, the hypothesis of homogeneity allows for the use of $(\mathbf{x},\mathbf{v})$ as angle action coordinates), but these cases do not apply to all observed spherical clusters.

Among the techniques developed to address this challenge is the seminal idea by Lin & Shu (1966), who linearised the Poisson equation by assuming that the perturbations are shaped as tightly wound spirals. The interest of this approach is that it gives a second, independent proportionality relation between ρ and ψ in configuration space. An actual dispersion relation can then be derived, linking the time frequency ω to the space frequency k_r, which represents the frequency of the oscillations in the radial direction. One issue concerning this assumption is that it is a WKB-like approximation, where perturbations are considered as local (they only have a gravitational influence at a small distance, and the over- and sub-densities average out at large distances), and this approach is therefore restricted to modes with a tightly-wound shape. I develop such methods for spherical clusters in Section 3.3.

Other authors (Fridman et al., 1984a; Palmer, 1994) performed a multipolar expansion of the potential perturbation, but in the end their dispersion relations still display integrals over radii. These methods are useful to demonstrate general stability properties for a variety of systems, by fully considering the global properties of the perturbations and not restricting them to a particular shape, but they usually fail to provide quantitative results in terms of growth rates, pattern speeds and shapes of the modes, as they only give access to integrated quantities. These specific methods, however, led to the description of particular destabilisation processes, and are discussed in Sections 3.2 and 4.2.

Here, I will first present Kalnajs' matrix method (Kalnajs, 1977), which uses bi-orthogonal bases in densities and potentials that are solutions to the Poisson equation, and projects all perturbations on such a basis. As I will show, this method, which transforms the problem into a matrix form, does not a priori assume a particular shape for the instabilities, nor assumes locality, and is able to provide a variety of quantitative results on the exhibited instabilities, such as their growth rates, pattern speeds and shapes in configuration space. Yet, this technique must deal with issues related to the actual truncation of the matrix.

The first step of the matrix method is to build a bi-orthogonal basis of potentials and densities that satisfies the Poisson equation. What is meant here is a set of potentials $(\psi^{(p)})_{p\geq 1}$ and densities $(\rho^{(p)})_{p\geq 1}$ that satisfies the three following conditions:

- Poisson equation: Whatever p, two corresponding elements must satisfy the Poisson equation, i.e.

$$\Delta\psi^{(p)} = 4\pi G\rho^{(p)}. \tag{2.9}$$

- Spanning condition: The (discrete) set of potentials (resp. densities) must be able to reconstruct any potential (resp. density). In other words, for every gravitational potential $\psi(\mathbf{x})$, there must exist a discrete set of numbers $(a_p)_{p\geq 1}$ so that[2]

$$\psi(\mathbf{x}) = \sum_p a_p \psi^{(p)}(\mathbf{x}). \tag{2.10}$$

  Note that this condition can be restricted to potentials with certain assumptions, for example a finite spatial extent, or some degree of symmetry. The span of a given set will determine the characteristics of the perturbers that the stability study can recover. In that respect, the WKB assumption can be seen as a particular choice of basis whose span only encompasses potentials with a fast radial oscillation, as I will develop in Section 3.3.1.

- Bi-orthogonality condition: The set of densities and potentials must satisfy the following bi-orthogonality condition. For any $p, q \geq 1$,

$$\int \mathrm{d}\mathbf{x}\, \psi^{(p)}(\mathbf{x})\, \rho^{(q)*}(\mathbf{x}) = -\delta_p^q. \tag{2.11}$$

  Note that in the present convention, the functions that represent potentials do not have the physical dimension of a potential, and the same goes for densities. Other conventions can be used (see, e.g., Hernquist & Ostriker, 1992), requiring to adapt the following results.

The construction of such bases was presented in previous studies for a variety of cases. These include bases for disks (Clutton-Brock, 1972; Kalnajs, 1976; Weinberg, 1999; Fouvry et al., 2015b) and for spheres (Clutton-Brock, 1973; Fridman et al., 1984b; Hernquist & Ostriker, 1992; Bertin et al., 1994; Zhao, 1996; Weinberg, 1999; Rahmati & Jalali, 2009; Lilley et al., 2018), with various properties (finite and infinite spatial extent, particular shape of the first term, tightly-wound spirals). Let me highlight the two types of bi-orthogonal basis sets which I will use in the following. The first one, which I use to test the response matrix implementation in Section 2.3, is presented in Fridman et al. (1984b) and relies on Bessel functions. It is suitable for spherical systems of finite extent. The second one, which I mainly use in the rest of the manuscript, was developed in Hernquist & Ostriker (1992) and relies on ultraspherical, or Gegenbauer, polynomials. It is suitable for potentials of infinite extent. In Section 3.3.1, I present a new basis for WKB-like perturbations in spherical systems.

2.2.3 The response matrix

The projection onto such a bi-orthogonal basis transforms the collisionless Boltzmann – Poisson system into a problem of linear algebra. In the end, the gravitational susceptibility of the system can be described by a response matrix. Here, I develop this argument and give the expression of that matrix as a function of the characteristics of the system, and of the basis. Following eq. (2.10), I can expand the potential perturbations on a given bi-orthogonal basis, so that

$$\psi^{\mathrm{s}}(\mathbf{x},t) = \sum_p a_p(t)\psi^{(p)}(\mathbf{x})\,;\ \psi^{\mathrm{e}}(\mathbf{x},t) = \sum_p b_p(t)\psi^{(p)}(\mathbf{x})\,;\ \psi(\mathbf{x},t) = \sum_p c_p(t)\psi^{(p)}(\mathbf{x}). \tag{2.12}$$

As a consequence of the Poisson property of the basis, the corresponding densities will have the same projection coefficients as the potentials, and the values of the coefficients are recovered through

$$a_p(t) = -\int \mathrm{d}\mathbf{x}\, \psi^{\mathrm{s}}(\mathbf{x},t)\, \rho^{(p)*}(\mathbf{x}) = -\int \mathrm{d}\mathbf{x}\, \rho^{\mathrm{s}}(\mathbf{x},t)\, \psi^{(p)*}(\mathbf{x}), \tag{2.13}$$

[2] The present definition may be somewhat unsatisfactory to readers attached to mathematical rigour. While this technique will be used on sufficiently regular potentials so that the measure of distances in the functional space can be considered rather intuitively in a point-by-point fashion, the particular measure that I consider here is that corresponding to multiplication with the complex conjugate of the density and integration over physical space. It is straightforward to show that, if I assume that the potential vanishes at infinity and has a square-integrable spatial derivative, this operation has the characteristics of a scalar product.

and similarly with b_p and $c_p = a_p + b_p$. Using the fact that the DF perturbation is linked to the density wake in the system through

$$\rho^{\mathrm{s}}(\mathbf{x}, t) = \int \mathrm{d}\mathbf{v}\, f(\mathbf{x}, \mathbf{v}, t), \tag{2.14}$$

I can develop eq. (2.13) as

$$a_p(t) = -\int \mathrm{d}\mathbf{x} \int \mathrm{d}\mathbf{v}\, f(\mathbf{x}, \mathbf{v}, t)\, \psi^{(p)*}(\mathbf{x}). \tag{2.15}$$

Developing the DF perturbation in resonance vectors, one gets

$$a_p(t) = -\int \mathrm{d}\mathbf{x} \int \mathrm{d}\mathbf{v} \sum_{\mathbf{n}} f_{\mathbf{n}}(\mathbf{J}, t)\, \mathrm{e}^{\mathrm{i}\mathbf{n}\cdot\boldsymbol{\theta}}\, \psi^{(p)*}(\mathbf{x}). \tag{2.16}$$

Performing a change of canonical variables in the integral from $(\mathbf{x}, \mathbf{v})$ to $(\boldsymbol{\theta}, \mathbf{J})$, whose Jacobian is equal to 1 owing to phase space volume conservation, I get

$$\begin{aligned} a_p(t) &= -\sum_{\mathbf{n}} \int \mathrm{d}\mathbf{J}\, f_{\mathbf{n}}(\mathbf{J}, t) \left(\int \mathrm{d}\boldsymbol{\theta}\, \mathrm{e}^{-\mathrm{i}\mathbf{n}\cdot\boldsymbol{\theta}}\, \psi^{(p)}(\mathbf{J}, \boldsymbol{\theta}) \right)^*, \\ &= -(2\pi)^3 \sum_{\mathbf{n}} \int \mathrm{d}\mathbf{J}\, f_{\mathbf{n}}(\mathbf{J}, t)\, \psi_{\mathbf{n}}^{(p)*}(\mathbf{J}), \end{aligned} \tag{2.17}$$

where the last expression was obtained thanks to eq. (2.2). I can now perform a temporal Laplace transform as prescribed by eq. (2.4), replace the angle Fourier-transformed DF perturbation by its expression in eq. (2.6), and obtain

$$\widehat{a}_p(\omega) = (2\pi)^3 \sum_{\mathbf{n}} \int \mathrm{d}\mathbf{J}\, \frac{\mathbf{n} \cdot \partial F / \partial \mathbf{J}}{\omega - \mathbf{n} \cdot \boldsymbol{\Omega}}\, \widehat{\psi}_{\mathbf{n}}(\mathbf{J}, \omega)\, \psi_{\mathbf{n}}^{(p)*}(\mathbf{J}). \tag{2.18}$$

Applying to ψ the decomposition of eq. (2.12), I get from eq. (2.18)

$$\widehat{a}_p(\omega) = \sum_q \widehat{c}_q(\omega) \left\{ (2\pi)^3 \sum_{\mathbf{n}} \int \mathrm{d}\mathbf{J}\, \frac{\mathbf{n} \cdot \partial F / \partial \mathbf{J}}{\omega - \mathbf{n} \cdot \boldsymbol{\Omega}}\, \psi_{\mathbf{n}}^{(p)*}(\mathbf{J})\, \psi_{\mathbf{n}}^{(q)}(\mathbf{J}) \right\}. \tag{2.19}$$

At a given frequency ω, the wake in the system, encoded in the vector $\widehat{\mathbf{a}}$, is expressed as the application of a given matrix to the vector of total perturbation $\widehat{\mathbf{c}}$. This matrix, called the response matrix, is defined as

$$\boxed{\widehat{M}_{pq}(\omega) = (2\pi)^3 \sum_{\mathbf{n}} \int \mathrm{d}\mathbf{J}\, \frac{\mathbf{n} \cdot \partial F / \partial \mathbf{J}}{\omega - \mathbf{n} \cdot \boldsymbol{\Omega}}\, \psi_{\mathbf{n}}^{(p)*}(\mathbf{J})\, \psi_{\mathbf{n}}^{(q)}(\mathbf{J}).} \tag{2.20}$$

This matrix for 3D systems was first derived by Polyachenko & Shukhman (1981). It contains all the information on the linear response of a system to any kind of gravitational perturbation. Its indexes reflect the basis elements, (m^p, ℓ^p, n^p) in one dimension and (m^q, ℓ^q, n^q) in the other. Again, at each frequency ω, the presence of orbits in the system that resonate at ω is critical to the response, which can be seen through the resonant denominator $\omega - \mathbf{n} \cdot \boldsymbol{\Omega}$. In practice, as I will show, the computation of the response matrix requires truncating the sum over resonance vectors at some order[3].

The problem of the response of the system to an external perturbation has now been rephrased in terms of linear algebra. To clarify this relationship, eq. (2.19) is developed at a given frequency ω as

$$\widehat{\mathbf{a}} = \widehat{\mathbf{M}} \cdot \widehat{\mathbf{c}} = \widehat{\mathbf{M}} \cdot (\widehat{\mathbf{a}} + \widehat{\mathbf{b}}). \tag{2.21}$$

Gathering the terms proportional to $\widehat{\mathbf{a}}$ on the left side and applying to both sides the inverse of $\mathbf{I} - \widehat{\mathbf{M}}$, one gets

$$\widehat{\mathbf{a}} = \left[\mathbf{I} - \widehat{\mathbf{M}}\right]^{-1} \cdot \widehat{\mathbf{M}} \cdot \widehat{\mathbf{b}} = \left(\left[\mathbf{I} - \widehat{\mathbf{M}}\right]^{-1} - \mathbf{I}\right) \cdot \widehat{\mathbf{b}}. \tag{2.22}$$

At that point, one should be careful with the existence and regular behaviour of the inverse of $\mathbf{I} - \widehat{\mathbf{M}}$, in particular regarding the necessary truncation of the matrix because of the finite number of basis

[3] Yet, this truncation is not physically meaningless: a very high angular Fourier number means that one is dealing with very small physical scales, where the mean field assumption is no longer valid. Hence, the definition of the response matrix will be understood as actually including a maximum value for the resonance vectors. This guarantees, in particular, that the matrix behaves like $|\omega|^{-1}$ when $|\omega| \to \infty$.

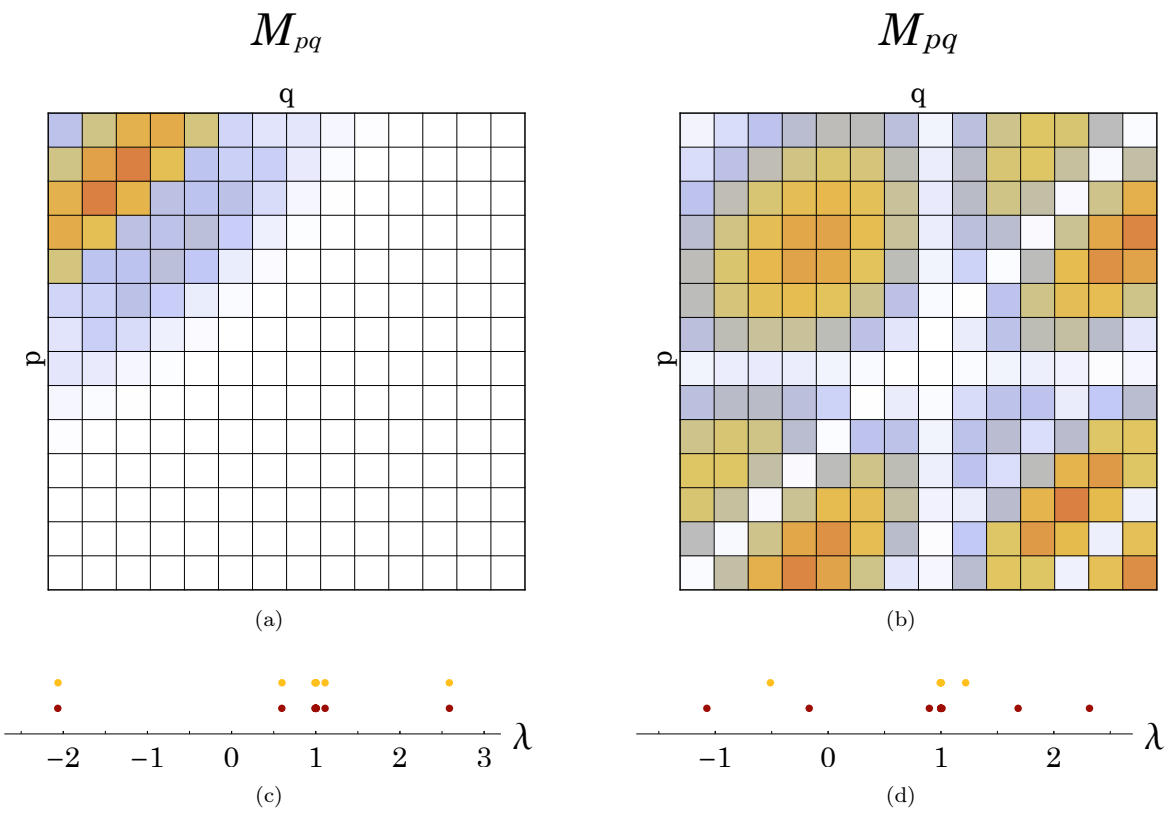

Figure 2.2: Sketch of the response matrix (top) and plot of its eigenvalues (bottom). The top plots show the absolute value of the matrix elements. In each case, the bottom plots shows two series of eigenvalues: the one of the full matrix $\mathbf{I}-\widehat{\mathbf{M}}$ (brown), and the one of the partial matrix made of the top-left quarter of $\mathbf{I}-\widehat{\mathbf{M}}$ (yellow). On the left, the matrix is well-represented by a low number of basis functions. Indeed, going from the top-left quarter to the full matrix only adds eigenvalues close to 1, and does not change the position of already existing eigenvalues. On the right, the matrix is poorly represented by a low number of basis functions: using only the top-left quarter leads to a bad estimate of the spectrum of the full matrix.

functions. Here comes into play the choice of a bi-orthogonal basis to treat a particular problem. Indeed, consider a basis which is able to describe the dynamics of the system at the perturbative order with a small number of basis functions. Then, the addition of extra lines and columns to the matrix (i.e. projecting the potential on a larger number of basis functions) will carry little information about the system, and the response matrix will take small values in these regions. In other words, the matrix $\widehat{\mathbf{M}}$ will have vanishing values when one goes towards ranks or columns of higher order (i.e. towards the bottom or the right). As a consequence, the addition of new small-scale basis functions will only add extra lines and columns to $\mathbf{I}-\widehat{\mathbf{M}}$ with 1 on the diagonal and vanishing values off the diagonal. Hence, if the linear dynamics of the system is well represented by a low number of basis functions, the truncation of the matrix has no influence on the invertibility of $\mathbf{I}-\widehat{\mathbf{M}}$. Figure 2.2 gives an example of this behaviour: when the coefficients of the matrix vanish when going to the bottom right, truncating the matrix at some order leads to a good reconstruction of its spectrum. The opposite goes for matrices which do not decay when going to the bottom right. This point shows the importance of a good choice of basis elements in relation to a particular stability problem.

The relation (2.22) determines the perturbation $\widehat{\mathbf{a}}$ in the system induced by any initial perturbation $\widehat{\mathbf{b}}$ at a given temporal frequency ω. Let me now elaborate on this relation to show that instabilities exist whenever $\mathbf{I}-\widehat{\mathbf{M}}(\omega)$ is singular (i.e. non-invertible) at a frequency ω with $\mathrm{Im}(\omega)>0$. To prove it, I will identify the conditions in which the response $\mathbf{a}(t)$ is an exponentially growing function of time. In order to recover the time evolution of the induced perturbation, the inverse Laplace transform can be applied, giving

$$\mathbf{a}(t)=\frac{1}{2\pi}\int_{\mathrm{i}\gamma-\infty}^{\mathrm{i}\gamma+\infty}\mathrm{d}\omega\,\widehat{\mathbf{a}}(\omega)\,\mathrm{e}^{-\mathrm{i}\omega t}=\frac{1}{2\pi}\int_{\mathrm{i}\gamma-\infty}^{\mathrm{i}\gamma+\infty}\mathrm{d}\omega\left(\left[\mathbf{I}-\widehat{\mathbf{M}}\right]^{-1}-\mathbf{I}\right)\cdot\widehat{\mathbf{b}}(\omega)\,\mathrm{e}^{-\mathrm{i}\omega t}. \tag{2.23}$$

Remember that $\gamma>0$ is large enough to ensure that $f_{\mathbf{n}}\,\mathrm{e}^{\mathrm{i}\omega t}\to 0$ as $t\to\infty$, so that the line of integration

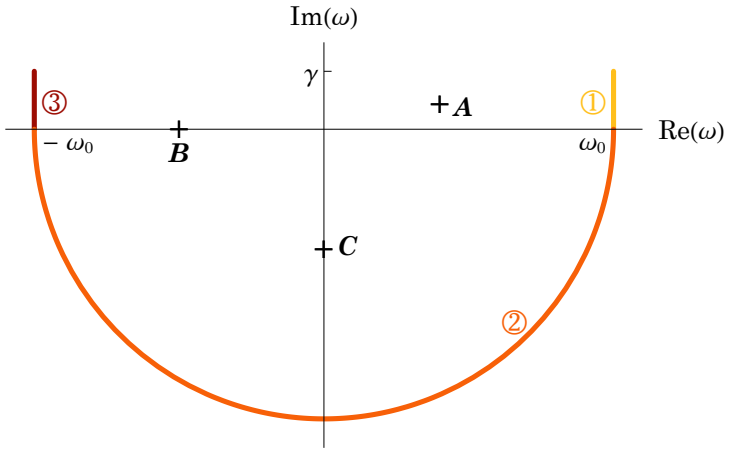

Figure 2.3: Integration path closing the horizontal line in the lower half plane. Integration proceeds from 1 to 3: 1 is the vertical line from $\omega_0 + \mathrm{i}\,\gamma$ to ω_0; 2 is the semi-circle of radius ω_0; 3 is the vertical line from $-\omega_0$ to $-\omega_0 + \mathrm{i}\,\gamma$. Three poles are given as examples: at point A sits an overstability with positive pattern speed; at point B is a neutral mode with negative pattern speed; at point C is a non-rotating, damped mode.

is above all poles of the integrand. It now remains to prove that this contour can be closed in the lower half plane without changing the value of the integral.

As I previously argued (see footnote 3), the response matrix behaves like $|\omega|^{-1}$ as $|\omega| \to \infty$. Additionally, the perturber $\widehat{\mathbf{b}}$ will be considered non-singular (e.g., $\omega \mapsto \widehat{\mathbf{b}}(\omega)$ is bounded). As a consequence, I can always find two positive numbers M and b so that at large $|\omega|$,

$$||[\mathbf{I} - \widehat{\mathbf{M}}(\omega)]^{-1} \cdot \widehat{\mathbf{M}}(\omega) \cdot \widehat{\mathbf{b}}(\omega)|| < Mb/|\omega|, \tag{2.24}$$

where $||\cdot||$ stands for the Euclidian norm. Now, consider a reference $\omega_0 > 0$ large enough so that the integrand is non-singular outside the circle of radius ω_0, and cut the integration contour in three parts: the first one from $\omega_0 + \mathrm{i}\gamma$ to ω_0, the second as the semi-circle of radius ω_0 in the lower-half plane, and the third from $-\omega_0$ to $-\omega_0 + \mathrm{i}\gamma$. Figure 2.3 displays the shape of this integration path in the complex plane. On the first portion, I have

$$\left| \int_{\omega_0 + \mathrm{i}\gamma}^{\omega_0} \mathrm{d}\omega \frac{Mb}{|\omega|} \mathrm{e}^{-\mathrm{i}\omega t} \right| \leq \frac{\gamma M b}{2\omega_0} \mathrm{e}^{\gamma t}, \tag{2.25}$$

and the same occurs in the last portion. On the lower-half semi-circle, I have

$$\left| \int_0^{-\pi} \mathrm{d}\theta \frac{Mb}{\omega_0} \mathrm{e}^{-\mathrm{i}\omega_0 \mathrm{e}^{\mathrm{i}\theta} t} \right| \leq \left| \int_0^{-\pi} \mathrm{d}\theta \frac{Mb}{\omega_0} \mathrm{e}^{\omega_0 \sin(\theta) t} \right| \leq \frac{\pi M b}{\omega_0}. \tag{2.26}$$

Hence, as $\omega_0 \to \infty$, the integral on the contour from $\mathrm{i}\gamma + \omega_0$ to $\mathrm{i}\gamma - \omega_0$ through the lower half plane amounts to 0 for each element of $\mathbf{a}$. The integral in eq. (2.23) can now be seen as closed in the complex plane, which allows for the application of the residue theorem

$$\mathbf{a}(t) = -\mathrm{i} \sum_k \mathbf{a}_k \mathrm{e}^{-\mathrm{i}\omega_k t}, \tag{2.27}$$

where k labels each pole of the integrand and $\mathbf{a}_k$ is the residue of the integrand at the pole $\omega = \omega_k$. In the search for instabilities, the goal is to find the places in the upper-half plane of complex frequencies where poles are. Once poles have been identified in the upper-half plane, eq. (2.27) shows that the corresponding residue will grow exponentially in time, with the fastest evolution associated with the largest value of $\mathrm{Im}\,\omega_k$. This equation also justifies that the real and imaginary parts of ω_k are called oscillation frequency and growth rate. The residue $\mathbf{a}_k$ is then defining the shape of the corresponding mode.

Equation (2.20) guarantees that the response matrix will never be singular in the upper-half plane of frequencies. Additionally, the assumption that $\widehat{\mathbf{b}}$ is not singular has already been made. Thus, the poles of the integrand can only be found when $[\mathbf{I} - \widehat{\mathbf{M}}(\omega)]^{-1}$ is singular. This singularity happens when the matrix $\mathbf{I} - \widehat{\mathbf{M}}(\omega)$ cannot be inverted, i.e.

$$\det(\mathbf{I} - \widehat{\mathbf{M}}(\omega)) = 0. \tag{2.28}$$

In that case, the matrix $\widehat{\mathbf{M}}(\omega)$ has an eigenvalue equal to 1, and the residue will be proportional to the corresponding eigenvector. If the external perturber is not orthogonal to this eigenvector, the perturbation will grow exponentially in time, which characterises the instability. Note that having the eigenvector orthogonal to the perturber would be unlikely, as they are usually uncorrelated, and the tiniest failure in orthogonality would lead to the exponential growth of the instability. In practice, particle noise is often sufficient to clutch the instability, but for low growth rates, the study of unstable modes may require artificially enhancing the power in the corresponding eigenvector in the initial conditions. Such techniques were used in Palmer et al. (1989), allowing for the detection of weakly growing overstabilities.

Equation (2.20) presents the Eulerian form of the response matrix for an isolated 3-dimensional self-gravitating collisionless system. As underlined earlier, this form is computed by considering the perturbations of the DF along the unperturbed orbits. Another point of view was taken in Kalnajs (1977), by considering the perturbations in the orbits as a consequence of the perturbing potential. It led to the Lagrangian formulation of the response matrix. Jalali & Hunter (2005) show that the Eulerian form has the disadvantage of mishandling the boundary terms in the integral over the actions. Therefore, I present in Appendix A the Lagrangian form of the response matrix, taking into account the boundary terms. In all spherical cases treated in the present manuscript, both formulations of the response matrix will be equivalent, as I only deal with potentials that are smooth in the centre.

In the following, I will simplify the response matrix in various contexts. I first focus on non-rotating systems. Therefore, I give the general expression of the non-rotating response matrix in Section 2.3.1, and further develop two particular versions of it in Chapter 3, namely for WKB perturbations, and for the Einstein sphere (i.e. a sphere where all orbits are circular). I then study rotating systems. Hence, in Chapters 4 and 5, I derive the matrix for rotating spheres, as well as for spheres where the degree of rotation depends on the latitude in the cluster.

2.3 Recovering the radial orbit instability

In order to present the specific methods implemented for the matrix method, let me first focus on the stability of a particular spherical system. In non-rotating spheres, the most documented non spherically symmetric instability is by far the radial orbit instability (see Section 1.4). I chose to probe the systems studied in Saha (1991), in order to simultaneously present the methods for mode detection, and to validate my implementation. I will first derive the response matrix for non-rotating systems, then I will describe my detection method for purely growing instabilities and for overstabilities.

2.3.1 The response matrix of a non-rotating sphere

The definition of global rotation in a collisionless sphere can be subject to debate. A variety of systems can be built with vanishing global angular momentum, with sub-systems that rotate in opposite directions (examples are given in Chapter 5). These specific effects will be investigated further in Chapter 5. For now, I will consider non-rotating systems that, at every point in physical space, present a velocity distribution which is symmetric and identical in all tangential directions (i.e. azimuthal and polar). This definition implies that the distribution of orbits that pass through a given point in the system is independent of the orientation of the angular momentum of these orbits. As a consequence, the system's phase space DF only depends on the radial action J_r (explicitly defined below by eq. (2.58)) and the norm of the angular momentum L, and incidentally one has $\partial F/\partial L_z = 0$. Similarly, since the system is spherically symmetric, $\Omega_3 = \partial H_0/\partial L_z = 0$. As a result, introducing the in-plane coordinates

$$\widetilde{\mathbf{n}} = (n_1, n_2) \quad ; \quad \widetilde{\mathbf{\Omega}} = (\Omega_1, \Omega_2) \quad ; \quad \widetilde{\mathbf{J}} = (J_r, L), \tag{2.29}$$

eq. (2.20) can be rewritten as

$$\widehat{M}_{pq}(\omega) = (2\pi)^3 \sum_{\mathbf{n}} \int \mathrm{d}\mathbf{J} \, \frac{\widetilde{\mathbf{n}} \cdot \partial F/\partial \widetilde{\mathbf{J}}}{\omega - \widetilde{\mathbf{n}} \cdot \widetilde{\mathbf{\Omega}}} \, \psi_{\mathbf{n}}^{(p)*}(\mathbf{J}) \, \psi_{\mathbf{n}}^{(q)}(\mathbf{J}). \tag{2.30}$$

For a spherically symmetric system, since the basis elements are related via the Poisson equation, it is natural to separate their angular dependence with spherical harmonics and write

$$\begin{aligned} \psi^{(p)}(\mathbf{x}) &= \psi_{\ell m n}(r, \theta, \phi) = Y_\ell^m(\theta, \phi) \, U_n^\ell(r), \\ \rho^{(p)}(\mathbf{x}) &= \rho_{\ell m n}(r, \theta, \phi) = Y_\ell^m(\theta, \phi) \, D_n^\ell(r), \end{aligned} \tag{2.31}$$

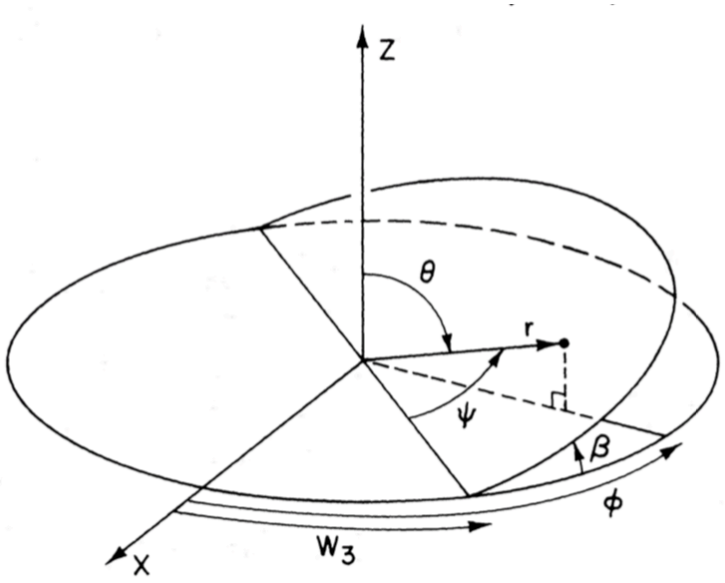

Figure 2.4: Reproduced from Tremaine & Weinberg (1984). Representation of a current position (heavy dot), with the corresponding spherical coordinates (r, θ, ϕ). The circle marks the equatorial (x, y) plane, and the half-circle is taken on the orbital plane. Here, β is the inclination angle, presently denoted i, while w_3 is the third angle (denoted θ_3), conjugate variable of the third action L_z. Another angle, ψ, is involved in eq. (2.37), and is also represented in Fig. 3.1.

where a given basis element is characterised by three indices, $\ell \geq 0$, $|m| \leq \ell$, and $n \geq 0$[4], and the convention followed for spherical harmonics is, here and throughout the manuscript,

$$\int \mathrm{d}\theta \, \mathrm{d}\phi \, \sin(\theta) \, |Y_\ell^m(\theta, \phi)|^2 = 1. \tag{2.32}$$

I also introduced the radial functions $U_n^\ell(r)$ and $D_n^\ell(r)$, and referred in Section 2.2.2 to the literature on the subject. In most of the following, I can assume that these radial functions are real. The only exception is the WKB basis, in Section 3.3.

In Tremaine & Weinberg (1984), the Fourier-transforms w.r.t. the angles (see eq. (2.2)) is performed on the basis elements from eq. (2.31). The result reads

$$\psi_{\mathbf{n}}^{(p)}(\mathbf{J}) = \delta_{m^p}^{n_3} \, \mathrm{i}^{m^p - n_2} \, Y_{\ell^p}^{n_2}(\tfrac{\pi}{2}, 0) \, R_{n_2 m^p}^{\ell^p}(i) \, W_{\ell^p n^p}^{\tilde{\mathbf{n}}}(\tilde{\mathbf{J}}), \tag{2.33}$$

where the inclination angle is defined by $\cos i = L_z/L$, and the imaginary number is noted "i". Figure 2.4 illustrates an orbit and the different angles defining the current position. The inclination of the orbit w.r.t. the equatorial plane (here, i) is the angle noted β. Additionally, the rotation matrix $R_{nm}^\ell(i)$ is defined as

$$R_{nm}^\ell(i) = \sum_t (-1)^t \frac{\sqrt{(\ell+n)!\,(\ell-n)!\,(\ell+m)!\,(\ell-m)!}}{(\ell-m-t)!\,(\ell+n-t)!\,t!\,(t+m-n)!} \big[\cos(i/2)\big]^{2\ell+n-m-2t} \big[\sin(i/2)\big]^{2t+m-n}, \tag{2.34}$$

where the sum over t is restricted to the values such that the arguments of the factorials are positive, i.e. $t_{\min} \leq t \leq t_{\max}$, with $t_{\min} = \mathrm{Max}[0, n-m]$ and $t_{\max} = \mathrm{Min}[\ell - m, \ell + n]$. In eq. (2.33), the Fourier-transformed "in-plane" radial coefficients $W_{\ell n}^{\tilde{\mathbf{n}}}(\tilde{\mathbf{J}})$ are defined as

$$\boxed{W_{\ell n}^{\tilde{\mathbf{n}}}(\tilde{\mathbf{J}}) = \frac{1}{\pi} \int \mathrm{d}\theta_1 \, U_n^\ell(r(\theta_1)) \, \cos[n_1\theta_1 + n_2(\theta_2 - \psi)],} \tag{2.35}$$

which are real for real radial basis functions. In this integral, the radial dependence of the angles θ_1 and

[4]Note that the minimal value of n depends on the specific basis. Some, such as those relying on Bessel functions (Fridman et al., 1984b), start at $n = 1$, while others (e.g., those constructed from ultraspherical polynomials, see Hernquist & Ostriker, 1992) start at $n = 0$.

$(\theta_2 - \psi)$ is given by

$$\theta_1 = \Omega_1 \int_{\mathcal{C}} \mathrm{d}r \, \frac{1}{\sqrt{2(E-\psi_0(r)) - L^2/r^2}}, \tag{2.36}$$

$$\theta_2 - \psi = \int_{\mathcal{C}} \mathrm{d}r \, \frac{\Omega_2 - L/r^2}{\sqrt{2(E-\psi_0(r)) - L^2/r^2}}, \tag{2.37}$$

where ψ is the angle between the ascending node and the current position, measured in the orbit plane along the orbital motion (see Figs. 2.4 and 3.1), E, L are the energy and angular momentum of the orbit, and $\mathcal{C}$ is the integration contour going from the pericentre r_p up to the current position $r = r(\theta_1)$ along the radial oscillation.

Owing to the Kronecker symbol, $\delta^{n_3}_{m^p}$, in eq. (2.33), the sums over n_3 in eq. (2.30) can be straightforwardly carried out. In eq. (2.30), all the dependences w.r.t. L_z are in the Fourier-transformed basis elements, via the rotation matrices from eq. (2.34). They satisfy in particular the orthogonality relation

$$\int_0^\pi \mathrm{d}i \, \sin(i) \, R^{\ell^p}_{n_2 m^p}(i) \, R^{\ell^q}_{n_2 m^p}(i) = \delta^{\ell^q}_{\ell^p} \, \frac{2}{2\ell^p + 1}. \tag{2.38}$$

Hence, the response matrix can be rewritten as

$$\widehat{M}_{pq}(\omega) = \delta^{m^q}_{m^p} (2\pi)^3 \sum_{\widetilde{\mathbf{n}}} \int \mathrm{d}\widetilde{\mathbf{J}} \, \frac{\widetilde{\mathbf{n}} \cdot \partial F / \partial \widetilde{\mathbf{J}}}{\omega - \widetilde{\mathbf{n}} \cdot \widetilde{\mathbf{\Omega}}} \, Y^{n_2}_{\ell^p} \, W^{\widetilde{\mathbf{n}}\,*}_{\ell^p n^p}(\widetilde{\mathbf{J}}) \, Y^{n_2}_{\ell^q} \, W^{\widetilde{\mathbf{n}}}_{\ell^q n^q}(\widetilde{\mathbf{J}}) \int_{-L}^{L} \mathrm{d}L_z \, R^{\ell^p}_{n_2 m^p}(i) \, R^{\ell^q}_{n_2 m^q}(i), \tag{2.39}$$

where I used the simplifying notation $Y^m_\ell = Y^m_\ell(\frac{\pi}{2}, 0)$. Applying the orthogonality relation (2.38), I get

$$\int_{-L}^{L} \mathrm{d}L_z R^{\ell^p}_{n_2 m^p}(i) \, R^{\ell^q}_{n_2 m^q}(i) = L \int_0^\pi \mathrm{d}i \, \sin(i) \, R^{\ell^p}_{n_2 m^p}(i) \, R^{\ell^q}_{n_2 m^p}(i) = L \, \delta^{\ell^q}_{\ell^p} \, \frac{2}{2\ell^p + 1}, \tag{2.40}$$

so that the response matrix becomes

$$\boxed{\widehat{M}_{pq}(\omega) = \delta^{\ell^q}_{\ell^p} \, \delta^{m^q}_{m^p} \sum_{\widetilde{\mathbf{n}}} C^{n_2}_{\ell^p} \, P^{\widetilde{\mathbf{n}}}_{\ell^p n^p \ell^p n^q}(\omega),} \tag{2.41}$$

with $C^n_\ell = 2\,(2\pi)^3 \left|Y^n_\ell\right|^2 / (2\ell + 1)$. In eq. (2.41), the coefficient $P(\omega)$ is also introduced as

$$\boxed{P^{\widetilde{\mathbf{n}}}_{\ell^p n^p \ell^q n^q}(\omega) = \int \mathrm{d}\widetilde{\mathbf{J}} L \, \frac{\widetilde{\mathbf{n}} \cdot \partial F / \partial \widetilde{\mathbf{J}}}{\omega - \widetilde{\mathbf{n}} \cdot \widetilde{\mathbf{\Omega}}(\widetilde{\mathbf{J}})} \, W^{\widetilde{\mathbf{n}}\,*}_{\ell^p n^p}(\widetilde{\mathbf{J}}) W^{\widetilde{\mathbf{n}}}_{\ell^q n^q}(\widetilde{\mathbf{J}}).} \tag{2.42}$$

While the distinction between ℓ^p and ℓ^q might seem redundant for now, it will appear handy when dealing with systems with more complex kinematics (see, e.g., Section 4.3.2). Note that Y^n_ℓ is non-vanishing only when $|n| \leq \ell$ and n and ℓ have the same parity, which reduces the number of terms in the sum of eq. (2.41).

The computation of the response matrix presents several technical difficulties. First, the Fourier-transformed radial functions (eq. (2.35)) appear as the results of nested integrals. In Rozier et al. (2019) (see also Section 2.4.2 below), I presented a method for their computation that drastically improves upon the method used in Fouvry et al. (2015a). Another complication arises because of the integral over the actions. In Sections 2.4.4 and 2.4.3, I will show how I perform this computation by cutting out the integration domain after a specific change of variables. Note that these numerical techniques are not specific to non-rotating spheres, and I will also use them in the treatment of rotating systems (Chapters 4 and 5).

2.3.2 A radially anisotropic spherical model

The particular model I consider here was investigated by Saha (1991). The potential is the isochrone sphere (Henon, 1959)

$$\psi_0(r) = -\frac{G M_\mathrm{tot}}{R_\mathrm{s}} \, \frac{1}{1 + \sqrt{1 + (r/R_\mathrm{s})^2}}, \tag{2.43}$$

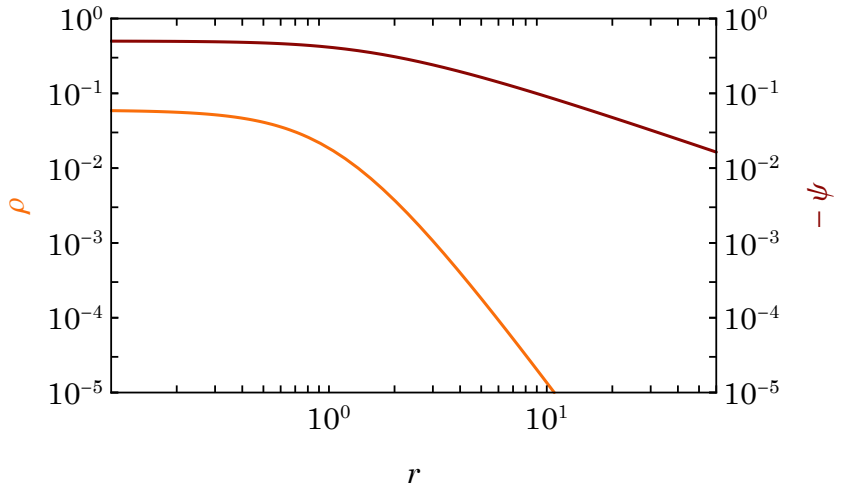

Figure 2.5: Radial profile of the density and potential of the isochrone sphere.

where R_s is the scale radius of the isochrone sphere[5]. In the following, the units are fixed so that $M_\mathrm{tot} = G = R_\mathrm{s} = 1$. The corresponding density in these units is

$$\rho_0(r) = \frac{3(1+\sqrt{1+r^2})(1+r^2) - r^2(1+3\sqrt{1+r^2})}{4\pi\big(1+\sqrt{1+r^2}\big)^3\big(1+r^2\big)^{3/2}}. \tag{2.44}$$

Figure 2.5 shows the radial dependence of the isochrone density and potential, with a core for $r \lesssim 1$ and $\rho \propto r^{-4}$, $\psi \propto r^{-1}$ decays at large radii. The equilibrium DF is that of the Osipkov-Merritt type (Osipkov, 1979; Merritt, 1985), which is isotropic in the central part of the cluster and fully radially anisotropic in the outskirts

$$\begin{aligned} F(Q) = \frac{1}{128\sqrt{2}\pi^3(1-Q)^4}\Bigg\{ & \sqrt{Q}\big[27 + 77R_\mathrm{a}^{-2} - (66+286R_\mathrm{a}^{-2})Q + (320+136R_\mathrm{a}^{-2})Q^2 \\ & - (240+32R_\mathrm{a}^{-2})Q^3 + 64Q^4\big] \\ & + \frac{3\arcsin\sqrt{Q}}{\sqrt{1-Q}}\big[17R_\mathrm{a}^{-2} - 9 + (28-44R_\mathrm{a}^{-2})Q + (16-8R_\mathrm{a}^{-2})Q^2\big]\Bigg\}. \end{aligned} \tag{2.45}$$

This DF has a single degree of freedom $Q = -(E + L^2/(2R_\mathrm{a}^2))$, and is only defined for $Q > 0$. The level of radial anisotropy of the cluster can be tuned through the anisotropy radius R_a, which is the scale of transition between the central isotropic region and the outer radially anisotropic region. In order to quantify anisotropy in the sphere, the anisotropy parameter is defined as

$$\beta(r) = 1 - \frac{\sigma_\theta^2(r)}{\sigma_r^2(r)}, \tag{2.46}$$

where $\sigma_\theta^2(r)$ and $\sigma_r^2(r)$ are the velocity dispersions in the polar and radial directions, defined as

$$\sigma_\theta^2(\mathbf{x}) = \frac{\int \mathrm{d}\mathbf{v}\, v_\theta^2\, F(\mathbf{x},\mathbf{v})}{\rho_0(r)} \quad ; \quad \sigma_r^2(\mathbf{x}) = \frac{\int \mathrm{d}\mathbf{v}\, v_r^2\, F(\mathbf{x},\mathbf{v})}{\rho_0(r)}, \tag{2.47}$$

given that in a non-rotating system, the velocity dispersions in all directions only depend on the radius. The anisotropy parameter takes values in the range $]-\infty, 1]$, where tangentially anisotropic regions have $\beta < 0$, isotropic regions have $\beta = 0$ and radially anisotropic regions have $\beta > 0$. Figure 2.6a shows the radial profile of the anisotropy parameter for $R_\mathrm{a} = 1, 2, 3$, underlining the role played by the anisotropy radius. For the isochrone sphere, ensuring that $F(Q) \geq 0$ everywhere requires that $R_\mathrm{a} \geq 0.87$. This limit represents the fact that at $R_\mathrm{a} = 0.87$, it is not possible to increase the amount of radial orbits without also increasing the density at the centre of the cluster.

[5]The scale radius of the isochrone sphere is usually referred to as b, yet this notation was changed here for the sake of clarity.

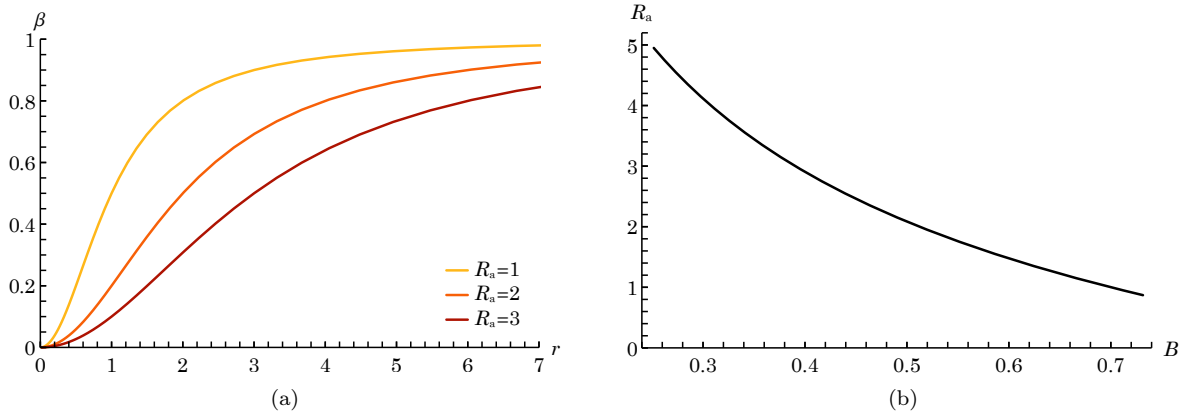

Figure 2.6: Anisotropy of the isochrone potential (eq. (2.43)) with an Osipkov-Merritt DF (eq. (2.45)). (a) Radial profile of the anisotropy parameter β (see eq. (2.46)) for three values of the anisotropy radius R_a. (b) Dependence of the global anisotropy B (see eq. (2.48)) on the anisotropy radius R_a.

In order to represent the global anisotropy of the sphere, a global anisotropy parameter can be defined as

$$B = 1 - \frac{\int \mathrm{d}\mathbf{x}\,\mathrm{d}\mathbf{v}\; v_\theta^2\, F(\mathbf{x},\mathbf{v})}{\int \mathrm{d}\mathbf{x}\,\mathrm{d}\mathbf{v}\; v_r^2\, F(\mathbf{x},\mathbf{v})} = 1 - \frac{\int \mathrm{d}r\, r^2\, \rho_0(r)\, \sigma_\theta^2(r)}{\int \mathrm{d}r\, r^2\, \rho_0(r)\, \sigma_r^2(r)}. \tag{2.48}$$

Figure 2.6b shows how the global anisotropy evolves with the anisotropy radius. When $R_\mathrm{a} = +\infty$, the cluster is completely isotropic, as the transition towards radial anisotropy within the cluster occurs at infinity. The maximum global anisotropy of the cluster is reached for $R_\mathrm{a} = 0.87$ and $B = 0.73$. In the following sections, I will focus on the results of the matrix method applied to this DF for a series of anisotropies.

2.3.3 Purely growing modes

In a system that has no preferred axis, an $m = 2$ instability with the highest degree of symmetry will be purely growing, i.e. non-rotating, so that there is only one fixed direction. In that particular case, the search for instabilities requires finding points on the $\eta > 0$ semi-axis where $\det(\mathbf{I} - \widehat{\mathbf{M}}(\mathrm{i}\eta)) = 0$. As will be proved in eq. (2.50), $\mathbf{I} - \widehat{\mathbf{M}}(\mathrm{i}\eta)$ is a Hermitian matrix, so that all its eigenvalues are real. Additionally, in the limit of large η, the response matrix is small compared to the identity, so that all eigenvalues of $\mathbf{I} - \widehat{\mathbf{M}}(\mathrm{i}\eta)$ are strictly positive. Saha (1991) proposes the following method to identify unstable systems. If one of the eigenvalues of $\mathbf{I} - \widehat{\mathbf{M}}(\mathrm{i}0^+)$ is strictly negative, then, since this eigenvalue is typically a continuous function of η, the intermediate value theorem implies that this eigenvalue will reach 0 for at least one $\eta > 0$, hence the system is unstable. As underlined by Saha, this method suffers from incompleteness in identifying unstable systems. Indeed, if the eigenvalues are non-monotonic functions of the growth rate (which is uncommon but possible), then the system might be unstable even though all eigenvalues of $\mathbf{I} - \widehat{\mathbf{M}}(\mathrm{i}0^+)$ are strictly positive. An additional problem of this method is that the response matrix can have a very intricate behaviour close to $\omega = 0$, so that $\mathbf{I} - \widehat{\mathbf{M}}(\mathrm{i}0^+)$ might be highly complicated to compute (see, e.g., Pichon & Cannon, 1997). Finally, this method does not allow for the computation of the actual growth rate and corresponding eigenvector of the instability.

The method I use to identify purely growing modes was also used by Saha (1991), and computes both the growth rates and the shapes of the unstable modes. It finds the roots of $\det(\mathbf{I} - \widehat{\mathbf{M}}(\mathrm{i}\eta)) = 0$, using known properties of the response matrix, such as its continuity and its decay at infinity. Starting from some large value of η, where $\mathbf{I} - \widehat{\mathbf{M}}(\mathrm{i}\eta)$ is positive definite, I successively compute the determinant for smaller and smaller growth rates. Every time the determinant crosses 0, I identify an instability. This method has the advantage of giving the instabilities in decreasing order of growth rates, so that the first instability which is identified is the one that would develop in a corresponding N-body simulation with initial conditions drawn from the equilibrium DF (provided the growth is sufficient). Additionally, it provides the eigenvector corresponding to each instability, from which the shape of the instability in density and potential can be reconstructed. However, one issue is that it can still have problems in

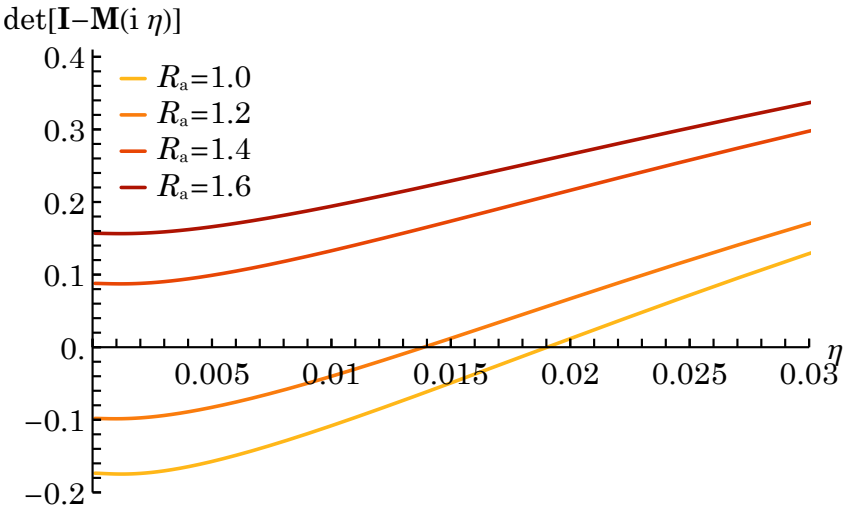

Figure 2.7: Graphs of $\eta \mapsto \det(\mathbf{I} - \widehat{\mathbf{M}}(i\eta))$ for several values of R_a, for an isochrone sphere with Osipkov-Merritt DF. An instability is identified when the curves cross the x axis.

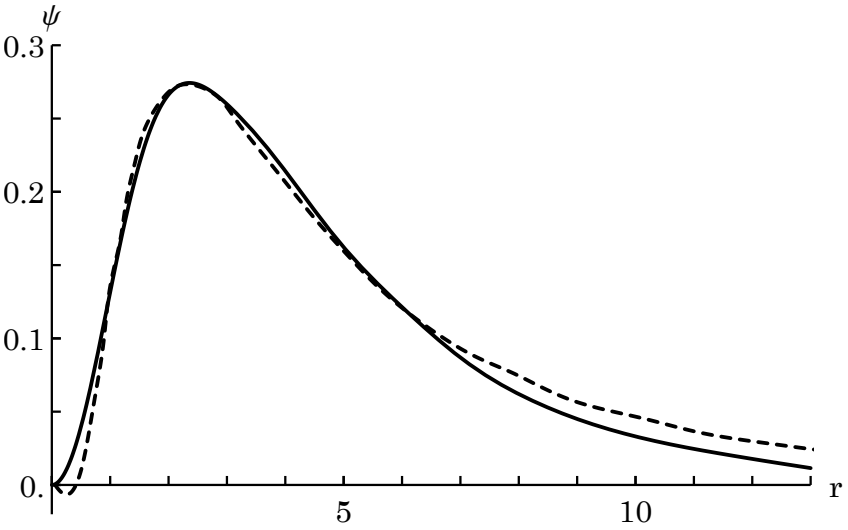

Figure 2.8: Radial profile of the fastest growing instability's potential detected with the matrix method in the $R_a = 1$ sphere. The ordinate is arbitrarily normalised. *Full curve:* my measurement. *Dashed curve:* extracted from Saha (1991), Fig. 4(b). This confirms that my implementation of the response matrix detects the same modes.

identifying instabilities with low growth rates, in particular if the response matrix has a very intricate behaviour close to $\omega = 0$.

I now apply this method to the system probed by Saha (1991). I use the numerical techniques described in Section 2.4 below to calculate the response matrix (eq. (2.41)), with the DF of eq. (2.45). In this computation, I use 10 elements of the radial basis from Fridman et al. (1984b), based on Bessel functions. Figure 2.7 shows $\det(\mathbf{I}-\widehat{\mathbf{M}}(i\eta))$ as a function of η for different values of R_a. In the $R_a = 1.4, 1.6$ cases, the determinant is always positive, hence the system is stable. In the $R_a = 1, 1.2$ cases, the system exhibits an instability. The trend is similar to that measured by Saha (1991). Indeed, systems with larger R_a (i.e. smaller B, see Fig. 2.6b) are stable, and those with smaller R_a (i.e. larger B) are unstable. Furthermore, the growth rate is an increasing function of B, and its values are consistent with those from Saha (1991), in the range $0 \leq \eta \leq 0.03$. The mismatch between particular values of η can mainly be attributed to differences in the projection strategy (basis functions, further discussed in the next paragraph) and in the choice of integration scheme. Indeed, as further highlighted in Section 2.4, the integrand for the computation of the response matrix goes through quasi-poles. Therefore, the choice of integration strategy has an important influence on the computational errors on the growth rate measurements.

To confirm that my code detects the same modes as in Saha (1991), I reconstruct the radial profile

of the detected mode's potential, in the $R_a = 1$ case. It is given by Fig. 2.8. Overplotted is the mode profile from Fig. 4(b) of Saha (1991). The radial profiles are strikingly similar. They both present a single peak at $2 < r < 3$, with a rather sharp increase at lower radii, and a rather shallow decrease at large radii. In both cases, the potential at $r = 10$ has dropped to about 10% of its peak value. A small dip at $r < 1$ is however absent from my profile, and could probably be recovered by using a larger number of radial basis elements. A slight mismatch can also be noted at large radii, and may also be attributed to the particular choice of basis. Indeed, the basis used in Saha (1991) is constructed via a Gram-Schmidt orthonormalisation of a series of polynomials applied on the variable $r/(1+r)$. It is therefore different from the one I use, i.e. the bi-orthogonal basis from Fridman et al. (1984b). The main difference is that the former has infinite extent, while the latter effectively truncates the potential at a finite radius. This truncation does not seem to affect the mode reconstruction, neither does the different shapes of the bases.

Overall, this shows that my implementation of the response matrix detects the same modes as those exhibited by Saha (1991). I can therefore confidently use it to produce new results in other contexts.

2.3.4 Overstabilities

Searching for overstabilities (i.e. modes which both grow and oscillate) will be particularly useful when dealing with rotating systems, as most of the instabilities in these systems have a non-zero pattern speed. Rotating instabilities are however not excluded from non-rotating systems. Let me first prove that any overstability in a non-rotating system will always be accompanied by its symmetric counterpart, sharing the same characteristics but having an opposite oscillation frequency. I then develop the tools that allow me to exhibit overstabilities in spherical systems. These tools will be used in the next chapters, e.g. Chapter 3 for circular orbit instabilities (COIs), and Chapter 4 for rotating spheres.

2.3.4.1 Two counter-rotating overstabilities

Some properties of the unstable modes are encoded in the symmetries of the response matrix. One of them in particular is a consequence of the conservation of all components of the total angular momentum from the initial to the final state of the system. This translates into the following property of the instability. If an $m \neq 0$ instability has a non-zero pattern speed, then it carries some angular momentum in the direction of its rotation axis. The easiest way to compensate for this angular momentum is by the symmetric and simultaneous development of a second rotating instability, sharing the same rotation axis and revolving at the same rate in the opposite direction. This phenomenon is naturally encoded in the properties of the response matrix (2.41). To exhibit it, let me compute the coefficient $P^{\widetilde{\mathbf{n}}}_{\ell^p n^p \ell^q n^q}$ at a frequency $-\omega_0 + \mathrm{i}\eta$

$$\begin{aligned} P^{\widetilde{\mathbf{n}}}_{\ell^p n^p \ell^q n^q}(-\omega_0 + \mathrm{i}\eta) =& \int \mathrm{d}\widetilde{\mathbf{J}}\, L \frac{\widetilde{\mathbf{n}} \cdot \partial F/\partial \widetilde{\mathbf{J}}}{-\omega_0 + \mathrm{i}\eta - \widetilde{\mathbf{n}} \cdot \widetilde{\mathbf{\Omega}}(\widetilde{\mathbf{J}})} W^{\widetilde{\mathbf{n}}\,*}_{\ell^p n^p}(\widetilde{\mathbf{J}})\, W^{\widetilde{\mathbf{n}}}_{\ell^q n^q}(\widetilde{\mathbf{J}}) \\ =& \int \mathrm{d}\widetilde{\mathbf{J}}\, L \frac{(-\widetilde{\mathbf{n}}) \cdot \partial F/\partial \widetilde{\mathbf{J}}}{\left[\omega_0 + \mathrm{i}\eta - (-\widetilde{\mathbf{n}}) \cdot \widetilde{\mathbf{\Omega}}(\widetilde{\mathbf{J}})\right]^*} W^{-\widetilde{\mathbf{n}}\,*}_{\ell^p n^p}(\widetilde{\mathbf{J}})\, W^{-\widetilde{\mathbf{n}}}_{\ell^q n^q}(\widetilde{\mathbf{J}}) \\ =& P^{-\widetilde{\mathbf{n}}\,*}_{\ell^q n^q \ell^p n^p}(\omega_0 + \mathrm{i}\eta), \end{aligned} \tag{2.49}$$

where I made use of the fact, evident from eq. (2.35), that $W^{-\widetilde{\mathbf{n}}}_{\ell^p n^p}(\widetilde{\mathbf{J}}) = W^{\widetilde{\mathbf{n}}}_{\ell^p n^p}(\widetilde{\mathbf{J}})$. If I additionally use the fact that $C^{-n_2}_{\ell^p} = C^{n_2}_{\ell^p}$ and is always a real number, I get

$$\begin{aligned} \widehat{M}_{pq}(-\omega_0 + \mathrm{i}\eta) &= \delta^{\ell^q}_{\ell^p}\, \delta^{m^q}_{m^p} \sum_{\widetilde{\mathbf{n}}} C^{n_2}_{\ell^p}\, P^{-\widetilde{\mathbf{n}}\,*}_{\ell^q n^q \ell^p n^p}(\omega_0 + \mathrm{i}\eta) \\ &= \left[\delta^{\ell^q}_{\ell^p}\, \delta^{m^q}_{m^p} \sum_{\widetilde{\mathbf{n}}} C^{n_2}_{\ell^q}\, P^{\widetilde{\mathbf{n}}}_{\ell^q n^q \ell^p n^p}(\omega_0 + \mathrm{i}\eta)\right]^* \\ &= \widehat{M}^\dagger_{pq}(\omega_0 + \mathrm{i}\eta), \end{aligned} \tag{2.50}$$

where $\widetilde{\mathbf{n}}$ and $-\widetilde{\mathbf{n}}$ could be interchanged because the sum is symmetric in both resonance numbers, and the dagger stands for the complex conjugate of the transposed matrix. Now assume that the system has an instability at the frequency $\omega = \omega_0 + \mathrm{i}\eta$, with $\omega_0 \neq 0$. Then $\det(\mathbf{I} - \widehat{\mathbf{M}}(\omega)) = 0$. Looking at what happens at the frequency $-\omega_0 + \mathrm{i}\eta$, I have

$$\det(\mathbf{I} - \widehat{\mathbf{M}}(-\omega_0 + \mathrm{i}\eta)) = \left[\det(\mathbf{I} - \widehat{\mathbf{M}}(\omega_0 + \mathrm{i}\eta))\right]^* = 0, \tag{2.51}$$

which proves that there is a second mode with the same growth rate and an opposite oscillation frequency.

Let me now focus on the shape of the mode in configuration space, and denote $\widehat{\mathbf{a}}_1$ (resp. $\widehat{\mathbf{a}}_2$) the eigenvector of $\widehat{\mathbf{M}}(\omega_0 + \mathrm{i}\eta)$ (resp. $\widehat{\mathbf{M}}(-\omega_0 + \mathrm{i}\eta)$) with eigenvalue equal to 1. I can always choose a bi-orthogonal basis set with real radial functions, and this demonstration will be restricted to this particular case. Now, the response matrix is symmetric in the sense that $\widehat{\mathbf{M}}^T(\omega) = \widehat{\mathbf{M}}(\omega)$, and I have

$$\widehat{\mathbf{M}}(-\omega_0 + \mathrm{i}\eta) \cdot \widehat{\mathbf{a}}_1^* = \widehat{\mathbf{M}}^*(\omega_0 + \mathrm{i}\eta) \cdot \widehat{\mathbf{a}}_1^* = \left[\widehat{\mathbf{M}}(\omega_0 + \mathrm{i}\eta) \cdot \widehat{\mathbf{a}}_1\right]^* = \widehat{\mathbf{a}}_1^*, \tag{2.52}$$

which implies

$$\widehat{\mathbf{a}}_2 = \widehat{\mathbf{a}}_1^*, \tag{2.53}$$

by definition[6] of $\widehat{\mathbf{a}}_2$. Since the singularity of the integrand occurs on these vectors, the residues of the inverse Laplace transform will then be proportional to them, hence, writing B_1 and B_2 the corresponding proportionality coefficients, I can apply eq. (2.27) to get

$$\mathbf{a}_1(t) = B_1\, \widehat{\mathbf{a}}_1\, \mathrm{e}^{-\mathrm{i}(\omega_0 + \mathrm{i}\eta)t}\,;\ \mathbf{a}_2(t) = B_2\, \widehat{\mathbf{a}}_1^*\, \mathrm{e}^{-\mathrm{i}(-\omega_0 + \mathrm{i}\eta)t}. \tag{2.54}$$

Using eq. (2.12), I can then recover the spatial structure of the response in potential as

$$\psi_2^{\mathrm{s}}(\mathbf{x}, t) = B_2\, \mathrm{e}^{-\mathrm{i}(-\omega_0 + \mathrm{i}\eta)t} \sum_p \widehat{a}_{1,p}^*\, \psi^{(p)}(\mathbf{x}). \tag{2.55}$$

Using the properties that $\left[Y_\ell^m(r, \theta, \phi)\right]^* = Y_\ell^m(r, \theta, -\phi)$ and that the potentials are real fields, I get

$$\psi_2^{\mathrm{s}}(r, \theta, \phi, t) = \frac{B_2}{B_1^*}\, \psi_1^{\mathrm{s}}(r, \theta, -\phi, t). \tag{2.56}$$

The second instability not only rotates at the opposite pattern speed, but its rotation axis is the same as the first instability, and their structures are mirror symmetric w.r.t. the $\phi = 0$ plane. The proportionality coefficient B_2/B_1^* reflects the symmetry of the external perturber: if one takes the particle noise in the initial conditions, which is very close to spherical symmetry, $B_2/B_1^* \simeq 1$. In cases where the external perturber is asymmetric, the growth of one of the instabilities in its early phase may act as an additional external perturber to the second, and vice versa, so that both instabilities may grow at the same rate. This argument shows that the particular case of two counter-rotating instabilities can be affected by non-linearities, which are beyond the subject of the present study.

2.3.4.2 Nyquist contours

Similarly to the situation for purely growing modes, the identification of overstabilities requires finding the roots of $\det(\mathbf{I} - \widehat{\mathbf{M}}(\omega_0 + \mathrm{i}\eta)) = 0$. However, for overstabilities, the eigenvalues of $\mathbf{I} - \widehat{\mathbf{M}}$ are in general complex, so that one now has to find places in the complex ω plane where the complex determinant goes through the origin. One could use some general root finding algorithm on the complex function $\omega \mapsto \det(\mathbf{I} - \widehat{\mathbf{M}}(\omega))$, yet the structure of this function can become very intricate in the vicinity of the origin, which tends to make such algorithms fail. Again, some knowledge of the response matrix helps in designing a root finding algorithm specific to the present problem: the drawing of Nyquist contours.

For a given value of $\eta > 0$, a Nyquist contour is defined as the complex curve $\omega_0 \mapsto \det(\mathbf{I} - \widehat{\mathbf{M}}(\omega_0 + \mathrm{i}\eta))$. These contours play the same role as successive real values of the determinant in the case of purely growing instabilities. At sufficiently large values of η, the whole contour remains close to 1 in the complex plane, hence it does not enclose the origin. When the value of η is progressively decreased, and if the model has an instability, then there will be some value of η at which the contour goes through the origin. Subsequently, for even lower values of η, the contour encloses the origin[7]. In practice, if Nyquist contours are drawn on a grid of η (which in passing defines a conformal map), one can identify two consecutive values of η where the winding number of the contour around the origin (i.e. the number of winds it

[6] Note that here, it is assumed that the dimension of the eigen-space is not larger than 1. This is not strictly true, since the matrix is block-diagonal in m with *identical* blocks (as the blocks are independent of m, see eq. (2.42)). This difficulty can easily be avoided by considering that I focus on a single value of m, which does not affect the generality of the demonstration. Then, for a single value of m, I can safely assume that the eigen-spaces are non-degenerate. A degenerate case would lead to the formation of two instabilities with exact same growth rate and pattern speed. Such a case surely requires a non-linear treatment.

[7] It is assumed here that the determinant is non-singular around the frequency of the instability. In that case, the Nyquist contour does not bounce off or stick to the origin and goes through it smoothly when η decreases.

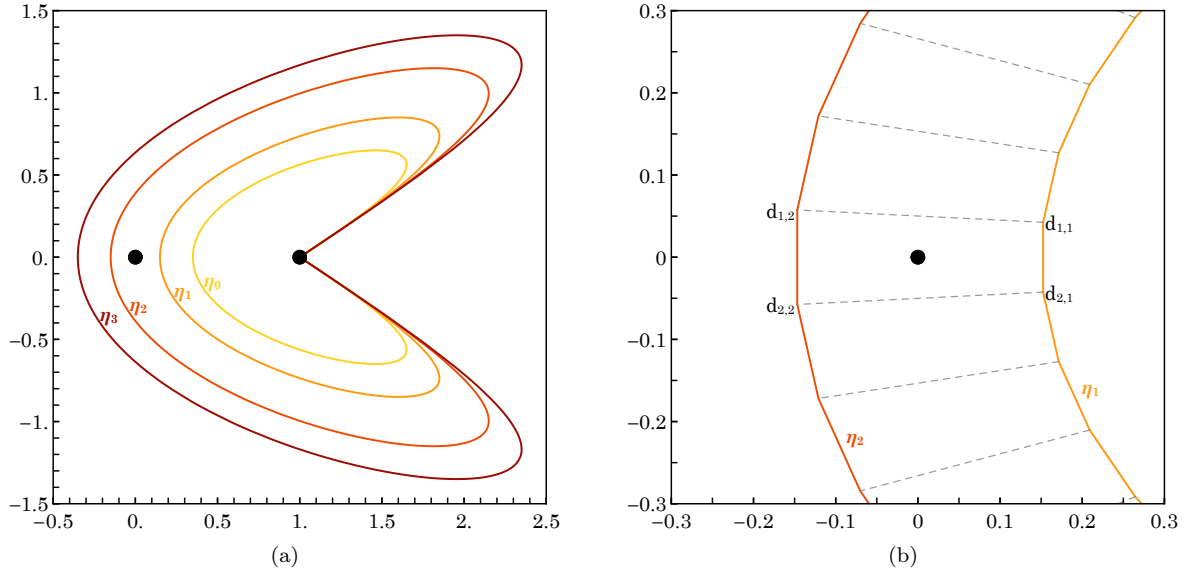

Figure 2.9: (a) Sketch representing some Nyquist contours around a value of η where the system has an instability. Here, $\eta_3 < \eta_2 < \eta_1 < \eta_0$, and an unstable mode is identified with growth rate $\eta_2 < \eta < \eta_1$. (b) Zoomed-in version of the contours around the origin. The dashed lines link equal values of ω_0 on each consecutive contours. With this method, the instability is further characterised by the oscillation frequency $\omega_{0,1} < \omega_0 < \omega_{0,2}$.

makes around it) changes from 0 to $n \geq 1$. Then, the two-dimensional version of the intermediate value theorem imposes that there is a value of η in the interval where the contour crosses the origin. As a consequence, the instability with the largest growth rate is given by the first time the contour encloses the origin from one value of η to the next. This situation is sketched in Fig. 2.9a: while the contours at η_1 does not enclose the origin, that at η_2 does. Hence, an instability is identified with growth rate $\eta_2 < \eta < \eta_1$. Note that when η is further decreased, instabilities with slower growth can be identified whenever the number of winds the contour makes around the origin changes from one value of η to the next.

2.3.4.3 Computing the oscillation frequency

In practice, Nyquist contours are drawn on a grid of values of η, and each Nyquist contour is itself $\det(\mathbf{I} - \widehat{\mathbf{M}}(\omega))$ computed on a grid of ω_0. Finding instabilities requires computing the winding number of each Nyquist contour, which is readily performed by computing the sum, over all the points on the contour, of the polar angles separating two consecutive points on the curve. Once two consecutive values of η are found, say $\eta_2 < \eta_1$, where the winding number changes, I identify the oscillation frequency ω_0 of the corresponding instability. This method is sketched in Fig. 2.9b. Let $\omega_{0,2} < \omega_{0,1}$ be the two consecutive values of the ω_0 grid that sandwich the oscillation frequency. Then the origin was crossed in the continuous transformation of the segment of the Nyquist contour that lies between $\omega_{0,2}$ and $\omega_{0,1}$, from η_1 to η_2. As a consequence, the origin is inside the quadrilateral $d_{1,1}d_{1,2}d_{2,2}d_{2,1}$, where the points in the complex plane are defined as $d_{i,j} = \det(\mathbf{I} - \widehat{\mathbf{M}}(\omega_{0,i} + \mathrm{i}\,\eta_j))$. Thus, I designed the following algorithm for computing the mode oscillation frequency. For all consecutive $\omega_{0,2} < \omega_{0,1}$ on the grid, compute the winding number of the quadrilateral $d_{1,1}d_{1,2}d_{2,2}d_{2,1}$. A mode oscillation frequency exists whenever this quantity is non-zero.

2.3.4.4 Application to the radial orbit instability

For non-rotating systems, the fact that the response matrix is self-adjoint (eq. (2.50)) has a consequence on the shape of the Nyquist contours. Each contour is indeed symmetric w.r.t. the real axis. It is then straightforward to understand the necessity of two counter-rotating instabilities in light of this symmetry.

In order to illustrate the Nyquist technique, I performed the same mode search as in Section 2.3.3, using the drawing of Nyquist contours. The resulting contours are represented Fig. 2.10 for the sphere with $R_\mathrm{a} = 1$. The contours are symmetric w.r.t. the real axis, and the origin is crossed at the point $\omega_0 = 0$ with the growth rates $0.018 < \eta < 0.020$. Fortunately, this is consistent with the results of

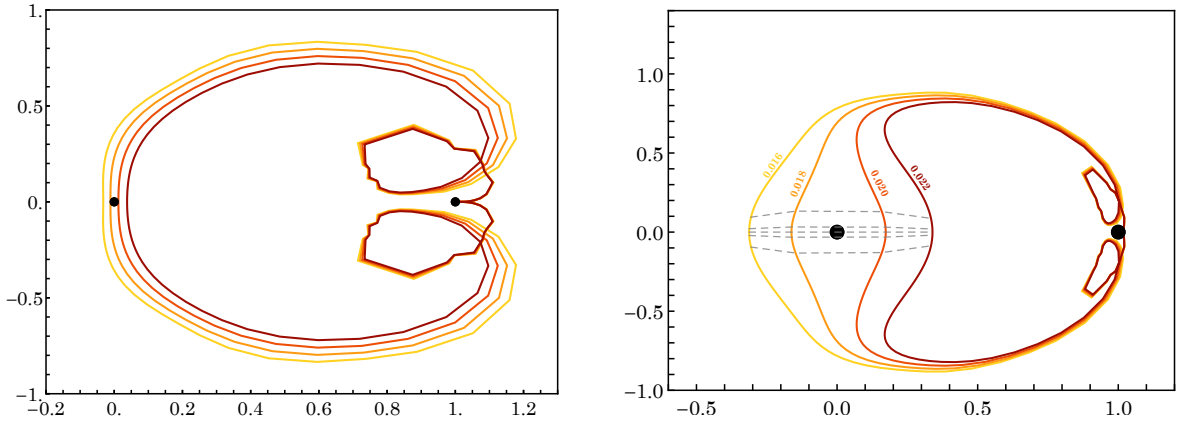

(a) Nyquist contour

(b) Logarithmically rescaled contour, highlighting the passage close to the origin.

Figure 2.10: Nyquist contours for the isochrone sphere with Osipkov-Merritt DF and anisotropy radius $R_\mathrm{a} = 1$. (a) Linear scale. (b) Following Pichon & Cannon (1997), in (b), a logarithmic scaling is applied, $r\mathrm{e}^{\mathrm{i}\theta} \mapsto \frac{1}{2}\log(1+10^2 r)\,\mathrm{e}^{\mathrm{i}\theta}$, to highlight the structure of the contour around the origin and make sure that the first growing mode is indeed selected.

Section 2.3.3. A second illustration of Nyquist contours is shown in Fig. 3.7 below in the case of an overstability. This particular system will be described in detail in Chapter 3.

2.4 Numerical techniques for computing the response matrix

Let me now present the algorithmic details of the computation of the response matrix given by eq. (2.20), which were used to find modes of the radial orbit instability in the previous section and will be used on various occasions in the next chapters. I developed a code in Mathematica[8], which is compatible with version 12.1. This software was chosen because it presents some handy built-in functions for numerical integration and formal calculus, and because it allows for fast testing of new methods. External compilation in `C` was used for faster operations on lists (e.g. for action-space integration). However, the software has a sub-optimal memory management, and rewriting the code in another language may allow for important efficiency improvements on that side. The code is parallelised on two levels. First, all relevant values of $W^{\tilde{\mathbf{n}}}_{\ell n}(\widetilde{\mathbf{J}})$ are computed in parallel. Then, these values are shared between the kernels, and the overall computation is straightforwardly parallelised by computing the response matrix for different values of ω on different kernels. The second step typically takes about an order of magnitude longer than the first (for about the same number of evaluations of $W^{\tilde{\mathbf{n}}}_{\ell n}(\widetilde{\mathbf{J}})$ as the number of ω grid points). With typical parameters used in the studies of e.g. Sections 2.3 and 4.4, the computation of a single matrix takes about 1 s, while the grid in ω has a few 10^4 points.

In the following, I will focus on four particular algorithmic points: (i) the mapping of quantities in the space of peri- and apocentres, which provides synthetic analytical expressions for all functions of interest; (ii) the computation of the $W^{\tilde{\mathbf{n}}}_{\ell n}$ functions defined by eq. (2.35), which involves nested integrals; (iii) a particular change of variables that allows for the sampling on a regular grid, while having a mixed linear and logarithmic grid in $(r_\mathrm{p}, r_\mathrm{a})$ space; (iv) a particular method used for computing integrals in action space, which uses a linear approximation of slowly varying functions in small square regions on the grid. These new numerical methods allow for a considerable improvement (a factor of about 1000) in the computational efficiency. This yields more precise results, because one can include more radial basis functions and increase the sampling of the Nyquist contours. Furthermore, it is now possible to perform large parameter space explorations with the response matrix, making it a more efficient tool than numerical simulations in certain contexts. In Chapter 4, I illustrate this with the stability of anisotropic, rotating systems.

2.4.1 Radial mapping

The relations reproduced here are demonstrated and discussed in the literature, e.g. in Tremaine & Weinberg (1984); Binney & Tremaine (2008). In all cases of interest to the present manuscript, the

[8] https://www.wolfram.com/mathematica

computation of terms of the form of eq. (2.42) involves an integral over the 2D action space (J_r, L). This space corresponds to the ensemble of possible shapes of the orbits in a given central potential, and hence has a bijective mapping with the space $(r_\mathrm{p}, r_\mathrm{a})$ of orbital peri- and apocentres. This change of variables can be performed via the series of transformation $(J_r, L) \mapsto (E, L)$, knowing that by definition $\partial E/\partial J_r = \Omega_1$, then $(E, L) \mapsto (r_\mathrm{p}, r_\mathrm{a})$, with the analytical relations

$$E = \frac{r_\mathrm{a}^2\,\psi_0(r_\mathrm{a}) - r_\mathrm{p}^2\,\psi_0(r_\mathrm{p})}{r_\mathrm{a}^2 - r_\mathrm{p}^2} \;\;;\;\; L = \sqrt{\frac{2(\psi_0(r_\mathrm{a}) - \psi_0(r_\mathrm{p}))}{r_\mathrm{p}^{-2} - r_\mathrm{a}^{-2}}}. \tag{2.57}$$

Note that I can "directly" recover J_r from $(r_\mathrm{p}, r_\mathrm{a})$ through

$$J_r = \frac{1}{\pi}\int_{r_\mathrm{p}}^{r_\mathrm{a}} \mathrm{d}r\, \sqrt{2(E - \psi_0(r)) - L^2/r^2}, \tag{2.58}$$

where $\sqrt{2(E - \psi_0(r)) - L^2/r^2}$ is the norm of the radial velocity of the particle on the orbit, when it is at a position with radius r. In the integrand of eq. (2.42), I can then express the frequencies as

$$\begin{aligned}\Omega_1 &= \frac{1}{\pi}\int_{r_\mathrm{p}}^{r_\mathrm{a}} \mathrm{d}r\, \frac{1}{\sqrt{2(E - \psi_0(r)) - L^2/r^2}},\\ \Omega_2 &= \frac{\Omega_1}{\pi}\int_{r_\mathrm{p}}^{r_\mathrm{a}} \mathrm{d}r\, \frac{L/r^2}{\sqrt{2(E - \psi_0(r)) - L^2/r^2}}.\end{aligned} \tag{2.59}$$

Here, one has to deal with integrable singularities at the edges of the integration domain, associated with the change of direction of the radial oscillation. The next section presents the change of variables I use to regularise this divergence (see Fig. 2.11). This way, the integrand is bounded on the full interval and the numerical stability of the integration is greatly improved. As I will show in Appendix A.3, this change of variables is also useful when computing derivatives of the frequencies w.r.t. the actions. The last point of concern is the function $W_{\ell n}^{\tilde{\mathbf{n}}}$, defined by eq. (2.35). By performing the change of variable $\theta_1 \mapsto r$, with the Jacobian straightforwardly computed from eq. (2.36)

$$\frac{\mathrm{d}\theta_1}{\mathrm{d}r} = \frac{\Omega_1}{\sqrt{2(E - \psi_0(r)) - L^2/r^2}}, \tag{2.60}$$

I get

$$W_{\ell n}^{\tilde{\mathbf{n}}}(\widetilde{\mathbf{J}}) = \frac{\Omega_1}{\pi}\int_{r_\mathrm{p}}^{r_\mathrm{a}} \mathrm{d}r\, \frac{U_n^\ell(r)\,\cos[n_1\theta_1(r) + n_2(\theta_2 - \psi)(r)]}{\sqrt{2(E - \psi_0(r)) - L^2/r^2}}, \tag{2.61}$$

where the angles are already given by eqs. (2.36) and (2.37) as a function of r_p, r_a and r, and U_n^ℓ is an element of the potential basis.

For the response matrix of a non-rotating sphere, eq. (2.42) can then be rewritten as

$$P_{\ell^p n^p \ell^q n^q}^{\tilde{\mathbf{n}}}(\omega) = \int \mathrm{d}r_\mathrm{p}\,\mathrm{d}r_\mathrm{a}\, \left|\frac{\partial(E, L)}{\partial(r_\mathrm{p}, r_\mathrm{a})}\right| \frac{L}{\Omega_1}\, \frac{\tilde{\mathbf{n}}\cdot\partial F/\partial\widetilde{\mathbf{J}}}{\omega - \tilde{\mathbf{n}}\cdot\widetilde{\boldsymbol{\Omega}}(r_\mathrm{p}, r_\mathrm{a})} W_{\ell^p n^p}^{\tilde{\mathbf{n}}\,*}(r_\mathrm{p}, r_\mathrm{a}) W_{\ell^q n^q}^{\tilde{\mathbf{n}}}(r_\mathrm{p}, r_\mathrm{a}). \tag{2.62}$$

A similar method can be used in the computation of analogous integrals in cases of matrices with additional kinematic complexity, e.g. the function $Q_{\ell^p n^p \ell^q n^q}^{\tilde{\mathbf{n}}}$ of eq. (4.26) for rotating spheres.

2.4.2 Computation of $W_{\ell n}^{\tilde{\mathbf{n}}}(\widetilde{\mathbf{J}})$

Let me now detail how the radial coefficients, $W_{\ell n}^{\tilde{\mathbf{n}}}$, from eq. (2.35) can be efficiently computed, improving upon the method presented in Fouvry et al. (2015a). Note that these coefficients only depend on the mean potential, $\psi_0(r)$, and the choice of basis elements, $U_n^\ell(r)$. As such, they are independent of the system's DF. They also satisfy the symmetry relation $W_{\ell n}^{-\tilde{\mathbf{n}}}(\widetilde{\mathbf{J}}) = W_{\ell n}^{\tilde{\mathbf{n}}}(\mathbf{J})$, which essentially halves the number of coefficients to evaluate.

As is shown by eq. (2.61), $W_{\ell n}^{\tilde{\mathbf{n}}}$ can be expressed as an integral over the radius. To compute $\theta_1(r)$ and $(\theta_2 - \psi)(r)$ in eq. (2.61), one has to compute the integrals from eqs. (2.36) and (2.37), with the boundaries $\int_{\mathcal{C}} \mathrm{d}r'_\mathrm{p} = \int_{r_\mathrm{p}}^{r} \mathrm{d}r'_\mathrm{p}$.

While all these integrals are well-defined, their integrands have a diverging behaviour at the boundaries $r = r_\mathrm{p}, r_\mathrm{a}$, originating from the vanishing of the radial velocity at the peri- and apocentre. This

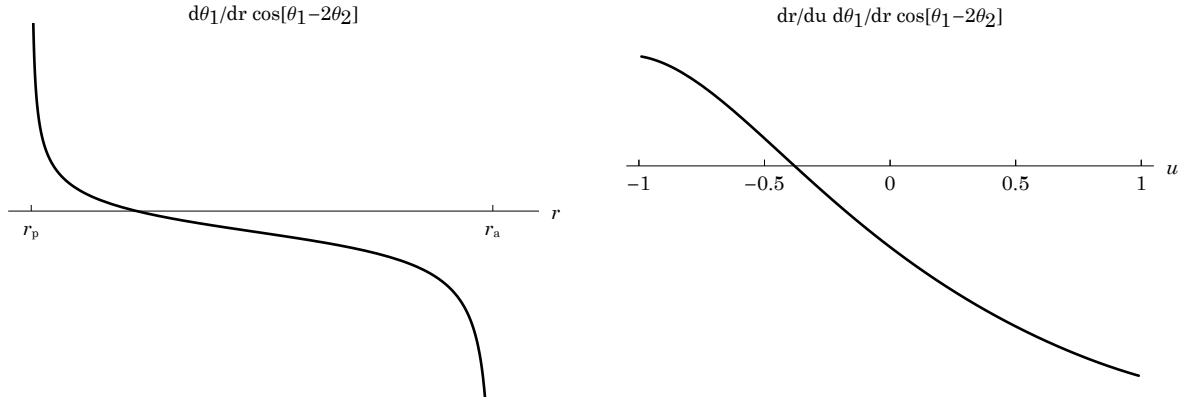

(a) Before remapping

(b) After remapping

Figure 2.11: (a) Integrand for the computation of $W_{\ell n}^{\tilde{\mathbf{n}}}$ when r is used as a variable. The integrand has integrable singularities at the boundaries of the integration region, r_p and r_a. (b) Integrand for the computation of $W_{\ell n}^{\tilde{\mathbf{n}}}$ when u is used as the integration variable (see eqs. (2.63) and (2.64)). The integrand has no more singularities.

behaviour is illustrated in Fig. 2.11a, where a simplified integrand is plotted against radius. In order to cure these divergences and ease the integration, I perform an additional change of variables. Rather than integrating w.r.t. r, one may integrate w.r.t. an (explicit) angular anomaly u. First, define $\Sigma=(r_\mathrm{p}+r_\mathrm{a})/2$ and $\Delta=(r_\mathrm{a}-r_\mathrm{p})/2$. A natural choice can be to consider the change of coordinates $r(u)=\Sigma+\Delta\sin(\frac{\pi}{2}u)$, with $u\in[-1;1]$, that is explicit, monotonic and satisfies $\mathrm{d}r/\mathrm{d}u=0$ for $u=\pm1$, therefore curing the boundary divergences. In practice, it can be numerically more efficient not to use a mapping based on a trigonometric function, but rather on a polynomial function of low degree. As a result, I consider the mapping

$$r(u)=\Sigma+\Delta\,f(u);\quad f(u)=u\big(3/2-u^2/2\big), \tag{2.63}$$

which is the appropriate third degree polynomial satisfying the four constraints $f(\pm1)=\pm1$ and $f'(\pm1)=0$ (see eq. (52) in Henon, 1971). This mapping has an explicit (and simple) Jacobian and can be evaluated very efficiently. Following this change of coordinate, eq. (2.61) becomes

$$W_{\ell n}^{\tilde{\mathbf{n}}}(\widetilde{\mathbf{J}})=\frac{1}{\pi}\int_{-1}^{1}\mathrm{d}u\,\frac{\mathrm{d}r}{\mathrm{d}u}\,\frac{\mathrm{d}\theta_1}{\mathrm{d}r}\,U_n^\ell(u)\cos\left[n_1\theta_1(u)+n_2(\theta_2-\psi)(u)\right], \tag{2.64}$$

with

$$\begin{aligned}\theta_1(u)&=\int_{-1}^{u}\mathrm{d}u'\,\frac{\mathrm{d}r}{\mathrm{d}u'}\,\frac{\Omega_1}{\sqrt{2(E-\psi_0(r))-J_2^2/r^2}},\\ (\theta_2-\psi)(u)&=\int_{-1}^{u}\mathrm{d}u'\,\frac{\mathrm{d}r}{\mathrm{d}u'}\,\frac{\Omega_2-J_2/r^2}{\sqrt{2(E-\psi_0(r))-J_2^2/r^2}}.\end{aligned} \tag{2.65}$$

The application of the change of variables (2.63) on the integrand of Fig. 2.11a gives the function represented Fig. 2.11b. The divergences have been smoothed, and the function is now much more easily integrated.

Naively, one could interpret the expression from eq. (2.64) as involving nested integrals, making the numerical evaluation cumbersome. Yet, the writing of eq. (2.64) can be improved to make the calculation even simpler. Forgetting about indices to simplify the notations, eq. (2.64) asks us to compute $W(u=1)$, for $W(u)$ of the generic form

$$W(u)=\int_{-1}^{u}\mathrm{d}u'\,w\big[u',T_1(u'),T_2(u')\big], \tag{2.66}$$

where T_1 (resp. T_2) stands for θ_1 (resp. $(\theta_2-\psi)$), and are given by expressions of the form

$$T_1(u)=\int_{-1}^{u}\mathrm{d}u'\,t_1(u');\quad T_2(u)=\int_{-1}^{u}\mathrm{d}u'\,t_2(u'). \tag{2.67}$$

Because the integration boundaries of $T_1(u)$ and $T_2(u)$ match that of $W(u)$, one can reinterpret eq. (2.66) not as a set of nested integrals, but rather as only one integral. To do so, note that $W(u)$, $T_1(u)$, and $T_2(u)$ satisfy the ordinary differential equations

$$\frac{\mathrm{d}W}{\mathrm{d}u} = w\big[u, T_1(u), T_2(u)\big] \quad ; \quad \frac{\mathrm{d}T_1}{\mathrm{d}u} = t_1(u) \quad ; \quad \frac{\mathrm{d}T_2}{\mathrm{d}u} = t_2(u), \tag{2.68}$$

with the initial conditions $(W(-1), T_1(-1), T_2(-1)) = (0, 0, 0)$. Introducing the state and velocity vectors as

$$\mathbf{S} = (W, T_1, T_2) \quad ; \quad \mathbf{s} = (w, t_1, t_2), \tag{2.69}$$

one can finally rewrite eq. (2.68) under the compact vector form

$$\frac{\mathrm{d}\mathbf{S}}{\mathrm{d}u} = \mathbf{s}\big[u, \mathbf{S}(u)\big] \quad ; \quad \mathbf{S}(-1) = 0. \tag{2.70}$$

Hence, computing the coefficients $W_{\ell n}^{\widetilde{\mathbf{n}}}(\widetilde{\mathbf{J}})$ amounts to computing the value of $\mathbf{S}(1)$, by integrating forward the differential eq. (2.70). Following this approach, one avoids the issue of having to compute nested integrals, and all the relevant quantities are moved forward simultaneously, which offers a significant speed-up of about 100 of the numerical computation. In practice, for the applications presented in this manuscript, eq. (2.70) is integrated with a fourth-order Runge-Kutta integrator (see eq. (17.1.3) in Press et al., 2007) with 100 fixed-size steps for $u \in [-1+\varepsilon; 1-\varepsilon]$ with $\varepsilon = 10^{-4}$ to avoid possible boundary overflows.

2.4.3 Action-space integration

Following eq. (2.62), computing the response matrix requires performing a 2D action space integration of the form

$$P_{\ell^p n^p \ell^q n^q}^{\widetilde{\mathbf{n}}}(\omega) = \int \mathrm{d}r_\mathrm{p}\, \mathrm{d}r_\mathrm{a}\, \frac{g_{\ell^p n^p \ell^q n^q}^{\widetilde{\mathbf{n}}}(r_\mathrm{p}, r_\mathrm{a})}{\omega - h^{\widetilde{\mathbf{n}}}(r_\mathrm{p}, r_\mathrm{a})}, \tag{2.71}$$

where the numerator and denominator read

$$\begin{aligned} g_{\ell^p n^p \ell^q n^q}^{\widetilde{\mathbf{n}}}(r_\mathrm{p}, r_\mathrm{a}) &= \left|\frac{\partial(E,L)}{\partial(r_\mathrm{p}, r_\mathrm{a})}\right| \frac{L}{\Omega_1}\, \widetilde{\mathbf{n}} \cdot \frac{\partial F}{\partial \widetilde{\mathbf{J}}}\, W_{\ell^p n^p}^{\widetilde{\mathbf{n}}\,*}(r_\mathrm{p}, r_\mathrm{a})\, W_{\ell^q n^q}^{\widetilde{\mathbf{n}}}(r_\mathrm{p}, r_\mathrm{a}), \\ h^{\widetilde{\mathbf{n}}}(r_\mathrm{p}, r_\mathrm{a}) &= \widetilde{\mathbf{n}} \cdot \widetilde{\mathbf{\Omega}}(r_\mathrm{p}, r_\mathrm{a}). \end{aligned} \tag{2.72}$$

As the denominator is (quasi-)resonant, one has to be careful with the way the integration is carried out. In order to deal with the resonant denominator, I implemented an integration algorithm based on the relatively slow variation of the functions g and h compared to the sharp variation of the rest of the integrand around the resonance, based on the so-called Gauss method. Note that here $(r_\mathrm{p}, r_\mathrm{a})$ are the integration variables, yet any relevant set of integration variables can be chosen, provided g is multiplied by the right Jacobian determinant. In particular, this algorithm is straightforwardly adapted to the variables defined in Section 2.4.4.

The procedure goes as follows. First, I define a square grid in $(r_\mathrm{p}, r_\mathrm{a})$ space with step Δr, and cut the integration space in small square pieces of side Δr centred on each grid point $(r_\mathrm{p}^0, r_\mathrm{a}^0)$. On each square, it is realistic to assume that the functions g and h are well approximated by their first order Taylor expansions. Then, the resulting integrand on the small square has an analytical expression in terms of functions that can be quickly computed, and which smoothly go through the near-resonant points. In practice, one has to distinguish the case of the Eulerian matrix from the Lagrangian form, as the latter presents terms that have a slightly different behaviour (see Appendix A). In the end, the integral across the singularity, which is extremely hard to perform by brute force numerical means, is smoothly computed via analytical functions.

In the case of the Eulerian matrix, given by eq. (2.20), the sub-region integration on the square S^0 of side Δr, centred on $(r_\mathrm{p}^0, r_\mathrm{a}^0)$, takes the form

$$\iint_{S_0} \mathrm{d}r_\mathrm{p}\, \mathrm{d}r_\mathrm{a} \frac{g(r_\mathrm{p}, r_\mathrm{a})}{\omega - h(r_\mathrm{p}, r_\mathrm{a})} \simeq \int_{-\frac{\Delta r}{2}}^{\frac{\Delta r}{2}} \mathrm{d}x_\mathrm{p} \int_{-\frac{\Delta r}{2}}^{\frac{\Delta r}{2}} \mathrm{d}x_\mathrm{a} \frac{g(r_\mathrm{p}^0, r_\mathrm{a}^0) + \frac{\partial g}{\partial r_\mathrm{p}} x_\mathrm{p} + \frac{\partial g}{\partial r_\mathrm{a}} x_\mathrm{a}}{\omega - (h(r_\mathrm{p}^0, r_\mathrm{a}^0) + \frac{\partial h}{\partial r_\mathrm{p}} x_\mathrm{p} + \frac{\partial h}{\partial r_\mathrm{a}} x_\mathrm{a})}, \tag{2.73}$$

where the partial derivatives are evaluated at the centre of the square. I note that the integrand is a homography, and present here a possible choice for the analytical expression replacing this integral. It can be

expressed as a particular function $\aleph^1(g(r_\mathrm{p}^0, r_\mathrm{a}^0), \partial g/\partial r_\mathrm{p}, \partial g/\partial r_\mathrm{a}, \omega_0 - h(r_\mathrm{p}^0, r_\mathrm{a}^0), -\partial h/\partial r_\mathrm{p}, -\partial h/\partial r_\mathrm{a}, \Delta r, \eta)$, defined by

$$\aleph^1(a_g, b_g, c_g, a_h, b_h, c_h, \Delta r, \eta) = \int_{-\frac{\Delta r}{2}}^{\frac{\Delta r}{2}} \mathrm{d}x_\mathrm{p} \int_{-\frac{\Delta r}{2}}^{\frac{\Delta r}{2}} \mathrm{d}x_\mathrm{a} \frac{a_g + b_g x_\mathrm{p} + c_g x_\mathrm{a}}{a_h + b_h x_\mathrm{p} + c_h x_\mathrm{a} + \mathrm{i}\,\eta}. \tag{2.74}$$

Assuming that $a_g, a_h \neq 0$ and using the change of variables $x = x_\mathrm{p}/\Delta r$ and $y = x_\mathrm{a}/\Delta r$, one can simplify this integral as

$$\aleph^1(a_g, b_g, c_g, a_h, b_h, c_h, \Delta r, \eta) = \frac{a_g}{a_h}\, \Delta r^2\, \aleph_\mathrm{D}^1\left(\frac{b_g \Delta r}{a_g}, \frac{c_g \Delta r}{a_g}, \frac{b_h \Delta r}{a_h}, \frac{c_h \Delta r}{a_h}, \frac{\eta}{a_h}\right), \tag{2.75}$$

with the dimensionless integral

$$\aleph_\mathrm{D}^1(b, c, e, f, \eta) = \int_{-\frac{1}{2}}^{\frac{1}{2}} \int_{-\frac{1}{2}}^{\frac{1}{2}} \mathrm{d}x \mathrm{d}y \, \frac{1 + bx + cy}{1 + ex + fy + \mathrm{i}\eta}\,. \tag{2.76}$$

The integral $\aleph_\mathrm{D}(b, c, e, f, \eta)$ is then computed by a suitable combination of the integrand's antiderivative

$$\begin{aligned}
G(x, y) &= \frac{1}{4e^2 f^2} \log[e^2 x^2 + 2e(fxy + x) + f^2 y^2 + 2fy + \eta^2 + 1] \\
&\times \left\{ bf(e^2 x^2 - (fy + \mathrm{i}\eta + 1)^2) + 2ef(ex + \mathrm{i}\eta + 1) - ce(ex + \mathrm{i}\eta + 1)^2 \right\} \\
&+ \frac{\mathrm{i}}{2e^2 f^2} \left\{ \frac{\pi}{2} - \arctan\left[\frac{ex + fy + 1}{\eta}\right] \right\} \left\{ bf(e^2 x^2 - (fy + \mathrm{i}\eta + 1)^2) + 2ef(ex + \mathrm{i}\eta + 1) - ce(ex + \mathrm{i}\eta + 1)^2 \right\} \\
&+ \frac{y}{4e^2 f} \left\{ f(-4e + b(2ex + fy + 2\mathrm{i}\eta + 2)) + ce(2ex - fy + 2\mathrm{i}\eta + 2) + 2ef(cy + 2) \log[ex + fy + \mathrm{i}\eta + 1] \right\}.
\end{aligned} \tag{2.77}$$

In practice, the computation of $\aleph_\mathrm{D}^1$ involves the addition of four terms $G(x, y)$, and this is done a large number of times (once for each point in the $r_\mathrm{p}, r_\mathrm{a}$ grid, and for many of the numerous possible combinations of n^p, n^q, ℓ and $\widetilde{\mathbf{n}}$). In order to further optimise this step, I reduced the number of required evaluations of log to only four for each computation of $\aleph_\mathrm{D}^1$.

2.4.4 Action space sampling

As shown in Section 2.4.3, the integral over action space is performed via the summation of approximate integrals on small square portions of the 2D plane. A priori, the variables are $(r_\mathrm{p}, r_\mathrm{a})$, so that the action space is regularly divided in squares of size Δr, and the functions g, h and their partial derivatives w.r.t. the peri- and apocentres are computed at the centre of these squares. However, I show now that this sampling is not optimal, as the variation of the functions g and h is not evenly distributed over the space of peri- and apocentres. To make the sampling more efficient, i.e. to concentrate the computation on the most relevant parts of action space, I change variables in a way that dilates the places where g and h vary the most, and contracts the rest of the plane.

Figure 2.12a shows a plot of the function g, for typical values of the parameters, in the plane $(r_\mathrm{p}, r_\mathrm{a})$. It appears that theses functions present an oscillatory behaviour at low values of the radii, while the behaviour at large radii is much smoother. As a consequence, a grid that presents more points at low values of r_p, r_a and less at higher values would achieve a better accuracy with the same number of computations of the function.

In order to match this requirement, I introduce a change of coordinates $(u, v) \mapsto (r_\mathrm{p}, r_\mathrm{a})$, which provides, for a regular grid in (u, v), a new $(r_\mathrm{p}, r_\mathrm{a})$ mapping with linear sampling at high radii, and logarithmic sampling at low radii, through the transformation

$$\begin{aligned}
r_\mathrm{p}(u) &= \frac{R_\mathrm{b}}{2(u_0 + 1)} \left[\mathrm{e}^{u_0 - u} \left(\mathrm{erf}\left(\frac{u_0}{\sigma}\right) + \mathrm{erf}\left(\frac{u - u_0}{\sigma}\right) \right) + (u_0 - u + 1) \left(\mathrm{erf}\left(\frac{u_0}{\sigma}\right) + \mathrm{erfc}\left(\frac{u - u_0}{\sigma}\right) \right) \right], \\
r_\mathrm{a}(u, v) &= r_\mathrm{p}(u) + r_\mathrm{p}(v),
\end{aligned} \tag{2.78}$$

where erf (resp. erfc) is the (resp. complementary) error function, σ is an ad hoc width, R_b is the radial scale of the basis functions. I also introduce $u_0 = p_\mathrm{b}\, n_\mathrm{max}\, \Delta u - 1$, with Δu the step size in the (u, v)-grid, n_max the maximum radial number for the basis functions and p_b a control parameter for the step size of the $(r_\mathrm{p}, r_\mathrm{a})$-grid in the region where it is linearly sampled. This transformation allows for the sampling

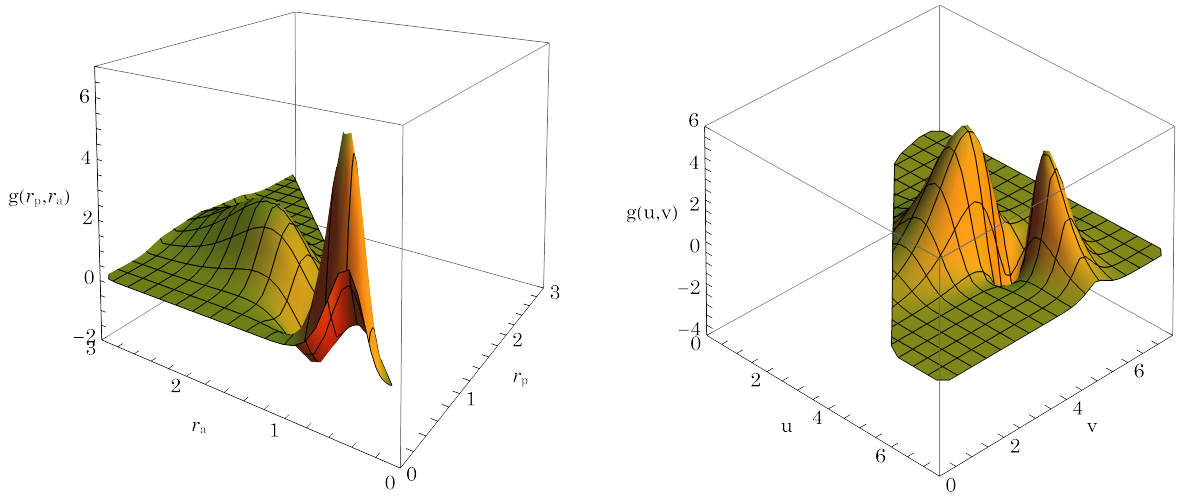

(a) Before remapping (b) After remapping

Figure 2.12: (a) Plot of a typical function $g(r_\mathrm{p}, r_\mathrm{a})$. The function has oscillations at large spatial frequencies and low radii, which makes it difficult to represent on a linear grid in $(r_\mathrm{p}, r_\mathrm{a})$. (b) Plot of a typical function $g(u, v)$. The oscillations of the function occur on smaller spatial frequencies. It is then easier to compute it on a linear grid in (u, v).

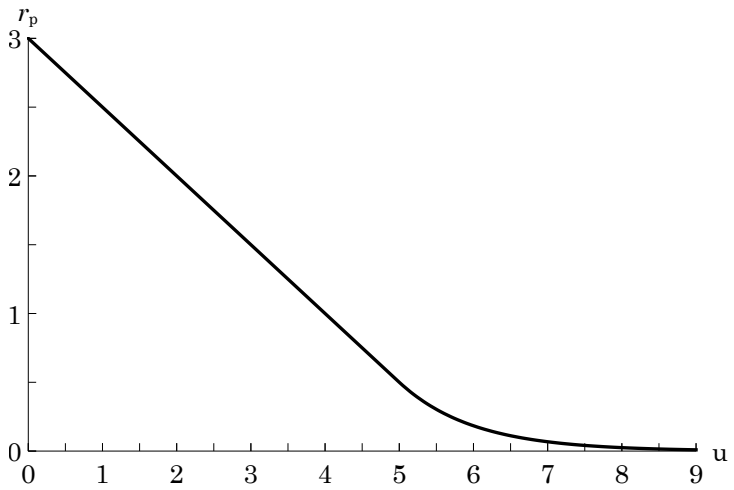

Figure 2.13: Plot of the radial remapping $r_\mathrm{p}(u)$ of eq. (2.78). A regular sampling in u will increase the sampling at low r_p (high u) and decrease it at high r_p (low u).

of r_p logarithmically near 0 and linearly further out, while r_a is sampled logarithmically near r_p (close to circular orbits) and linearly further out. On top of involving an explicit Jacobian, eq. (2.78) offers a smooth transition between the logarithmic and linear samplings, with $\sigma = 10^{-3}$ the typical width of the transition region. The sampling in $(r_\mathrm{p}, r_\mathrm{a})$ becomes linear when the radial step size reaches $R_\mathrm{b}/(p_\mathrm{b}\, n_\mathrm{max})$, hence the parameter p_b represents the minimal number of points in the r_p-grid per radial oscillation for the highest order radial basis function.

To illustrate this change of variables, Fig. 2.13 represents the profile of the transformation $r_\mathrm{p} \mapsto u$, displaying a clear transformation from exponential to linear scaling, with a continuous transition. The resulting function $g(u, v)$, obtained after the change of variables and multiplication by the Jacobian of the transformation, has a smoother structure in (u, v) space. This is illustrated by Fig. 2.12b.

This change of variables opened the possibility to accurately compute the response matrix using a smaller number of grid points than previously used (by, e.g., Fouvry et al., 2015a; Hamilton et al., 2018). This improvement complemented the new integration scheme for W (see Section 2.4.2), and overall decreased the matrix computation time by a factor of about 1000.

2.4.5 Improving the integration scheme

In order to perform the approximate integrals of Section 2.4.3, one needs to evaluate the partial derivatives of the numerator and denominator w.r.t. r_p and r_a. For now, most of the present work uses derivatives computed via finite differences, on the same grid as the one on which the values of g and h are computed. It is however very likely that the precise evaluation of these partial derivatives would increase the numerical precision and stability of the computation. The methods developed in Section 2.4.2 for the computation of W can be adapted to the computation of $\partial W/\partial r_\mathrm{p}$ and $\partial W/\partial r_\mathrm{a}$, allowing for an efficient computation of the partial derivatives of g. Such techniques are used to compute the Lagrangian matrix. Therefore, some useful methods for the computation of the partial derivates of W are given in Section A.3.1.

An important difference is to be noted with previous versions in terms of optimisation. Previously, the computation of the linear response of a system was dominated by the computation of the values of W at every grid point in $r_\mathrm{p}, r_\mathrm{a}$, for every value of n^p, n^q, ℓ and $\widetilde{\mathbf{n}}$. Note that the same values of W are used in the integration to get the response matrix at each frequency ω. In my implementation, the computation time is dominated by the integral computations at each complex frequency, and no more by individual computations of W. This has an important consequence on the constraints of the method in terms of accuracy. Computing the same matrix at extra values of ω was essentially costless, whereas increasing the accuracy of a single value of the matrix was expansive. Now, improving the integration scheme is relatively cheap, while increasing the sampling of the frequency space is expansive. It is therefore a good time to improve the matrix computation through more accurate integration schemes, such as one involving a better handling of the partial derivatives.

2.5 Conclusions

Since its derivation, the response matrix was successfully used in various contexts to identify instabilities in self-gravitating collisionless systems. Sawamura (1988); Vauterin & Dejonghe (1996); Pichon & Cannon (1997); Evans & Read (1998a,b); Jalali & Hunter (2005); Jalali (2007, 2008) used it to detect instabilities in a variety of disk models. Weinberg (1991b) detected modes in axisymmetric systems. More recent developments in De Rijcke & Voulis (2016); De Rijcke et al. (2019b) were dedicated to instabilities in grooved disks (i.e. disks with a narrow depleted region in the angular momentum distribution), accurately reproducing results from simulations. De Rijcke et al. (2019a) focused on the influence of the softening length on disk stability in N-body simulations. For spheres, Tremaine (2005) used the matrix method to detect modes in spherical systems with a central mass, while Polyachenko & Shukhman (1981); Saha (1991); Weinberg (1991a); Polyachenko & Shukhman (2015) used it to detect modes in radially anisotropic, spherical systems, hence characterising the radial orbit instability in these systems. Weinberg (1991a) also applied it to a tangentially anisotropic model, without finding any instability. Finally, in Rozier et al. (2019), I used the matrix method to study the stability of a series of rotating spheres, with both radial and tangential anisotropy. Some of these results are presented in Chapter 4.

I also presented a derivation of the Eulerian response matrix, as well as a proof that, for 3D systems, this Eulerian form is equivalent to the Lagrangian form initially proposed in Kalnajs (1977) (see Appendix A). I described my implementation of the computation of the response matrix, which is flexible, so that adapting it to a new potential and DF is easy, and optimised w.r.t. previous implementations. In my work, I alternatively use the Eulerian and Lagrangian forms of the response matrix, depending on the problem at hand. Ideally, the chosen form should make the integrand in eqs. (2.20) or (A.1) as smooth as possible. In cases where the DF is very peaked or diverging, it is therefore more efficient to use the Lagrangian version.

Although this method was developed in the 70s, the computation of the response matrix is still costly. First, it requires computing many 2D action space integrals, which is intricate since the integrand presents a resonant denominator. *I developed several techniques which led to a significant improvement in the numerical cost of this computation.* In particular, I applied an efficient integration scheme for the orbit-average of the potential basis elements, and a change of variables for the computation of action space integrals, based on the general characteristics of the functions at play. As proved by my results of the next chapters, thanks to these improvements, it is now possible to compute the matrix on a large number of systems, and hence to evaluate the role of different parameters on the instabilities. Such parameters explorations are impossible using N-body methods in a reasonable time.

In order to accurately measure low amplitude growth rates, oscillation frequencies and spatial structures of the instabilities, it is necessary to compute matrices of large sizes. I addressed this issue using

well chosen basis functions, designed to provide a good reconstruction of both the mean background and the mode of interest with a few basis elements. Unfortunately, meeting this requirement is not always possible with analytical bases, as only a few such bases exist in the literature. A solution can be to rely on a numerically constructed basis (see, e.g. Weinberg, 1999), however one would then loose the benefits of the analytical formulae, and possibly affect the code's numerical efficiency. Building flexible bi-orthogonal bases should also bring important improvements to stability analyses with the matrix method. Such a basis was proposed in Lilley et al. (2018), with a variable parameter controlling the shape of the basis elements, although this particular basis is more suitable to cuspy potentials.

Then, in order to scan the space of frequencies ω in a way that does not miss any instability, one must compute the matrix for a large number of frequencies. Indeed, the behaviour of a single Nyquist contour when it gets close to the origin becomes very intricate (the more so when the matrix is large), and an exquisite ω_0 sampling is usually required to make an accurate measurement of the growth rate. Using such a fine grid, *I implemented an algorithm which uses Nyquist contours to automate the identification of instabilities.* I was able to reproduce, at a lower cost, mode measurements for the radial orbit instability in isochrone spheres. The automated method I used to detect a mode from a given set of matrix values $\widehat{\mathbf{M}}(\omega)$ can be further improved. For now, the Nyquist contours are evaluated from the determinant $\det[\mathbf{I} - \widehat{\mathbf{M}}(\omega)]$. A refined version could rely on the spectrum of $\mathbf{I} - \widehat{\mathbf{M}}(\omega)$. Indeed, the intricacy of the response matrix around the origin is partly driven by several eigenvalues of $\mathbf{I} - \widehat{\mathbf{M}}(\omega)$ becoming small at the same time. If one computes separate series of Nyquist contours for each of the eigenvalues, this problem may be partly solved. Furthermore, the algorithm directly yields the corresponding eigenvector, i.e. the shape of the mode. To draw the Nyquist contour of a single eigenvalue, it is necessary to associate the eigenvalues of $\mathbf{I} - \widehat{\mathbf{M}}(\omega)$ at different values of ω. This can be safely done by matching both the eigenvalue and the eigenvector at the same time. In other words, one can rely on the continuity of both the eigenvalue and the eigenvector w.r.t. ω.

The response matrix still presents some issues, as compared to, e.g., N-body simulations. First, its results are hard to interpret, because of the highly non-intuitive nature of the tool. A critical passage seems to be that of the determinant, which mixes all contributions from individual integrals. Then, the efficiency of the method decisively relies on the assumptions on the bi-orthogonal basis. Indeed, the necessary truncation imposes that the modes should be well represented by the first basis elements. The choice also restricts the mode shapes which can be represented, so that no single basis can represent all modes equally well. Finally, an accurate matrix computation is impacted by the choice of action space integration variables. This choice is non-trivial, and may also depend on the specific problem of interest. I elaborate on possible changes of variables in the following section.

2.6 Prospects

Let me now highlight future works which could extend the results of this chapter. I insist on several improvements which could be implemented for the matrix computation, as well as other problems where the matrix method could bring interesting results.

Other analytical techniques were developed to study in a systematic way the linear response of stellar systems. Many of them rely on a description in terms of matrices, as they use a certain representation of potentials and densities, yet not under the present form, which specifically uses bi-orthogonal basis sets. A comparison of different techniques in the study of disks is performed in Polyachenko & Just (2015). Among such techniques, the one developed in Vauterin & Dejonghe (1996) (see also Hunter, 2002), and implemented in the code `pystab` (see, e.g., De Rijcke & Voulis, 2016), deserves to be highlighted, since one of its features could be implemented in the present formulation. Relying on a change of variables $J_r \mapsto \widetilde{\mathbf{n}} \cdot \widetilde{\mathbf{\Omega}}$, one could take the resonant denominator in eq. (2.30) out of the sum over $\widetilde{\mathbf{n}}$, so that the integral over action space could be computed only once, with only one (or a few) quasi-singular point. This extra step could lead to an improvement in the computational efficiency of the method.

Before taking this leap, it may be easy and profitable to refine the change of variables for the action space integration (in the spirit of Section 2.4.4). For now, a unique set of variables is used for integrating on all values of $\widetilde{\mathbf{n}}, n^p, n^q$, the angle Fourier numbers and the orders in the radial basis functions. Since each set $\widetilde{\mathbf{n}}, n^p, n^q$ leads to a different structure for the function $g(r_\mathrm{p}, r_\mathrm{a})$, it may be efficient to design tailor-made changes of variables for each of these pairs.

Another computational improvement may come from the use of exact derivatives instead of finite differences in the linear developments for the action space integration (see Section 2.4.3). As discussed in Section 2.4.5, I already implemented the computation of partial derivatives of the angle-averaged basis

elements (the function W), using the integration method described in Section 2.4.2. Even if the results presented here do not use this new feature, an improvement in the accuracy of the matrix computation is expected.

Finally, let me highlight new problems for which the response matrix may yield interesting results. First, the numerical improvements I presented *can also be implemented in other versions of the response matrix.* One of them, obtained by a temporal inverse Laplace transform on the matrix of eq. (2.20), describes the time evolution of the response of a stellar system to an external perturbation. This method was used by Weinberg (1989, 1998); Vesperini & Weinberg (2000) to describe the response of spherical and disky systems to the interaction with a companion, by Ideta (2002) for the evolution of lopsidedness in a stellar disk, and by Aubert et al. (2004) to describe the response of a dark matter halo to infalling matter. It is likely that the present numerical methods would improve the efficiency of such calculations. In particular, I specifically intend in the near future to apply this method to describe the time evolution of a perturbed disk. This topic gained interest recently, due to the detection by Gaia of signs of dynamical perturbations in the disk of the Milky Way (see, e.g., Antoja et al., 2018). Such a study may benefit from the framework of inverse problems. Indeed, the response matrix represents the linear operator connecting an initial perturber and the complete time response of the perturbed system. As such, one may put constraints on the initial perturbers by inverting the observed data via the response matrix. These constraints may complement those from forward modelling, which relies on parameter space exploration with N-body simulations.

Another line of work concerns the detection of neutral and weakly damped modes. In my thesis, I only presented methods for the identification of instabilities, i.e. growing modes. However, Weinberg (1994) showed that star clusters could also have modes which are neutral, or very weakly damped (see also the resent confirmation from numerical simulations by Heggie et al., 2020). His results relied on an analytic continuation of the response matrix in the half-plane of negative growth rates. Such a continuation may benefit from a fine sampling of the half-plane of positive growth rates, hence the present numerical methods may lead to improvements in the characterisation of these weakly damped modes. As underlined by Weinberg, these neutral or weakly damped modes may have observational counterparts, especially oscillatory displacements of the centre of spherical clusters from dipolar modes ($m = 1$).

The matrix method can also be adapted to study the stability of multi-component systems, e.g. disk-halo systems representing disk galaxies, or systems formed of a stellar and a gaseous sphere[9]. Such an adaptation requires describing the response of both component with separate matrices, which independently describe the response of the different components and off diagonal blocks describing the (gravitational) coupling between both components (Weinberg, 1998). Then, these matrices can be united into a block-matrix, accounting simultaneously for the joint response of the full system. For a disk-halo system, the matrices both have the form derived in the present chapter, however they rely on different bi-orthogonal basis expansions due to the respective form of the Poisson equation that the basis should solve. The inclusion of a gaseous disk should rely on a different version of the response matrix, because the equation describing the dynamics becomes the Euler equation. An issue of such a treatment concerns the self-consistency of the potential with the multi-component DF. Indeed, I derived the response matrix of a spherical system assuming that the potential is spherically symmetric. This derivation will be impacted by the addition of a non-spherical component.

The derivation of the response matrix with an axisymmetric potential would also be of great interest for the stability of axisymmetric systems, such as thick disks or spheroidal galaxies. One of the issues of such systems is the definition of isolating integrals which can be used as action coordinates. To avoid such difficulties, one can rely on Stäckel potentials, which are axisymmetric potentials with three isolating integrals (see de Zeeuw, 1985, and references therein). Distribution functions for such models can be obtained using Schwarzschild's method (Schwarzschild, 1979), although the resulting distribution would be numerical. The construction of a bi-orthogonal basis can be performed via the numerical method of Weinberg (1999), although, again, the resulting basis is numerical. Robijn (1995) performs a stability analysis of such systems, and it would be interesting to follow a similar protocol with my optimised numerical methods.

I can now use numerical techniques I developed for the computation of the response matrix on models of spherical stellar clusters. In the next chapters, I will particularly focus on systems with varying anisotropy and rotation.

[9]Note that for a spheroidal system embedded in a larger potential, such as a live elliptical galaxy in an inert DM halo, one only needs to replace the response matrix $\widehat{\mathbf{M}}$ by $\epsilon\,\widehat{\mathbf{M}}$ with $0 \leq \epsilon \leq 1$.

Chapter 3

Non-rotating tangential clusters

3.1 Introduction

Based on results of simulations of both structure formation (van Albada, 1982) and long-term evolution (Giersz & Heggie, 1994), radial anisotropy has emerged as the major type of anisotropy in many spherical structures of astrophysical interest. It has been known for a while, from both an analytical and a numerical perspective (Antonov, 1973; Henon, 1973), that this type of anisotropy leads to a particular sort of destabilising process, now called the radial orbit instability (ROI, see Section 1.4 for more details).

Meanwhile, little work was devoted to tangentially anisotropic systems (but, see Mikhaĭlovskiĭ et al., 1971; Synakh et al., 1971; Fridman et al., 1984a; Barnes et al., 1986; Polyachenko, 1987; Weinberg, 1991a), partly because few equilibria with tangential anisotropy are available (some examples of them are given in An & Evans, 2006). Yet, evidence for tangentially anisotropic star clusters was recently exhibited in different setups. On the simulation side, several results on the formation and evolution of star clusters embedded in a tidal field showed that these systems could be at least partly tangentially anisotropic. Indeed, Baumgardt & Makino (2003) showed that the preferential removal of stars on elongated orbits in the outer parts of the cluster could progressively build some tangential anisotropy in the outer parts of the system. Bianchini et al. (2017) recently showed that the amount of tangential anisotropy is related to the strength of the external tidal field. Furthermore, simulations of forming star clusters in a tidal field by Vesperini et al. (2014) showed that the Coriolis force from the motion of the cluster can bias the velocity distribution towards tangential anisotropy. On the observational side, astrometric observations of galactic globular clusters (GCs) using Gaia showed that some objects are partially tangentially anisotropic (Watkins et al., 2015; Jindal et al., 2019). This recent evidence renewed the interest for the theoretical study of tangentially anisotropic star clusters.

Palmer et al. (1989) gave the first demonstration of the existence of the circular orbit instability (COI), a particular dynamical instability specific to tangentially anisotropic spheres. Given its renewed interest, in this chapter, I will develop a thorough study of this particular type of instability, through the use of the matrix method. Using this method, I will confirm and complement the results of Fridman et al. (1984a); Palmer et al. (1989). In Section 3.2, I will revisit and adapt the demonstration of the existence of the COI developed in Palmer et al. (1989). This demonstration will rely on the epicyclic approximation, which is appropriate for tangentially anisotropic clusters, since the orbits are quasi-circular. In Section 3.3, I will propose a version of the response matrix based on the tight-winding approximation, also known as the WKB approximation. Under this assumption, the response matrix is diagonal and I get direct access to an analytical expression for its eigenvalues. I will show that the COI is necessarily a large scale mode, as the system is stable to WKB-like perturbations. As a consequence, in Section 3.4, I will look for this instability using the full matrix apparatus, which is the adequate framework to study large scale instabilities. I will exhibit instabilities in a series of tangentially anisotropic clusters, develop a method to confirm that this instability is of the COI type, and track the marginal point of this instability on the line of decreasing tangential anisotropy. Finally, I will present preliminary results on the linear stability of the Einstein sphere which has maximal tangential anisotropy (i.e. orbits are all circular). In that case, it appears that the instability is suppressed, which is consistent with a prediction made in Palmer et al. (1989).

3.2 Existence of a circular orbit instability

The circular orbit instability (COI) concerns spheres with high tangential anisotropy, i.e. where orbits are quasi-circular rather than very radial. It emerges from the resonant interactions between orbits and a neutral mode, leading it to becoming unstable. Here, I reproduce the analytical arguments that led to its discovery. First, I will derive the integro-differential equation which must be satisfied by a mode of the system. Then, I will show that this equation has a spectrum of neutral modes in tangentially anisotropic systems, where resonant interactions can be neglected. Finally, I will show that proper accounting of the resonant stars destabilises the neutral modes, hence giving birth to an instability.

3.2.1 Derivation of the eigen-equation

The argument developed in Palmer et al. (1989) to identify the circular orbit instability does not use a projection on a bi-orthogonal basis, hence it does not explicitly involve a response matrix, although it could certainly be adapted to the language of matrices.

Consider the linearised collisionless Boltzmann eq. (2.1), and more precisely its angle-Fourier-transformed version, eq. (2.3). Now, instead of applying a time Laplace transform, I assume that the only time dependence of the perturbations $f_{\mathbf{n}}$, $\psi_{\mathbf{n}}$, $\rho_{\mathbf{n}}$ is through a factor $\mathrm{e}^{-\mathrm{i}\omega t}$

$$\begin{aligned} f(\boldsymbol{\theta},\mathbf{J},t) &= f(\boldsymbol{\theta},\mathbf{J})\,\mathrm{e}^{-\mathrm{i}\omega t},\\ \psi(\boldsymbol{\theta},\mathbf{J},t) &= \psi(\boldsymbol{\theta},\mathbf{J})\,\mathrm{e}^{-\mathrm{i}\omega t}. \end{aligned}$$

Here, what defines a mode of the system is that this perturbation should be self-sustained, which corresponds to the fact that the perturbation f to the DF F that is triggered by the potential perturbation ψ can be self-consistently integrated to recover the potential perturbation. I then have

$$\begin{aligned} \rho(\mathbf{x}) &= \int \mathrm{d}\mathbf{v}\, f(\mathbf{x},\mathbf{v}),\\ \Delta\psi &= 4\pi G\rho. \end{aligned} \tag{3.1}$$

The eigen-equation used in Palmer et al. (1989) follows from these two equations. On the one hand, through the Poisson equation, the perturbation in density can be expressed as a function of the potential and its derivative. On the other hand, eq. (2.6) gives an expression of the DF perturbation as a function of the potential. The resulting integro-differential equation should be satisfied by any mode of the system.

To proceed forward, following closely Palmer et al. (1989), I exploit the properties of solutions to the Poisson equation in a spherically symmetric system, i.e. that the potential is separable in radius and spherical angles, and that its dependence on the spherical angles is through a single spherical harmonic

$$\psi(\mathbf{x}) = \psi_r(r)Y_\ell^m(\theta,\phi). \tag{3.2}$$

Hence, characterising an eigen-mode of eq. (3.1) amounts to finding the potential function ψ_r, and the associated complex frequency ω.

For non-rotating spheres, eq. (2.41) implies that the matrix is independent of m and block-diagonal in ℓ, so that an instability will generally have the form (3.2), up to a rotation of the spherical coordinate system. Using that assumption and the linearised Poisson equation, I can express the density as

$$\rho(\mathbf{x}) = \frac{1}{4\pi G}\Delta\psi = \frac{Y_\ell^m(\theta,\phi)}{4\pi G r^2}\left[\frac{\mathrm{d}}{\mathrm{d}r}\left(r^2\frac{\mathrm{d}\psi_r}{\mathrm{d}r}\right) - \ell(\ell+1)\psi_r\right]. \tag{3.3}$$

Developing the DF in Fourier series over the angles and using eq. (2.6), eq. (3.3) becomes

$$\frac{Y_\ell^m(\theta,\phi)}{4\pi G r^2}\left[\frac{\mathrm{d}}{\mathrm{d}r}\left(r^2\frac{\mathrm{d}\psi_r}{\mathrm{d}r}\right) - \ell(\ell+1)\psi_r\right] = -\sum_{\mathbf{n}}\int\mathrm{d}\mathbf{v}\left[\frac{\mathbf{n}\cdot\partial F/\partial\mathbf{J}}{\omega-\mathbf{n}\cdot\boldsymbol{\Omega}}\right]\psi_{\mathbf{n}}(\mathbf{J})\,\mathrm{e}^{\mathrm{i}\mathbf{n}\cdot\boldsymbol{\theta}}. \tag{3.4}$$

My goal is to transform this equation into an integro-differential equation on ψ_r. First, I multiply it by $\sin\theta\, Y_\ell^{m\,*}(\theta,\phi)$ and I integrate over the angles, leading to

$$\frac{\mathrm{d}}{\mathrm{d}r}\left(r^2\frac{\mathrm{d}\psi_r}{\mathrm{d}r}\right) - \ell(\ell+1)\psi_r = -4\pi G\, r^2\sum_{\mathbf{n}}\int\mathrm{d}\mathbf{v}\sin\theta\,\mathrm{d}\theta\,\mathrm{d}\phi\,\frac{\mathbf{n}\cdot\partial F/\partial\mathbf{J}}{\omega-\mathbf{n}\cdot\boldsymbol{\Omega}}\,\psi_{\mathbf{n}}(\mathbf{J})\,\mathrm{e}^{\mathrm{i}\mathbf{n}\cdot\boldsymbol{\theta}}\,Y_\ell^{m\,*}(\theta,\phi). \tag{3.5}$$

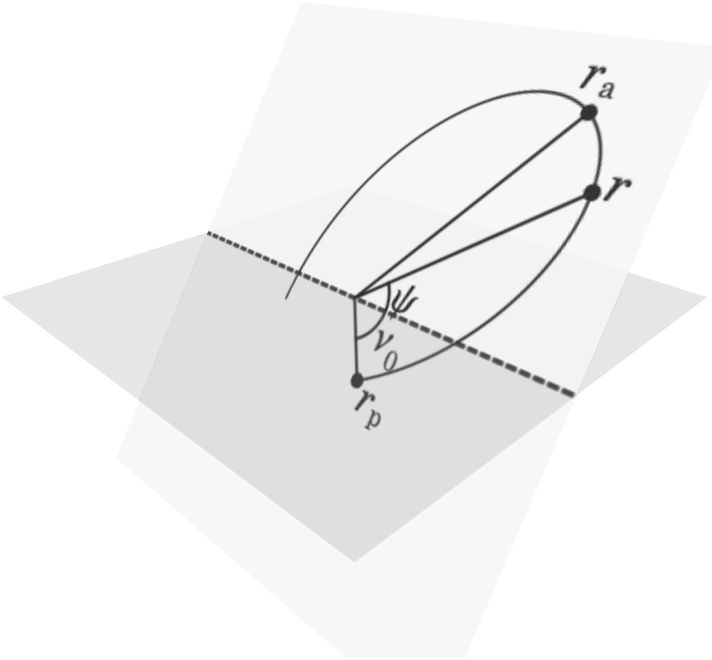

Figure 3.1: Sketch of an orbit in a central potential. The origin is in O, the pericentre in r_p, the apocentre in r_a, and r marks the current position. The dashed line symbolises the line of nodes. When the shape of the orbit is chosen, as well as the radius of the current position, the only remaining degree of freedom is the orientation of the pericentre w.r.t. the line of nodes. Varying ν_0 only makes the set of points $r_\mathrm{p}, r, r_\mathrm{a}$ rotate about the origin, conserving the sum $\psi + \nu_0$.

Now, I apply the rotation formula from Tremaine & Weinberg (1984) to the spherical harmonics

$$Y_\ell^m(\theta,\phi) = \mathrm{e}^{\mathrm{i}m\theta_3} \sum_{k=-\ell}^{\ell} R^\ell_{km}(i)\, Y_\ell^k\, \mathrm{e}^{\mathrm{i}k\psi}\, \mathrm{i}^{m-k}, \tag{3.6}$$

where $R^\ell_{nm}(i)$ is defined by eq. (2.34), Y_ℓ^k is introduced in eq. (2.39), $\cos i = L_z/L$ and ψ is the angle between the ascending node and the current position, measured in the orbit plane along the orbital motion (see Figs. 2.4 and 3.1). Furthermore, I transform the integration variables following Palmer & Papaloizou (1987)

$$\mathrm{d}\mathbf{x}\,\mathrm{d}\mathbf{v} = r^2\,\mathrm{d}r\,\sin\theta\,\mathrm{d}\theta\,\mathrm{d}\phi\,\mathrm{d}\mathbf{v} = \frac{4\pi\,\mathrm{d}\nu_0\,\mathrm{d}(\cos i)\,L\,\mathrm{d}L\,\mathrm{d}E\,\mathrm{d}r}{\sqrt{2(E-\psi_0(r)) - L^2/r^2}}, \tag{3.7}$$

where ν_0 is the angle between the pericentre and the ascending node, measured in the orbit plane along the orbital motion, and $\psi_0(r)$ is the background mean field potential. For a given orbit plane, and a given radius r, the angle ν between the pericentre and the current point, measured in the orbit plane along the orbital motion, is fixed, and we have $\nu = \nu_0 + \psi$. Figure 3.1 shows how these angles are graphically related. As a consequence, the integration variable can be transformed through $\mathrm{d}\psi = -\mathrm{d}\nu_0$. Equation (3.5) now becomes

$$\begin{aligned}\mathcal{L}(\psi_r) = -4\pi G \sum_{\mathbf{n}} \int \frac{4\pi\,\mathrm{d}\psi\,\mathrm{d}(\cos i)\,L\,\mathrm{d}L\,\mathrm{d}E}{\sqrt{2(E-\psi_0(r)) - L^2/r^2}}\, \frac{\mathbf{n}\cdot\partial F/\partial\mathbf{J}}{\omega - \mathbf{n}\cdot\mathbf{\Omega}}\, \psi_\mathbf{n}(\mathbf{J})\, \mathrm{e}^{\mathrm{i}(n_1\theta_1 + n_2(\theta_2-\psi))} \\ \times \sum_{k=-\ell}^{\ell} R^\ell_{km}(i)\, Y_\ell^k\, \mathrm{e}^{\mathrm{i}(n_2-k)\psi}\, \mathrm{i}^{k-m},\end{aligned} \tag{3.8}$$

where the operator $\mathcal{L}$ is defined as

$$\boxed{\mathcal{L}(\psi_r) = \frac{\mathrm{d}}{\mathrm{d}r}\left(r^2\frac{\mathrm{d}\psi_r}{\mathrm{d}r}\right) - \ell(\ell+1)\psi_r.} \tag{3.9}$$

Here, $\mathcal{L}(\psi_r)$ is the radial part of the density perturbation ρ (times $4\pi G r^2$), as computed from ψ_r using the Poisson equation. The right hand side of eq. (3.8) is the same quantity, yet obtained from ψ_r using

the CBE. In the integrand of eq. (3.8), θ_1 and $\theta_2 - \psi$ are functions of (E, L, r) only, so the integral over ψ only applies to the $\mathrm{e}^{\mathrm{i}(n_2-k)\psi}$ term, yielding $2\pi\delta_k^{n_2}$. Additionally, following Tremaine & Weinberg (1984), a potential with the form of eq. (3.2) will have the angle Fourier-transform

$$\psi_{\mathbf{n}}(\mathbf{J}) = \delta_m^{n_3}\, \mathrm{i}^{m-n_2}\, Y_\ell^{n_2}\, R^\ell_{n_2 m}(i)\, W^{\widetilde{\mathbf{n}}}(\widetilde{\mathbf{J}}), \tag{3.10}$$

where $\widetilde{\mathbf{n}} = (n_1, n_2)$, $\widetilde{\mathbf{J}} = (J_r, L)$ and

$$W^{\widetilde{\mathbf{n}}}(\widetilde{\mathbf{J}}) = \frac{1}{\pi}\int_0^\pi \mathrm{d}\theta_1\, \psi_r(r(\theta_1))\, \cos[n_1\theta_1 + n_2(\theta_2 - \psi)]. \tag{3.11}$$

Note that $W^{\widetilde{\mathbf{n}}}$ corresponds to the same operation on the test function ψ_r as the $W^{\widetilde{\mathbf{n}}}_{\ell n}$ of eq. (2.35) on the potential basis elements. Equation (3.8) therefore becomes

$$\mathcal{L}(\psi_r) = -32\pi^3 G \sum_{\mathbf{n}} \delta_m^{n_3} \int \frac{\mathrm{d}(\cos i)\, L\, \mathrm{d}L\, \mathrm{d}E}{\sqrt{2(E-\psi_0(r)) - L^2/r^2}}\, \frac{\mathbf{n}\cdot\partial F/\partial \mathbf{J}}{\omega - \mathbf{n}\cdot\mathbf{\Omega}}\, \mathrm{e}^{\mathrm{i}(n_1\theta_1 + n_2(\theta_2-\psi))} \left|Y_\ell^{n_2}\right|^2 R^\ell_{n_2 m}(i)^2\, W^{\widetilde{\mathbf{n}}}(\widetilde{\mathbf{J}}). \tag{3.12}$$

Considering that the system is spherical and non-rotating, so that $\partial F/\partial L_z = 0$, the sum over $\mathbf{n}$ can be restricted to $\widetilde{\mathbf{n}} = (n_1, n_2)$ due to the $\delta_m^{n_3}$ term. I can then readily perform the integral over $\cos i$, using the orthogonality relation (2.38), giving

$$\mathcal{L}(\psi_r) = -\frac{64\pi^3 G}{2\ell+1} \sum_{\widetilde{\mathbf{n}}} \left|Y_\ell^{n_2}\right|^2 \int \frac{L\, \mathrm{d}L\, \mathrm{d}E}{\sqrt{2(E-\psi_0(r)) - L^2/r^2}}\, \frac{\widetilde{\mathbf{n}}\cdot\partial F/\partial \widetilde{\mathbf{J}}}{\omega - \widetilde{\mathbf{n}}\cdot\widetilde{\mathbf{\Omega}}}\, \mathrm{e}^{\mathrm{i}(n_1\theta_1 + n_2(\theta_2-\psi))}\, W^{\widetilde{\mathbf{n}}}(\widetilde{\mathbf{J}}). \tag{3.13}$$

An additional simplification can be made through the following argument: given a radius r, the integrand corresponds to a quantity computed on all trajectories with the actions $\widetilde{\mathbf{J}}$ that go through a point at radius r. In particular, it takes into account both directions of orbital motion that go through that particular point. I can then compute the exact same integrand by relabelling the orbits as rotating in the opposite direction. This relabelling will only affect the definition of the angles in the following way

$$\theta_1 \to -\theta_1 \;\; ; \;\; \theta_2 - \psi \to -(\theta_2 - \psi). \tag{3.14}$$

One can take the mean of the two equivalent integrands, so that

$$\mathcal{L}(\psi_r) = -\frac{64\pi^3 G}{2\ell+1} \sum_{\widetilde{\mathbf{n}}} \left|Y_\ell^{n_2}\right|^2 \int \frac{L\, \mathrm{d}L\, \mathrm{d}E}{\sqrt{2(E-\psi_0(r)) - L^2/r^2}}\, \frac{\widetilde{\mathbf{n}}\cdot\partial F/\partial \widetilde{\mathbf{J}}}{\omega - \widetilde{\mathbf{n}}\cdot\widetilde{\mathbf{\Omega}}}\, \cos[n_1\theta_1 + n_2(\theta_2-\psi)]\, W^{\widetilde{\mathbf{n}}}(\widetilde{\mathbf{J}}). \tag{3.15}$$

Finally, let me change the integration variable from E to J_r in the main integral, with the Jacobian $\partial E/\partial J_r = \Omega_1$. Let me also change the integration variable from θ_1 to r' in $W^{\widetilde{\mathbf{n}}}$, with the Jacobian derived from eq. (2.36)

$$\frac{\mathrm{d}\theta_1}{\mathrm{d}r} = \frac{\Omega_1}{\sqrt{2(E-\psi_0(r)) - L^2/r^2)}}, \tag{3.16}$$

and change the order of integration, so that eq. (3.15) finally becomes

$$\boxed{\mathcal{L}(\psi_r)(r) = \mathcal{K}(\psi_r)(r),} \tag{3.17}$$

where the operator $\mathcal{K}$ is defined as the integral operator

$$\boxed{\mathcal{K}(\psi_r)(r) = \int \mathrm{d}r'\, K(r, r', \omega)\, \psi_r(r'),} \tag{3.18}$$

while the kernel K is given by

$$\boxed{K(r, r', \omega) = \sum_{\widetilde{\mathbf{n}}} K_{\widetilde{\mathbf{n}}}(r, r', \omega),} \tag{3.19}$$

with

$$\boxed{K_{\widetilde{\mathbf{n}}}(r, r', \omega) = -\frac{64\pi^2 G}{2\ell+1} \left|Y_\ell^{n_2}\right|^2 \int \mathrm{d}J_r\, \mathrm{d}L\, L\, \frac{\widetilde{\mathbf{n}}\cdot\partial F/\partial \widetilde{\mathbf{J}}}{\omega - \widetilde{\mathbf{n}}\cdot\widetilde{\mathbf{\Omega}}}\, \mathcal{B}_{\widetilde{\mathbf{n}}}(\widetilde{\mathbf{J}}, r)\, \mathcal{B}_{\widetilde{\mathbf{n}}}(\widetilde{\mathbf{J}}, r'),} \tag{3.20}$$

and

$$\boxed{\mathcal{B}_{\widetilde{\mathbf{n}}}(\widetilde{\mathbf{J}},r)=\frac{\Omega_1}{\sqrt{2(E-\psi_0(r))-L^2/r^2}}\cos[n_1\theta_1(r)+n_2(\theta_2-\psi)(r)].} \tag{3.21}$$

Equation (3.17) is the integro-differential equation satisfied by a mode of the system of the form (3.2), for a non-rotating sphere with arbitrary anisotropy. This equation displays all the characteristics of the large scale gravitational interactions giving birth to a mode. On the left, the operator $\mathcal{L}$ is the radial part of the Laplace operator in the Poisson equation. On the right, $\mathcal{K}(\psi_r)$ represents the density perturbation generated by the perturbing potential ψ_r. The integral over r' in eq. (3.17) reflects the non-locality of the link between the potential and the density. Indeed, the potential perturbation slightly modifies the orbits everywhere in the system, and the subsequent dynamics propagates these orbital changes in different locations. This propagation along the orbits is represented by the integral over the actions in eq. (3.20). In eq. (3.19), $K(r,r',\omega)$ represents the influence of any perturbing potential at position r' on the density at position r. In other words, the potential perturbs the orbits at position r', and this perturbation is propagated through the orbits to position r. The integral over the actions in eq. (3.20) is therefore restricted to all orbits which go through the radii r and r'. Let me now focus on the integrand of eq. (3.20). It is the product of two terms. On the one hand, $\mathcal{B}_{\widetilde{\mathbf{n}}}(\widetilde{\mathbf{J}},r)$ describes the effect of the orbital perturbations on the density at radius r. On the other, the rest of the integrand describes the way a perturbing potential affects individual orbits at radius r'. A particular feature of this latter term is the resonant denominator $\omega-\widetilde{\mathbf{n}}\cdot\widetilde{\mathbf{\Omega}}$. It accounts for the fact that the orbits change all the more under the effect of the perturbing potential that they are close to a resonance with the (real) frequency of the perturber (i.e. its oscillation frequency).

Note that the integration over the actions in eq. (3.20) spans the orbits that go through both r and r'. As a consequence, the kernel K is insensitive to the exchange of r and r', and is therefore symmetric. Hence, the operator $\mathcal{K}$ is self-adjoint, i.e. for any pair of test functions ψ_1,ψ_2, one has

$$\langle\psi_1,\mathcal{K}(\psi_2)\rangle=\int\mathrm{d}r\,\mathrm{d}r'\,\psi_1(r)\,K(r,r',\omega)\,\psi_2(r')=\langle\mathcal{K}(\psi_1),\psi_2\rangle. \tag{3.22}$$

Furthermore, from eq. (3.9), one can show that

$$\langle\psi_r,\mathcal{L}(\psi_r)\rangle=-\int\mathrm{d}r\left[r^2\left(\frac{\mathrm{d}\psi_r}{\mathrm{d}r}\right)^2+\ell(\ell+1)\psi_r^2\right]. \tag{3.23}$$

Hence, $\mathcal{L}$ is a definite negative operator (i.e. $\langle\psi_r,\mathcal{L}(\psi_r)\rangle$ is strictly negative unless ψ_r is identically vanishing). As a consequence, $\mathcal{L}$ can be inverted.

Another important property of $\mathcal{L}$ is that this operator is unbounded, i.e. the ratio $\langle\psi_r,\mathcal{L}(\psi_r)\rangle/\langle\psi_r,\psi_r\rangle$ can take arbitrarily large values. To show this property, it is sufficient to exhibit a sequence of test functions with constant $\langle\psi_r,\psi_r\rangle$ and diverging $\langle\psi_r,\mathcal{L}(\psi_r)\rangle$. This can be done with the sequence $\psi_r^{(n)}(x)=\sin(nx)$ for $n\geq 0$, defined on $[0,2\pi]$. I can see that whatever n, $\langle\psi_r^{(n)},\psi_r^{(n)}\rangle=\pi$, and that

$$\langle\psi_r^{(n)},\mathcal{L}(\psi_r^{(n)})\rangle=-\left\{\frac{4\pi^3}{3}n^2-\frac{\pi\cos(8n\pi)}{8}+\left(\frac{1}{64n}-\frac{\pi^2}{2}n\right)\sin(8n\pi)+\ell(\ell+1)\pi\right\}, \tag{3.24}$$

so it diverges as $-4\pi^3n^2/3$ when $n\to\infty$.

Upon inversion, eq. (3.17) becomes

$$\left[\mathcal{L}^{-1}\,\mathcal{K}\right](\psi_r)=\psi_r. \tag{3.25}$$

Hence, modes of the system can be identified by studying the spectrum of the operator $\mathcal{L}^{-1}\,\mathcal{K}$, and finding cases where it has an eigenvalue equal to 1. More explicitly, I can study the eigen-equation

$$\boxed{\left[\mathcal{L}^{-1}\,\mathcal{K}\right](\psi_r)=\lambda\,\psi_r,} \tag{3.26}$$

and then restrict myself to the physical case $\lambda=1$.

In order to constrain the properties of the operator $\mathcal{L}^{-1}\,\mathcal{K}$, I assume that the boundary conditions are fixed so that the space of test functions ψ_r is separable, in the sense that it can be represented by a discrete functional basis[1]. This can be achieved, e.g., by considering that the spherical system of

[1]Note that the assumption of separability is also made implicitly when using the matrix method, to guarantee the existence of complete bases (see Section 2.2.2).

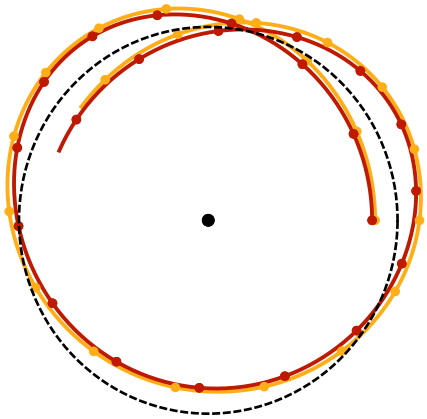

Figure 3.2: A nearly circular orbit (yellow) and its epicyclic approximation (red) in the Plummer potential. Dots are represented at regular times on the orbits. The dashed line corresponds to the guiding radius. The black dot is the centre of the cluster. The trajectory is well approximated by its epicyclic approximation, however there is a systematic drift due to a slight difference in frequencies.

interest has a cutoff at some large radius R[2]. This assumption guarantees that, for a given value of ω, the eigen-equation (3.26) has a discrete spectrum of eigenvalues $\lambda_i(\omega)$, with corresponding eigenvectors $\psi_i(r)$ (which also depend on ω). For some values of ω, one of these eigenvalues may be equal to 1, which identifies the corresponding eigenvector as a mode of the system. Hence, finding modes of the system corresponds to exhibiting specific frequencies ω_i where the eigenvalue λ_i verifies

$$\lambda_i(\omega_i) = 1. \tag{3.27}$$

The purpose of the next section is to prove that, when I neglect the stars at a resonance with the pattern, a sequence of such solutions exists with purely real ω_i (i.e. neutral mode solutions). The final evidence for the COI will then be given by the fact that stars at resonances with these neutral modes destabilise them.

3.2.2 A spectrum of neutral modes

The evidence for the COI is given in Palmer et al. (1989) by the following argument. First, they prove that, when restricting the orbits to epicycles and when the resonances are not populated, the system has a spectrum of neutral modes (i.e. a spectrum of purely real frequencies ω_i where the eigenvalue $\lambda_i(\omega_i) = 1$). Then, they prove that these particular neutral modes are destabilised by resonant stars.

3.2.2.1 The epicyclic approximation

For systems with sufficient tangential anisotropy, a dominant fraction of the orbits display low eccentricity. The epicyclic approximation is relevant for these orbits, and corresponds to approximating the orbit by a combination of two harmonic librations. The first one, called the guiding orbit, describes the bulk rotation of the orbit at its azimuthal frequency Ω_2 and radius approximately equal to $(r_\mathrm{p} + r_\mathrm{a})/2$. The second circle, called the epicycle, describes the small deviations from circularity at the radial frequency Ω_1 and with radius approximately equal to $(r_\mathrm{a} - r_\mathrm{p})/2$. Figure 3.2 shows an approximately circular orbit and its epicyclic approximation.

Following Binney & Tremaine (2008), at given actions J_r, L, the guiding radius R_g of the orbit is the radius of a circular orbit with the same angular momentum, defined by the relation

$$L = \sqrt{R_\mathrm{g}^3 \left.\frac{\mathrm{d}\psi_0}{\mathrm{d}r}\right|_{R_\mathrm{g}}}, \tag{3.28}$$

and the radius (known as the amplitude) A_R of the epicycle is defined by

$$A_R = \sqrt{\frac{2J_r}{\kappa}}, \tag{3.29}$$

[2]This assumption is made by, e.g., Fridman et al. (1984a); Weinberg (1989) in the construction of a basis for that space.

where κ is the radial frequency of circular orbits with the same angular momentum. This frequency is also called the epicycle frequency, and is given by

$$\kappa(R_{\rm g}) = \sqrt{\left.\frac{{\rm d}^2\psi_0}{{\rm d}r^2}\right|_{R_{\rm g}} + 3\frac{L^2}{R_{\rm g}^4}}. \tag{3.30}$$

The current radius and the azimuthal angle can be expressed as a function of the radial angle through

$$R = R_{\rm g} - A_R\cos\theta_1 \quad ; \quad \theta_2 - \psi = -\frac{2\Omega}{\kappa}\frac{A_R}{R_{\rm g}}\sin\theta_1, \tag{3.31}$$

where in the last expression ψ is the angle between ascending node and current position (see Fig. 3.1), and Ω is the azimuthal frequency of the circular orbit at radius $R_{\rm g}$, given by

$$\Omega(R_{\rm g}) = \sqrt{\left.\frac{1}{R_{\rm g}}\frac{{\rm d}\psi_0}{{\rm d}r}\right|_{R_{\rm g}}}. \tag{3.32}$$

Note that the convention for the angles is chosen such that $\theta_1 = \theta_2 - \psi = 0$ at the pericentre, in agreement with eqs. (2.36) and (2.37). I can then derive simple expressions which will be useful in the following sections

$$L = R_{\rm g}^2\,\Omega \quad ; \quad \kappa^2 = R_{\rm g}\left.\frac{{\rm d}\Omega^2}{{\rm d}r}\right|_{R_{\rm g}} + 4\Omega^2 \quad ; \quad \kappa^2 - \Omega^2 = 4\pi G\rho. \tag{3.33}$$

Finally, at this level of approximation, the norm of the radial velocity is given by

$$|v_r| = \sqrt{2(E - \psi_0(r)) - L^2/r^2} = A_R\,\kappa\,|\sin\theta_1|. \tag{3.34}$$

3.2.2.2 The distribution function

In order to be more quantitative on the tangential anisotropy introduced here, let me consider a DF with the same characteristics as the one used in Palmer et al. (1989). This DF has the form

$$F(\widetilde{\mathbf{J}}) = f_L(L) f_r(J_r), \tag{3.35}$$

where $f_r(J_r)$ is strongly peaked around $J_r = 0$, and is a strictly decreasing function of J_r up to a point J_0 where it vanishes, corresponding to an epicycle radius A_0 independent of $R_{\rm g}$. These simplifying and conservative assumptions help guaranteeing the convergence of integrals over J_r, e.g. in eq. (3.20). However, the properties derived here can certainly be extended to DFs with different structures, e.g. a fast decay of $f_r(J_r)$ without necessarily dropping to 0.

In order to warrant the unicity of the decomposition in eq. (3.35), I normalise f_r so that

$$\int {\rm d}J_r\, f_r(J_r) = 1. \tag{3.36}$$

From these properties of the DF, I will show in Section 3.5.1.1 that I can derive an explicit expression for f_L, given by

$$f_L(L) = \frac{\rho_0(R_{\rm g})}{2\pi^2\,R_{\rm g}\,\kappa^2}. \tag{3.37}$$

Note that in this expression, the self-consistency of the DF with the density is ensured only approximately, in the limit where the spread of $f_r(J_r)$ is low (i.e. $A_0 \ll R_{\rm g}$). Under the epicyclic approximation, the frequencies in eq. (3.20) do not depend on J_r anymore, and the integration variable can be changed from L to $R_{\rm g}$, so that

$$K_{\widetilde{\mathbf{n}}}(r, r', \omega) = -\frac{64\pi^2 G}{2\ell+1}\left|Y_\ell^{n_2}\right|^2 \int {\rm d}R_{\rm g}\,\frac{\kappa^2 R_{\rm g}^3}{2}\,\frac{1}{\omega - (n_1\kappa + n_2\Omega)} \int {\rm d}J_r\,\widetilde{\mathbf{n}}\cdot\frac{\partial F}{\partial \widetilde{\mathbf{J}}}\,\mathcal{B}_{\widetilde{\mathbf{n}}}(\widetilde{\mathbf{J}}, r)\mathcal{B}_{\widetilde{\mathbf{n}}}(\widetilde{\mathbf{J}}, r'), \tag{3.38}$$

where, in the epicyclic approximation, $\mathcal{B}_{\widetilde{\mathbf{n}}}$ simplifies to

$$\mathcal{B}_{\widetilde{\mathbf{n}}}(\widetilde{\mathbf{J}}, r) = \frac{\cos[n_1\theta_1 + n_2(\theta_2 - \psi)]}{A_R|\sin\theta_1|}, \tag{3.39}$$

and the actions are now defined through $\widetilde{\mathbf{J}} = (J_r, L(R_\mathrm{g}))$. Equation (3.38) underlines the key role of the epicyclic approximation. Indeed, the orbital frequencies only depend on a single phase space coordinate (here, R_g), hence the resonant integral is now unidimensional. This allows for a refined analysis of the integrals. Given the prescription that the orbit described by (R_g, J_r) must go through r and r', and knowing the support of the DF, the integration over R_g is performed on the interval $[\max(r,r') - A_0\,;\, \min(r,r') + A_0]$. In particular, if $|r - r'| > 2A_0$, then $K(r,r',\omega) = 0$. Equation (3.38) can be directly compared to eq. (54) of Palmer et al. (1989), the only difference being a factor 2 coming from the fact that the sum over n_2 here is kept symmetric, and keeping in mind our opposite definitions of the complex frequency ω.

3.2.2.3 The spectrum of neutral modes

Let me start by sketching the argument for the existence of the spectrum of neutral modes. I will consider what happens in the region of frequency space above the maximum of the inner Lindblad resonance (ILR) frequency (i.e. $\widetilde{\mathbf{n}} = (-1, 2)$), and show that in this region, the ILR term in the sum of eq. (3.19) is real and dominates over all other real parts, so that the real parts of all other terms can be neglected. I will assume, arbitrarily for now, that there are no stars at resonances, which will guarantee that the imaginary part of all terms vanishes. Hence, the kernel K is only composed of the ILR term, which is real. I will finally show that this results in the existence of a series of modes with real frequencies ω, i.e. neutral modes.

From eq. (3.38), I can identify different behaviours of the resonant denominator in $\omega - (n_1\kappa + n_2\Omega)$, depending of the value of ω and the resonance of interest. In some cases, the resonance will be crossed one or a few times when integrating over R_g, while in others it will never be crossed over the whole R_g range. As I will show, when the resonance is crossed, the diverging integrals on both sides of the resonance will in fact balance the result into a bounded value. This is represented by the principal value in the formulae. Of particular interest are the points at which the frequency $n_1\kappa + n_2\Omega$ has an extremum as a function of R_g. In those cases, when ω is close to that extremum, the resonance condition can never be met, however the integral may take very large values. Figure 3.3 shows several combinations of orbital frequencies for a typical cored potential (Plummer). Among all frequencies with $|n_2| \leq 2$, it shows that the ILR is the only one to present an extremum out of the edges of its definition domain. Therefore, a similar process as the one I am discussing cannot occur with $\ell = 0, 1$ (i.e. spherically symmetric and lopsided modes), and starts to appear only for $\ell \geq 2$. Note that in usual spherical potentials, the ILR frequency, defined by

$$\Omega_\mathrm{ILR} = \Omega - \kappa/2, \tag{3.40}$$

is positive as soon as $\mathrm{d}\psi/\mathrm{d}r > 0$, equal to 0 at the centre for a cored potential, and goes to zero at infinity if the potential does too. Apart from the homogeneous sphere, where $\Omega_\mathrm{ILR} = 0$ everywhere, Ω_ILR will then usually reach a maximum for cored potentials. Let me then focus on the particular type of modes with $\ell = 2$, because it is the lowest order which is affected by the ILR. Indeed, I recall that the values of n_2 are now restricted to $n_2 = 0, \pm 2$ due to the $Y_\ell^{n_2}$ term in eq. (3.20). Let me further focus on the particular region of frequency space just above the maximum value of $2\Omega - \kappa = 2\,\Omega_\mathrm{ILR}$, which I will denote

$$\omega_\mathrm{I} = 2\,\max(\Omega_\mathrm{ILR}). \tag{3.41}$$

Finally, for clarity, let me rename

$$K_{-1,2} = K_\mathrm{ILR}. \tag{3.42}$$

When ω is just above ω_I, the integral over R_g in K_ILR has a quasi-resonant denominator, yet it does nor go through any resonant point. As a consequence, the integral can take arbitrarily large values as ω approaches ω_I. On the contrary, all the other $K_{\widetilde{\mathbf{n}}}(r,r',\omega)$ are bounded in the vicinity of ω_I. Indeed, either the frequency $\widetilde{\mathbf{n}}\cdot\widetilde{\mathbf{\Omega}}$ never comes close to ω_I, and the denominator is non-resonant, or the frequency goes through the resonance. In the latter case, one can rely on the Plemelj formula

$$\frac{1}{x \pm \mathrm{i}\,0^+} = \mathcal{P}\left(\frac{1}{x}\right) \mp \mathrm{i}\,\pi\,\delta(x), \tag{3.43}$$

which, when applied to the resonant denominator, gives

$$\frac{1}{\omega - (n_1\kappa + n_2\Omega)} = \mathcal{P}\left(\frac{1}{\omega - (n_1\kappa + n_2\Omega)}\right) - \mathrm{i}\,\pi\,\delta(\omega - (n_1\kappa + n_2\Omega)). \tag{3.44}$$

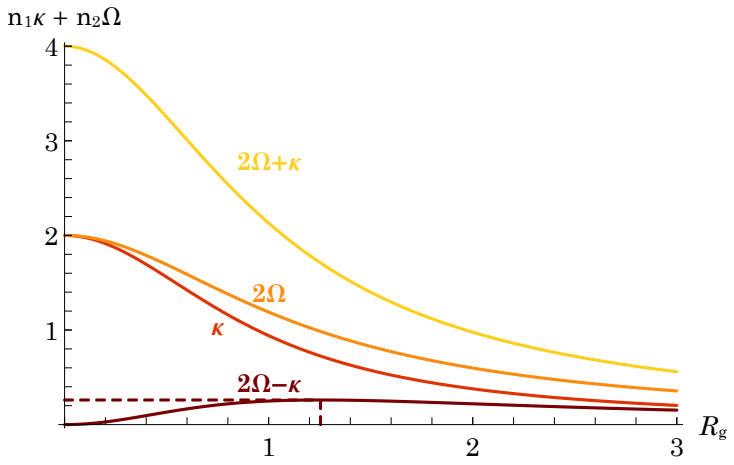

Figure 3.3: Low-order combinations of the orbital frequencies of epicyclic orbits. Each frequency also has a counterpart in the negative half-plane. Resonances occur when the oscillation frequency ω is equal to one of these frequencies. The position of the maximum of $2\Omega - \kappa = 2\Omega_{\rm ILR}$ is marked by dashed lines. From these lines, $\omega_{\rm I} \simeq 0.26$ can be read on the vertical axis, and $R_{\rm I} \simeq 1.25$ can be read on the horizontal axis. Notice that $\Omega_{\rm ILR}$ is the only non-monotonic resonance with $\ell \leq 2$. Indeed, n_2 is restricted to $0, \pm 2$ and other values of n_1 will produce monotonous combinations. Notice also that if $\omega > \omega_{\rm I}$, the resonance condition is never met twice by a single resonance.

Here, the sign corresponds to the addition of a small positive imaginary part to ω. Therefore, one has, for each resonance vector where the resonance is crossed,

$$K_{\widetilde{\mathbf{n}}}(r,r',\omega) = -\frac{64\pi^2 G}{2\ell+1}\left|Y_\ell^{n_2}\right|^2 \left\{ \mathcal{P}\int \mathrm{d}R_{\rm g}\, \frac{\kappa^2 R_{\rm g}^3}{2}\, \frac{1}{\omega - (n_1\kappa + n_2\Omega)} \int \mathrm{d}J_r\, \widetilde{\mathbf{n}}\cdot\frac{\partial F}{\partial \widetilde{\mathbf{J}}}\, \mathcal{B}_{\widetilde{\mathbf{n}}}(\widetilde{\mathbf{J}},r)\mathcal{B}_{\widetilde{\mathbf{n}}}(\widetilde{\mathbf{J}},r') \right. \\ \left. - \mathrm{i}\,\pi\, \frac{\kappa^2 R_{\rm g}^3}{2} \int \mathrm{d}J_r\, \widetilde{\mathbf{n}}\cdot\frac{\partial F}{\partial \widetilde{\mathbf{J}}}\, \mathcal{B}_{\widetilde{\mathbf{n}}}(\widetilde{\mathbf{J}},r)\mathcal{B}_{\widetilde{\mathbf{n}}}(\widetilde{\mathbf{J}},r') \right\}, \tag{3.45}$$

where, in the last term, κ, $R_{\rm g}$ and L are implicit and unambiguous functions of ω, defined by the resonance condition

$$\omega = n_1\kappa + n_2\Omega. \tag{3.46}$$

This implicit definition is unambiguous, because for $\ell = 2$, no combination of the frequencies with $|n_2| \leq 2$ can have multiple solutions of the resonance condition, in the region of ω considered (see Fig. 3.3).

My purpose is now to prove that these terms $K_{\widetilde{\mathbf{n}}}$ for which the resonance is crossed have (i) a vanishing imaginary part when there are no stars at the resonance, and (ii) a real part which is negligible w.r.t. that of $K_{\rm ILR}$.

Using the assumption that the DF is vanishing at the resonance, one has that whatever J_r, $F(J_r, L(\omega)) = 0$. Hence $\partial F/\partial J_r = 0$ at the resonance. Furthermore, since the DF is non-negative, all points on the line $L = L(\omega)$ where the DF vanishes are global minima of the DF. As a consequence, one also has $\partial F/\partial L = 0$ at the resonance, whatever J_r. Hence, in the absence of resonant stars, one has

$$\mathrm{Im}[K_{\widetilde{\mathbf{n}}}(r,r',\omega)] = \pi\, \frac{\kappa^2 R_{\rm g}^3}{2} \int \mathrm{d}J_r\, \widetilde{\mathbf{n}}\cdot\frac{\partial F}{\partial \widetilde{\mathbf{J}}}\, \mathcal{B}_{\widetilde{\mathbf{n}}}(\widetilde{\mathbf{J}},r)\mathcal{B}_{\widetilde{\mathbf{n}}}(\widetilde{\mathbf{J}},r') = 0. \tag{3.47}$$

Now, the real part of $K_{\widetilde{\mathbf{n}}}$ is given by

$$\mathrm{Re}[K_{\widetilde{\mathbf{n}}}(r,r',\omega)] = -\frac{64\pi^2 G}{2\ell+1}\left|Y_\ell^{n_2}\right|^2 \mathcal{P}\int \mathrm{d}R_{\rm g}\, \frac{\kappa^2 R_{\rm g}^3}{2}\, \frac{1}{\omega - (n_1\kappa + n_2\Omega)} \int \mathrm{d}J_r\, \widetilde{\mathbf{n}}\cdot\frac{\partial F}{\partial \widetilde{\mathbf{J}}}\, \mathcal{B}_{\widetilde{\mathbf{n}}}(\widetilde{\mathbf{J}},r)\mathcal{B}_{\widetilde{\mathbf{n}}}(\widetilde{\mathbf{J}},r'). \tag{3.48}$$

It involves the principal value of the integral over $R_{\rm g}$, which is bounded when $\omega \to \omega_{\rm I}$. Indeed, $\omega_{\rm I}$ is not singular for that particular resonance (the frequency $n_1\kappa + n_2\Omega$ crosses it smoothly), so the behaviour of the principal value around $\omega_{\rm I}$ is not divergent. As a consequence, *when I consider values of ω closer and closer to $\omega_{\rm I}$ (from above), $K_{\rm ILR}$ is real and diverges towards infinity (this point is proved in further details by eq. (3.54)), while all other $K_{\widetilde{\mathbf{n}}}$ are bounded.* Hence, I can always consider a value of ω close enough to $\omega_{\rm I}$ so that $K \simeq K_{\rm ILR}$.

Let me elaborate on that point and consider the case of $K_{\rm ILR}$. I can expand $\Omega_{\rm ILR}$ around $R_{\rm I}$ at the second order in $(R_{\rm g} - R_{\rm I})$, where $2\,\Omega_{\rm ILR}(R_{\rm I}) = \omega_{\rm I}$. Since that position is a local maximum by

construction, the first order term vanishes and I get

$$2\,\Omega_{\rm ILR} = \omega_{\rm I} - u\,(R_{\rm g} - R_{\rm I})^2, \tag{3.49}$$

where

$$u = -\left.\frac{{\rm d}^2\Omega_{\rm ILR}}{{\rm d}R_{\rm g}^2}\right|_{R_{\rm I}} > 0. \tag{3.50}$$

Considering that the integral giving $K_{\rm ILR}$ is dominated by the region around $R_{\rm I}$, provided $R_{\rm I}$ is in the range $[\max(r,r') - A_0\,;\,\min(r,r') + A_0]$, I can approximate it with

$$K_{\rm ILR}(r,r',\omega) \simeq -\frac{64\pi^2 G}{2\ell+1}\left|Y_\ell^2\right|^2 \frac{\kappa(R_{\rm I})^2 R_{\rm I}^3}{2}\left[\int {\rm d}J_r \left(2\frac{\partial F}{\partial L} - \frac{\partial F}{\partial J_r}\right)\mathcal{B}_{\rm ILR}(\widetilde{\mathbf{J}},r)\mathcal{B}_{\rm ILR}(\widetilde{\mathbf{J}},r')\right] \times\int {\rm d}R_{\rm g}\,\frac{1}{\omega - \omega_{\rm I} + u\,(R_{\rm g}-R_{\rm I})^2}, \tag{3.51}$$

where $\mathcal{B}_{\rm ILR} = \mathcal{B}_{-1,2}$, and the integral over J_r is performed at $L = L(R_{\rm I})$[3], and I recall that there is no need for a principal value since $\omega > \omega_{\rm I}$. Hence, the integral over J_r is independent of ω. Focusing on the integral over $R_{\rm g}$, I can define the change of variables

$$y = \sqrt{\frac{u}{\omega - \omega_{\rm I}}}\,(R_{\rm g} - R_{\rm I}), \tag{3.52}$$

giving

$$\int {\rm d}R_{\rm g}\,\frac{1}{\omega - \omega_{\rm I} + u\,(R_{\rm g}-R_{\rm I})^2} = \frac{1}{\sqrt{u\,(\omega-\omega_{\rm I})}}\int {\rm d}y\,\frac{1}{1+y^2}. \tag{3.53}$$

As ω is close to $\omega_{\rm I}$, I can extend the integral over y to $\pm\infty$[4] without loss of accuracy, so the integral can be approximated by its value over the full real range, which is equal to π. I then have

$$K_{\rm ILR}(r,r',\omega) \simeq -3\pi^2 G\,\kappa(R_{\rm I})^2 R_{\rm I}^3\,\frac{1}{\sqrt{u}}\left[\int {\rm d}J_r \left(2\frac{\partial F}{\partial L} - \frac{\partial F}{\partial J_r}\right)\mathcal{B}_{\rm ILR}(\widetilde{\mathbf{J}},r)\mathcal{B}_{\rm ILR}(\widetilde{\mathbf{J}},r')\right]\frac{1}{\sqrt{\omega-\omega_{\rm I}}}, \tag{3.54}$$

which proves that when $\omega \to \omega_{\rm I}$, $|K_{\rm ILR}| \to \infty$ because of the term $1/\sqrt{\omega-\omega_{\rm I}}$, hence it dominates the sum in K. Considering ω close enough to $\omega_{\rm I}$ so that $K \simeq K_{\rm ILR}$, I can then rewrite the eigen-equation (3.26) as

$$\left[\mathcal{L}^{-1}\,\mathcal{K}_{\rm ILR}\right](\psi_r) = \lambda\,\psi_r, \tag{3.55}$$

where

$$\mathcal{K}_{\rm ILR}(\psi_r) = \int {\rm d}r'\,K_{\rm ILR}(r,r',\omega)\psi_r(r'). \tag{3.56}$$

Now, the dependence over ω of the operator $\mathcal{L}^{-1}\,\mathcal{K}_{\rm ILR}$ can be explicitly extracted using eq. (3.54), so that I can write

$$\sqrt{\omega-\omega_{\rm I}}\left[\mathcal{L}^{-1}\,\mathcal{K}_{\rm ILR}\right](\psi_r) = \sqrt{\omega-\omega_{\rm I}}\,\lambda\,\psi_r, \tag{3.57}$$

where the right-hand side is independent of ω because the left-hand side is.

Consider the eigenvalues $\mu_i = \sqrt{\omega-\omega_{\rm I}}\,\lambda_i$ of the operator on the left-hand side, and let me prove that *at a fixed value of* ω, the sequence μ_i has an accumulation point at 0. Since the kernel $K_{\rm ILR}$ is square integrable, the operator $\mathcal{K}_{\rm ILR}$ is bounded. Let me note $K_{\max} > 0$ a value which dominates all possible ratios $\langle\psi_r, \mathcal{K}_{\rm ILR}(\psi_r)\rangle/\langle\psi_r,\psi_r\rangle$. On the other hand, $\mathcal{L}$ is unbounded definite negative (see Section 3.2.1), so that I can define a sequence p_j of its eigenvalues which diverges towards $-\infty$, with corresponding eigenvectors ϕ_j. Now, applying $\mathcal{L}^{-1}\,\mathcal{K}_{\rm ILR}$ to these eigenvectors, I have

$$\frac{\langle\phi_j, \mathcal{L}^{-1}\,\mathcal{K}_{\rm ILR}(\phi_j)\rangle}{\langle\phi_j,\phi_j\rangle} = p_j^{-1}\,\frac{\langle\phi_j, \mathcal{K}_{\rm ILR}(\phi_j)\rangle}{\langle\phi_j,\phi_j\rangle} \le K_{\max}\,p_j^{-1}. \tag{3.58}$$

Since $p_j^{-1} \to 0$, I have exhibited a set of independent vectors ϕ_j for which the ratios $\langle\phi_j, \mathcal{L}^{-1}\,\mathcal{K}_{\rm ILR}(\phi_j)\rangle/\langle\phi_j,\phi_j\rangle$ takes values closer and closer to 0. According to the min-max theorem, $\mathcal{L}^{-1}\,\mathcal{K}_{\rm ILR}$ therefore

[3] The underlying assumption here is that the integral over J_r is differentiable w.r.t. $R_{\rm g}$ at the point $R_{\rm I}$, which is actually not the case, but this subtlety is treated in detail in Palmer et al. (1989) and does not modify the essence of this proof.

[4] This point assumes that the range of the integral over $R_{\rm g}$ is not reduced to a single point, which will be the case of the Einstein sphere. Section 3.5 treats this particular case in detail.

has a set of eigenvalues which converges towards 0. In other words, for any ω, the sequence λ_i has a subsequence which converges towards 0. Hence, the sequence μ_i, which is independent of ω, has a subsequence that converges towards 0.

Now consider the eigenvectors ψ_i of $\sqrt{\omega-\omega_{\rm I}}\mathcal{L}^{-1}\,\mathcal{K}_{\rm ILR}$ corresponding to the eigenvalues μ_i, which are also independent of ω. This sequence of eigenvectors is solution to eq. (3.26) whatever ω, and only the eigenvalues λ_i are varying with ω. Since the frequencies are real, each of the ψ_i is a neutral mode of the system at some frequency ω_i. Indeed, if I consider the frequency

$$\boxed{\omega_i = \omega_{\rm I} + \mu_i^2,} \tag{3.59}$$

then ψ_i is solution to the eigen-equation (3.26), with the eigenvalue

$$\lambda_i(\omega_i) = \frac{\mu_i}{\sqrt{\omega_i-\omega_{\rm I}}} = \frac{\mu_i}{\mu_i} = 1. \tag{3.60}$$

Hence, *I exhibited a spectrum of neutral modes, with frequencies ω_i closer and closer to $\omega_{\rm I}$.*

Using a standard DF for a spherical system with high tangential anisotropy, as well as the epicyclic approximation, I have proved, following closely Palmer et al. (1989), that, in the region of frequency space just above the maximum of $\Omega_{\rm ILR}$, and neglecting the presence of resonant stars at other resonances, the resonant interactions around the ILR are responsible for the formation of a series of neutral modes.

I may now incorporate back the stars which resonate with the pattern at other resonances. This has the effect of perturbing the eigen-equation (3.26) by including the imaginary parts in eq. (3.45). I will then prove, as done in Palmer et al. (1989), that the eigenvectors ψ_i are now solutions of the eigen-equation when the frequency ω has a positive imaginary part, so that they become unstable.

3.2.3 Destabilisation by resonant interactions

Consider an element ψ_i with frequency ω_i of the spectrum of neutral modes obtained in the absence of stars at the resonance. Let me further assume that the growth rate of a possible instability is smaller than its oscillation frequency, i.e. that the growth of the bar amplitude is adiabatic. Since it is pure imaginary, the influence of the resonant interactions can be treated as a perturbation and I can write, from eq. (3.17)

$$\langle\psi_r,\mathcal{L}(\psi_r)\rangle = \int\!\mathrm{d}r\,\mathrm{d}r'\,K(r,r',\omega)\psi_r(r)\psi_r(r'), \tag{3.61}$$

where $\omega=\omega_i+\delta\omega$, $\psi_r=\psi_i+\delta\psi_r$. The left-hand side is real negative because $\mathcal{L}$ is negative definite, and I can detail the right hand side with what is known of the frequencies and the kernel. Indeed, since the frequency was assumed to be close to $\omega_{\rm I}$, the real part of $K_{\rm ILR}$ dominates that of the other terms in the sum. As a consequence, I have

$$\langle\psi_r,\mathcal{L}(\psi_r)\rangle = \int\!\mathrm{d}r\,\mathrm{d}r'\,K_{\rm ILR}(r,r',\omega)\psi_r(r)\psi_r(r') + \mathrm{i}\,\mathrm{Im}\left[\int\!\mathrm{d}r\,\mathrm{d}r'\,(K(r,r',\omega)-K_{\rm ILR}(r,r',\omega))\psi_r(r)\psi_r(r')\right]. \tag{3.62}$$

Expanding on both sides on the perturbed quantities and taking the imaginary part, I have

$$0 = \mathrm{Im}\left[\int\!\mathrm{d}r\,\mathrm{d}r'\,(K(r,r',\omega)-K_{\rm ILR}(r,r',\omega))\psi_i(r)\psi_i(r') + \int\!\mathrm{d}r\,\mathrm{d}r'\,\frac{\partial K}{\partial\omega}\,\delta\omega\,\psi_i(r)\psi_i(r')\right]. \tag{3.63}$$

On the one hand, considering that the frequency is just above $\omega_{\rm I}$, K is dominated by $K_{\rm ILR}$, which has no resonant denominator, hence the real part of the corresponding term dominates over the imaginary part. On the other hand, the integral involving all the other resonance vectors is dominated by the resonant region of the integration path, so it is dominated by its imaginary part. I can then write

$$\mathrm{Im}\,\delta\omega = -\frac{\mathrm{Im}\left[\int\!\mathrm{d}r\,\mathrm{d}r'\,(K(r,r',\omega_i)-K_{\rm ILR}(r,r',\omega_i))\psi_i(r)\psi_i(r')\right]}{\mathrm{Re}\left[\int\!\mathrm{d}r\,\mathrm{d}r'\,\dfrac{\partial K_{\rm ILR}}{\partial\omega}\,\psi_i(r)\psi_i(r')\right]}. \tag{3.64}$$

Using eq. (3.38), I have

$$\int\!\mathrm{d}r\,\mathrm{d}r'\,\frac{\partial K_{\rm ILR}}{\partial\omega}\,\psi_i(r)\psi_i(r') = 6\pi G\int\!\mathrm{d}R_{\rm g}\,\frac{\kappa^2R_{\rm g}^3}{2}\,\frac{1}{\left[\omega_i-\Omega_{\rm ILR}\right]^2}\int\!\mathrm{d}J_r\left(2\frac{\partial F}{\partial L}-\frac{\partial F}{\partial J_r}\right)\left[\int\!\mathrm{d}r\,\mathcal{B}_{\rm ILR}(\widetilde{\mathbf{J}},r)\psi_i(r)\right]^2. \tag{3.65}$$

Considering that $|\partial F/\partial J_r| \gg |\partial F/\partial L|$ and $\partial F/\partial J_r \leq 0$, the corresponding term is positive, so that the sign of $\mathrm{Im}\,\delta\omega$ is always opposite to that of the numerator. Hence, the effect of the resonances will be destabilising if

$$\sum_{\widetilde{\mathbf{n}}} \mathrm{Im}\left[\int \mathrm{d}r\,\mathrm{d}r'\,K_{\widetilde{\mathbf{n}}}(r,r',\omega_i)\,\psi_i(r)\,\psi_i(r')\right] < 0, \tag{3.66}$$

where the sum is over pairs of integers (n_1, n_2) with $n_2 = 0, \pm 2$ and excludes $(\pm 1, \mp 2)$. Note that resonances with high Fourier number n_1 occur at a distance from the centre, so they involve fewer stars and hence must have a smaller effect. Therefore, the sum can also be restricted to low absolute values of n_1. The condition (3.66) separates the different resonances in two categories: those which give a positive contribution to the sum, which will have a stabilising effect on the neutral mode and tend to make it damp, and those which give a negative contribution to the sum, which will have a destabilising effect as they increase the growth rate. In general, the ability of a particular resonance to be stabilising or destabilising may depend on the resonance of interest, as well as the shape and oscillation frequency of the considered neutral mode. However, looking in detail at the properties of the corresponding term in the sum (3.66), using eq. (3.38), I get

$$\begin{aligned}\langle \psi_r, \mathcal{K}_{\widetilde{\mathbf{n}}}(\psi_r)\rangle &= \int \mathrm{d}r\,\mathrm{d}r'\,K_{\widetilde{\mathbf{n}}}(r,r',\omega_i)\,\psi_i(r)\,\psi_i(r') \\ &= -\frac{64\pi^2 G}{2\ell+1}\left|Y_\ell^{n_2}\right|^2 \int \mathrm{d}R_\mathrm{g}\,\frac{\kappa^2 R_\mathrm{g}^3}{2}\,\frac{1}{\omega_i - (n_1\kappa + n_2\Omega)} \int \mathrm{d}J_r\,\widetilde{\mathbf{n}}\cdot\frac{\partial F}{\partial \widetilde{\mathbf{J}}}\left[\int \mathrm{d}r\,\mathcal{B}_{\widetilde{\mathbf{n}}}(\widetilde{\mathbf{J}},r)\psi_i(r)\right]^2. \end{aligned} \tag{3.67}$$

The integral over R_g has a singular denominator. This singularity can be treated via the Landau prescription (see eq. (3.44))

$$\frac{1}{\omega_i - (n_1\kappa + n_2\Omega)} = \mathcal{P}\left(\frac{1}{\omega_i - (n_1\kappa + n_2\Omega)}\right) - \mathrm{i}\,\pi\,\delta(\omega_i - (n_1\kappa + n_2\Omega)). \tag{3.68}$$

As Cauchy's principal value gives a real term, the imaginary part of the result will then be

$$\mathrm{Im}\,\langle \psi_r, \mathcal{K}_{\widetilde{\mathbf{n}}}(\psi_r)\rangle = \frac{64\pi^3 G}{2\ell+1}\left|Y_\ell^{n_2}\right|^2 \int \mathrm{d}R_\mathrm{g}\,\frac{\kappa^2 R_\mathrm{g}^3}{2}\,\delta(\omega_i - (n_1\kappa + n_2\Omega)) \int \mathrm{d}J_r\,\widetilde{\mathbf{n}}\cdot\frac{\partial F}{\partial \widetilde{\mathbf{J}}}\left[\int \mathrm{d}r\,\mathcal{B}_{\widetilde{\mathbf{n}}}(\widetilde{\mathbf{J}},r)\psi_i(r)\right]^2. \tag{3.69}$$

Considering that any term with $n_1 = 0$ will give a contribution $f_r\,\mathrm{d}f_L/\mathrm{d}L$ to the integral over J_r, which is negligible compared to the contribution from terms with $n_1 \neq 0$, and that $|\partial F/\partial J_r| \gg |\partial F/\partial L|$, I have

$$\mathrm{Im}\,\langle \psi_r, \mathcal{K}_{\widetilde{\mathbf{n}}}(\psi_r)\rangle = \frac{64\pi^3 G}{2\ell+1}\left|Y_\ell^{n_2}\right|^2 \int \mathrm{d}R_\mathrm{g}\,\frac{\kappa^2 R_\mathrm{g}^3}{2}\,\delta(\omega_i - (n_1\kappa + n_2\Omega)) \int \mathrm{d}J_r\,n_1\,\frac{\partial F}{\partial J_r}\left[\int \mathrm{d}r\,\mathcal{B}_{\widetilde{\mathbf{n}}}(\widetilde{\mathbf{J}},r)\psi_i(r)\right]^2. \tag{3.70}$$

Since $\partial F/\partial J_r < 0$, a necessary condition for the right hand side to be negative is that $n_1 > 0$. The destabilising resonances can therefore be identified by the two following condition: (i) there exists a guiding radius R_g where stars are at resonance with the mode (i.e. where $\omega_i = (n_1\kappa + n_2\Omega)$, so that the delta Dirac term is not vanishing everywhere in eq. (3.70)); (ii) $n_1 > 0$. Conversely, stabilising resonances are identified with the same resonance condition (i), and $n_1 < 0$. Resonances where either the resonance condition is not met anywhere in the cluster, or $n_1 = 0$, are passive w.r.t. the mode (i.e. they neither stabilise nor destabilise it). From these criteria, it appears that the ILR would tend to stabilise the mode ($n_1 = -1$), but it is passive since I assumed $\omega_i > \omega_\mathrm{I}$, thus the resonance condition is never met. All resonances with $n_1 \leq -2$ are also passive. Indeed, since $\Omega \leq \kappa$ and $|n_2| \leq 2$, one necessarily has $n_1\kappa + n_2\Omega \leq 0 < \omega_i$. Among other resonances with $n_1 < 0$, only $\widetilde{\mathbf{n}} = (-1, 0)$ and $(-1, -2)$ remain, which are also passive because the corresponding frequency is always negative. Therefore, I showed that all resonances with $n_1 < 0$ are passive, which implies that no resonance has a stabilising effect on the mode.

To show that the neutral mode is destabilised, it then remains to prove that there exists a destabilising resonance, i.e. matching both the resonance condition and $n_1 > 0$. *For infinite systems, the neutral mode will always be destabilised*, as regions of the system at the OLR with the pattern ($\widetilde{\mathbf{n}} = (1, 2)$) can always be found. Indeed, at R_I, $2\Omega + \kappa > \omega_i \gtrsim \omega_\mathrm{I}$, and as $r \to \infty$, $2\Omega + \kappa \to 0$ (see also Fig. 3.3). For a finite sphere, assuming there is no sharp boundary, the frequencies are equal at the surface of the sphere. Indeed, they verify (see eq. (3.33))

$$\kappa(R_\mathrm{max})^2 - \Omega(R_\mathrm{max})^2 = 4\pi G\rho(R_\mathrm{max}) = 0, \tag{3.71}$$

where $R_{\rm max}$ is the surface's radius. As a consequence, I get

$$\kappa(R_{\rm max}) = 2\Omega(R_{\rm max}) - \kappa(R_{\rm max}) = 2\Omega_{\rm ILR}(R_{\rm max}). \tag{3.72}$$

Since ω_i is larger than any value of $2\Omega_{\rm ILR}$, then $\kappa(R_{\rm max}) < \omega_i$. Since $\kappa(R_{\rm I}) > \omega_i$, the intermediate value theorem imposes that the resonance condition is met for $R_{\rm I} < r < R_{\rm max}$. Since the $\widetilde{\mathbf{n}} = (1,0)$ resonance is destabilising, *COI modes will also be destabilised in finite spheres.* Palmer et al. (1989) give an interpretation of this instability in terms of the wave energy. While the neutral mode has a negative wave energy in the absence of resonant stars, the effect of other resonances will be to extract energy from the system, leading to an amplification loop.

To conclude, I have therefore proved that the effect of resonant interactions on the neutral modes I identified in Section 3.2.2 was pushing them towards exponential growth, transforming them into instabilities. Overall, it proves that spherical systems with high tangential anisotropy present a series of unstable $\ell = 2$ modes, produced via the process of circular orbit instability. At a pattern speed just above the maximum of $\Omega_{\rm ILR}$, the drift in the apsidal precession of the orbits around that maximum leads to the formation of a neutral mode. When this neutral mode resonates with orbits at other resonances, such as the OLR or the $(n_1, n_2) = (1, 0)$ resonance (which I later call the epicyclic resonance, see Chapter 5), it starts to grow exponentially, and becomes an instability.

3.3 Stability to tightly wound perturbations

While the argument presented in the previous section is sufficient to prove the existence of a COI, being able to precisely characterise the pattern speed, the growth rate and the spatial profile of the instability requires relying on other techniques such as the full matrix method. Unfortunately, this explicit method, while efficient, does not give direct insight on the particular processes that destabilise the system. Before developing the matrix apparatus, one may gain intuition about the COI by looking for it in the regime of tightly wound spirals.

The WKB approximation was used on several occasions to study self-gravitating systems, e.g. in the context of disk stability (Toomre, 1964; Kalnajs, 1965; Lin & Shu, 1966) and of disk secular evolution (Fouvry et al., 2015b). Indeed, in the tightly wound limit, the perturbations act as if gravity was local, hence the Poisson equation is diagonalised. It is therefore possible to derive analytical dispersion relations. Here, I will develop and adapt results from Fridman et al. (1984a); Palmer (1994); Polyachenko (1987). My purpose is to propose a dispersion relation for tightly wound perturbations in tangentially anisotropic spheres. To do so, I will re-express the response matrix of eq. (2.41) with a bi-orthogonal basis made of tightly-wound spiral "blobs", which I will prove to be solutions of the Poisson equation. The dispersion relation will finally provide me with global stability conditions in special cases. However, I will also show that the WKB approximation fails at describing the COI.

3.3.1 A WKB basis for spherical systems

Let me first build a WKB potential-density basis. This construction was inspired by the 2D WKB basis constructed in Fouvry et al. (2015b), and has many similarities with it. Consider a potential element of the form

$$\boxed{\psi^{[m,\ell,k_r,R_0]}(r,\theta,\phi) = \mathcal{A}\,\mathrm{e}^{\mathrm{i}k_r r} B_{R_0}(r) Y_\ell^m(\theta,\phi),} \tag{3.73}$$

where the radial window function $B_{R_0}(r)$ is given by

$$B_{R_0}(r) = \mathrm{e}^{-(r-R_0)^2/(2\sigma^2)}, \tag{3.74}$$

with σ the typical radial extent of the wave, fixed for the whole basis. The basis element depends on four numbers. The harmonic numbers m and ℓ control the angular shape of the function. The radius R_0 represents the average location of the wave. The radial frequency k_r represents the frequency of oscillation of the basis function inside its envelope of size σ. Finally, $\mathcal{A}$ is the amplitude of the basis element, and will be later fixed by a normalisation condition. The corresponding density element is found

through the Poisson equation

$$\begin{aligned}\rho^{[m,\ell,k_r,R_0]}(r,\theta,\phi) &= \frac{\Delta\psi^{[m,\ell,k_r,R_0]}}{4\pi G}\\ &= \frac{\mathcal{A}}{4\pi G}\,Y_\ell^m(\theta,\phi)\,\frac{1}{r^2}\left[\frac{\mathrm{d}}{\mathrm{d}r}\left(r^2\frac{\mathrm{d}\,\mathrm{e}^{\mathrm{i}k_r r}B_{R_0}(r)}{\mathrm{d}r}\right)-\ell\,(\ell+1)\,\mathrm{e}^{\mathrm{i}k_r r}B_{R_0}(r)\right]\\ &= -\frac{\psi^{[m,\ell,k_r,R_0]}(r,\theta,\phi)}{4\pi G}\,k_r^2\left[1+\frac{2}{k_r r}\left(\frac{r-R_0}{k_r\sigma^2}-\mathrm{i}\right)+\frac{1}{k_r^2\sigma^2}-\left(\frac{r-R_0}{k_r\sigma^2}\right)^2\right.\\ &\qquad\left.+\,2\,\mathrm{i}\,\frac{r-R_0}{k_r\sigma^2}+\frac{\ell(\ell+1)}{r^2\,k_r^2}\right]. \end{aligned} \tag{3.75}$$

One can simplify this expression by making the assumptions

$$k_r r \gg 1 \quad ; \quad k_r\sigma \gg \frac{R_{\rm sys}}{\sigma}, \tag{3.76}$$

where $R_{\rm sys}$ represents the size of the system. The first assumption ensures that the basis elements are tightly wound, while the second imposes that the number of oscillations in the envelope ($k_r\sigma$) is larger than the number of envelopes which can fit in the whole system ($R_{\rm sys}/\sigma$). As a consequence, one has $|(r-R_0)/(k_r\sigma^2)| \ll 1$, $1/(k_r r) \ll 1$, and since the study is restricted to low ℓ, $\ell(\ell+1)/(r^2\,k_r^2) \ll 1$. Hence, all the terms can be neglected w.r.t. 1, which gives the (much) simpler expression

$$\rho^{[m,\ell,k_r,R_0]}(r,\theta,\phi) = -\frac{k_r^2}{4\pi G}\,\psi^{[m,\ell,k_r,R_0]}(r,\theta,\phi). \tag{3.77}$$

The next step of the construction is to require that the basis be biorthogonal. The scalar product D_{pq} of two basis functions is given by

$$\begin{aligned} D_{pq} &= \int r^2\,\sin\theta\,\mathrm{d}r\,\mathrm{d}\theta\,\mathrm{d}\phi\,\psi^{[m^p,\ell^p,k_r^p,R_0^p]}(r,\theta,\phi)\,\rho^{[m^q,\ell^q,k_r^q,R_0^q]*}(r,\theta,\phi)\\ &= -\frac{{k_r^q}^2}{4\pi G}\int r^2\,\sin\theta\,\mathrm{d}r\,\mathrm{d}\theta\,\mathrm{d}\phi\,\mathcal{A}_p\,\mathcal{A}_q^*\,\mathrm{e}^{\mathrm{i}(k_r^p-k_r^q)r}\,\mathrm{e}^{-(r-R_0^p)^2/(2\sigma^2)}\,\mathrm{e}^{-(r-R_0^q)^2/(2\sigma^2)}\,Y_{\ell^p}^{m^p}(\theta,\phi)\,Y_{\ell^q}^{m^q\,*}(\theta,\phi). \end{aligned} \tag{3.78}$$

The integration over the angles straightforwardly relies on the properties of the spherical harmonics, and I get

$$D_{pq} = -\frac{{k_r^q}^2}{4\pi G}\delta_{m^p}^{m^q}\delta_{\ell^p}^{\ell^q}\int r^2\mathrm{d}r\,\mathcal{A}_p\mathcal{A}_q^*\,\mathrm{e}^{\mathrm{i}(k_r^p-k_r^q)r}\mathrm{e}^{-(r-R_0^p)^2/(2\sigma^2)}\mathrm{e}^{-(r-R_0^q)^2/(2\sigma^2)}. \tag{3.79}$$

In order to ensure the biorthogonality of the basis, let me consider that the smallest separation between two different R_0 satisfies $|R_0^p - R_0^q| \gg \sigma$. Due to the product of window functions, the element D_{pq} is then non-zero only when $R_0^p = R_0^q$. This yields

$$D_{pq} = -\frac{{k_r^q}^2}{4\pi G}\mathcal{A}_p\mathcal{A}_q^*\delta_{m^p}^{m^q}\delta_{\ell^p}^{\ell^q}\delta_{R_0^p}^{R_0^q}\int r^2\mathrm{d}r\,\mathrm{e}^{\mathrm{i}(k_r^p-k_r^q)r}\mathrm{e}^{-(r-R_0^p)^2/\sigma^2}. \tag{3.80}$$

The last integral then has the following explicit expression

$$\begin{aligned}\int r^2\mathrm{d}r\,\mathrm{e}^{\mathrm{i}\Delta k r}\mathrm{e}^{-(r-R_0)^2/(\sigma^2)} &= \frac{1}{8}\sigma\mathrm{e}^{-\frac{1}{4}\Delta k\left(\Delta k\sigma^2-4\mathrm{i}R_0\right)}\left\{\sqrt{\pi}\left(2\sigma^2+\left(2R_0+\mathrm{i}\Delta k\sigma^2\right)^2\right)\mathrm{erf}\left(\frac{R_0}{\sigma}+\frac{\mathrm{i}\Delta k\sigma}{2}\right)\right.\\ &\left.+\,\sigma\left[\mathrm{e}^{\frac{(\Delta k\sigma^2-2\mathrm{i}R_0)^2}{4\sigma^2}}\left(4R_0+2\mathrm{i}\Delta k\sigma^2\right)+\sqrt{\pi}\sqrt{\frac{1}{\sigma^2}}\left(2\sigma^2+\left(2R_0+\mathrm{i}\Delta k\sigma^2\right)^2\right)\right]\right\}. \end{aligned} \tag{3.81}$$

Let me now impose that the minimal frequency separation between two basis elements with different frequencies satisfies $|k_r^p - k_r^q|\,\sigma \gg 1$, i.e. that two different basis elements probe sufficiently different radial frequencies. Together with the natural condition $R_0 \gg \sigma$, this implies that the integral vanishes whenever $k_r^p \neq k_r^q$. I can then rewrite

$$D_{pq} = -\frac{{k_r^p}^2}{4\pi G}\mathcal{A}_p\mathcal{A}_q^*\delta_{m^p}^{m^q}\delta_{\ell^p}^{\ell^q}\delta_{R_0^p}^{R_0^q}\delta_{k_r^p}^{k_r^q}\int r^2\mathrm{d}r\,\mathrm{e}^{-(r-R_0^p)^2/\sigma^2}. \tag{3.82}$$

This expression proves the biorthogonality of the basis, i.e. $D_{pq} \propto \delta_p^q$.

Figure 3.4: Three dimensional representation of three examples of $\ell = m = 2$ WKB density basis functions defined by eq. (3.77). In each case, the function represented is the real part of the basis, and only places where it is positive are shown. The contour corresponds to 50% of the maximum value.

The final step of the definition is to set a normalisation condition for the basis. I re-use the convention defined in eq. (2.11) and apply the condition $D_{pq} = -\delta^{m^q}_{m^p}\delta^{\ell^q}_{\ell^p}\delta^{R_0^q}_{R_0^p}\delta^{k_r^q}_{k_r^p}$, which sets the value of the amplitude $\mathcal{A}_p$. Consider the explicit expression

$$\int r^2 \mathrm{d}r\, \mathrm{e}^{-(r-R_0^p)^2/\sigma^2} = \frac{\sigma}{4}\left(2R_0\sigma \mathrm{e}^{-R_0^2/\sigma^2} + \sqrt{\pi}(2R_0^2+\sigma^2) + \sqrt{\pi}(2R_0^2+\sigma^2)\mathrm{erf}(r/\sigma)\right), \tag{3.83}$$

which, under the assumption $R_0 \gg \sigma$, simplifies to

$$\int r^2 \mathrm{d}r\, \mathrm{e}^{-(r-R_0^p)^2/\sigma^2} = \sigma\sqrt{\pi}R_0^2. \tag{3.84}$$

This finally implies that

$$\mathcal{A}_p^2 = \frac{4\sqrt{\pi}G}{\sigma {R_0^p}^2 {k_r^p}^2}. \tag{3.85}$$

The present WKB basis for spherical systems can be seen as a series of waves with a spiral shape on the equatorial plane, and a spherical harmonic structure off the plane. In that sense, they can be considered as a series of 3-dimensional spiral blobs. Figure 3.4 represents several elements of this basis. Most importantly, as highlighted in eq. (3.77), they are local solutions of the Poisson equation.

3.3.2 Matrix eigenvalues in the WKB approximation

I now consider the linear stability of a tangentially anisotropic sphere to WKB-like perturbations by computing the matrix with the present WKB basis. In order to simplify the function P of eq. (2.42) in the WKB approximation, I need to express the function W defined by eq. (2.35). Since I consider the case of tangentially anisotropic spheres, I can again rely on the epicyclic approximation, so that I can use eq. (3.31). Let me consider a slightly different but equivalent expression of W (see eq. (52) in Tremaine & Weinberg, 1984) to write

$$W^{\tilde{\mathbf{n}}}_{R_0 k_r}(\tilde{\mathbf{J}}) = \frac{\mathcal{A}\mathrm{e}^{\mathrm{i}k_r R_\mathrm{g}}}{2\pi}\int_{-\pi}^{\pi} \mathrm{d}\theta_1 B_{R_0}(r)\mathrm{e}^{-\mathrm{i}n_1\theta_1}\mathrm{e}^{-\mathrm{i}(k_r A_R\cos(\theta_1) - n_2\frac{2\Omega}{\kappa}\frac{A_R}{R_\mathrm{g}}\sin(\theta_1))}. \tag{3.86}$$

I can express the phase in the integrand as

$$k_r A_R\cos(\theta_1) - n_2\frac{2\Omega}{\kappa}\frac{A_R}{R_\mathrm{g}}\sin(\theta_1) = H_{n_2}(k_r)\sin(\theta_1+\theta_1^0), \tag{3.87}$$

where

$$H_{n_2}(k_r) = A_R|k_r|\sqrt{1+\left(\frac{2\Omega}{\kappa}\frac{n_2}{k_r R_\mathrm{g}}\right)^2} \quad ; \quad \theta_1^0 = \arctan\left(-\frac{\kappa}{2\Omega}\frac{k_r R_\mathrm{g}}{n_2}\right). \tag{3.88}$$

The WKB assumptions let me approximate these terms by $H_{n_2}(k_r) \simeq A_R|k_r|$ and $\theta_1^0 \simeq -\pi/2$. Following Palmer (1994), since the radial variations of the basis function are mainly driven by the $\mathrm{e}^{\mathrm{i}k_r r}$ term, I can neglect the variations of $B_{R_0}(r)$ on the small radial scale A_R, and replace it with $B_{R_0}(R_\mathrm{g})$ in the integral from eq. (3.86). I can then use the sum decomposition formula of the Bessel functions

$$\mathrm{e}^{\mathrm{i}z\sin\theta} = \sum_{\ell\in\mathbb{Z}} J_\ell(z)\,\mathrm{e}^{\mathrm{i}\ell\theta}, \tag{3.89}$$

which gives the final result for W

$$W^{\widetilde{\mathbf{n}}}_{R_0 k_r}(\widetilde{\mathbf{J}}) = \mathcal{A}\mathrm{e}^{\mathrm{i}k_r R_\mathrm{g}}\mathrm{e}^{\mathrm{i}n_1\theta_1^0}J_{n_1}(-H_{n_2}(k_r))B_{R_0}(R_\mathrm{g}). \tag{3.90}$$

Using this result in eq. (2.42), I get

$$\begin{aligned} P^{\widetilde{\mathbf{n}}}_{R_0^p k_r^p R_0^q k_r^q}(\omega) = &\int \mathrm{d}\widetilde{\mathbf{J}}\, L\frac{\widetilde{\mathbf{n}}\cdot\partial F/\partial\widetilde{\mathbf{J}}}{\omega-\widetilde{\mathbf{n}}\cdot\widetilde{\boldsymbol{\Omega}}(\widetilde{\mathbf{J}})}\,\mathcal{A}_p\mathcal{A}_q\mathrm{e}^{\mathrm{i}(k_r^q-k_r^p)R_\mathrm{g}}\mathrm{e}^{\mathrm{i}n_1(\theta_1^{0q}-\theta_1^{0p})} \\ &\times J_{n_1}(-H_{n_2}(k_r^p))J_{n_1}(-H_{n_2}(k_r^q))B_{R_0^p}(R_\mathrm{g})B_{R_0^q}(R_\mathrm{g}). \end{aligned} \tag{3.91}$$

The assumption on the separation between two values of R_0 imposes that the product of Gaussian windows is non-zero only when $R_0^p = R_0^q$. Additionally, let me assume that the properties of the sphere vary on scales larger than σ, so that I can apply the same reasoning as in simplifying eq. (3.80). Due to the separation between consecutive k_r values, the only non-negligible contribution will come from $k_r^p = k_r^q$. As a result, P is diagonal in p and q, with the value

$$\boxed{P^{\widetilde{\mathbf{n}}}_{R_0 k_r}(\omega) = \mathcal{A}^2\int \mathrm{d}\widetilde{\mathbf{J}} L\frac{\widetilde{\mathbf{n}}\cdot\partial F/\partial\widetilde{\mathbf{J}}}{\omega-\widetilde{\mathbf{n}}\cdot\widetilde{\boldsymbol{\Omega}}(\widetilde{\mathbf{J}})}J_{n_1}(H_{n_2}(k_r))^2 B_{R_0}(R_\mathrm{g})^2,} \tag{3.92}$$

using the relation $J_n(-x) = (-1)^n J_n(x)$. Equation (3.92) is a key result of this section, showing that the response matrix is diagonal, since it depends on a single value of R_0, k_r. This implies that the system's linear response to a WKB perturbation can be recovered via the computation of a single function, instead of the series of matrix elements required for general bases. Furthermore, one has a direct analytical access to the matrix eigenvalues, so that the condition for instability can be phrased in an explicit equation, without resorting to a matrix determinant. In the rest of the section, I will simplify eq. (3.92) for a specific tangentially anisotropic DF, in order to recover a simple and explicit stability condition.

Since the spread of the Gaussian window B is assumed to be small compared to any other characteristic scale, it behaves like a Dirac delta function, and eq. (3.92) becomes, with the right normalisation,

$$P^{\widetilde{\mathbf{n}}}_{R_0 k_r}(\omega) = \mathcal{A}^2\sqrt{\pi}\sigma L(R_0)\left|\frac{\mathrm{d}L}{\mathrm{d}R_\mathrm{g}}\right|\int \mathrm{d}J_r\frac{\widetilde{\mathbf{n}}\cdot\partial F/\partial\widetilde{\mathbf{J}}}{\omega-\widetilde{\mathbf{n}}\cdot\widetilde{\boldsymbol{\Omega}}(J_r,R_0)}J_{n_1}^2(\sqrt{2J_r/\kappa}\,|k_r|). \tag{3.93}$$

Replacing the frequencies by their values in the epicyclic approximation, I get

$$P^{\widetilde{\mathbf{n}}}_{R_0 k_r}(\omega) = \frac{2\pi G}{k_r^2}\frac{R_0\kappa^2}{\omega-n_1\kappa-n_2\Omega}\int \mathrm{d}J_r\,\widetilde{\mathbf{n}}\cdot\frac{\partial F}{\partial\widetilde{\mathbf{J}}}J_{n_1}^2(\sqrt{2J_r/\kappa}\,|k_r|). \tag{3.94}$$

As the sphere is assumed to be cold or tepid, $|\partial F/\partial J_r| \gg |\partial F/\partial L|$. As a consequence, I can approximate P as

$$P^{\widetilde{\mathbf{n}}}_{R_0 k_r}(\omega) = \frac{2\pi G}{k_r^2}\frac{R_0\kappa^2}{\omega-n_1\kappa-n_2\Omega}\begin{cases} \displaystyle\int \mathrm{d}J_r n_2\frac{\partial F}{\partial L}J_0^2(\sqrt{2J_r/\kappa}\,|k_r|) \text{ if } n_1 = 0, \\ \displaystyle\int \mathrm{d}J_r n_1\frac{\partial F}{\partial J_r}J_{n_1}^2(\sqrt{2J_r/\kappa}\,|k_r|) \text{ if } n_1 \neq 0. \end{cases} \tag{3.95}$$

From that point, I will consider a particular form of the DF that will be used to represent the general case of a cold sphere. Let me define a quasi-isothermal DF with

$$F(J_r, L) = \frac{\kappa}{\sigma_r^2}f_L(L)\,\exp\left[-\frac{\kappa J_r}{\sigma_r^2}\right], \tag{3.96}$$

where σ_r is the dispersion in radial velocities and f_L is defined in eq. (3.37). To ensure that this DF yields the self-consistent density of eq. (3.37), I have to assume that the system is sufficiently cold, i.e. $\sigma_r \ll \sqrt{GM_{\rm tot}/R_{\rm s}}$. Equation (3.95) then becomes

$$P^{\tilde{\mathbf{n}}}_{R_0 k_r}(\omega) = \frac{2\pi G}{k_r^2} \frac{R_0 \kappa^2}{\omega - n_1\kappa - n_2\Omega} \begin{cases} \displaystyle\int \mathrm{d}J_r n_2 \frac{\partial}{\partial L}\left(\frac{\kappa}{\sigma_r^2} f_L(L) \mathrm{e}^{-\frac{\kappa J_r}{\sigma_r^2}}\right) J_0^2(\sqrt{2J_r/\kappa}\,|k_r|) \text{ if } n_1 = 0, \\ \displaystyle\int \mathrm{d}J_r n_1 \frac{\partial}{\partial J_r}\left(\frac{\kappa}{\sigma_r^2} f_L(L) \mathrm{e}^{-\frac{\kappa J_r}{\sigma_r^2}}\right) J_{n_1}^2(\sqrt{2J_r/\kappa}\,|k_r|) \text{ if } n_1 \neq 0. \end{cases}$$

In the case $n_1 = 0$, I need to evaluate the term

$$\begin{aligned} \int \mathrm{d}J_r \frac{1}{\sigma_r^2} \mathrm{e}^{-\frac{\kappa J_r}{\sigma_r^2}} \left(\frac{\partial(\kappa f_L)}{\partial L} - \frac{\kappa f_L}{\sigma_r^2}\frac{\partial \kappa}{\partial L} J_r\right) J_0^2(\sqrt{2J_r/\kappa}\,|k_r|) &= \frac{1}{\sigma_r^2}\frac{\partial(\kappa f_L)}{\partial L} \int \mathrm{d}J_r \mathrm{e}^{-\frac{\kappa J_r}{\sigma_r^2}} J_0^2(\sqrt{2J_r/\kappa}\,|k_r|) \\ &\quad - \frac{1}{\sigma_r^2}\frac{\kappa f_L}{\sigma_r^2}\frac{\partial \kappa}{\partial L} \int \mathrm{d}J_r\, J_r \mathrm{e}^{-\frac{\kappa J_r}{\sigma_r^2}} J_0^2(\sqrt{2J_r/\kappa}\,|k_r|). \end{aligned} \tag{3.97}$$

For both integrals, I can rely on the integration formulae from Gradshteyn & Ryzhik (2007) (formulae (6.615) and (6.633))

$$\int_0^\infty \mathrm{d}J_r\, \mathrm{e}^{-\alpha J_r} J_{n_1}^2(\beta\sqrt{J_r}) = \frac{\mathrm{e}^{-\beta^2/2\alpha}}{\alpha} \mathcal{I}_{|n_1|}\!\left(\frac{\beta^2}{2\alpha}\right), \tag{3.98}$$

$$\begin{aligned} \int_0^\infty \mathrm{d}J_r\, J_r\, \mathrm{e}^{-\alpha J_r} J_0^2(\beta\sqrt{J_r}) &= 2\int_0^\infty \mathrm{d}u\, u^3\, \mathrm{e}^{-\alpha u^2} J_0^2(\beta u) \\ &= \alpha^{-2}\, \mathrm{e}^{-\beta^2/2\alpha}\left[\left(1 - \frac{\beta^2}{2\alpha}\right)\mathcal{I}_0\!\left(\frac{\beta^2}{2\alpha}\right) + \frac{\beta^2}{2\alpha}\mathcal{I}_1\!\left(\frac{\beta^2}{2\alpha}\right)\right]. \end{aligned} \tag{3.99}$$

Replacing with $\alpha = \kappa/\sigma_r^2$ and $\beta = \sqrt{2/\kappa}\,|k_r|$, and defining the dimensionless parameter χ and the dimensionless frequency s_n as

$$\chi = \left(\frac{k_r\,\sigma_r}{\kappa}\right)^2 \quad ; \quad s_n = \frac{\omega - n\,\Omega}{\kappa}, \tag{3.100}$$

I now have

$$\begin{aligned} P^{(0,n_2)}_{R_0 k_r}(\omega) = &-\frac{1}{R_0^2 k_r^2}\frac{4\pi G\rho}{\kappa^2}\frac{1}{2\pi^2}\frac{1}{s_{n_2}}\frac{n_2\Omega}{\kappa}\mathrm{e}^{-\chi} \\ &\times\left\{\left(1 + R_0\frac{\kappa'}{\kappa} - R_0\frac{\rho'}{\rho}\right)\mathcal{I}_0(\chi) + R_0\frac{\kappa'}{\kappa}\left[(1-\chi)\mathcal{I}_0(\chi) + \chi\mathcal{I}_1(\chi)\right]\right\}, \end{aligned} \tag{3.101}$$

where primes denote derivatives w.r.t. $R_{\rm g}$.

In the case where $n_1 \neq 0$, I can use eq. (3.98) again to get

$$P^{\tilde{\mathbf{n}}}_{R_0 k_r}(\omega) = -\frac{4\pi G\rho}{\kappa^2}\frac{1}{s_{n_2}/n_1 - 1}\frac{1}{4\pi^2}\frac{\mathrm{e}^{-\chi}}{\chi}\mathcal{I}_{|n_1|}(\chi).$$

Due to the $(R_0\,k_r)^{-2}$ dependence in eq. (3.101), terms with $n_1 = 0$ can be neglected w.r.t. those with $n_1 \neq 0$ in the response matrix, so that

$$\begin{aligned} \widehat{M}^0_{pq}(\omega) &= -\delta^{\ell^q}_{\ell^p}\,\delta^{m^q}_{m^p}\,\delta^{R^q_0}_{R^p_0}\,\delta^{k^q_r}_{k^p_r}\sum_{\tilde{\mathbf{n}}} C^{n_2}_{\ell^p}\frac{4\pi G\rho}{\kappa^2}\frac{1}{(s_{n_2}/n_1) - 1}\frac{1}{4\pi^2}\frac{\mathrm{e}^{-\chi^p}}{\chi^p}\mathcal{I}_{|n_1|}(\chi^p) \\ &= \delta^q_p\,\frac{4\pi G\rho}{\kappa^2}\frac{\mathrm{e}^{-\chi^p}}{\chi^p}\frac{8\pi}{2\ell^p+1}\sum_{\substack{n_1>0 \\ |n_2|\leq\ell^p}}\frac{\left|Y^{n_2}_{\ell^p}\right|^2\mathcal{I}_{n_1}(\chi^p)}{1 - (s_{n_2}/n_1)^2}. \end{aligned} \tag{3.102}$$

The matrix is therefore diagonal, so that I can restrict the study to its eigenvalues

$$\boxed{\lambda_{R_0 k_r}(\omega) = \frac{4\pi G\rho}{\kappa^2}\frac{\mathrm{e}^{-\chi}}{\chi}\frac{8\pi}{2\ell+1}\sum_{\substack{n_1>0 \\ |n_2|\leq\ell}}\frac{\left|Y^{n_2}_{\ell}\right|^2\mathcal{I}_{n_1}(\chi)}{1 - (s_{n_2}/n_1)^2}.} \tag{3.103}$$

The present expression is fully consistent with that found through similar methods in Fridman et al. (1984a), in Polyachenko (1987) or in Palmer et al. (1989). One can then derive the dispersion relation for self-sustained tightly wound perturbations in tangentially anisotropic spherical systems by equating an eigenvalue to 1, which gives

$$1 = \frac{4\pi G\rho}{\kappa^2}\,\frac{\mathrm{e}^{-\chi}}{\chi}\,\frac{8\pi}{2\ell+1}\sum_{\substack{n_1>0\\|n_2|\leq\ell}}\frac{\left|Y_\ell^{n_2}\right|^2\mathcal{I}_{n_1}(\chi)}{1-(s_{n_2}/n_1)^2}. \tag{3.104}$$

This equation is the spherical equivalent of the dispersion relation in disks derived in Lin & Shu (1966), which is given by

$$1 = \frac{4\pi G\Sigma|k_r|}{\kappa^2}\,\frac{\mathrm{e}^{-\chi}}{\chi}\sum_{n>0}\frac{\mathcal{I}_n(\chi)}{1-(s_m/n)^2}, \tag{3.105}$$

where Σ is the disk surface density. Although eqs. (3.104) and (3.105) look similar, their differences can be associated with critical differences between 2D and 3D systems. In the spherical case, the extra sum over n_2 accounts for the extra angular dimension in the problem. This increases the number of possible resonances, which in turns increases the number of resonant branches in the resonant denominator of eq. (3.104). Furthermore, the density ρ in eq. (3.104) is replaced by $\Sigma|k_r|$ in eq. (3.105). This has important consequences on the stability behaviour of these different systems. On the one hand, the stability of spherical systems is controlled by the parameter χ only, so that increasing the velocity dispersion in the system is equivalent to considering perturbations on larger scales. Hence, the response of spheres with different dynamical temperatures to WKB perturbations is not fundamentally different. However, the disk's stability both depends on χ and $|k_r|$, so that disks at different dynamical temperatures have fundamentally different behaviours regarding the response to perturbations. As developed in the next section, this difference has an interesting impact on the most responsive WKB modes in both systems. While the response of the disk peaks at an intermediate spatial frequency, that of the sphere is largest for the largest scale perturbations, where the WKB approximation breaks down by design.

3.3.3 Simple stability criteria in special cases

The dispersion relation I presented in eq. (3.104) allows me to derive explicit stability criteria in special cases. In general, a stability criterion can be derived from a dispersion relation as a criterion on the physical state of the system, which guarantees that the dispersion relation has no growing solutions. Here, I will focus on the case of spherically symmetric (i.e. $\ell = 0$) disturbances in cold systems, and on that of two-armed disturbances in the Einstein sphere, i.e. a sphere made of purely circular orbits. I will also show that the WKB approximation is not able to recover the COI.

3.3.3.1 WKB stability to $\ell = 0$ perturbations

For local spherically symmetric disturbances, corresponding to $\ell = 0$, the sum over n_2 is reduced to $n_2 = 0$, so the matrix eigenvalue can be expressed as

$$\begin{aligned}\lambda(\omega) &= \frac{4\pi G\rho}{\kappa^2}\,\frac{\mathrm{e}^{-\chi}}{\chi}\sum_{n_1>0}\frac{2\,\mathcal{I}_{n_1}(\chi)}{1-(s_0/n_1)^2}\\ &= \frac{4\pi G\rho}{\kappa^2}\,\frac{\mathrm{e}^{-\chi}}{\chi}\sum_{n_1>0}2\,n_1^2\,\kappa^2\,\mathcal{I}_{n_1}(\chi)\,\frac{n_1^2\kappa^2-\omega_0^2+\eta^2-2\,\mathrm{i}\,\omega_0\eta}{(n_1^2\kappa^2-\omega_0^2+\eta^2)^2+4\omega_0^2\eta^2}.\end{aligned} \tag{3.106}$$

Since $\mathcal{I}_{n_1}(\chi) > 0$ for any $n_1 > 0$ and $\chi > 0$, a necessary condition for an instability to exist is $\omega_0 = 0$, because $\mathrm{Im}[\lambda(\omega)]$ must vanish. Then, eq. (3.106) becomes

$$\lambda(\omega) = \frac{4\pi G\rho}{\kappa^2}\,\frac{\mathrm{e}^{-\chi}}{\chi}\sum_{n_1>0}\frac{2\,n_1^2\,\kappa^2\,\mathcal{I}_{n_1}(\chi)}{n_1^2\kappa^2+\eta^2}. \tag{3.107}$$

Hence the eigenvalue in eq. (3.107) is a decreasing function of η, and will always be smaller than $\lambda(\omega = 0 + 0\mathrm{i})$. As a consequence, a sufficient condition for stability is $\lambda(\omega = 0 + 0\mathrm{i}) < 1$. This translates into the condition

$$1 > \frac{4\pi G\rho}{\kappa^2}\,\frac{\mathrm{e}^{-\chi}}{\chi}\sum_{n_1>0}2\,\mathcal{I}_{n_1}(\chi) = \frac{4\pi G\rho}{\kappa^2}\,\frac{1-\mathrm{e}^{-\chi}\,\mathcal{I}_0(\chi)}{\chi}. \tag{3.108}$$

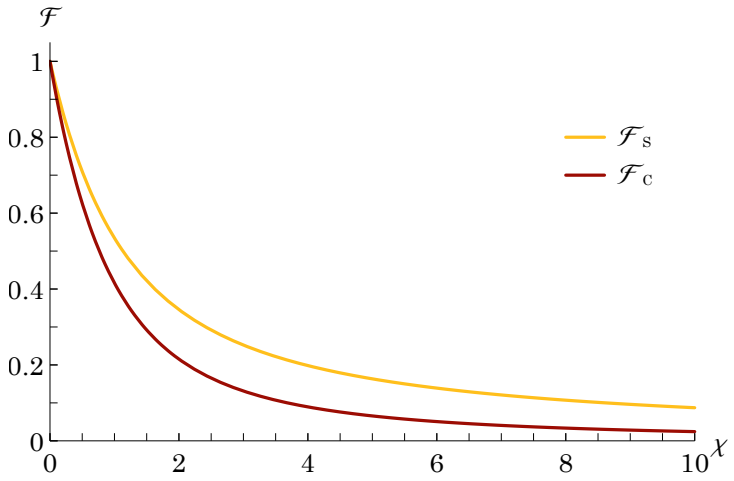

Figure 3.5: Functions $\mathcal{F}_{\rm S} : \chi \mapsto \left[1 - {\rm e}^{-\chi}\,\mathcal{I}_0(\chi)\right]/\chi$ and $\mathcal{F}_{\rm C} : \chi \mapsto 2\,{\rm e}^{-\chi}\,\mathcal{I}_1(\chi)/\chi$ corresponding to the 3D WKB reduction factors of, resp., $\ell = 0$ and $\ell = 2$ disturbances.

The function $\mathcal{F}_{\rm S} : \chi \mapsto \left[1 - {\rm e}^{-\chi}\,\mathcal{I}_0(\chi)\right]/\chi$ is plotted in Fig. 3.5. Notice the particular structure of this function, which makes it essentially different from the disk reduction factor. Indeed, unlike the disk case, the present function peaks at $\chi = 0$. If I look along the k_r line for the most amplified perturbation, the naive conclusion is that the largest scale waves are the ones which are best sustained. However, considering global modes is forbidden by the WKB assumption, which focuses on local perturbations. Hence, the behaviour at too low k_r should be discarded, but still it remains that the sphere response increases when the radial frequency, k_r, of the perturber decreases. Furthermore, as expected, eq. (3.108) indicates that all WKB perturbations undergo an increasing amplification in spheres with decreasing dynamical temperature, because $\mathcal{F}_{\rm S}$ is a decreasing function of χ.

As this function is always smaller than 1, eq. (3.108) can be recast into a Jeans like stability condition as

$$Q_{\rm cold} = \frac{\kappa^2}{4\pi G\rho} > 1. \tag{3.109}$$

To be more explicit on the meaning of $Q_{\rm cold}$, I can make use of the relation (3.33) so that the stability parameter can be rewritten

$$\boxed{Q_{\rm cold} = \frac{1}{1 - \left(\Omega/\kappa\right)^2}.} \tag{3.110}$$

This is the key result of this WKB calculation. For a monotonically decreasing density profile, $\Omega \leq \kappa \leq 2\,\Omega$. As a consequence, I always have $Q_{\rm cold} > 4/3 > 1$, i.e. *spheres with decreasing density are always stable to $\ell = 0$ WKB perturbations.* Interestingly enough, the stability of the cold sphere to local spherically symmetric disturbances does not depend on the temperature (via σ_r) of the sphere. This reveals the essential difference between disks and spheres regarding their response to radial perturbations. In a razor-thin disk, a perturbation in the form of a thin annulus will be destabilised if the radial wandering of the orbits is not high enough to dilute the perturbation. However, when the disk is thick, the destabilising power of an overdense annulus is damped (see, e.g., Vandervoort, 1970). In the spherical limit, considered as a very thick disk, this damping turns into the impossibility of shell-like overdensities to destabilise the system, whatever the radial velocity dispersion.

3.3.3.2 WKB stability of the Einstein sphere

The Einstein sphere is a system where all orbits are on purely circular trajectories. It corresponds to the quasi-isothermal case with vanishing radial velocity dispersion: $\sigma_r = 0$. As discussed in Section 3.3.2, the WKB dispersion relation in that case is independent of k_r. As a consequence, if a solution ω to the dispersion relation exists, it is independent of the radial frequency of the wave. Hence, the group velocity of any wave propagating in the system is vanishing: the system has lost the ability to propagate waves.

The stability of the Einstein sphere to spherically symmetric disturbances is described by eq. (3.110). Let me now focus on the stability of the sphere to $\ell = 2$ perturbations. In the Einstein case, the sum

over n_1 in eq. (3.104) can be reduced to $n_1 = 1$, because $\mathcal{I}_{n_1}(\chi) \propto \chi^{n_1}$. Furthermore, n_2 takes the values $0, \pm 2$ only. As a consequence, I get

$$1 = \pi G\rho \left[\frac{1}{\kappa^2 - \omega^2} - 3 \frac{\omega^2 + 4\Omega^2 - \kappa^2}{\left[\kappa^2 - \left(\omega - 2\Omega\right)^2\right]\left[\kappa^2 - \left(\omega + 2\Omega\right)^2\right]} \right]. \tag{3.111}$$

Replacing with eq. (3.33), eq. (3.111) can be written as a 3$^{\text{rd}}$ order equation on ω^2

$$\left(\omega^2\right)^3 - \left(2\kappa^2 + 9\Omega^2\right)\left(\omega^2\right)^2 + \left(\kappa^4 + 3\kappa^2\Omega^2 + 15\Omega^4\right)\omega^2 - \Omega^2(2\kappa^2 + \Omega^2)(4\Omega^2 - \kappa^2) = 0. \tag{3.112}$$

From here, the derivation of a stability criterion is readily done by the analysis of the roots of eq. (3.112). I compute the discriminant of this polynomial, giving

$$\Delta = \Omega^2 \left(\kappa^2 - \Omega^2\right)^2 \left(441\kappa^4\Omega^2 + 3402\kappa^2\Omega^4 + 16\kappa^6 + 2349\Omega^6\right) \geq 0. \tag{3.113}$$

Hence, the solutions of eq. (3.112) are all real. The problem is now the following: if one or more roots are negative, i.e. $\omega^2 < 0$, then the system has purely growing modes. Otherwise, the system is stable. Fortunately, I can use Descartes' rule of signs to determine the number of positive and negative roots of eq. (3.112). The first, second and third coefficients are resp. positive, negative and positive. In the case where the last coefficient is negative, the number of sign changes is 3, so the number of positive roots is 1 or 3. Reproducing the method with $x \to -x$, I can refine this estimate to three positive roots and no negative root. If the last coefficient is positive, the same argument can be used to prove that there is two positive and one negative roots. As a consequence, a stability criterion for $\ell = 2$ disturbances in an Einstein sphere is given by

$$\boxed{4\Omega^2 - \kappa^2 > 0.} \tag{3.114}$$

This criterion is always satisfied in spheres where density is a decreasing function of radius. Hence, *the linear stability of the Einstein sphere to two-armed WKB perturbations is guaranteed for all models where the density is a decreasing function of radius.*

3.3.3.3 No COI in the WKB approximation

Let me now attempt to identify the COI in the WKB approximation. I proved in Section 3.2 that, if it exists, the COI could be tracked down by analysing the $\widetilde{\mathbf{n}} = (-1, 2)$ term together with at least one other resonance, e.g. $\widetilde{\mathbf{n}} = (1, 0)$, and that all other resonances are also destabilising. I can therefore use eq. (3.104) as the dispersion relation, and restrict the sum over n_1 to $n_1 = 1$. The dispersion relation therefore has the same form as in the Einstein sphere case, except for an extra reduction factor. It reads

$$1 = \pi G\rho\, \mathcal{F}_{\text{C}}(\chi) \left[\frac{1}{\kappa^2 - \omega^2} - 3 \frac{\omega^2 + 4\Omega^2 - \kappa^2}{\left[\kappa^2 - \left(\omega - 2\Omega\right)^2\right]\left[\kappa^2 - \left(\omega + 2\Omega\right)^2\right]} \right], \tag{3.115}$$

where

$$\mathcal{F}_{\text{C}}(\chi) = 2\,\mathcal{I}_1(\chi)\,\frac{\mathrm{e}^{-\chi}}{\chi}. \tag{3.116}$$

This yields a new 3$^{\text{rd}}$ order equation on ω^2

$$\begin{aligned}\left(\omega^2\right)^3 - \left\{\left[3 - \mathcal{F}_{\text{C}}(\chi)\right]\kappa^2 + \left[8 + \mathcal{F}_{\text{C}}(\chi)\right]\Omega^2\right\}\left(\omega^2\right)^2 + \left\{\left[3 - 2\mathcal{F}_{\text{C}}(\chi)\right]\kappa^4 + 3\kappa^2\Omega^2 + \left[16 - \mathcal{F}_{\text{C}}(\chi)\right]\Omega^4\right\}\omega^2 \\ - \left\{\kappa^2(4\Omega^2 - \kappa^2) + \mathcal{F}_{\text{C}}(\chi)\left(\kappa^2 - \Omega^2\right)^2\right\}(4\Omega^2 - \kappa^2) = 0.\end{aligned} \tag{3.117}$$

The discriminant of this polynomial is

$$\begin{aligned}\Delta = \Omega^2\left(\kappa^2 - \Omega^2\right)^2 \Big[& 16\,\mathcal{F}_{\text{C}}^4\,\kappa^6 + \left(488(1 - \mathcal{F}_{\text{C}}) + 47(1 - \mathcal{F}_{\text{C}}^2) + 441\right)\mathcal{F}_{\text{C}}^2\,\kappa^4\,\Omega^2 \\ & + \left[16384(1 - \mathcal{F}_{\text{C}}) + 2400\mathcal{F}_{\text{C}}^2 + 956\mathcal{F}_{\text{C}}^3 + 46\mathcal{F}_{\text{C}}^4\right]\kappa^2\,\Omega^4 \\ & + \left[3312(1 - \mathcal{F}_{\text{C}}) + 468(1 - \mathcal{F}_{\text{C}}^2) + 15(1 - \mathcal{F}_{\text{C}}^3) + 2389\right]\mathcal{F}_{\text{C}}\,\Omega^6 \Big] \geq 0.\end{aligned} \tag{3.118}$$

In a sphere with decreasing density, the discriminant is positive, because $0 \leq \mathcal{F}_{\text{C}}(\chi) \leq 1$, as shown by Fig. 3.5. Equation (3.117) therefore has three real solutions. This is enough to prove that the COI cannot be recovered by this method. Indeed, the COI mode should be an overstability, with oscillation frequency $\omega > \omega_{\text{I}}$. If eq. (3.117) has only real solutions in ω^2, it means that it can only account for either neutral modes or purely growing (non-rotating) instabilities. As a consequence, I have shown that *the COI overstability cannot be recovered by means of a WKB analysis.* The COI is therefore a large-scale mode.

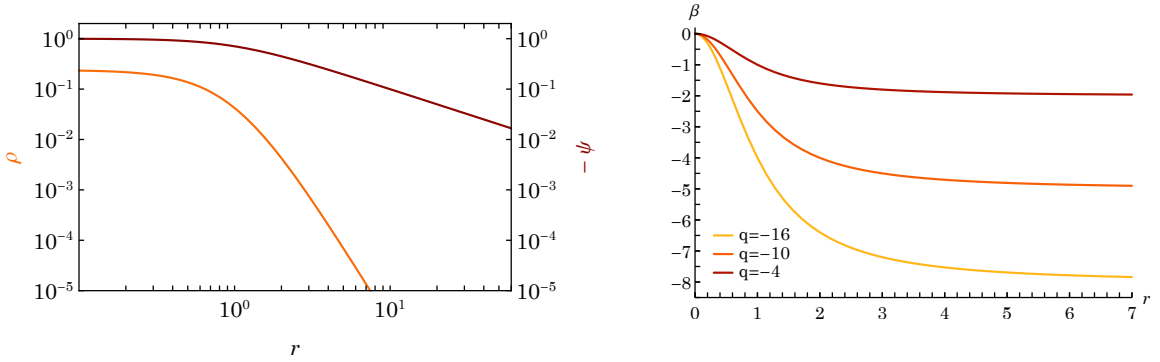

(a) (b)

Figure 3.6: (a) Radial profile of the density and potential of the Plummer sphere. (b) Radial profile of the anisotropy parameter β (see eq. (3.124)) for various values of q, using the Dejonghe DF from eq. (3.121). The overall profile of the anisotropy is constant, only its amplitude is proportional to q.

3.4 Identifying the COI with the matrix method

Since the circular orbit instability cannot be recovered in the WKB approximation, I must search for it as a large scale mode of the system. Consequently, I will now rely on the full response matrix method. Here, I will apply the response matrix apparatus to a family of non-rotating, tangentially anisotropic spheres, where the degree of tangential anisotropy can be varied at will. I will identify the circular orbit instability in these spheres, and look for the marginal stability boundary in terms of a critical anisotropy at which the system becomes unstable.

3.4.1 A tangentially anisotropic spherical model

In order to exhibit the circular orbit instability in tangentially anisotropic spheres, I will focus on the Plummer sphere, with potential (Plummer, 1911)

$$\psi(r) = -\frac{GM_{\rm tot}}{R_{\rm s}}\frac{1}{\sqrt{1+(r/R_{\rm s})^2}}, \tag{3.119}$$

and work in the dimensionless units $G = R_{\rm s} = M_{\rm tot} = 1$, with $M_{\rm tot}$ the system's total active mass. The density of such a cluster is given by (Binney & Tremaine, 2008)

$$\rho(r) = \frac{3}{4\pi}\left(1+r^2\right)^{-5/2}. \tag{3.120}$$

Figure 3.6a shows the radial dependence of the Plummer potential and density, the density being cored in the centre (as for the isochrone potential, see Fig. 2.5) and decaying as r^{-5} at large radius (unlike the isochrone potential, which undergoes a r^{-4} decay). The Plummer potential is known for approaching the distribution of stars in globular clusters, as was first proposed in Plummer (1911). As in the investigation conducted in Rozier et al. (2019), in order to study possible effects associated with velocity anisotropies, I will consider the family of DFs for the Plummer sphere proposed in Dejonghe (1987)

$$F(q,E,L) = \frac{3\Gamma(6-q)}{2(2\pi)^{5/2}}(-E)^{\frac{7}{2}-q}\mathcal{F}\left(0,q/2,\frac{9}{2}-q,1;-\frac{L^2}{2E}\right), \tag{3.121}$$

with q controlling the flavour and degree of velocity anisotropy of the system, and $\Gamma(x)$ the gamma function. Here, $\mathcal{F}$ is expressed in terms[5] of the hypergeometric function ${}_2F_1$

$$\mathcal{F}(a,b,c,d;x) = \begin{cases} x^a \dfrac{{}_2F_1(a+b,1+a-c;a+d;x)}{\Gamma(c-a)\Gamma(a+d)}, & \text{if } x \le 1, \\ \dfrac{1}{x^b}\dfrac{{}_2F_1(a+b,1+b-d;b+c;\frac{1}{x})}{\Gamma(d-b)\Gamma(b+c)}, & \text{if } x \ge 1. \end{cases} \tag{3.122}$$

[5] This formulation slightly simplifies Dejonghe's by suppressing vanishing $\Gamma(q/2)$ terms, which are indeterminate when q is an even, negative integer.

The parameter q controls the degree of velocity anisotropy in the system, with decreasing negative q associated with increasing tangential anisotropy. One of the advantages of this DF is the simple forms taken by its velocity dispersions in all directions. Indeed, with the definitions given by eq. (2.47), one has

$$\begin{aligned}\sigma_r^2(r) &= \frac{(1+r^2)^{-1/2}}{6-q},\\ \sigma_\theta^2(r) &= \sigma_\phi^2(r) = \sigma_r^2(r)\left(1-\frac{q}{2}\frac{r^2}{1+r^2}\right),\end{aligned} \tag{3.123}$$

leading to the anisotropy parameter defined by eq. (2.46)

$$\beta(r) = 1 - \frac{\sigma_\theta^2(r)}{\sigma_r^2(r)} = \frac{q}{2}\frac{r^2}{1+r^2}. \tag{3.124}$$

An analytic simple expression can also be found for the global anisotropy (eq. (2.48)), given by

$$B = \frac{q}{4}. \tag{3.125}$$

Figure 3.6b shows how q influences the distribution of velocity anisotropy in the sphere. As in the Osipkov-Merritt type DF, the sphere is isotropic in the centre. However, while an Osipkov-Merritt DF fixes the value of the anisotropy in the outskirts, and has a variable transition radius, the Dejonghe DF fixes the radial profile of the anisotropy, and has a variable amplitude.

Once the characteristics of the tangentially anisotropic systems have been set, let me now present the results of the matrix method w.r.t. the circular orbit instability.

3.4.2 Matrix results

I search for overstabilities using the matrix method as developed in Section 2.3.4. In the $q = -16$ case, the corresponding Nyquist contours (i.e. contours of the complex function $\omega_0 \mapsto \det(\mathbf{I} - \widehat{\mathbf{M}}(\omega_0 + \mathrm{i}\eta))$ for several values of η) of the $\ell = 2$ matrix are represented in Fig. 3.7. One can immediately notice the symmetry of the contours w.r.t. the real axis, discussed in Section 2.3.4.1, sourcing the formation of two unstable solutions with opposite frequencies. This symmetry is associated with the spherical symmetry of the system, and breaks down when rotation is introduced (see, e.g., Fig. 4.6).

As shown by the Nyquist contours, the system presents an instability at $\eta \simeq 0.0027$. The spatial structure is represented in Fig. 3.8, using eq. (2.12) to reconstruct the density from the eigenvector and the basis elements. The mode has a low spatial frequency, in agreement with the relatively low (10) number of basis functions used for its reconstruction. This is why a WKB treatment cannot detect it. Interestingly enough, this mode shares similarities with the one detected in Palmer et al. (1989) (see their Fig. 2). Indeed, even though the background potential is different (in particular, the sphere is finite), both potentials have the property of being cored, leading to a similar behaviour of the orbital frequencies in the system (compare their Fig. 1 with Fig. 3.3 in the present manuscript).

While Breen et al. (2017) performed numerical simulations of the same cluster on secular timescales, their results do not seem to display any such unstable behaviour. It is likely that the long timescale required for this instability to develop (hundreds of dynamical times, $\eta = 0.0027$) and the relatively low number of particles ($N = 2^{13}$) make the timescale for secular effects shorter than that for linear instability, preventing the unperturbed growth of the unstable mode. In such circumstances, the system may evolve through secular diffusion out of unstable equilibrium before the linear instability has had time to develop from the initial Poisson noise. Recent numerical results of Breen et al. (2020) tend to confirm this interpretation, as we measured instabilities in a non-rotating, tangentially anisotropic cluster using a larger number of particles ($N = 2^{15}$) and a tailor-made detection method for low-amplitude oscillations (see Section 5.3.3.2).

Another way to measure the instability in numerical simulations despite its low growth rate was used in Palmer et al. (1989). Instead of relying on Poisson noise to seed the instability, the mode is artificially excited in the initial conditions, so that it can stand out of the noise quickly enough. In practice, this procedure can be implemented in any sort of N-body simulation (whether it is a direct N-body, a tree code or a self-consistent field integrator) by a fairly simple procedure. First, construct a time-variable potential corresponding to that which should be excited. Then consider that this potential acts as a background potential to the whole simulation. At each time step, the force applied to each particle should be the sum of that computed from the regular code, plus that applied from the excited perturber.

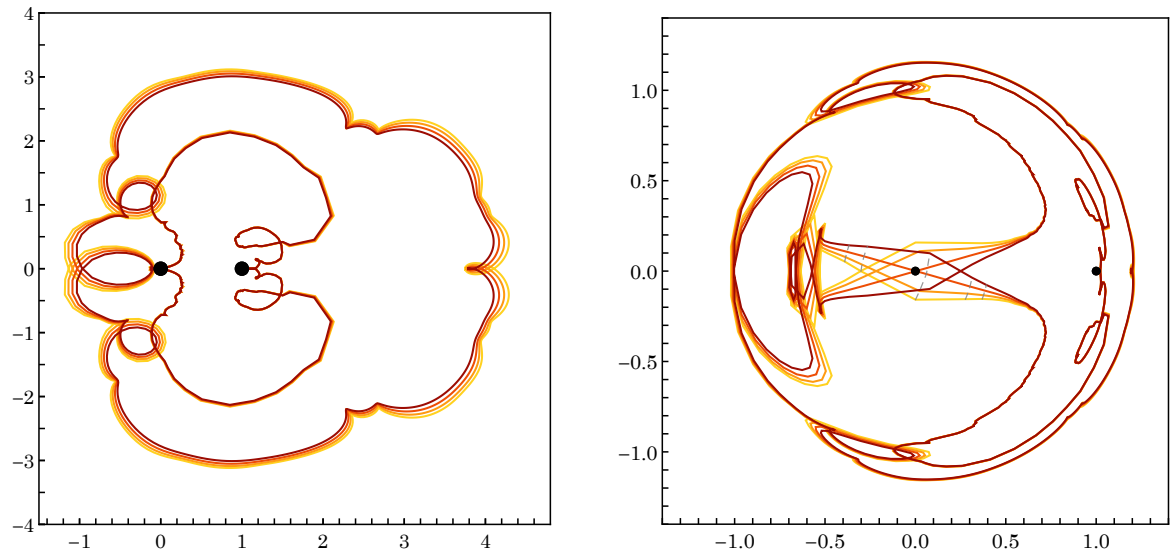

(a) Linear scale (b) Logarithmically rescaled

Figure 3.7: Nyquist contours at growth rates around the detected COI. (a) Nyquist contours in linear scale. (b) Logarithmically rescaled contours, with a similar law as the one described in the caption of Fig. 2.10. Four contours are drawn between $\eta = 0.0018$ (yellow) and $\eta = 0.0033$ (red). The dashed grey lines on panel (b) are lines of constant ω_0, between 0.274 and 0.286. The same lines could be drawn on the other symmetric branch for negative values of ω_0. The logarithmic rescaling stretches the contours around the origin to reveal the fact that the origin is crossed between two values of η.

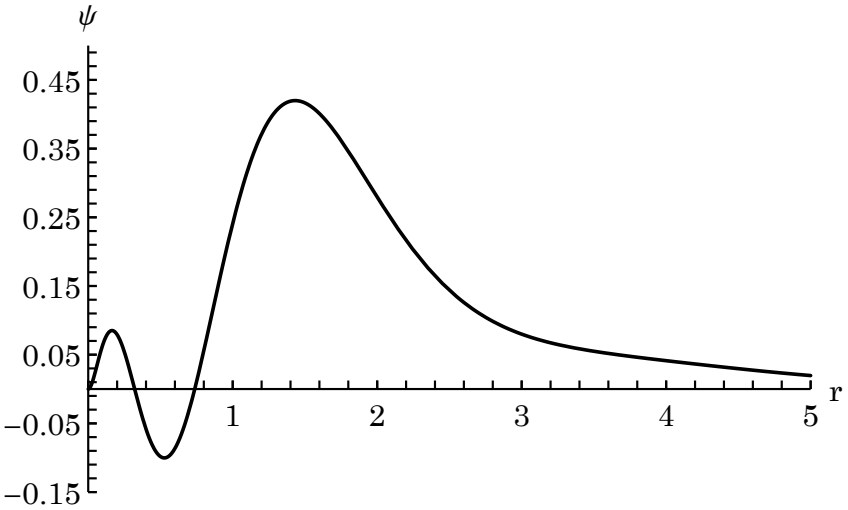

Figure 3.8: Radial profile of the modes' potential for $q = -16$. The profile resembles that of Fig. 2 in Palmer et al. (1989). The potential has few nodes, and is mainly made of one large fluctuation.

In order to prove the nature of the instabilities in tangentially anisotropic spheres, I now develop a method adapted from the response matrix, which will allow me to identify this instability as a circular orbit instability.

3.4.3 Identifying the COI with the restricted matrix method

As I have shown in Section 3.2, the circular orbit instability can be identified via the following criteria:

- Because it has an extremum in its effective frequency $\Omega_{\rm ILR}$, the ILR is at the source of the neutral mode, hence it is the fundamental cause of the instability.
- The mode rotates at a pattern speed higher, but close to the maximum value of the ILR frequency $\Omega_{\rm ILR}$, $\omega_{\rm I}/2$ (see Fig. 3.3).
- The destabilisation is achieved via coupling to other resonances, at the oscillation frequency of the mode.

Obviously, the second requirement is already met. Indeed, the oscillation frequency of the present mode is $\omega_0 \simeq 0.28$, while Fig. 3.3 shows that $\omega_{\rm I} \simeq 0.26$. In order to test the two other requirements, i.e. to disentangle the role of different resonances in the development of the instability, I implemented an algorithm adapted from the matrix method. This method relies on the advantage that different resonances have additive contributions to the response matrix.

Each integral term in the sum of eq. (2.20) can be regarded as the contribution to the response matrix from the orbits that are at the $\mathbf{n}^{\rm th}$ resonance with the instability. Hence, in order to investigate the role of each resonance in the development of instabilities, I must separately study the influence of each corresponding term in the matrix. I decided to follow this principle in order to study the interplay between resonances. Some relevant information could come from comparing the amplitude of each resonant term in eq. (2.20). However, I opted for the full mode search developed in Chapter 2, applied to response matrices in which only a smaller sample of the resonant terms were kept. In other words, if $\mathcal{I}$ is such a sub set of $\mathbb{Z}^3$, I searched for modes assuming the response matrix is restricted to

$$\widehat{M}_{pq}(\omega) = (2\pi)^3 \sum_{\mathbf{n}\in\mathcal{I}} \int \mathrm{d}\mathbf{J}\, \frac{\mathbf{n}\cdot\partial F/\partial \mathbf{J}}{\omega - \mathbf{n}\cdot\boldsymbol{\Omega}(\mathbf{J})}\, \psi_{\mathbf{n}}^{(p)*}(\mathbf{J})\, \psi_{\mathbf{n}}^{(q)}(\mathbf{J}). \tag{3.126}$$

An important freedom on the ensemble of resonances to consider comes from the fact that for non-rotating systems, the response matrix is independent on m^p, hence the resonant terms are independent on n_3. Therefore, $\mathcal{I}$ will be considered as a sub-ensemble of $\mathbb{Z}^2$, and its elements will be noted $\widetilde{\mathbf{n}}$. Additionally, each resonance should be understood through the relative value of the vector elements, so for each resonance vector $\widetilde{\mathbf{n}}$, its opposite $-\widetilde{\mathbf{n}}$ corresponds to the same kind of resonance[6]. Hence, whenever a resonance vector will be included in the ensemble $\mathcal{I}$, it will be assumed that its opposite is also included. As shown in Rozier et al. (2019) (see Section 4.5.2.1, in particular Fig. 4.10a), little influence is expected from $|n_1| > 2$ to the instabilities in tangentially anisotropic systems, because the resonance condition would then only be matched by a depleted population of remote particles. Thus, the study will be restricted to the pairs $\widetilde{\mathbf{n}}$ with $|n_1| \leq 2$. Since n_2 is restricted to $|n_2| \leq \ell$ and $|\ell - n_2|$ even, the complete matrix has seven different resonance vectors: $\mathcal{I}_0 = \{(0,2), (-1,2), (1,0), (1,2), (-2,2), (2,0), (2,2)\}$.

To quantify the role of the different resonances in the development of the instabilities, I applied the mode search on matrices in which each resonant term was removed in turn. My purpose is to measure how much it affects the instability in terms of growth rate and oscillation frequency. Table 3.1 presents the results of these measurements on matrices with the same parameters as in Section 3.4.2. One can unambiguously identify the specific role of the ILR, as it is the only resonance that is absolutely necessary for the development of the mode. All the other resonances contribute somewhat to the increase of the growth rate, and have little influence on the oscillation frequency. These results provide a definitive confirmation that *the destabilising process is the circular orbit instability.* Let me now explore the behaviour of this particular type of instability when the tangential anisotropy changes.

[6] Note that the role of opposite resonance vectors at a given frequency is not identical, they only correspond to the same *kind* of resonance. This gets even more intricate for rotating clusters (e.g., see Chapter 5).

$\mathcal{I}_0 \setminus \mathcal{I}$ (removed)	η	ω_0
$\varnothing$ (reference)	0.0022	0.27
$(-1, 2)$ ILR	$< 10^{-4}$	-
$(1, 2)$	0.0016	0.27
$(0, 2)$	0.0013	0.27
$(1, 0)$	0.0011	0.27
$(-2, 2)$	0.0012	0.27
$(2, 2)$	0.0020	0.27
$(2, 0)$	0.0020	0.27

Table 3.1: Values of the growth rate and oscillation frequency found through the restricted matrix method applied to the $q = -16$ tangentially-biased system. Comparison between the reference matrix (complete) and the series of matrices obtained by removing a single resonance.

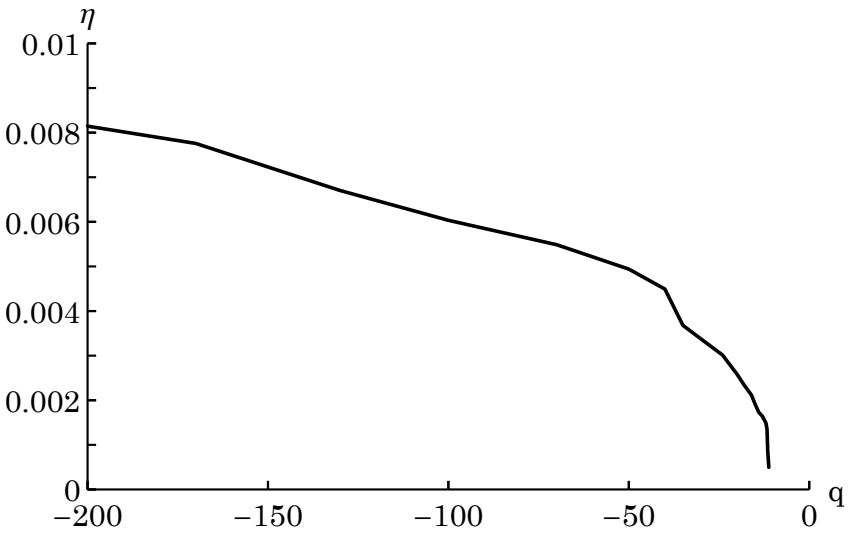

Figure 3.9: Growth rate η as a function of the anisotropy parameter q in the region of the circular orbit instability. Systems become unstable around $q = -11$ and the growth rate grows as q decreases.

3.4.4 Mapping the stability of tangentially anisotropic clusters

On the one hand, the circular orbit instability occurs in the $q = -16$ tangentially anisotropic Plummer sphere. On the other hand, Antonov's second law and the Doremus-Feix-Baumann theorem ensure that the isotropic Plummer sphere, corresponding to $q = 0$, is linearly stable to any type of perturbations. Indeed, the isotropic DF is given by

$$F_{\rm iso}(E) = \frac{3}{7\pi^3}(-2E)^{7/2}, \tag{3.127}$$

so that $F'_{\rm iso}(E) < 0$. As a consequence, there is a point on the line of increasing tangential anisotropy where the circular orbit instability builds up. This is usually called the marginal point of the instability. Figure 3.9 shows the growth rates measured by the matrix method in a series of tangentially anisotropic Plummer spheres. The marginal point is located around $q = -11$. Below this value, the system becomes more and more unstable when the tangential anisotropy is increased.

In Palmer et al. (1989), it is argued that systems with too high tangential anisotropy would be stable to the circular orbit instability. More precisely, the authors argue that the spatial structure of the mode is related to the typical radius of the epicycles. Hence, when this radius decreases, the radial frequency of the mode increases, so that the requirement of a global mode (as demonstrated in Section 3.3) is not met anymore, and the system becomes stable again. My results do not show any decrease in growth rate at high tangential anisotropy (low q). Indeed, Fig. 3.10 shows the radial profile of the modes' potential when q is decreased from -12 to -200. The structure seems to remain constant, despite the variety of tangential anisotropies tested. Yet, there are some fluctuations at $r < 0.2$, which have an important

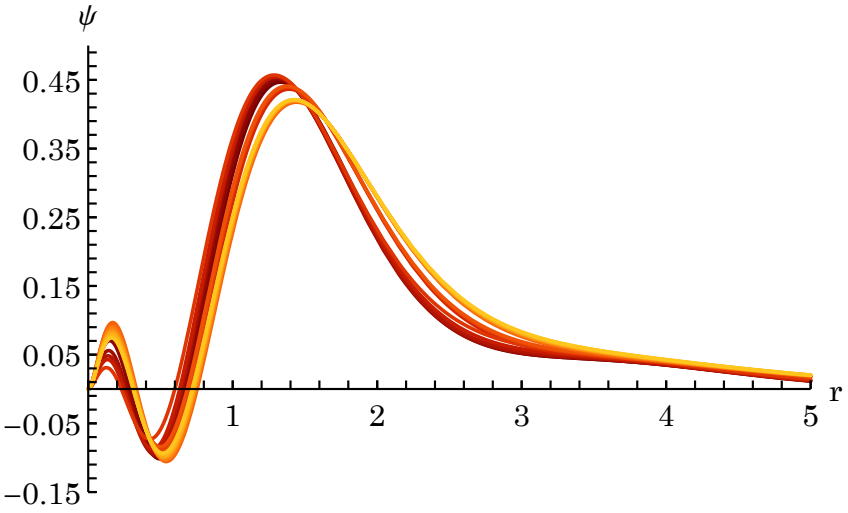

Figure 3.10: Radial profile of the modes' potentials for 18 values of q between -200 (red) and -11.7 (yellow). The profiles are remarkably similar along the q line.

impact on the mode's density. It is hard to determine whether these fluctuations are physical or due to projection effects.

Unfortunately, my current implementation of the response matrix does not allow for an accurate mode search on systems too biased towards circular orbits. Indeed, for now, the computation of the energy, the angular momentum, the radial action, and the orbital frequencies for each pair of peri- and apocentres relies on general analytical formulae (eqs. (2.57), (2.58) and (2.59), resp.). For nearly circular orbits, these formulae start to be subject to important numerical errors, hence are excluded from the current implementation. Note that despite the large value of $q = -200$, the tangential anisotropy is in fact not that large everywhere, in particular at low radius, where the mode's density can be important. For example, at $r = 0.1$, one has $\beta(r) = -1$. As a consequence, Fig. 3.9 does not go far enough in negative q's to represent the behaviour of the system at extreme tangential anisotropies. It is therefore inconsistent to extrapolate from Fig. 3.9 the behaviour of the Einstein sphere, where all orbits are purely circular. As such, the prediction from Palmer et al. (1989), that the Einstein sphere is stable, is not contradictory with these results.

In order to test for the presence of global modes in fully tangentially anisotropic systems, the Einstein sphere should be treated via a simplified implementation. It is the focus of the next section.

3.5 The Einstein sphere

For an Einstein sphere, the DF is proportional to a Dirac delta function of the radial action, i.e. all orbits are exactly circular. Hence, the action space integral in the response matrix must be computed separately, as it can be turned into a 1D integral. I will present the formulation of its response matrix, as well as the numerical techniques developed for its implementation, and preliminary results regarding its linear stability.

3.5.1 The response matrix of an ice-cold sphere

3.5.1.1 Distribution function

For the Einstein sphere, all orbits are spherical, hence the DF can be written as

$$F(J_r, L) = f_L(L)\,\delta(J_r). \tag{3.128}$$

Here, the angular momentum is bijectively implicitly related to the radius through $L(r) = r^2\,\Omega(r)$, hence the function $f_L(L)$ can be expressed as a function of r. Consider the mass $\mathrm{d}m(r)$ of material contained in the spherical shell between radii r and $r + \mathrm{d}r$. This mass can be directly expressed as a function of the density at radius r

$$\mathrm{d}m(r) = 4\pi\,r^2\,\rho(r)\,\mathrm{d}r. \tag{3.129}$$

This shell also corresponds to all orbits with angular momentum between $L(r)$ and $L(r) + \mathrm{d}L$, where $\mathrm{d}L = (\mathrm{d}L/\mathrm{d}r)\,\mathrm{d}r$. The mass can therefore be expressed independently as

$$\mathrm{d}m(r) = \left(\int \mathrm{d}\boldsymbol{\theta}\,\mathrm{d}J_r\,\mathrm{d}L_z\,f_L(L)\,\delta(J_r)\right)\mathrm{d}L = (2\pi)^3\,2L\,f_L(L)\,\mathrm{d}L. \tag{3.130}$$

Using the fact that $L = r^2\,\Omega$ and $\mathrm{d}L/\mathrm{d}r = \kappa^2\,r/(2\Omega)$, I get

$$4\pi\,r^2\,\rho(r) = (2\pi)^3\,r^3\,\kappa^2\,f_L(L). \tag{3.131}$$

Finally, the phase space DF can be expressed

$$F(J_r, L) = \frac{1}{2\pi^2}\frac{\rho(r)}{r\,\kappa^2}\,\delta(J_r), \tag{3.132}$$

where $r(L)$ is implicitly defined by $L = r^2\,\Omega$.

3.5.1.2 Response matrix

In order to compute the response matrix of the Einstein sphere, I can rely on the Lagrangian formulation (see Appendix A). Indeed, in this formulation, the $\delta(J_r)$ in the DF can be more easily accounted for in the integral over action space. Developing eq. (A.23), I get

$$\begin{aligned} P^{\widetilde{\mathbf{n}}}_{\ell^p n^p \ell^q n^q}(\omega) = -\int \mathrm{d}\widetilde{\mathbf{J}}\,F_0(\widetilde{\mathbf{J}})\Bigg[& W^{\widetilde{\mathbf{n}}}_{\ell^p n^p}(\widetilde{\mathbf{J}})\,W^{\widetilde{\mathbf{n}}}_{\ell^q n^q}(\widetilde{\mathbf{J}})\,\widetilde{\mathbf{n}}\cdot\frac{\partial}{\partial\widetilde{\mathbf{J}}}\left(\frac{L}{\omega - \widetilde{\mathbf{n}}\cdot\widetilde{\boldsymbol{\Omega}}(\widetilde{\mathbf{J}})}\right) \\ & + \frac{L}{\omega - \widetilde{\mathbf{n}}\cdot\widetilde{\boldsymbol{\Omega}}(\widetilde{\mathbf{J}})}\,\widetilde{\mathbf{n}}\cdot\frac{\partial(W^{\widetilde{\mathbf{n}}}_{\ell^p n^p}(\widetilde{\mathbf{J}})\,W^{\widetilde{\mathbf{n}}}_{\ell^q n^q}(\widetilde{\mathbf{J}}))}{\partial\widetilde{\mathbf{J}}}\Bigg]. \end{aligned} \tag{3.133}$$

In the present case, the DF is separable in (J_r, L) and proportional to $\delta(J_r)$, so that simplifications in the integral will come from: (i) the use of the epicyclic approximation, and (ii) the computation of the functions inside brackets in eq. (3.133) at $J_r = 0$. In the epicyclic approximation, it is convenient to use the relations defined in Section 3.2.2.1 and replace dependencies w.r.t. (J_r, L) with dependencies w.r.t. (A_R, R_g). In that case, I can express the orbit-averaged basis elements as

$$W^{\widetilde{\mathbf{n}}}_{\ell n}(\widetilde{\mathbf{J}}) = \frac{1}{\pi}\int_0^\pi \mathrm{d}\theta_1\,U^\ell_n(R_\mathrm{g} - A_R\cos\theta_1)\,\cos\left[n_1\theta_1 - n_2\frac{2\Omega}{\kappa}\frac{A_R}{R_\mathrm{g}}\sin\theta_1\right]. \tag{3.134}$$

Here, I am interested in computing the value of $W^{\widetilde{\mathbf{n}}}_{\ell n}$ and $\partial W^{\widetilde{\mathbf{n}}}_{\ell n}/\partial J_r$ at $J_r = 0$, so that I can rely on the few first orders of $W^{\widetilde{\mathbf{n}}}_{\ell n}$ around $A_R = 0$. Performing a Taylor expansion of U^ℓ_n around R_g, I get

$$W^{\widetilde{\mathbf{n}}}_{\ell n}(\widetilde{\mathbf{J}}) = \sum_{k=0}^{\infty}\frac{U^{\ell\,(k)}_n(R_\mathrm{g})}{k!}\,(-1)^k\,A^k_R\,T^{\widetilde{\mathbf{n}}}_k, \tag{3.135}$$

with

$$T^{\widetilde{\mathbf{n}}}_k = \frac{1}{\pi}\int_0^\pi \mathrm{d}\theta_1\,\cos^k\theta_1\,\cos\left(n_1\theta_1 - n_2\frac{2\Omega}{\kappa}\frac{A_R}{R_\mathrm{g}}\sin\theta_1\right). \tag{3.136}$$

Using some integral calculus, the series $T^{\widetilde{\mathbf{n}}}_k$ can alternatively be defined by the recurrence relation

$$\begin{aligned} T^{\widetilde{\mathbf{n}}}_0 &= J_{n_1}\left(n_2\frac{2\Omega}{\kappa}\frac{A_R}{R_\mathrm{g}}\right), \qquad T^{\widetilde{\mathbf{n}}}_1 = \frac{n_1}{n_2\frac{2\Omega}{\kappa}\frac{A_R}{R_\mathrm{g}}}J_{n_1}\left(n_2\frac{2\Omega}{\kappa}\frac{A_R}{R_\mathrm{g}}\right), \\ T^{\widetilde{\mathbf{n}}}_k &= \frac{1}{n_2\frac{2\Omega}{\kappa}\frac{A_R}{R_\mathrm{g}}}\left[(n_1 - 1)\,T^{\widetilde{\mathbf{n}}}_{k-1} + T^{(n_1+1,n_2)}_{k-2}\right], \end{aligned} \tag{3.137}$$

verified for all $n_1 \geq 0$, and $n_1 < 0$ can be recovered via $T^{\widetilde{\mathbf{n}}}_k = T^{-\widetilde{\mathbf{n}}}_k$. Using this recurrence relation, a proof by induction would show that for all $n_1 \geq 2$, the expansion of $T^{\widetilde{\mathbf{n}}}_k$ around $A_R = 0$ verifies

$$T^{\widetilde{\mathbf{n}}}_k = \mathcal{O}(A_R^{n_1-k}). \tag{3.138}$$

As a consequence, for all $|n_1| \geq 2$, I can expand $W^{\tilde{\mathbf{n}}}_{\ell n}$ as

$$W^{\tilde{\mathbf{n}}}_{\ell n} = \mathcal{O}(A_R^{|n_1|}) = \mathcal{O}(J_r^{|n_1|/2}). \tag{3.139}$$

Hence, for all $|n_1| \geq 2$, I have

$$W^{\tilde{\mathbf{n}}}_{\ell^p n^p} W^{\tilde{\mathbf{n}}}_{\ell^q n^q} = \mathcal{O}(J_r^{|n_1|}), \qquad \frac{\partial}{\partial L}[W^{\tilde{\mathbf{n}}}_{\ell^p n^p} W^{\tilde{\mathbf{n}}}_{\ell^q n^q}] = \mathcal{O}(J_r^{|n_1|}), \qquad W^{\tilde{\mathbf{n}}}_{\ell^p n^p} \frac{\partial W^{\tilde{\mathbf{n}}}_{\ell^q n^q}}{\partial J_r} = \mathcal{O}(J_r^{|n_1|-1}), \tag{3.140}$$

so in the end, all terms in eq. (3.133) with $|n_1| \geq 2$ vanish and for these terms, I get

$$P^{\tilde{\mathbf{n}}}_{\ell^p n^p \ell^q n^q}(\omega) = 0. \tag{3.141}$$

In the case $|n_1| = 1$, a proof by induction shows that for all $k \geq 2$, $T^{\tilde{\mathbf{n}}}_k = \mathcal{O}(A_R^{3-k})$. Consequently, I can expand $W^{\tilde{\mathbf{n}}}_{\ell n}$ as

$$W^{\tilde{\mathbf{n}}}_{\ell n} = U^\ell_n \, T^{\tilde{\mathbf{n}}}_0 - U^{\ell\,\prime}_n \, A_R \, T^{\tilde{\mathbf{n}}}_1 + \mathcal{O}(A_R^3), \tag{3.142}$$

where prime denotes a derivative w.r.t. R_g, and $U^\ell_n, U^{\ell\,\prime}_n$ are implicitly evaluated at $r = R_\mathrm{g}$. Since $T^{\tilde{\mathbf{n}}}_0 = \mathcal{O}(A_R)$ and $T^{\tilde{\mathbf{n}}}_1 = \mathcal{O}(1)$, I have

$$\begin{aligned} W^{\tilde{\mathbf{n}}}_{\ell^p n^p} W^{\tilde{\mathbf{n}}}_{\ell^q n^q} &= \mathcal{O}(J_r), \qquad \frac{\partial}{\partial L}[W^{\tilde{\mathbf{n}}}_{\ell^p n^p} W^{\tilde{\mathbf{n}}}_{\ell^q n^q}] = \mathcal{O}(J_r), \\ W^{\tilde{\mathbf{n}}}_{\ell^p n^p} \frac{\partial W^{\tilde{\mathbf{n}}}_{\ell^q n^q}}{\partial J_r} &= \big(U^{\ell^p}_{n^p} \, T^{\tilde{\mathbf{n}}}_0 - U^{\ell^p\,\prime}_{n^p} \, A_R \, T^{\tilde{\mathbf{n}}}_1\big) \frac{\partial}{\partial J_r}\big(U^{\ell^q}_{n^q} \, T^{\tilde{\mathbf{n}}}_0 - U^{\ell^q\,\prime}_{n^q} \, A_R \, T^{\tilde{\mathbf{n}}}_1\big) + \mathcal{O}(J_r). \end{aligned} \tag{3.143}$$

Thus, only one term will contribute to the response. After changing variables from L to $r = R_\mathrm{g}$ in the integral of eq. (3.133), applying the epicyclic approximation to the frequencies, using the explicit form of the DF from eq. (3.132), and making some simplifications, I get

$$\boxed{P^{(\pm 1, n_2)}_{\ell^p n^p \ell^q n^q}(\omega) = \mp \int \mathrm{d}r \, \frac{1}{8\pi^2} \frac{r^2 \rho(r)}{\kappa} \frac{1}{\omega \mp \kappa - n_2 \Omega} \left(U^{\ell^p}_{n^p} U^{\ell^q}_{n^q} \, n_2^2 \left(\frac{2\Omega}{r\kappa}\right)^2 + U^{\ell^p\,\prime}_{n^p} U^{\ell^q\,\prime}_{n^q} \mp n_2 \left(\frac{2\Omega}{r\kappa}\right) \frac{\partial (U^{\ell^p}_{n^p} U^{\ell^q}_{n^q})}{\partial r} \right).} \tag{3.144}$$

Finally, in the case $n_1 = 0$, a careful analysis of eq. (3.136) shows that for all odd k, $T^{(0,n_2)}_k(A_R, R_\mathrm{g}) = 0$, and I can again prove by induction that for all even $k \geq 4$, $T^{(0,n_2)}_k(A_R, R_\mathrm{g}) = \mathcal{O}(A_R^{3-k})$. Using the same methods as in the other cases, I can then compute $P^{(0,n_2)}_{\ell^p n^p \ell^q n^q}(\omega)$ as

$$\boxed{P^{(0,n_2)}_{\ell^p n^p \ell^q n^q}(\omega) \; = -\int \mathrm{d}r \, \frac{1}{2\pi^2} \frac{\rho(r)}{r\,\kappa^2} \, n_2 \, \frac{\partial}{\partial r} \left(\frac{r^2 \, \Omega \, U^{\ell^p}_{n^p} U^{\ell^q}_{n^q}}{\omega - n_2 \Omega} \right).} \tag{3.145}$$

For the Einstein sphere, as expected, the computation of the response matrix is then reduced to a few one-dimensional integrals for $n_1 = 0, \pm 1$, instead of the larger number of 2D integrals required in the general spherical case. The response matrix of an Einstein sphere with a given potential can therefore be computed at significantly lower cost, via the specific numerical techniques that are developed in the following section.

3.5.2 Numerical implementation

As in general spheres, the integrands of eqs. (3.144) and (3.145) present resonant denominators, so that one has to design a specific integration algorithm in order not to miss the quasi-divergence around the resonance. The algorithm for the Einstein matrix is similar to that used in the general spherical case (see Section 2.4.3), and adapted to the case of a 1D integral. More precisely, in each case $n_1 = 0, \pm 1$, one can rewrite

$$P^{\tilde{\mathbf{n}}}_{\ell^p n^p \ell^q n^q}(\omega) = \int \mathrm{d}r \, \frac{g^{\tilde{\mathbf{n}}}_{\ell^p n^p \ell^q n^q}(r)}{\omega - h^{\tilde{\mathbf{n}}}(r)}. \tag{3.146}$$

Now, the integral is expressed as a sum over small segments of length Δr, centred around grid points r_i, where the numerator and the denominator are replaced by their first order approximation

$$\int_{r_i - \frac{\Delta r}{2}}^{r_i + \frac{\Delta r}{2}} \mathrm{d}x \, \frac{g(r)}{\omega - h(r)} \simeq \int_{r_i - \frac{\Delta r}{2}}^{r_i + \frac{\Delta r}{2}} \mathrm{d}x \, \frac{g(r_i) + g'(r_i)\, x}{\omega - h(r_i) - h'(r_i)\, x}. \tag{3.147}$$

I express this term as a particular function $\aleph^{\mathrm{E}}(g(r_i), g'(r_i), \omega_0 - h(r_i), -h'(r_i), \Delta r, \eta)$, defined by

$$\aleph^{\mathrm{E}}(a_g, b_g, a_h, b_h, \Delta r, \eta) = \int_{-\frac{\Delta r}{2}}^{\frac{\Delta r}{2}} \mathrm{d}x_{\mathrm{p}} \frac{a_g + b_g x}{a_h + b_h x + \mathrm{i}\,\eta}. \tag{3.148}$$

Assuming that $a_g, a_h \neq 0$ and using the change of variables $u = x/\Delta r$, I simplify this integral as

$$\aleph^{\mathrm{E}}(a_g, b_g, a_h, b_h, \Delta r, \eta) = \frac{a_g}{a_h}\,\Delta r\,\aleph_{\mathrm{D}}^{\mathrm{E}}\left(\frac{b_g \Delta r}{a_g}, \frac{b_h \Delta r}{a_h}, \frac{\eta}{a_h}\right), \tag{3.149}$$

with the dimensionless integral

$$\aleph_{\mathrm{D}}^{\mathrm{E}}(b, c, \eta) = \int_{-\frac{1}{2}}^{\frac{1}{2}} \mathrm{d}x\, \frac{1+bx}{1+cx+\mathrm{i}\eta}\,. \tag{3.150}$$

The integral $\aleph_{\mathrm{D}}^{\mathrm{E}}(b, c, \eta)$ is then computed by a suitable combination of the integrand's antiderivative

$$G(x) = \frac{1}{2\,c^2}\left\{(c - b\,(1 + \mathrm{i}\eta))\left(\log\left[(c\,x+1)^2 + \eta^2\right] - 2\,\mathrm{i}\,\arctan\left[\frac{c\,x+1}{\eta}\right]\right) + 2\,b\,c\,x\right\}. \tag{3.151}$$

3.5.3 Preliminary exploration

Let me now sum up some preliminary results on the implementation of the response matrix of the Einstein sphere. First, let me insist on the fact that the stability study of this sphere is only remotely related to any published results, so that my numerical implementation of the Einstein sphere is quite difficult to validate. Mikhaĭlovskiĭ et al. (1971); Synakh et al. (1971) showed that this sphere is stable, resp. for a non-rotating and rotating sphere, yet only in the (pathological) case of a homogeneous system. To continuously tie the Einstein sphere to a less extreme case would require to study the stability of the Dejonghe DF with $q \to -\infty$, however, as stated above, this needs further numerical developments.

From my first attempts, I could nonetheless exhibit no definitive proof of the stability or instability of the Einstein sphere. Indeed, the Nyquist contours present a very intricate behaviour around the origin, with multiple smaller and smaller loops. It is therefore hard to determine whether the crossing of the origin in a given setup is due to a physical mode, or to either numerical errors or a too low number of radial basis elements. To avoid such issues, it is generally useful to increase the number of radial basis elements. In the Einstein sphere case, increasing the number of basis elements from 10 to 25 indeed allowed for a seemingly better constrained behaviour of the Nyquist contours. In particular, some crossings of the origin were excluded by this method, indicating that these were artefacts of a badly reconstructed system. However, extra basis elements also had the effect of concentrating the contours around the origin and increasing the number of tiny loops.

A clue which tends to validate this implementation is the position of the contour where it starts to wind around the origin. Indeed, this occurs for $0.26 \lesssim \omega_0 < 0.35$, i.e. slightly above ω_{I}. This is the range where I expect to find the COI, if it exists as a growing or a neutral mode. In the end, this preliminary exploration hints that the sphere is stable to the COI, or that, if unstable, its growth rate is below 0.003. This would indicate that the prediction from Palmer et al. (1989) is true. Moreover, it indicates that the stability of tangentially anisotropic spheres to the COI is non-monotonic w.r.t. the increase of the tangential anisotropy, something that cannot yet be seen in Fig. 3.9. At low anisotropy, increasing the anisotropy raises the growth rate, while at extreme anisotropies, the growth rate decreases. This would therefore tentatively indicate that the COI requires some radial velocity dispersion to develop, which is absent from a completely dynamically cold system.

3.6 Conclusions

Since the discovery of slowly growing instabilities in tangentially anisotropic clusters by Palmer et al. (1989), little work was dedicated to the study of such structures. The recent evidence for some tangential anisotropy in GCs and in spheroidal galaxies (Watkins et al., 2015; Read et al., 2018) led me to explore in detail their linear stability.

In Section 3.2, I revisited the demonstration from Palmer et al. (1989), which characterised the process of the circular orbit instability from an analytical point of view. This demonstration relies on the epicyclic approximation, which is appropriate in tangentially anisotropic clusters, since the orbits are close to circular. In the absence of resonant stars, tangentially anisotropic clusters present a sequence

of neutral modes with pattern speeds close to the maximum of Ω_{ILR}. Indeed, this frequency is the only combination of orbital frequencies which presents an extremum at intermediate radius. When present and accounted for, the resonant stars unavoidably destabilise these neutral modes. Note that the existence of such modes was shown via N-body simulations in Palmer et al. (1989), and that recent simulations in Breen et al. (2020) confirm this result (see also Section 5.3.3.2).

I then tried to obtain more information on the general characteristics of the modes from an analytical point of view. In Section 3.3, I tested the stability of tangentially anisotropic systems to tightly wound spiral perturbations. In this case, the stability of the cluster can be described by an explicit analytical criterion, eq. (3.107). I showed that such patterns could not be the source of the COI, as stability to such tightly wound patterns is generically ensured in regular potentials.

This result led me to apply the full response matrix apparatus, which allowed me to detect global, large scale modes for these clusters. Thus, I confirmed, via a quantitative analysis of the growth rates, pattern speeds and shapes of the modes, as well as the use of a restricted version of the response matrix, the presence of the COI in tangentially anisotropic clusters. I explored the line of increasing anisotropy, and showed that the clusters are more unstable when the tangential anisotropy increases.

Unfortunately, the DF I used for this study (see eq. (3.121)) does not allow to control at will the distribution of anisotropy in the cluster. In particular, it imposes the presence of radially elongated orbits in the centre. I hence adapted the response matrix for the Einstein sphere. In that case, preliminary tests seem to indicate that the instability is suppressed, or at least much damped w.r.t. the previous case. I then concluded that, even if the nearly circular orbits are at the source of the COI, its growth requires that at least part of the orbits be not exactly circular. This tentative result would impose that the growth rate of the COI is a non-monotonic function of the tangential anisotropy.

These results complement previous studies of anisotropic clusters, which mainly focused on radial anisotropy. *A mild amount of tangential anisotropy is enough to destabilise the system, forming a slowly growing rotating pattern.* Unlike thin stellar disks, tangentially anisotropic clusters are dynamically much hotter and therefore generally stable to tightly wound spirals. Hence, the COI necessarily develops as a bar, or a loosely wound spiral. Furthermore, the COI requires the presence of some small radial anisotropy, which is generally not the case of instabilities in stellar disks (see, e.g., Zang, 1976).

Setting aside the formation scenario and the environment for now, these results imply that an anisotropic spherical system tends to evolve either by breaking its spherical symmetry, or by decreasing its anisotropy. A plausible scenario involves the growth of the instability as an intermediate state of the system. Once the bar has developed and saturated, it decays through dynamical friction, leaving the system with more balanced velocity dispersions than in the initial one. In the meantime, the structure of the system may change, both in terms of density profile and in terms of triaxiality.

In actual spheroidal stellar systems, it is likely that these instabilities play a significant role around periods of large potential fluctuations, when they are subject to the growth of new kinematic components. In these periods, such as structure formation or mergers, these dynamical instabilities can be the source of further density variations, or responsible for the settlement onto an ellipsoidal or triaxial shape. They can also explain the lack of strong tangential anisotropy in observed spheroidal structures. As radial anisotropy also leads to the radial orbit instability (ROI), both instabilities combined lead to the conclusion that *a spheroidal system will rather settle in a state of low anisotropy, or a triaxial shape.*

3.7 Prospects

Let me discuss some lines of work which could improve my findings, and link them more closely to current questions of astrophysical interest.

First, let me highlight possible improvements of the characterisation of the COI. For now, there still seems to be an important gap between the DFs I used and the Einstein sphere. Bridging this gap requires solving two important issues. First, the DFs I used do not display a balanced distribution of the tangential anisotropy in the cluster. Figure 3.6b shows that the anisotropy in the centre will always be vanishing, so that one must go to extreme values of $q < 0$ to probe systems with strong anisotropy close to the centre. This problem could be solved by using DFs with more balanced tangential anisotropy. The DF from An & Evans (2006) is not fit for that purpose, because the anisotropy is also vanishing in the centre. This is not the case of the DF from Baes & van Hese (2007), where the level of anisotropy is tuneable from the centre to the outskirts. However, this form relies on an alternate sum, which may require summing opposite diverging components in the highly tangential case. More self-consistent DFs with tangentially anisotropic cores should therefore be developed.

A second issue involves the current implementation of the response matrix. For the purpose of flexibility, the computation of the energy, the angular momentum, the radial action, and the orbital frequencies for each pair of peri- and apocentres relies on general analytical formulae (eqs. (2.57), (2.58) and (2.59)). For nearly circular orbits, these formulae are subject to numerical errors (for example, the computation of the energy and the angular momentum rely on the quotient of two very small numbers), so that they are excluded from the current implementation. In my results, this was not a problem because only a tiny fraction of the orbits were excluded, but it will become problematic when one needs to deal with a significant fraction of nearly circular orbits. A way to solve this problem is to treat nearly circular orbits with some easily computable approximation, such as the epicyclic approximation. Another option is to use explicitly integrable models, such as the isochrone, for which some integrals can be computed exactly. However, the flexibility of the code w.r.t. the change of potential would be lost. Such an improvement would certainly allow me to push the exploration of Section 3.4 further on the negative q line.

Finally, Section 3.5 showed that the stability results of the Einstein sphere are particularly difficult to interpret. Not only is there no consistency check of the matrix implementation available, but the behaviour of the Nyquist contours is intricate, further complicating the mode detection. This problem reflects a general issue of the matrix method for the detection of neutral and weakly damped modes (see Section 2.5). A possible solution is to push the parameters controlling the accuracy of the computation (accuracy of the integral computations, large number of radial basis elements, fine grid in ω_0 for the computation of Nyquist contours) to sufficiently high values, so that a robust result can be obtained. This result may take the form of a mode detection, or an upper bound on the growth rate. Eventually, producing results which continuously evolve from the ergodic sphere to the Einstein one will certainly inform us on the behaviour of the COI in that extreme regime.

Let me finally discuss my results in the context of spheroidal systems dynamics. Recent measurements of GC kinematics showed that their anisotropy profile is often complex, with alternatively radial and tangential anisotropy in the cluster (Watkins et al., 2015; Jindal et al., 2019). Similarly, astrometric observations of the Milky Way's stellar halo showed a sharp transition between two radially anisotropic regions in the centre (0-15 kpc) and the outskirts (from 20 kpc), and a tangentially anisotropic one around 15-20 kpc (Kafle et al., 2012; King et al., 2015). It should therefore be interesting to perform linear stability studies on clusters with these kinds of intricate profiles. In particular, one could try to answer the question whether or not the radial orbit instability and the circular orbit instability can develop in systems with both radial and tangential anisotropy in different regions. Fortunately, such explorations would not require a re-design of the matrix method's algorithm.

Such studies may also bring interesting results on the regions in the clusters where each of these instabilities occur. For now, we still do not have a consensus for the ROI (see Section 1.4), so that more detailed measurements should bring important information. One may for example focus on particular regions in the cluster where the process takes place. This could be done through a stability analysis with either N-body simulations or the matrix method (or both) of spherical clusters with the same degree of anisotropy (e.g. the same value of B, see eq. (2.48)), but different radial profiles of the anisotropy parameter β. The same goes for tangentially anisotropic systems. In that case, one could try to identify regions in the cluster where the presence of circular orbits is particularly important for its destabilisation, or where a small radial velocity distribution is required for the system to be unstable. A priori, from the characteristics exhibited by my analytical study, it seems that the orbits located around $R_{\rm I}$ (i.e. with a precession rate close to the maximum of $\Omega_{\rm ILR}$) play an important role. However, this finding remains to be characterised in detail. The results of Chapter 5 correspond to a first step in this direction, through the measurement of frequency distributions over the evolution of simulated clusters.

A detailed characterisation of the COI would better constrain the destabilising processes at the source of the instabilities, hence pave the way for the construction of a general stability criterion. For now, what my tentative results on the Einstein sphere show is that no criterion varying monotonically with the radial or tangential velocity can represent the stability of the sphere to the COI. In particular, the COI's stability criterion cannot take the same form as that of the ROI from Polyachenko & Shukhman (1981), which sets a stability limit on the global anisotropy of the system.

Apart from describing the short term evolution of unstable systems, the unstable modes I identified can also appear as neutral or damped modes in stable equilibria which are close to the stability limit. Hence, the destabilisation process of the COI can also be considered as an important process in the context of the secular evolution of tangentially anisotropic clusters. Indeed, Breen et al. (2017) shows that these clusters undergo a faster secular evolution towards core collapse than their isotropic counterparts. Such a mode would then join the $\ell = 1$ weakly damped mode from Weinberg (1994) (see also Heggie et al., 2020)

among the family of possible catalysers of the secular evolution in tangentially anisotropic clusters. Work in this direction would require dedicated analytical and numerical studies. In particular, the framework used by Hamilton et al. (2018) could be used, with a focus on tangentially anisotropic systems, and on $\ell \leq 2$ terms in the diffusion coefficients. Note that, as discussed in Section 3.4.2, slowly growing instabilities may also never grow, because the system secularly changes on timescales faster than the growth timescale of the instability. Consequently, *slowly growing instabilities may also play the role of neutral or weakly damped modes in real astrophysical systems, or in N-body simulations.*

Chapter 4

The linear response of rotating spheres

4.1 Introduction

In the first chapters, I mainly focused on the stability of non-rotating clusters, and on the mechanisms which could destabilise them. I showed that in clusters where the density profile guarantees the stability in the isotropic case, some anisotropy in the velocity distribution can destabilise the system. In the next chapters, I focus on systems with both anisotropy and non-zero net angular momentum, and study the role of rotation in their destabilisation. In particular, I describe a process, the tumbling process, specific to rotating clusters, which may have a destabilising effect. I study the interplay between this process and other destabilising mechanisms, the radial orbit instability (ROI) in radially anisotropic systems and the circular orbit instability (COI) in tangentially anisotropic systems.

The interest in the role of angular momentum in the evolution of stellar clusters is peaking, due to recent evidence from observations and simulations on various scales. The rotation of DM halos is now confirmed in many cosmological simulations, such as the Millenium simulation (Bett et al., 2007), the Horizon simulation (Dubois et al., 2014), or the Illustris simulation (Zjupa & Springel, 2017). This global angular momentum is explained by tidal torques at the time of structure formation (Peebles, 1969; Doroshkevich, 1970; White, 1984), merging activity (Vitvitska et al., 2002) and tidal interaction with the Large Scale Structure (Codis et al., 2015). The rotation of elliptical and spheroidal galaxies is observed both through large integral field spectroscopic surveys (Kuntschner et al., 2006; Cappellari et al., 2011; Wisnioski et al., 2019) and by astrometric measurements on nearby dwarfs (see, e.g., Massari et al., 2018; Vasiliev, 2018). This rotation is mainly explained by tidal interactions over the galaxies' lifetime (Choi et al., 2018). In GCs, recent astrometric measurements precisely characterised the global angular momentum in a number of galactic objects (Bianchini et al., 2018; Vasiliev, 2019; Sollima et al., 2019). This rotation may be pristine (Vesperini et al., 2014), and may significantly evolve on relatively short timescales (Tiongco et al., 2018). Finally, NSCs are now considered as fast rotators (Seth et al., 2008; Feldmeier et al., 2014). The formation scenario of NSCs is still controversial, but their acquired significant angular momentum can be accounted for in different scenarios, whether it is transferred from the gas by in-situ star formation, acquired through the accretion of galactic stars (for both scenarios, see Seth et al., 2008), or via the accretion of star clusters (Tsatsi et al., 2017).

Hence, it appears that both anisotropy and angular momentum are universal in stellar clusters, whatever their size, age or number of particles. As in non-rotating systems, the question of their linear stability, as well as the processes by which they may be destabilised, is fundamental to understand the way such structures formed, survived, and evolved. Disentangling the specific characteristics of stable clusters is also critical in their consistent modelling. Indeed, since these systems are often modelled with Jeans and Schwarzschild techniques, it is important to pin down the subset of stable equilibria identified in such studies.

In the study of rotating stellar dynamical systems, stability analyses have been strongly focused on disks. Hohl (1971) and Kalnajs (1972) provided the numerical and analytical evidence that uniformly rotating disks can be strongly unstable w.r.t. global bar modes, if the ordered kinetic energy dominates the energy budget of the system. Ostriker & Peebles (1973) extended this numerical investigation to the case of differentially rotating disks and conjectured the condition $T/|W| < 0.14 \pm 0.02$ as an *empirical* necessary (but not sufficient) criterion for the dynamical stability of any rotating stellar system w.r.t. global bar-like modes. Here, T is the kinetic energy in ordered motions, or rotational kinetic energy, and W is the total gravitational potential energy of the system. Note that this parameter will be used as a

reference in Chapter 5.

Over the years, a number of studies, mostly based on N-body simulations, have been carried out to investigate the stability of stellar disks (see, e.g., Hohl, 1976; Sellwood, 1981), so that the nature of the rotational instability w.r.t. bar-like modes was indeed confirmed to be dynamical. Few attempts at providing a physical interpretation of the Ostriker & Peebles (1973) criterion have been made (see, e.g., Vandervoort, 1982); several counterexamples or alternative stability criteria have also been suggested (see, e.g., Zang & Hohl, 1978; Berman & Mark, 1979; Aoki et al., 1979; Efstathiou et al., 1982; Pichon & Cannon, 1997; Evans & Read, 1998b; Athanassoula, 2008).

However, with the exception of some pioneering studies on the counterparts of uniformly rotating polytropes (see especially Vandervoort, 1980), very few investigations of the stability properties of spheroidal, rotating stellar systems have been conducted so far (but see Synakh et al., 1971, for an analytical study of the rotating homogeneous Einstein sphere). Furthermore, when available, it was mostly done by means of numerical approaches (see, e.g., Kuijken & Dubinski, 1994; van der Marel et al., 1997; Sellwood & Valluri, 1997; Alimi et al., 1999; Meza, 2002; Varri, 2012), partly with the hope of exploring the validity of the classical Ostriker & Peebles (1973) stability criterion in that context. It is therefore timely to explore the role of angular momentum in the early evolution of spheroidal stellar systems and investigate the possible interplay between velocity anisotropies and internal rotation.

Here, I will rely on analytic methods, complemented by N-body simulations, to study the linear stability of star clusters with different degrees and flavours of anisotropy, and varying initial global angular momentum. I will first revisit the arguments from Allen et al. (1992) for the existence of a tumbling instability (TI) in rotating stellar clusters. This instability corresponds to oscillations of the orientation of orbital planes where a weak rotating bar is growing. I will show that this process may be at the source of a series of slowly rotating neutral modes, in systems where resonances are not populated. In contrast to the neutral mode of the COI, where resonant stars destabilise the system, the impact of the interaction of the tumbling mode with resonant stars is more difficult to predict, and may depend on the anisotropy of the cluster. In order to carry out the stability study of a number of clusters with various anisotropy and rotation, I will generalise the response matrix formalism to rotating systems, validated against N-body simulations. I will prove the robustness of the results via convergence studies of both methods, and cross comparisons in terms of growth rates, oscillation frequencies and mode shapes. My study will identify several instability islands, one in the tangentially anisotropic, rotating regime, and two in the radially anisotropic, rotating regime. Based on fits of the growth rate planes, I will present phenomenological stability criteria in the different regimes. Finally, I will discuss a physical process for the ROI in rotating systems, which explains both instability islands of the radially anisotropic regime.

Many of these results are part of a published paper, Rozier et al. (2019).

4.2 A possible tumbling instability?

Allen et al. (1992) presented simulations of rotating spherical clusters, together with an analytical study, which identified a specific destabilising process in rotating spheres. This process, which the authors coined the tumbling instability (TI), comes from the impact of a quadrupolar perturbation on the orientation of orbital planes. They show that the torque applied by such a slowly rotating perturbation can modify the inclination angle of orbits, as well as the position of their ascending node. In turn, some orbital planes can be caught into libration with the pattern, leading to a 3-dimensional instability similar to the tumbling instability in disks described in Lynden-Bell (1979).

The analytical demonstration presented in Allen et al. (1992) and in Palmer (1994) is similar to that leading to the COI in tangentially anisotropic clusters: the tumbling process is the source of a neutral mode, which is destabilised by processes that can extract energy from the mode, such as resonant interactions with the stars in the system. Here, I will revisit the arguments for the existence of this instability. Using a general DF describing a rotating cluster, I will derive the eigen-equation which should be satisfied by a mode of the rotating system. I will then show, neglecting all resonant interactions, that the tumbling process is at the source of a spectrum of neutral modes. Finally, I will discuss the destabilisation of these neutral modes by resonant interactions.

4.2.1 A general distribution function for spherical rotating systems

According to the Jeans theorem, an equilibrium DF for a spherical system will always take the form $F(J_r, L, L_z)$. Here, I consider a family of rotating clusters derived from a non-rotating DF F_0 using the

procedure

$$F(\alpha, \mathbf{J}) = F_0(E, L)\left[1 + \alpha\, g\left(\frac{L_z}{L}\right)\right], \tag{4.1}$$

where $\mathbf{J} = (J_r, L, L_z)$, g is an odd function of $L_z/L = \cos(i)$ taking values in the interval $[-1; 1]$, and $-1 \leq \alpha \leq 1$. This procedure is equivalent to taking a non-rotating cluster, and at each inclination angle i, flipping a fraction $\alpha\, g(\cos i)$ of the retrograde orbits (i.e. orbits with $L_z < 0$) into prograde orbits on the same trajectory (resp. prograde into retrograde if $\alpha\, g(\cos i) < 0$). This definition produces the same potential as the non-rotating DF F_0, since the potential depends only on the even component of the DF, and the distribution of orbital shapes is independent of the inclination angle. While the function g fixes the rotation profile as a function of the inclination angle, the parameter α fixes the amplitude of the overall rotation. In order to avoid degeneracies, I can then always consider g so that $\max(|g|) = 1$.

4.2.2 Derivation of the eigen-equation

The eigen-equation solved by a mode in a non-rotating, spherical system was investigated in Section 3.2. The case of a rotating system is very similar, except for the addition of the new rotating part to the DF. Let me start from eq. (3.12), which does not depend on whether the system is rotating or not, and let me rewrite this equation as

$$\mathcal{L}(\psi_r) = \mathcal{K}(\psi_r), \tag{4.2}$$

where $\mathcal{L}$ is defined by eq. (3.9) and $\mathcal{K}(\psi_r)$ represents the right hand side of eq. (3.12). It is now also assumed that the mode has a single (ℓ, m) component, (see eq. (3.2)), keeping in mind that this constraint does not fundamentally modify the following discussion. Using the DF from eq. (4.1), the DF gradient takes the form

$$\mathbf{n} \cdot \frac{\partial F}{\partial \mathbf{J}} = \widetilde{\mathbf{n}} \cdot \frac{\partial F_0}{\partial \widetilde{\mathbf{J}}} + \alpha \left[\widetilde{\mathbf{n}} \cdot \frac{\partial F_0}{\partial \widetilde{\mathbf{J}}}\, g\left(\frac{L_z}{L}\right) + n_3 \frac{F_0}{L}\, g'\left(\frac{L_z}{L}\right) - n_2 \frac{F_0\, L_z}{L^2}\, g'\left(\frac{L_z}{L}\right)\right], \tag{4.3}$$

where g' is the derivative of g w.r.t. its argument. As a consequence, I can decompose $\mathcal{K}$ as

$$\mathcal{K} = \mathcal{K}_0 + \alpha\, \mathcal{K}_1, \tag{4.4}$$

where $\mathcal{K}_0$ is the operator of the non-rotating cluster, defined by eq. (3.17), and $\mathcal{K}_1$ is the rotating part of the operator, defined by

$$\begin{aligned}
\mathcal{K}_1(\psi_r) = &-32\pi^3 G \sum_{\widetilde{\mathbf{n}}} \int \frac{L\, \mathrm{d}L\, \mathrm{d}E}{\sqrt{2(E - \psi_0(r)) - L^2/r^2}}\, \frac{\widetilde{\mathbf{n}} \cdot \partial F_0/\partial \widetilde{\mathbf{J}}}{\omega - \widetilde{\mathbf{n}} \cdot \widetilde{\mathbf{\Omega}}}\, \mathrm{e}^{\mathrm{i}(n_1\theta_1 + n_2(\theta_2 - \psi))}\, W^{\widetilde{\mathbf{n}}}(\widetilde{\mathbf{J}})\, \left|Y_\ell^{n_2}\right|^2 \\
&\times \int \mathrm{d}(\cos i)\, g(\cos i)\, R^\ell_{n_2 m}(i)^2 \\
&-32\pi^3 G \sum_{\widetilde{\mathbf{n}}} \int \frac{\mathrm{d}L\, \mathrm{d}E}{\sqrt{2(E - \psi_0(r)) - L^2/r^2}}\, \frac{F_0}{\omega - \widetilde{\mathbf{n}} \cdot \widetilde{\mathbf{\Omega}}}\, \mathrm{e}^{\mathrm{i}(n_1\theta_1 + n_2(\theta_2 - \psi))}\, W^{\widetilde{\mathbf{n}}}(\widetilde{\mathbf{J}})\, \left|Y_\ell^{n_2}\right|^2 \\
&\times \int \mathrm{d}(\cos i) \left[m\, g'(\cos i) - n_2\, \cos i\, g'(\cos i)\right] R^\ell_{n_2 m}(i)^2.
\end{aligned} \tag{4.5}$$

Following the methods presented in Section 3.2.1, I can rewrite $\mathcal{K}_1(\psi_r)$ as

$$\boxed{\mathcal{K}_1(\psi_r) = \int \mathrm{d}r'\, P(r, r', \omega)\, \psi_r(r') + \int \mathrm{d}r'\, Q(r, r', \omega)\, \psi_r(r'),} \tag{4.6}$$

where

$$\boxed{P(r, r', \omega) = \sum_{\widetilde{\mathbf{n}}} P_{\widetilde{\mathbf{n}}}(r, r', \omega) \quad ; \quad Q(r, r', \omega) = \sum_{\widetilde{\mathbf{n}}} Q_{\widetilde{\mathbf{n}}}(r, r', \omega),} \tag{4.7}$$

with[1]

$$\boxed{\begin{aligned}
P_{\widetilde{\mathbf{n}}}(r, r', \omega) &= -32\pi^2 G\, \mathcal{I}^\ell_{n_2 m} \left|Y_\ell^{n_2}\right|^2 \int \mathrm{d}J_r\, \mathrm{d}L\, L\, \frac{\widetilde{\mathbf{n}} \cdot \partial F_0/\partial \widetilde{\mathbf{J}}}{\omega - \widetilde{\mathbf{n}} \cdot \widetilde{\mathbf{\Omega}}}\, \mathcal{B}^{\widetilde{\mathbf{n}}}(\widetilde{\mathbf{J}}, r)\, \mathcal{B}^{\widetilde{\mathbf{n}}}(\widetilde{\mathbf{J}}, r'), \\
Q_{\widetilde{\mathbf{n}}}(r, r', \omega) &= -32\pi^2 G\, \mathcal{J}^\ell_{n_2 m} \left|Y_\ell^{n_2}\right|^2 \int \mathrm{d}J_r\, \mathrm{d}L\, \frac{F_0}{\omega - \widetilde{\mathbf{n}} \cdot \widetilde{\mathbf{\Omega}}}\, \mathcal{B}^{\widetilde{\mathbf{n}}}(\widetilde{\mathbf{J}}, r)\, \mathcal{B}^{\widetilde{\mathbf{n}}}(\widetilde{\mathbf{J}}, r'),
\end{aligned}} \tag{4.8}$$

[1] Note that the notations P and Q can be related to those used in Section 4.3.2 for the computation of the response matrix. The main difference is that the multiplicative prefactors have been included in the present kernels.

where $\mathcal{B}_{\tilde{\mathbf{n}}}$ is defined by eq. (3.21), and the information on the rotation is contained in the coefficients

$$\mathcal{I}^{\ell}_{n_2 m} = \int \mathrm{d}(\cos i)\, g(\cos i)\, R^{\ell}_{n_2 m}(i)^2,$$
$$\mathcal{J}^{\ell}_{n_2 m} = \int \mathrm{d}(\cos i)\, (n_3 - n_2\, \cos i)\, g'(\cos i)\, R^{\ell}_{n_2 m}(i)^2. \tag{4.9}$$

Hence, the operator $\mathcal{K}$ is defined by integration with the kernel $K + \alpha\,(P+Q)$, where K is defined by eq. (3.19) with F replaced by F_0. This kernel is still symmetric, and $\mathcal{L}$ can again be inverted in eq. (4.2), yielding

$$\left[\mathcal{L}^{-1}\,(\mathcal{K}_0 + \alpha\,\mathcal{K}_1)\right](\psi_r) = \psi_r. \tag{4.10}$$

I hence consider the eigen-problem

$$\boxed{\left[\mathcal{L}^{-1}\,(\mathcal{K}_0 + \alpha\,\mathcal{K}_1)\right](\psi_r) = \lambda\,\psi_r,} \tag{4.11}$$

and know that modes of the systems correspond to eigenvectors with eigenvalues $\lambda = 1$ of the operator $\mathcal{L}^{-1}\,(\mathcal{K}_0 + \alpha\,\mathcal{K}_1)$. As for the COI, I will now exhibit neutral mode solutions (i.e. solutions of the form $\lambda_i(\omega_i) = 1$, with real frequency) of this eigen-equation in the absence of resonant stars (i.e. assuming that the DF does not allow for the presence of stars exactly in resonance), and then discuss the interaction of the neutral modes with resonances.

4.2.3 A spectrum of neutral modes

Let me look for $\ell = 2$ neutral modes with purely real frequency ω. Let me further consider the region of low frequency, i.e. $\omega \simeq 0$ of the real line. In the $\alpha \neq 0$ case, a specific term in the kernel Q will dominate over the others: $Q_{(0,0)}$, which corresponds to the $\tilde{\mathbf{n}} = (0,0)$ resonance vector. Indeed, this term is proportional to $1/\omega$, as can be seen from the resonant denominator of eq. (4.8). It is therefore unbounded as $\omega \to 0$. From this observation, Palmer (1994) makes the following argument, similar to that of Section 3.2.2.3. In the absence of resonant stars (which is assumed for now), all the other terms in K, P and Q are again to be taken in the principal value sense. Therefore, the integrals are all bounded when $\omega \to 0$, in the same manner as the principal values in Section 3.2.2.3.

Let me assume for now that $Q_{(0,0)}$ dominates. Therefore, $\mathcal{Q}_{(0,0)}$ dominates over all other terms in $\mathcal{K}$ and one can approximate eq. (4.11) as

$$\alpha\left[\mathcal{L}^{-1}\,\mathcal{Q}_{(0,0)}\right](\psi_r) = \lambda\,\psi_r, \tag{4.12}$$

where $\mathcal{Q}_{(0,0)}$ is defined by

$$\mathcal{Q}_{(0,0)}(\psi_r) = \int \mathrm{d}r'\, Q_{(0,0)}(r, r', \omega)\psi_r(r'). \tag{4.13}$$

Note that assuming $\omega \to 0$ does not imply that the modes will have $\omega = 0$. This limit is taken to show that this term may dominate over the others. Modes will indeed form at finite values of ω, related to the dynamical structure of the system through the subsequent eigen-equation (4.12). Allen et al. (1992) further elaborates on the link between the mode frequency, the system's DF and the mode's structure.

Let me rewrite eq. (4.12) as

$$\left[\mathcal{L}^{-1}\,\omega\,\mathcal{Q}_{(0,0)}\right](\psi_r) = \frac{\omega}{\alpha}\,\lambda\,\psi_r, \tag{4.14}$$

where the term in brackets is now independent of ω, so the right-hand side is too. From here, the argument is the same as before: the operator $\omega\,\mathcal{Q}_{(0,0)}$ is self-adjoint and bounded, while the operator $\mathcal{L}$ is unbounded. Hence, the operator $\mathcal{L}^{-1}\,\omega\,\mathcal{Q}_{(0,0)}$ has a sequence of eigenvectors ψ_i, with corresponding eigenvalues μ_i which converge towards 0. Since the operator $\mathcal{L}^{-1}\,\omega\,\mathcal{Q}_{(0,0)}$ is also independent of α and ω, the solution of the eigen-problem (4.12) is given by the eigenvectors ψ_i and the eigenvalues

$$\lambda_i(\alpha, \omega) = \frac{\alpha}{\omega}\,\mu_i. \tag{4.15}$$

Then, each function of this sequence will give a neutral mode solution at a given frequency ω_i. Indeed, at the frequency

$$\boxed{\omega_i = \alpha\,\mu_i,} \tag{4.16}$$

the function ψ_i is an eigenvector of the eigen-equation (4.12) with the eigenvalue $\lambda_i(\alpha, \omega_i) = 1$. Finally, since the sequence μ_i converges towards 0, it is also the case of the sequence ω_i. Interestingly enough,

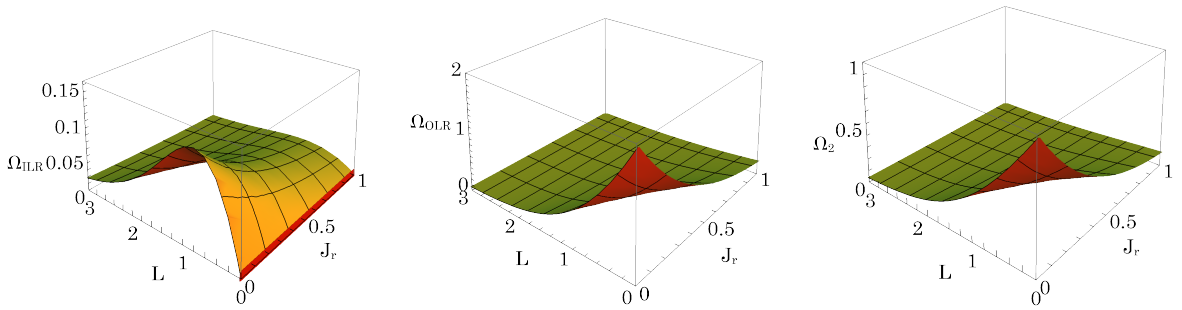

(a) Ω_{ILR} (b) Ω_{OLR} (c) Ω_2

Figure 4.1: Graphs of three combinations of the orbital frequencies of the Plummer sphere, in the space of actions (J_r, L). (a) ILR frequency, $\Omega_{\mathrm{ILR}} = \Omega_2 - \frac{1}{2}\Omega_1$. (b) OLR frequency, $\Omega_{\mathrm{OLR}} = \Omega_2 + \frac{1}{2}\Omega_1$. (c) Azimuthal frequency (i.e. corotation, CR), Ω_2. Here, Ω_{ILR} is the only frequency to vanish inside the cluster, as marked by the red line. This occurs for low-angular momentum orbits ($L = 0$). Note the differences in the vertical scales, showing that Ω_{ILR} always takes significantly lower values than any other resonance. Note also that the slice $J_r = 0$ of each of these graphs, corresponding to purely circular orbits, presents the same behaviour as Fig. 3.3, i.e. decreasing for Ω_{OLR} and Ω_2, and non-monotonic for Ω_{ILR} (note that the L axis grows when going towards the left). Indeed, for circular orbits, $L(r)$ is a strictly growing function, so $\Omega(r)$ and $\Omega(L)$ show the same behaviour.

eq. (4.16) shows that on a single sequence of tumbling modes (i.e. the sequence of a given eigenvector ψ_i), the oscillation frequency ω_i of the mode is proportional to α. This characteristic can be a possible indicator of the influence of the tumbling process in the development of linear instabilities in rotating star clusters. Some results of the following sections seem to correspond to this behaviour, in both regimes of anisotropy (see in particular Figs. 4.12b and 4.15b). Notice that the present argument does not make any assumption on α, and is therefore valid for all $-1 \leq \alpha \leq 1$. Note finally that in contrast to the argument given for non-rotating spheres in Chapter 3, I did not assume that the motion of the stars was epicyclic.

The assumption that ω be small sets constraints on the acceptable solutions of eq. (4.16). Indeed, the regime of validity of this assumption depends on a threshold ratio between $\mathcal{Q}_{(0,0)}$ and the other terms in $\mathcal{K}$, in order to guarantee that $\mathcal{Q}_{(0,0)}$ dominates. This may restrict the acceptable solutions of eq. (4.16) to high orders in i. Indeed, the largest elements μ_i may be too large to satisfy the constraint on ω_i. However, I have shown that a sub-sequence of μ_i converges towards 0, so that the solutions ω_i will exist at sufficiently high order i.

Let me now revisit the weaker assumption mentioned above. I have indeed assumed, as was done in Palmer (1994), that the divergence of the $\widetilde{\mathbf{n}} = (0,0)$ term in the operator $\mathcal{K}$ as $\omega \to 0$ dominates over all others. However, this is not guaranteed, and may represent an important limitation for the formation of a tumbling mode. Indeed, this argument considers that ω does not approach the extremum of another resonance as it vanishes. This is in fact not the case: when $\omega \to 0^-$, it approaches the minimum of $2\Omega_{\mathrm{ILR}} = 2\Omega_2 - \Omega_1$, and when $\omega \to 0^+$, it approaches the maximum of $-2\Omega_{\mathrm{ILR}}$. As illustrated by Fig. 3.3, the ILR frequency is the only (low-order) combination of orbital frequencies which vanishes inside the cluster. Figure 4.1a further shows that this minimum is reached in the region $L \simeq 0$ of orbital space, i.e. both for nearly radial orbits and for all orbits around the centre of the cluster. Hence, the integral term associated with the ILR may diverge as $\omega \to 0$. If I consider that the tumbling term does not dominate as $\omega \to 0$ (e.g., if it competes with the ILR), then the other dominant terms will also be unbounded as $\omega \to 0$, and it is likely that the full operator $\mathcal{K}$ is therefore still unbounded. Even if it were still possible to exhibit a sequence of neutral modes, and therefore perhaps destabilise the system, these modes would no more be directly limited to the tumbling process, i.e. solely related to the resonance $\widetilde{\mathbf{n}} = (0,0)$. In the following, I will focus on the tumbling mode, which may still exist. Undoubtedly, it would definitely be worthwhile to further investigate the behaviour of other possibly unbounded terms in $\mathcal{K}$ as $\omega \to 0$.

4.2.4 The effect of resonant interactions

The specific destabilisation of the tumbling neutral mode is discussed in detail in Palmer (1994). It is shown that it is a negative energy mode, and that any dissipative process, such as gas dissipation, will extract energy from the mode and lead to its destabilisation. The gravitational interaction of the mode with stars at the orbital resonances is also discussed. While the resonant interactions were unambiguously

destabilising the neutral mode of the COI, the role of resonances is less straightforward for the tumbling neutral mode.

This complexity arises from the existence of an ILR. Indeed, the neutral modes of the tumbling instability rotate at a low frequency, which implies that there will generally be stars at the ILR. In cored potentials, low-angular momentum orbits, i.e. radial orbits, have a vanishing ILR frequency. This is illustrated in Fig. 4.1a. A low-frequency pattern may therefore interact with such stars, either highly eccentric orbits at any energy, or any orbit which remains close to the centre. This resonance can operate either way, and there are hints that the interaction between a rotating pattern and stars at the ILR with it depends on the orbit's eccentricity. On the one hand, Palmer (1994) shows that, in radially anisotropic systems, the inner radial orbits which are at the ILR with the neutral mode will extract energy from it, so that the mode will be destabilised. On the other hand, in tangentially anisotropic systems, I have shown in Section 3.2.3 that if the resonance condition is met (which is the case here), the ILR is a stabilising resonance for neutral modes, because it has $n_1 < 0$. It is therefore likely that the role of the ILR in the destabilisation of a neutral mode depends on the proportions of nearly radial and nearly circular orbits in the system, i.e. on its velocity anisotropy. This question will be further discussed in Sections 4.6 and 5.5.

Interaction of density waves with resonant stars is a well studied subject in disks (see, e.g., Lynden-Bell & Kalnajs, 1972; Mark, 1971, 1974; Polyachenko & Shukhman, 2019). In these systems, the presence of an ILR usually corresponds to wave absorption, which prevents the system from forming an instability. Toomre (1981) proposes that the bulge's stabilising role comes from the fact that it extends the presence of an ILR to higher values of the possible pattern speeds, which was later confirmed by observations (Barazza et al., 2008) and N-body simulations (Sellwood & Evans, 2001). In the spirit of Lynden-Bell (1979), the bulge stabilises the instability because it deflects ILR orbits, preventing their realignment[2]. The case of tangentially anisotropic spheres, developed in Section 3.2.3, is similar to the disk case. In particular, the equations describing WKB wave propagation in tangentially anisotropic spheres are similar to those of disk systems (see Section 3.3.2). It is then plausible that wave absorption at the ILR also happens in tangentially anisotropic spheres. This seems to correspond to the $n_1 < 0$ condition.

The consequence of the unspecified role of resonant stars is that *this method does not provide a definitive proof for the existence of the tumbling instability.* Hence, advancements on that topic must rely on complementary methods, such as the matrix method, or N-body simulations. In Allen et al. (1992), N-body simulations of rotating spheres with various anisotropies were performed, leading to the identification of linear instabilities in a large fraction of the highly anisotropic fast rotators. In the following sections, I will present complementary results using both the matrix method and our own N-body simulations, which scan the parameter space of rotation and anisotropy searching for linear instabilities. These results were published in Rozier et al. (2019). They confirm and complement the results from Allen et al. (1992) for the linear stability of rotating systems. In the end of this chapter, I will focus on the radially anisotropic regime, and try to disentangle the radial orbit instability from the tumbling one. The specific role of the TI in tangentially anisotropic systems will be studied in detail in the next chapter.

4.3 The response matrix of rotating systems

In order to study the linear stability of rotating spherical systems, I now extend the response matrix method to rotating spheres. I present here a particular way to introduce rotation in a non-rotating equilibrium, following eq. (4.1), and develop the response matrix for a general DF which rotates accordingly.

4.3.1 Lynden-Bell's demon

In order to consider the linear response of rotating systems, I rely on a family of DFs that both allows for a certain variety in how rotation is introduced in the system, yet enough symmetry so that they can be studied efficiently with analytical tools. The way rotation is introduced, referred to as Lynden-Bell's demon (Lynden-Bell, 1960), proceeds as follows:

- Take a non-rotating DF for a spherical system.
- Define an axis of rotation labelled z. This definition allows for the separation of the orbits in two categories: the prograde orbits, which have a positive projection of the angular momentum in the z axis, i.e. $L_z > 0$, and the retrograde orbits, which have $L_z < 0$.

[2]One could imagine that for cuspy spheres (beyond the scope of this thesis) the same mechanism operates.

- Flip a fraction of the retrograde orbits to prograde motion, without changing the shape and position of the orbit. The fraction of the orbits that are flipped is independent of the shape and position of the orbits, i.e. independent of their energy and norm of the angular momentum.

From the description of this procedure, one can straightforwardly derive the DF of a system with the resulting characteristics. If $F_0(\widetilde{\mathbf{J}})$ is the DF of the initial non-rotating sphere, and α is the fraction of retrograde orbits that are flipped, the final rotating DF is

$$F(\mathbf{J}) = F_0(\widetilde{\mathbf{J}})(1 + \alpha\,\mathrm{Sign}(L_z)), \tag{4.17}$$

where Sign is the sign function defined by

$$\mathrm{Sign}(x) = \begin{cases} 1 \text{ if } x > 0, \\ 0 \text{ if } x = 0, \\ -1 \text{ if } x < 0. \end{cases} \tag{4.18}$$

Note that the DF produced by Lynden-Bell's demon (eq. (4.17)) is a particular case of the general DF introduced in eq. (4.1), with the function introducing the angular momentum, $g = \mathrm{Sign}$. The function Sign matches all the prerequisites for g: it is an odd function of its argument, and its maximum is 1. Note that other choices for the function g are studied in Section 5.2 and Appendix B.

4.3.2 The response matrix with Lynden-Bell's rotation

In Section 2.2, I derived the general form of the response matrix for spherical systems (eq. (2.20)). The purpose here is to derive the particular form of the response matrix for a rotating system with the DF of eq. (4.17). It can be written

$$\widehat{M}_{pq}(\alpha,\omega) = (2\pi)^3 \sum_{\mathbf{n}} \int \mathrm{d}\mathbf{J}\, \frac{\mathbf{n}\cdot\partial(F_0 + \alpha\, F_0\,\mathrm{Sign}(L_z))/\partial \boldsymbol{J}}{\omega - \mathbf{n}\cdot\boldsymbol{\Omega}}\, \psi^{(p)*}_{\mathbf{n}}(\mathbf{J})\, \psi^{(q)}_{\mathbf{n}}(\mathbf{J}). \tag{4.19}$$

Owing to its linear dependence w.r.t. α, the matrix can also be decomposed as

$$\boxed{\widehat{\mathbf{M}}(\alpha,\omega) = \widehat{\mathbf{M}}_0(\omega) + \alpha\,\widehat{\mathbf{M}}_1(\omega),} \tag{4.20}$$

where $\widehat{\mathbf{M}}_0$ and $\widehat{\mathbf{M}}_1$ are defined as

$$\widehat{M}^0_{pq}(\omega) = (2\pi)^3 \sum_{\mathbf{n}} \int \mathrm{d}\mathbf{J}\, \frac{\mathbf{n}\cdot\partial F_0/\partial\mathbf{J}}{\omega - \mathbf{n}\cdot\boldsymbol{\Omega}(\mathbf{J})}\, \psi^{(p)*}_{\mathbf{n}}(\mathbf{J})\, \psi^{(q)}_{\mathbf{n}}(\mathbf{J}), \tag{4.21}$$

$$\widehat{M}^1_{pq}(\omega) = (2\pi)^3 \sum_{\mathbf{n}} \int \mathrm{d}\mathbf{J}\, \frac{\mathbf{n}\cdot\partial(F_0\,\mathrm{Sign}(L_z))/\partial\mathbf{J}}{\omega - \mathbf{n}\cdot\boldsymbol{\Omega}(\mathbf{J})}\, \psi^{(p)*}_{\mathbf{n}}(\mathbf{J})\, \psi^{(q)}_{\mathbf{n}}(\mathbf{J}). \tag{4.22}$$

Here, $\widehat{M}^0_{pq}$ corresponds to the response matrix of a non-rotating system, and is simplified through eq. (2.41). In order to simplify $\widehat{M}^1_{pq}$, I can develop the gradient as

$$\mathbf{n}\cdot\frac{\partial(F_0(\widetilde{\mathbf{J}})\mathrm{Sign}(L_z))}{\partial\mathbf{J}} = \widetilde{\mathbf{n}}\cdot\frac{\partial F_0}{\partial\widetilde{\mathbf{J}}}\,\mathrm{Sign}(L_z) + 2\,n_3\,\delta_{\mathrm{D}}[L_z]\,F_0(\widetilde{\mathbf{J}}). \tag{4.23}$$

Introducing the coefficients

$$I^{\ell^p\ell^q}_{n_2m^p} = (2\pi)^3\, Y^{n_2}_{\ell^p}\, Y^{n_2}_{\ell^q} \int_0^\pi \mathrm{d}i\, \sin(i)\,\mathrm{Sign}(\cos(i))\, R^{\ell^p}_{n_2m^p}(i)\, R^{\ell^q}_{n_2m^p}(i) \tag{4.24}$$

and

$$J^{\ell^p\ell^q}_{n_2m^p} = 2\,m^p\,(2\pi)^3\, Y^{n_2}_{\ell^p}\, Y^{n_2}_{\ell^q}\, R^{\ell^p}_{n_2m^p}(\pi/2)\, R^{\ell^q}_{n_2m^p}(\pi/2), \tag{4.25}$$

as well as a new set of functions

$$Q^{\widetilde{\mathbf{n}}}_{\ell^p n^p \ell^q n^q}(\omega) = \int \mathrm{d}\widetilde{\mathbf{J}}\, \frac{F_0(\widetilde{\mathbf{J}})}{\omega - \widetilde{\mathbf{n}}\cdot\widetilde{\boldsymbol{\Omega}}(\widetilde{\mathbf{J}})}\, W^{\widetilde{\mathbf{n}}}_{\ell^p n^p}(\widetilde{\mathbf{J}}) W^{\widetilde{\mathbf{n}}}_{\ell^q n^q}(\widetilde{\mathbf{J}}), \tag{4.26}$$

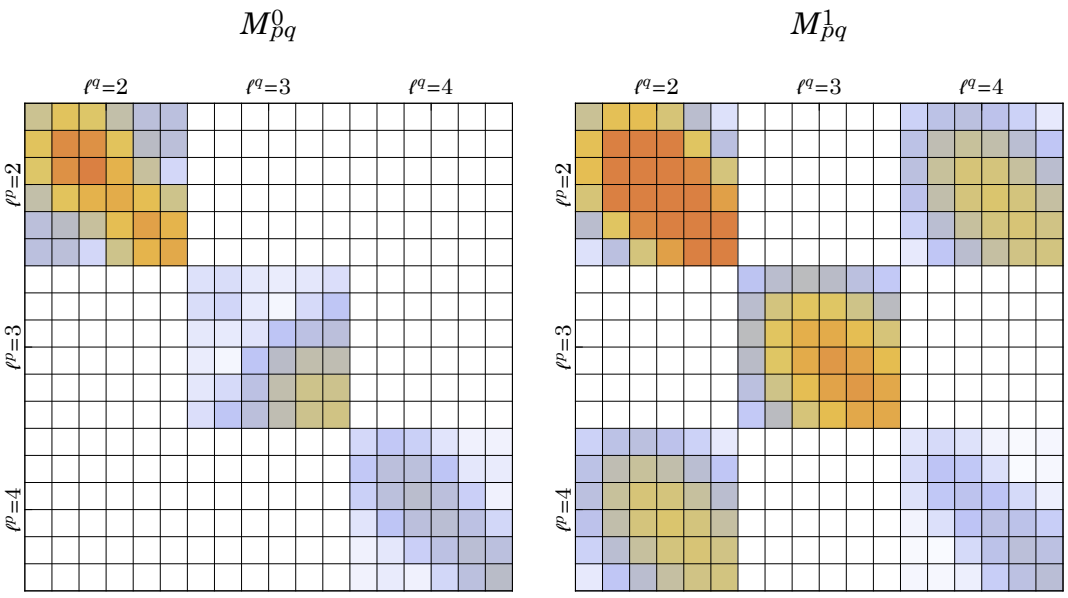

Figure 4.2: Sketch of the $\widehat{M}^0_{pq}$ and $\widehat{M}^1_{pq}$ matrices in a particular unstable case. The characteristics of the DF are developed in the next section. The colours scale with the norm of each cell from white, light blue up to orange. Note that $\widehat{M}^1_{pq}$ is not block-diagonal anymore. The matrices were computed in the $q=-6$, $\alpha=1$, $n_{\max}=5$, $\ell_{\max}=4$ case, with $(\eta,\omega_0)=(0.074, 0.60)$, corresponding to an $m=2$ unstable mode. The fact that the upper left block dominates indicates that the modes will be well represented by keeping only that harmonic (see Fig. 2.2).

I can rewrite $\widehat{M}^1_{pq}$ as

$$\boxed{\widehat{M}^1_{pq}(\omega) = \delta^{m^q}_{m^p} \sum_{\tilde{\mathbf{n}}} \left\{ P^{\tilde{\mathbf{n}}}_{\ell^p n^p \ell^q n^q}(\omega)\, I^{\ell^p \ell^q}_{n_2 m^p} + Q^{\tilde{\mathbf{n}}}_{\ell^p n^p \ell^q n^q}(\omega)\, J^{\ell^p \ell^q}_{n_2 m^p} \right\}.} \tag{4.27}$$

Here, the reason why $P^{\tilde{\mathbf{n}}}_{\ell^p n^p \ell^q n^q}$ was defined in eq. (2.42) with two different values of ℓ becomes apparent. For rotating systems, the response matrix is block-diagonal in m^p, because the system is axisymmetric, however it is no more block-diagonal in ℓ^p, since the spherical symmetry has been lost. Indeed, terms with different values of ℓ can interact, and the resulting modes now involve a superposition of spherical harmonics. Figure 4.2 sketches the structure of the response matrix for rotating systems, as well as its non-rotating component. The chessboard-like structure of $\widehat{M}^1_{pq}$ is due to the $Y^{n_2}_{\ell^p}\, Y^{n_2}_{\ell^q}$ term in both $I^{\ell^p \ell^q}_{n_2 m^p}$ and $J^{\ell^p \ell^q}_{n_2 m^p}$ (eqs. (4.24) and (4.25)), which is non-zero only when ℓ^p and ℓ^q have the same parity. Note that all following stability results are using a single $\ell = 2$ block of the matrix, because higher ℓ were found to have little impact on the mode measurements. This indicates that the instabilities I detect in spheres are well represented by a single harmonic $\ell = 2$.

Once the expression of the response matrix has been derived, it can be computed via the same numerical techniques as for non-rotating systems (see Section 2.4). In order to produce complementary and independent results regarding the linear stability of anisotropic, rotating spheres, I also used N-body simulations of such equilibria. Before discussing comparative results of both techniques, I present the numerical methods used in these simulations.

4.4 Numerical simulations of rotating clusters

The numerical simulations performed by P. G. Breen and presented in Rozier et al. (2019) mainly used the `gyrfalcON` tree code (Dehnen, 2002), while some consistency tests were performed using the direct N-body `NBODY6` code (Nitadori & Aarseth, 2012). Here, I focus on the DF used to sample the initial conditions in the different simulations, the particular method used for this sampling, as well as the method used to measure the frequencies of the mode (growth rate and oscillation frequency), which I compare to those obtained via the matrix method.

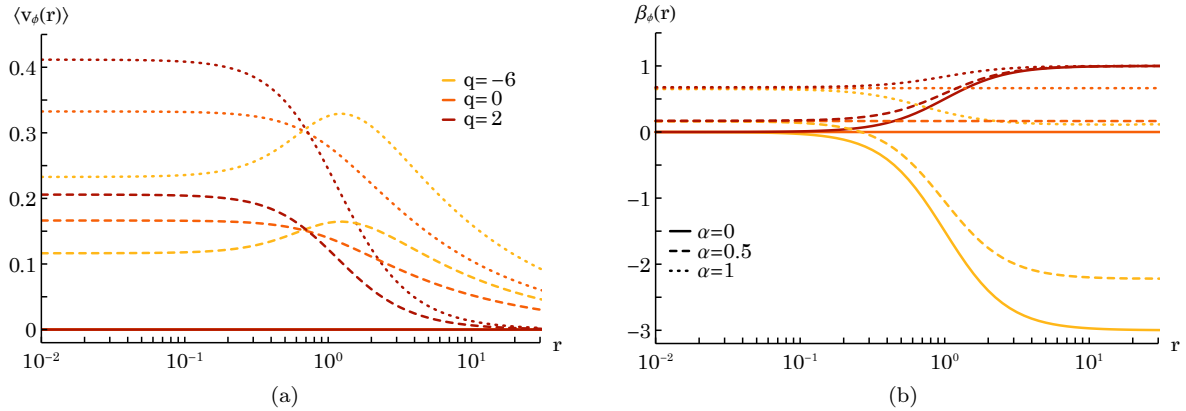

Figure 4.3: Illustration of the radial dependence of $\langle v_\phi(r)\rangle$ (a) and $\beta_\phi(r)$ (b) for various velocity anisotropies (via q, indicated by the shade of colour) and total angular momentum (via α, indicated by the line style). Here, α controls $\langle v_\phi(r)\rangle$, while q controls β_ϕ, noticeably in the outer region of the cluster. Note that for $(\alpha, q) = (1, -6)$ a significant fraction of the radial support is centrifugal, whereas σ_ϕ remains comparatively small. The sphere has therefore a large reservoir of kinetic energy, which can be converted into thermal energy through an instability.

4.4.1 A distribution function with anisotropy and rotation

The systems I studied are Plummer spheres, already presented in Section 3.4.1. I used the same DF as that presented for the non-rotating DF F_0 (see eq. (3.121)). Yet, instead of restricting q to negative values, which produces tangentially anisotropic clusters, I also considered the case of positive q, which produces radially anisotropic clusters. From this non-rotating DF, rotation is introduced via Lynden-Bell's demon (see eq. (4.17)).

Let me highlight a few selected features of these DFs. Figure 4.3 illustrates how α creates some mean azimuthal motion in an otherwise non-rotating system. It should also be noted that α induces an anisotropy in the azimuthal motions, by breaking the symmetry in the two tangential directions, as given by the azimuthal anisotropy parameter

$$\beta_\phi(r) = 1 - \frac{\sigma^2_{\phi,\alpha}(r)}{\sigma^2_r(r)}. \tag{4.28}$$

Figure 4.3b also shows how α biases the azimuthal anisotropy towards radial motions by increasing the mean azimuthal velocity. Similarly, increasing q increases the mean azimuthal velocity in the central region of the cluster and decreases it in the outer region. For $q \neq 0$, a radial variation of β_ϕ is also introduced in the outer region of the cluster. Moreover, increasing q increases β_ϕ. Note that by construction $\langle v_\phi(r)\rangle \propto \alpha$. Finally, note that even for $q = -6$, when $\alpha = 1$, $\sigma_r > \sigma_\phi$.

Figure 4.4, illustrates the PDF of (v_r, v_ϕ) for various values of α and q. Note that Lynden-Bell's demon introduces a sharp discontinuity in the distribution of stars in the v_ϕ-direction as soon as $\alpha \neq 0$. Appendix B shows that this discontinuity plays no role in driving the instabilities.

4.4.2 Sampling the initial conditions

The sampling algorithm designed to produce initial conditions for the N-body realisations of these DFs is publicly available via the Python `PlummerPlus` code[3]. First, the particles' positions are randomly drawn using the inverse cumulative distribution of radii in the Plummer sphere. More precisely, the cumulative distribution function (CDF) of radii in a spherical cluster is formally given by the enclosed mass within radius r. In the Plummer sphere, this mass is

$$M(r) = 4\pi \int_0^r \mathrm{d}r'\, r'^2\, \rho_0(r') = \frac{r^3}{(1+r^2)^{3/2}}. \tag{4.29}$$

As a consequence, randomly drawing radii to build a Plummer sphere amounts to drawing a random variable x_1 uniformly on the segment $[0; 1]$, and associating it to the radius $r = M^{-1}(x_1)$ by the application of the inverse CDF defined by

$$M^{-1}(x) = \frac{1}{\sqrt{x^{-2/3} - 1}}. \tag{4.30}$$

[3] https://github.com/pgbreen/PlummerPlus

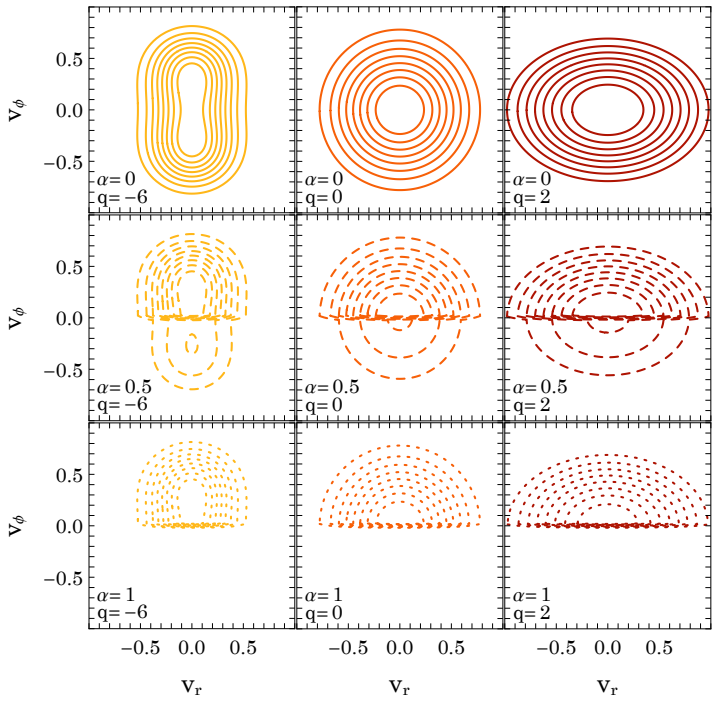

Figure 4.4: Level contours of the number density of stars in the (v_r, v_ϕ)-space at the constant radius $r = 1$. Whenever $\alpha \neq 0$, the PDF is discontinuous on the line $v_\phi = 0$. As q increases, the spread in v_ϕ decreases, and the system becomes more radially biased. As α increases, stars are swapped towards positive v_ϕ.

Once radii have been drawn, the polar angle can be drawn as $\theta = \cos(2x_2 - 1)$, where x_2 follows a uniform law on $[0; 1]$. The azimuthal angle can be drawn as $\phi = 2\pi\, x_3$, where x_3 follows a uniform law on $[0; 1]$.

Once the positions of the particles are drawn, one needs to associate a velocity to each particle, so that the overall DF corresponds to F_0. This is done via a sampling by rejection. Here, I give the outline of this procedure. For a particle at radius r, the region of velocity space where the particle can be is bounded by the condition $E \leq 0$, hence each radius is associated with a maximum velocity $v_{\rm max}(r) = \sqrt{-2\psi_0(r)}$. As the $(v_r, v_{\rm t})$-space DF at radius r is bounded on $[-v_{\rm max}(r); v_{\rm max}(r)] \times [0; v_{\rm max}(r)]$, the independent variables required for the sampling by rejection can be drawn from uniform distributions on resp. $[-v_{\rm max}(r); v_{\rm max}(r)]$ and $[0; v_{\rm max}(r)]$ for v_r and $v_{\rm t}$. Then, the multiplying factor of the algorithm will be taken at the maximum of the $(v_r, v_{\rm t})$-space DF on the rectangle. In practice, this DF is computed on a sufficiently fine grid, and the maximum value is multiplied by 1.1 for sanity. Checks were made that this is enough to guarantee that this number is always above the DF. Finally, as F_0 is symmetric w.r.t. the exchange of v_θ and v_ϕ, the angle of the tangential velocity w.r.t. a fixed direction is drawn as a uniform variable on $[0; 2\pi]$.

The last step concerns the introduction of rotation, to transform a cluster sampled following F_0 into one following $F = F_0 + \alpha\, {\rm Sign}(L_z)$. Section 4.3.1 already presented that procedure. In practice, a direction is arbitrarily chosen as the z axis. Then, the particles with negative L_z are identified. For each of these retrograde particles, a random variable x_4, uniformly distributed on $[0; 1]$, is drawn. If $x_4 > \alpha$, the initial position and velocity of the corresponding particle remain the same. If $x_4 < \alpha$, the position of the particle stays the same, but its velocity is multiplied by -1. This places the particle on the same orbit, but now it revolves in the prograde direction.

4.4.3 Measuring instabilities - Comparison with the matrix results

The characterisation of the instabilities relies on three observables: the real and imaginary parts of the frequency (oscillation frequency and growth rate), and the shape of the mode in physical space. To characterise the frequencies of the unstable modes in numerical simulations, the space density was Fourier-analysed as follows. For a given pattern number $m = 2$, one can define $A_m(t) = C_m(t)/C_0(t)$, where

$$C_m(t) = \int_0^{+\infty} {\rm d}r\, r \int_{-\infty}^{+\infty} {\rm d}z \int_0^{2\pi} \frac{{\rm d}\phi}{2\pi}\, \rho_0(r, z, \phi, t)\, {\rm e}^{-{\rm i}m\phi}, \tag{4.31}$$

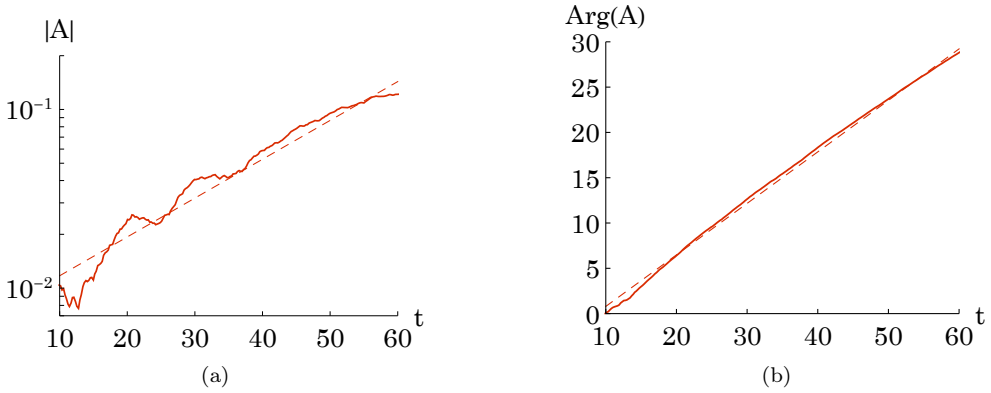

Figure 4.5: Illustration of the time-dependence of (a) $|A_m(t)|$ and (b) $\mathrm{Arg}(A_m(t))$ for the fiducial $q = -6, \alpha = 1$ cluster, as measured in numerical simulations. Following eq. (4.32), linear fits are also represented. The method gives $(\omega_0, \eta) = (0.57, 0.022)$, which can be compared with the measurements of Fig. 4.6 using the matrix method.

with $\rho_0(R, z, \phi, t)$ the simulation's instantaneous density (i.e. a sum of N delta functions). Notice that these measurements are now relying on a cylindrical view of the cluster, i.e. average quantities are computed on cylindrical shells parallel to the axis of rotation of the cluster (z coordinate). Should the cluster support an unstable mode, one can in principle extract its frequencies from the numerically-measured function $t \mapsto A_m(t)$, as one has

$$\frac{\mathrm{d}\,\log(|A_m(t)|)}{\mathrm{d}t} = \eta; \quad \frac{\mathrm{d}\,\mathrm{Arg}(A_m(t))}{\mathrm{d}t} = \omega_0\,. \tag{4.32}$$

In practice, measuring the growth rate of an instability in N-body data presents two major difficulties. The first is noise due to the discrete nature of the system. The second is that the N-body system cannot sustain an exponential growth indefinitely, and the mode must saturate at some point. In practice, both effects are connected. The larger N, the smaller the Poisson fluctuations and the longer one can wait before the mode's saturation. The transition from exponential growth to saturation is not easy to model, and may have some dependence on the phase space DF. The result is that this transition can possibly result in a bias such that growth rates based on an exponential fit may systematically underestimate the true growth actually experienced by the mode in its early linear phase.

In order to automatically detect and measure growth rates in a grid of N-body simulations, an iterative scheme is used. It involves fitting an exponential curve to the amplitude $|A_m(t)|$ of the mode, first over the full duration of the simulation, but then reducing the time interval of the fit, until the maximum absolute difference between the fit and data (the normalised amplitude) falls below a predetermined value of tolerance. The choice of tolerance should be small enough such that the time interval is reduced when there is a poor fit to a mode (because of its saturation) but large enough so that the interval is not reduced merely by the presence of noise. Based on a grid of 300 different realisations of the reference model with $N = 2^{17}, q = -6, \alpha = 1$, a tolerance value of 0.009 was found to produce robust measurements of the growth rate η. Similarly, ω_0 is determined by a linear fit to $\mathrm{Arg}(A_m(t))$ (mod 2π to account for complete revolutions) over the same time interval. Figure 4.5 illustrates such measurements of η and ω_0 for the fiducial model.

These measurements can be directly compared to those produced with the matrix method. Using the matrix of eq. (4.20), and the numerical techniques developed in Section 2.4, I compute the Nyquist contours drawn in Fig. 4.6. These contours identify a mode with growth rate $0.045 \leq \eta \leq 0.049$ and oscillation frequency $0.547 \leq \omega_0 \leq 0.550$. The comparison between linear theory and N-body simulations in the fiducial model shows a $\sim 15\%$ discrepancy in the measured value of η, and a $\sim 3\%$ discrepancy in ω_0. These close results indicate that both methods are measuring the same instability. A definitive proof is given by the comparison of the shapes of the modes.

To do so, the simulation's particles are projected onto the same $\rho^{(p)}(r, \theta, \phi)$ basis as for the matrix method, to reconstruct the mode using eq. (2.10). This is illustrated in Fig. 4.7b. In parallel, once the matrix method has identified an unstable mode, the response matrix's eigenvector associated with the eigenvalue nearly equal to 1 can be determined, which allows me to obtain the mode's shape via eq. (2.10). Figure 4.7a represents the density of the mode of the fiducial model, as predicted by the matrix method.

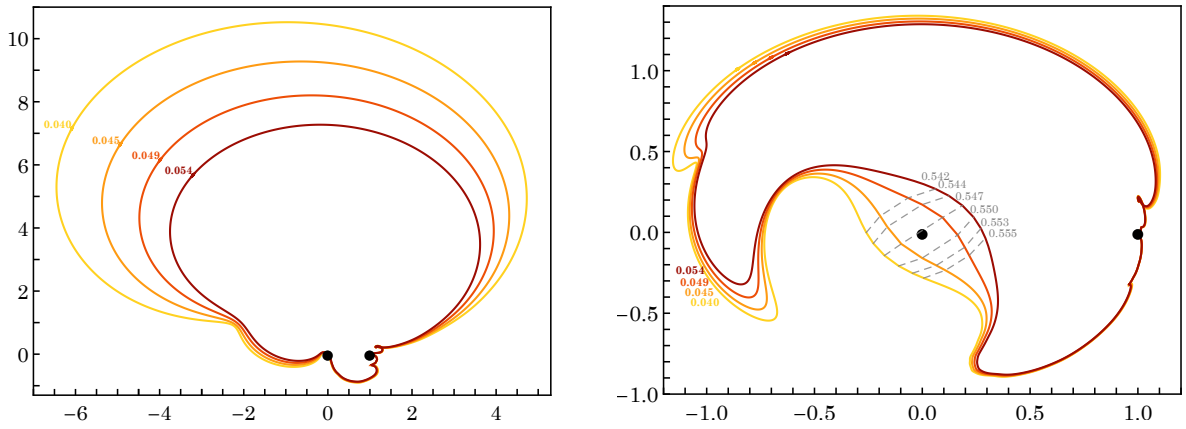

(a) (b)

Figure 4.6: Nyquist diagram of the fastest growing mode of the model $(\alpha, q) = (1, -6)$, as given by the curves $\omega_0 \mapsto \det[\mathbf{I} - \widehat{\mathbf{M}}(\omega_0 + \mathrm{i}\eta)]$, using the matrix method. (a) Nyquist diagram without rescaling. (b) Nyquist diagram after logarithmic rescaling (see the caption of Fig. 2.10 for details). Different colours are associated with different growth rates, while the changes in ω_0 along each curve are indicated with the gray dashed lines. This diagram shows that the cluster supports an unstable mode with a growth rate, $0.045 \leq \eta \leq 0.049$, and oscillation frequency, $0.547 \leq \omega_0 \leq 0.550$.

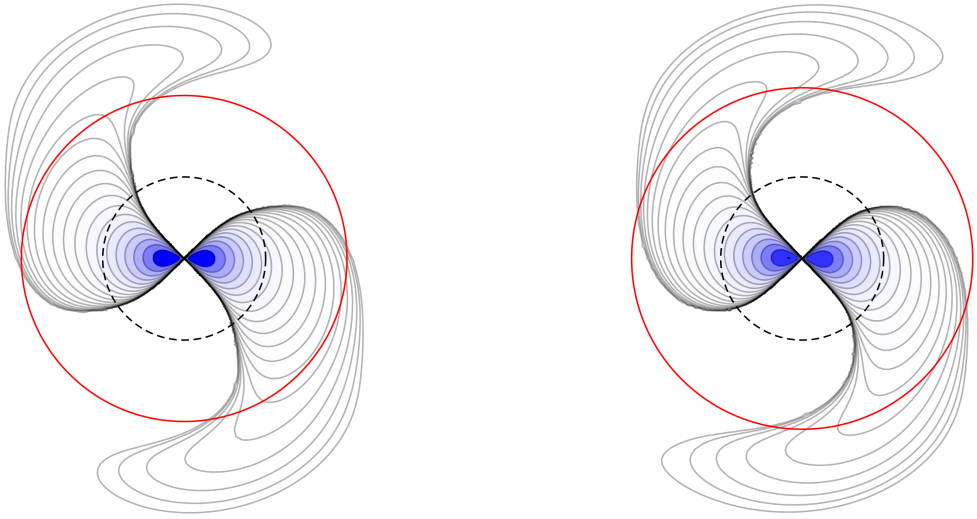

(a) Linear theory (b) N-body simulation

Figure 4.7: Radial dependence in the equatorial plane of the density of the unstable mode recovered in Figs. 4.5 and 4.6. (a) Linear theory's prediction. (b) Measurement from N-body simulations. The black dashed circle represents the scale radius of the background Plummer potential, and the red circle the mode's corotation radius. Isocontours are logarithmically sampled, with a factor $\sim$1.6 between two consecutive lines, so that the outermost line has a density 1.5×10^4 times smaller than the peak value. The similarity between the two results is striking.

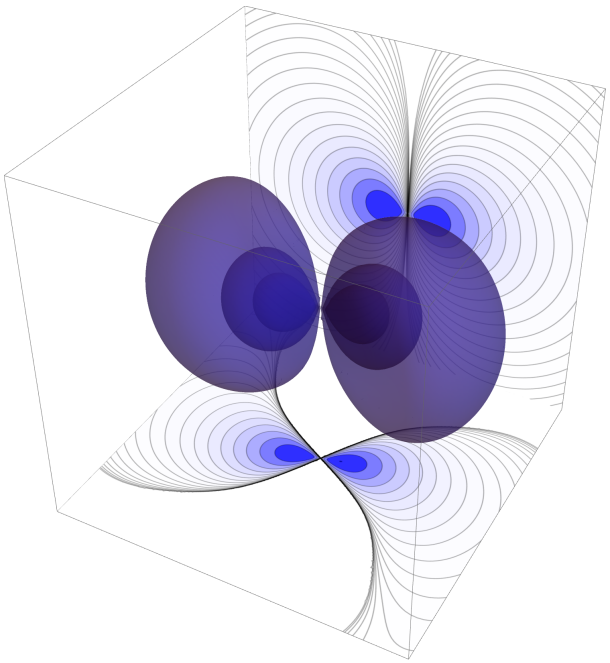

Figure 4.8: $3D$ isosurfaces of the density of the unstable mode recovered in Fig. 4.6, and their intersection with the equatorial and meridional planes.

Strikingly, the mode shapes reconstructed from the matrix method and measured in N-body simulations are in close agreement. *This allows me to quantitatively validate the implementation of the matrix method as well as my extension of the linear stability analysis to rotating systems.*

Finally, Fig. 4.8 illustrates the $3D$ density isocontours of the same unstable mode, showing that the mode's thickness in the vertical direction is significant. This vertical structure is expected from the fact that it is proportional to an $\ell = 2$ spherical harmonic, and therefore has a $\sin^2\theta$ dependence w.r.t. the polar angle θ.

4.5 A stability survey with the matrix and N-body methods

In the previous section, I demonstrated the quantitative agreement between the matrix and N-body methods in identifying an instability in a rotating cluster. This allows me to confidently characterise the cluster's stability in the space of anisotropy (q) and rotation (α) with the matrix and N-body methods. Thanks to its fast computation, I will mainly use the matrix method, as it allows me to perform large parameters explorations. The simulations results are therefore used as a consistency check. I will first present the general results of this exploration, I will then validate the robustness of the results via convergence studies, before presenting detailed descriptions of different instability regions.

4.5.1 Mapping the (α, q)-space

I chart the (α, q)-space using the response matrix method, as well as N-body simulations. The resulting frequencies are illustrated in Figure 4.9.

In that figure, one can straightforwardly identify two types of instabilities. The first one, corresponding to the pyramid on the top of the $\eta(\alpha, q)$ panel ($q<0, \alpha \gtrsim \frac{1}{2}$) appears to be specific to tangentially-biased and rotating systems. These instabilities are studied in detail in Section 4.5.4. A second type of instability can be also be noted in the bottom right part of the $\eta(\alpha, q)$ panel ($q>0$). These instabilities appear to be specific to radially-biased systems. I investigate these instabilities in Section 4.5.3. The two right panels of Fig. 4.9 show the N-body counterparts of the measurements using the matrix method. Again, the quantitative matchings between the left and right panels validate my generalisation of the matrix method. On all these panels, for both η and ω_0, the lower blue plane corresponds to a growth rate threshold, $\eta = 0.01$, below which I stopped the search for unstable modes. Indeed, the reliability of the matrix method is poor at low growth rate (see Section 2.3.4.2 for a discussion of this point), and the same occurs in N-body simulations.

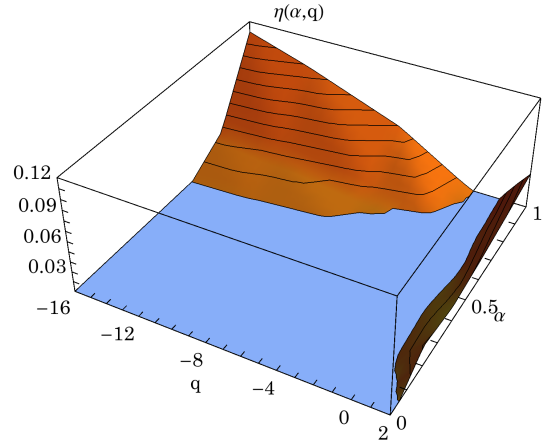

(a) Growth rate, matrix method.

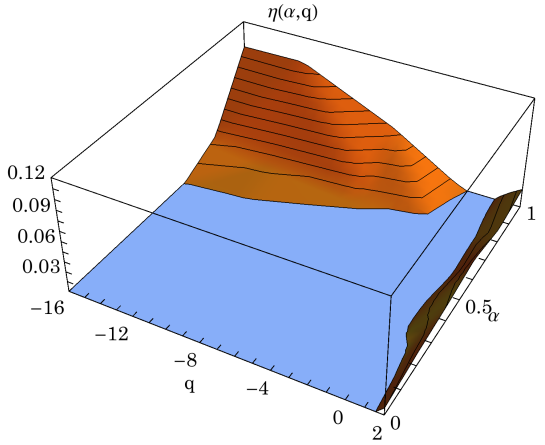

(b) Growth rate, N-body measurements.

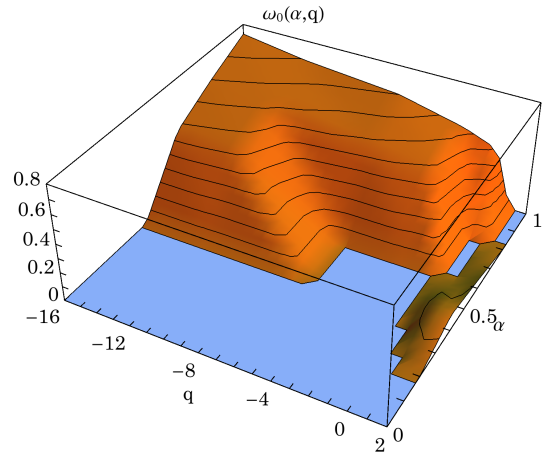

(c) Oscillation frequency, matrix method.

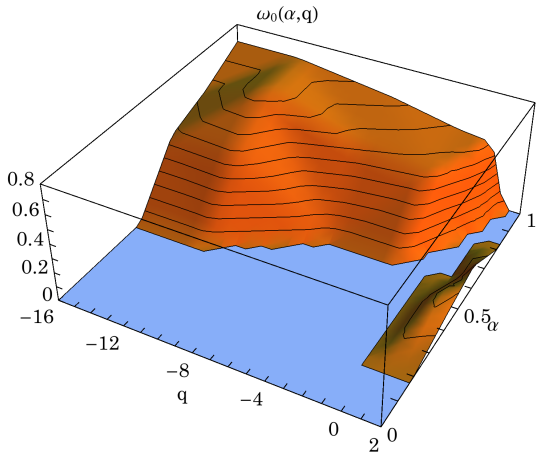

(d) Oscillation frequency, N-body measurements.

Figure 4.9: Illustration of the dependence of the growth rates η (top panels) and oscillation frequencies ω_0 (bottom panels), as a function of the cluster's parameters (α, q), measured using the response matrix method (left panels) and N-body methods (right panels). I searched for unstable modes on a (α, q)-grid composed of the locations $\alpha = 0, 0.2, 0.4, 0.6, 0.8, 1$ and $q = -16, -12, -6, -2, 0, 1, 2$. The blue plane represents my growth rate threshold, $\eta = 0.01$, for mode selection. At this level of accuracy, it appears that rotation introduces a new island of instability in the top-left region of each panel (corresponding to $q<0, \alpha>\frac{1}{2}$) and an extension of the known ROI instability island on the right (near $q\sim 2$). The comparisons of the matrix method's and N-body measurements highlights again the reliability of my implementation of the linear theory.

Note that the $q = 0$ line, where the isotropic, rotating systems sit, is found to be stable by both methods. This is consistent with the N-body measurements of Meza (2002), where this exact series of systems is investigated. Note also that the matrix results required only $\ell = 2$ components of the matrix, so that the agreement between the matrix and N-body simulations shows that there is little to no interaction between different ℓ harmonics in these instabilities.

4.5.2 Convergence studies

Let me investigate the convergence of the numerical methods used to characterise unstable modes. Section 4.5.2.1 focuses on the matrix method, while Section 4.5.2.2 considers the convergence of the N-body runs. In these two sections, I will use the same fiducial model as in Section 4.4.3, namely $(\alpha, q) = (1, -6)$.

4.5.2.1 Convergence of the matrix implementation

The different approximations in the computation of the response matrix introduce various control parameters that can be tuned to increase the precision (and the computational complexity) of the resulting growth rate and oscillation frequency measurements. These parameters involve on the one hand the

Parameter	Interval	Standard	η	ω_0
	Standard		0.045	0.54
$r_{\min}$	0.01 - 0.001	0.01	0.045	0.54
$r_{\max}$	5 - 30	10	0.045	0.54
Δu	2 - 0.15	1	0.027 - 0.045	0.44 - 0.54
$p_{\rm b}$	3 - 8	4	0.054 - 0.037	0.54 - 0.49
$R_{\rm b}$	3 - 6	5	0.024 - 0.045	0.44 - 0.54
$n_1^{\max}$	1 - 5	2	0.030 - 0.060	0.49 - 0.54
$n_{\max}$	5 - 10	5	0.045 - 0.054	0.54 - 0.60
$\ell_{\max}$	2 - 7	2	0.045 - 0.081	0.54 - 0.60
	Fiducial		0.054	0.60

Table 4.1: Growth rates and oscillation frequencies computed for various values of the parameters that control the precision of the matrix method calculations, for the $(\alpha, q) = (1, -6)$ cluster. Having chosen a particular set of parameters as a standard case, I present the computed growth rate and oscillation frequency when each control parameter is varied independently. The second column presents the interval of variation of each parameter, while the third column gives the standard value of each parameter. The last two columns show the interval of variation of the growth rate and oscillation frequency in each case. When no significant variation is measured, a single value is given. The first line gives the values of η and ω_0 for the standard case. Note that this standard case differs from the fiducial case of Section 4.4.3, which had $n_{\max} = 10$ and $p_{\rm b} = 2$, and is shown in the last line of the table. The standard computation of the convergence study therefore involves fewer basis functions, however the sampling of action space for the integration will tend to be better.

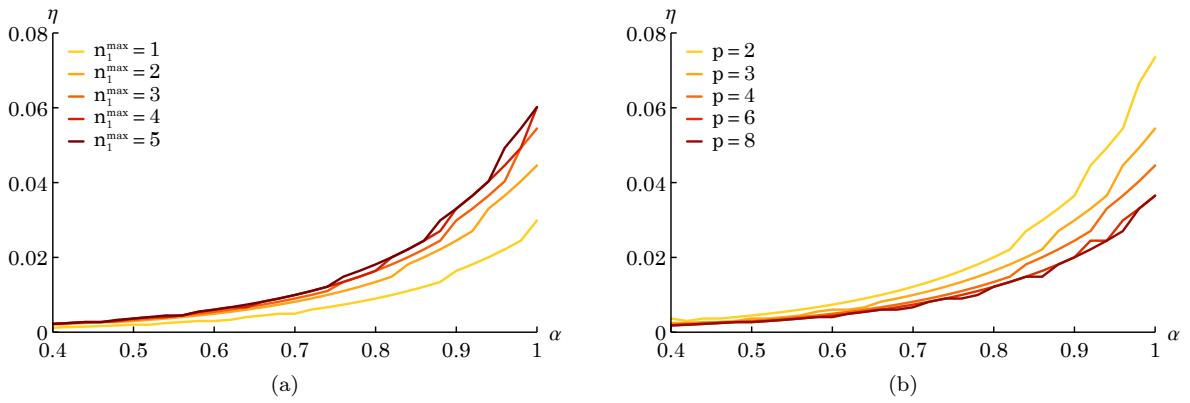

Figure 4.10: Illustration of the convergence of the matrix method for the measurement of the growth rate η for different rotation parameters α. (a) Dependence of the measured growth on the maximum resonance number, $n_1^{\max}$. (b) Dependence of the measured growth rate with the parameter $p_{\rm b}$ controlling the density of the $(r_{\rm p}, r_{\rm a})$-grid, see eq. (2.78).

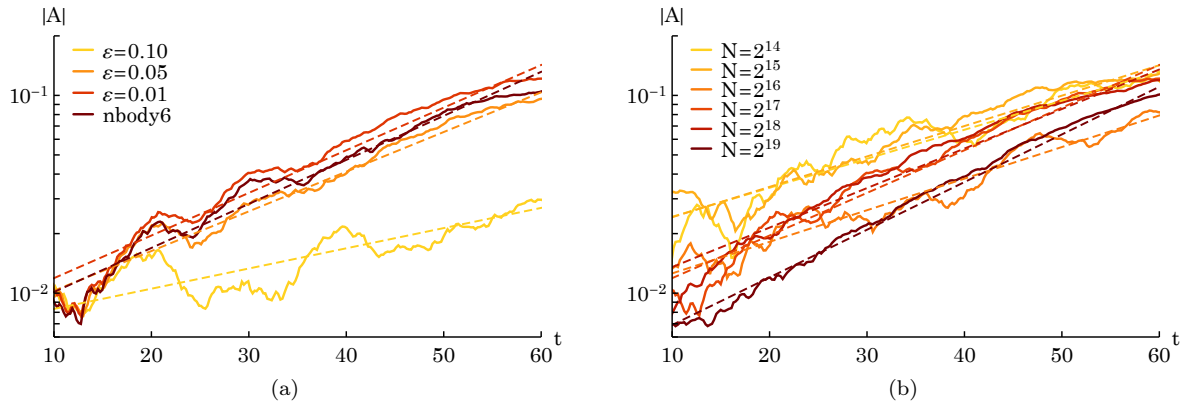

Figure 4.11: Illustration of the convergence of the N-body measurements for the fiducial cluster $(\alpha, q) = (1, -6)$, as illustrated by the time evolution of the amplitude $|A|$ (continuous lines) and the associated exponential fit (dashed lines). (a) Dependence w.r.t. the softening length ε. This panel also includes a fully collisional run. All runs were performed with $N = 2^{17}$ particles. (b) Dependence w.r.t. the number of particles N. All runs were performed with the same softening length $\varepsilon = 0.01$.

sampling of action space in the integral of eqs. (4.21) and (4.22), which is turned into a $(r_\mathrm{p}, r_\mathrm{a})$-grid by a change of variables, and on the other hand the number of harmonics both in the Fourier decomposition in angles and in the projection onto the biorthogonal set of basis elements. The parameters controlling the $(r_\mathrm{p}, r_\mathrm{a})$-grid are r_min, r_max, Δu, p_b, R_b and were introduced in Section 2.4.4. The parameters controlling the level of projection are n_1^max, the maximum wave number in the Fourier decomposition over the radial angle, n_max the maximum order of radial basis functions, which also sets the size of a block in the response matrix, and ℓ_max the maximum harmonic number ℓ, which also defines the number of blocks in the response matrix (see Fig. 4.2). Note that these two sets of parameters are not independent. Here, R_b also controls the quality of the projection onto the radial basis set, and should be chosen so that the important information is contained inside this radius. Similarly, n_max also controls the grid refinement, as can be seen in eq. (2.78). In the following study, I made sure that varying n_max would not change the grid sampling but only the level of projection onto the radial basis.

Table 4.1 presents the results of the computation of growth rates and oscillation frequencies of the fiducial model $(\alpha, q) = (1, -6)$ when these control parameters are varied. As expected (see also, e.g., Hamilton et al. (2018)), the results are mildly dependent on some of these parameters. Here, I show that I reached a sufficient level of convergence to confirm the existence of unstable modes, as well as the value of their growth rates and oscillation frequencies.

Figure 4.10 shows typical converging $\eta(\alpha)$ curves when I increase the level of precision of two of the parameters, here p_b and n_1^max. In closing, the choice of control parameters ensures that for $\eta > 0.01$ the stability manifolds are properly mapped.

4.5.2.2 Convergence of the N-body simulations

The main control parameters for the force calculation in the `gyrfalcON` code are ε (softening parameter), θ (tolerance parameter) and the softening kernel. The softening kernel used has a density proportional to $(1 + x^2)^{-7/2}$ which, as shown by Dehnen (2001), results in much less of a force bias than Plummer softening. The parameter θ controls the accuracy of the force calculation (and is related to the opening angle in traditional tree codes). The default value of 0.6 gives relative force errors of the order of 0.001 in near-spherical systems (Dehnen, 2001). Besides N, the softening length ε is the main parameter of interest since, if its value is too large, the perturbation which drives the growth of instability might not be resolved.

In Fig. 4.11, the effect of varying ε (left panel) and N (right panel) is explored. The default value of $\varepsilon = 0.05$ was found to give good agreement with results using lower values of ε, and with a direct N-body simulation using `NBODY6` (Nitadori & Aarseth, 2012), which in effect has no softening, i.e. $\varepsilon = 0$. The reference number of particles $N = 2^{17}$ was also found to give good agreement with larger N-body simulations. Indeed, no obvious dependence of the growth rate with increasing N was found.

Now that the matrix results are confirmed via both a convergence study and a successful comparison with N-body simulations, I present more precise results using the matrix method only, in the different instability manifolds which were identified in Fig. 4.9.

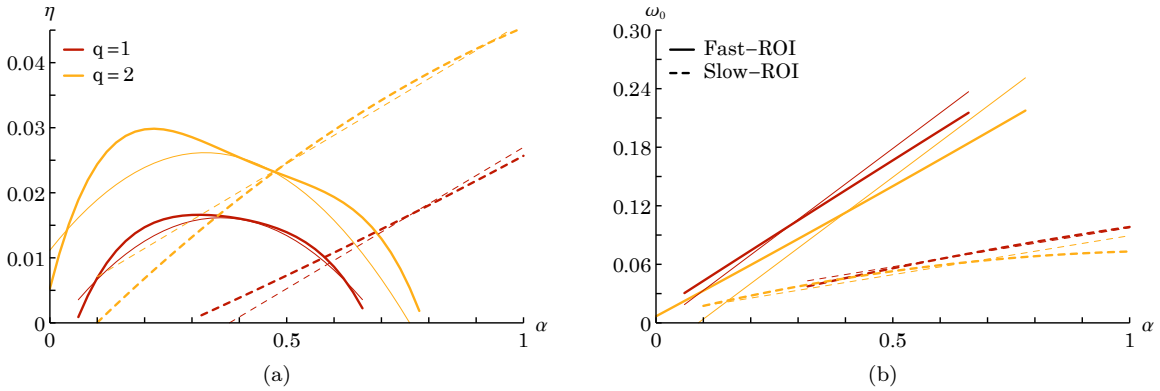

Figure 4.12: Illustration of (a) the growth rate and (b) the oscillation frequency as a function of α for fixed values of q, in the $q>0$ region, as measured with the matrix method. The thin lines represent the global polynomial fits from eq. (4.33).

4.5.3 Focusing on radial anisotropy

The results in the radially anisotropic regime present hints of competing behaviours, corresponding to different types of instabilities. To disentangle the modes of one type of instability from the other, I applied a clustering algorithm on a dataset made of growth rates, oscillation frequencies, and matrix eigenvectors (representing the shape of the mode), spanning the (α, q)-space. This dataset usually included several modes for each point in (α, q)-space. The algorithm found clusters of data, owing to similarities in the shape of the corresponding modes. These clusters correspond to different instability regimes, as illustrated by Figs. 4.12, 4.13 and 4.14.

In Fig. 4.12, I illustrate cuts of constant q in the $\eta(\alpha, q)$ and $\omega(\alpha, q)$ surfaces in the $q>0$ region. Similarly, in Fig. 4.13, I explore the $\eta(\alpha, q)$ surface, and represent the shapes of the associated unstable modes. The shapes of the modes clearly suggest the existence of two types of instabilities, depending on the region considered.

The first type of instability dominates for slow-rotating systems ($\alpha \lesssim \frac{1}{2}$). It is represented with the solid lines in Fig. 4.12, and the dark grey surface in Fig. 4.13. It can be identified as the continuation in the rotating regime of the standard ROI (see Section 1.4). This type will be referred to hereafter as "Fast-ROI", since the oscillation frequency of the instability is large. For that particular instability, the modes evolve from a bar-like shape around $q=0$ to a loosely-wound trailing spiral around $q=2$, as shown in Fig. 4.13.

The second type of instability dominates for fast-rotating systems ($\alpha \gtrsim \frac{1}{2}$). It is represented with the dashed lines in Fig. 4.12, and the light grey surface in Fig. 4.13. Note that the oscillation frequencies of these modes are small, and I therefore refer to this instability as "Slow-ROI". As illustrated in Fig. 4.13, for that second instability regime, the modes present a barred shape, with a more wound trailing spiral departing from the bar, which qualitatively differs from the shape of the Fast-ROI modes. The characterisation of the processes leading to these two competing regimes is discussed in Section 4.6.

Both instability surfaces $(\alpha, q) \mapsto \omega_0, \eta$ can be fitted globally by simple polynomial functions as

$$\begin{aligned} \omega_0 &= \frac{4\alpha}{11} - \frac{q}{34} + \frac{1}{38}, & \eta &= \frac{q}{76} + \frac{11\alpha}{100} - \frac{q\alpha}{109} - \frac{7\alpha^2}{50} - \frac{1}{66}, \\ \omega_0 &= \frac{2\alpha}{25} - \frac{q}{123} + \frac{1}{39}, & \eta &= \frac{q}{52} + \frac{\alpha}{23} - \frac{1}{28}, \end{aligned} \tag{4.33}$$

for the Fast- and the Slow-ROI respectively. These fitting formulae, as well as the fitting formulae presented for the other instability surface, were obtained by applying a least squares algorithm to different low order polynomial forms, and choosing the fit that both guarantees a reasonable accuracy w.r.t. the data and a simple functional form. In practice, these fits can be used as simple stability criteria for the present DF. In Section 4.5.5, similar fits are presented, using global kinematic properties of the cluster, which can represent the properties of general rotating clusters.

In Fig. 4.14, I finally illustrate isocontours of the growth rates of the dominant instabilities in the $(\alpha, q>0)$-space. This figure clearly highlights the transition between the two regions of instability, Fast-ROI vs. Slow-ROI.

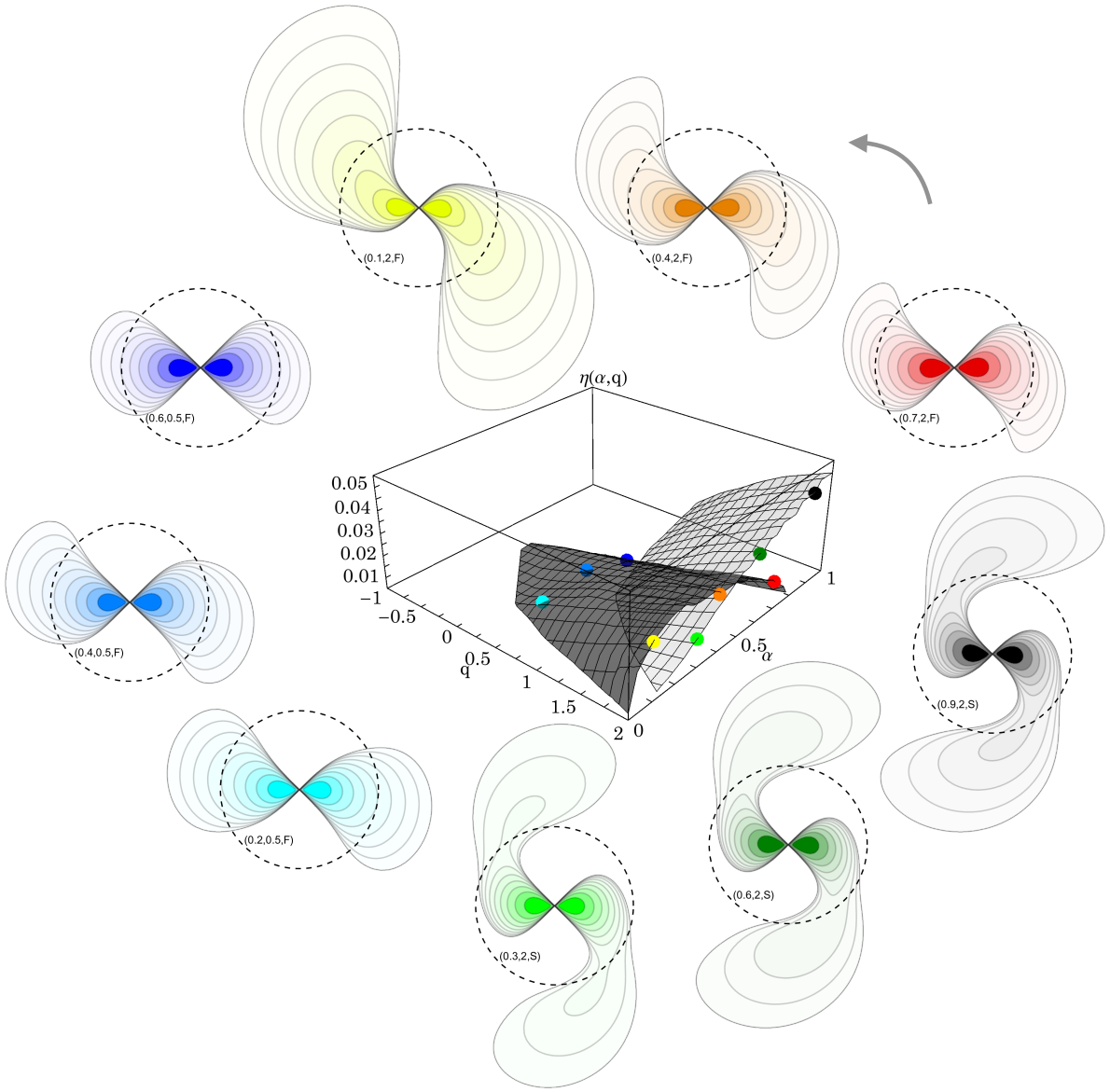

Figure 4.13: Illustration of various modes' shapes as one explores both surfaces of instability in the $q>0$ region. For each coloured point, the mode's density in the equatorial plane is represented. Two lines of points were chosen with constant q and varying α: $q=0.5$, and $q=2$. The grey arrow indicates the direction of rotation of both the global rotation and the instability patterns. On each mode, the value of (α, q) is written inside the circle, as well as a letter indicating whether the mode is on the Fast-ROI (F) or Slow-ROI (S) surface. In contrast to Fig. 4.16, the shapes of the modes of the "Fast" and "Slow" families are strikingly different.

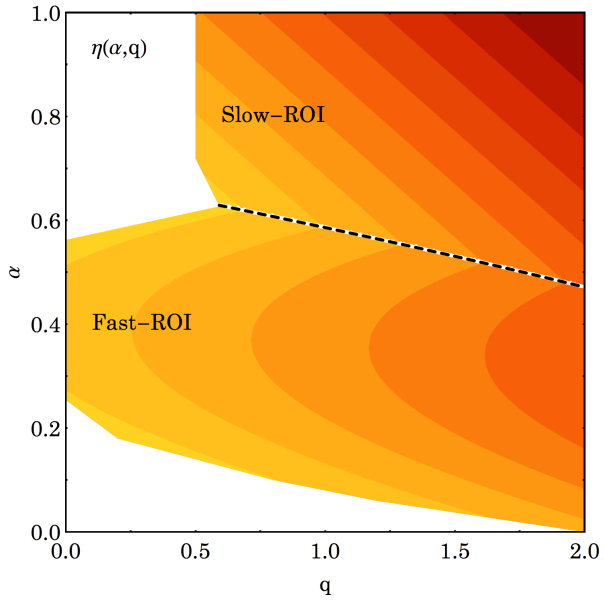

Figure 4.14: Isocontours of the growth rate in the (α, q)-space for $q>0$, as given by the fits from eq. (4.33). Contours are spaced linearly between the maximum growth rate and zero. The dashed line highlights the transition between the Fast-ROI and Slow-ROI instabilities, as already visible in Fig. 4.13. The transition occurs at all radial anisotropies (provided the instabilities exist), at a degree of rotation which merely depends on the anisotropy.

4.5.4 Focusing on tangential anisotropy

In Fig. 4.15, I illustrate cuts of constant q in the $\eta(\alpha, q)$ and $\omega(\alpha, q)$ surfaces in the $q < 0$ region, i.e. the region of tangential anisotropy. In the relevant region, the instability surface $(\alpha, q) \mapsto \omega_0, \eta$ can be fitted globally by the simple polynomial expressions

$$\omega_0 = \frac{11\alpha}{15} - \frac{q}{66} - \frac{2}{9}, \quad \eta = \frac{29\alpha^2}{50} - \frac{q^2}{8333} - \frac{2q\alpha}{111} + \frac{q}{103} - \frac{47\alpha}{50} + \frac{37}{100}. \tag{4.34}$$

The cuts of the present fitting formulae are represented in Fig. 4.15, showing their level of accuracy.

In Figure 4.16, I represent the $\eta(\alpha, q)$ surface for tangentially-biased systems. I emphasise that in this regime, both η and ω_0 increase with α, and increase as q decreases, i.e. the more rotating and the more tangentially anisotropic the system, the larger the growth rate and the pattern speed of the instability. Note that the reason why the COI (see Chapter 3) is not recovered at $\alpha = 0$ is the conservative threshold imposed on the matrix measurements of the growth rate. I also emphasise that the specific shape of the surface depends on the adopted choice of the angular momentum distribution (i.e. follows from the

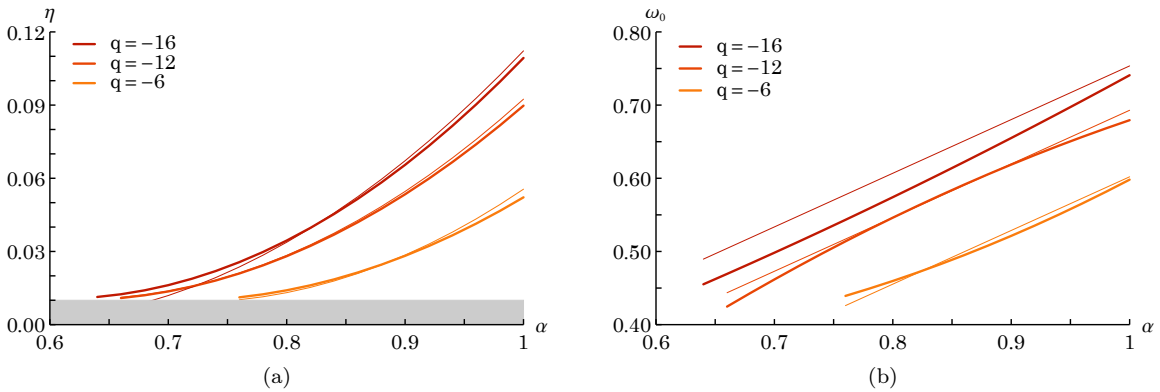

Figure 4.15: Illustration of (a) the growth rate and (b) the oscillation frequency as a function of α for fixed values of q, in the $q<0$ region, as measured from the matrix method. The grey region represents the threshold for the measurement of instabilities. At this level of accuracy, the η and ω_0 surfaces can be fitted globally by quadratic functions of α and q, represented with the thin lines.

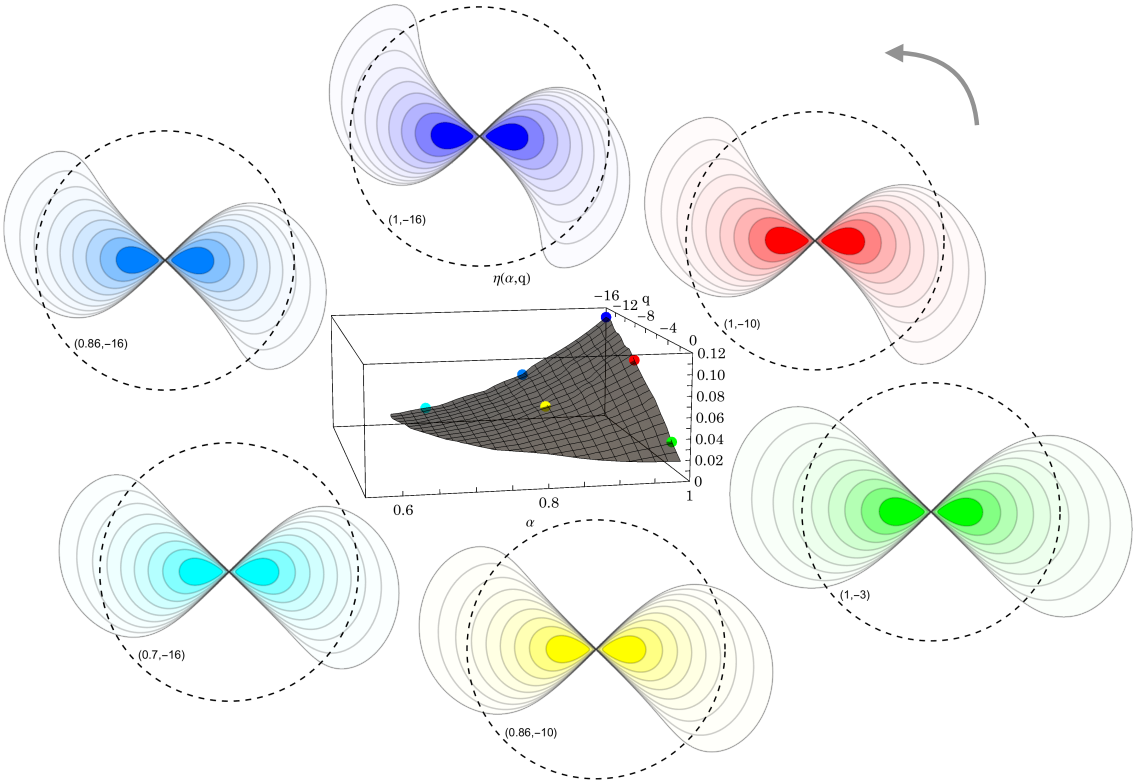

Figure 4.16: Illustration of the various mode shapes as one explores the plane of instability in the $q<0$ region, i.e. tangentially anisotropic systems. The black dashed circle represents the scale radius of the Plummer potential. The grey arrow indicates the direction of rotation of both the global rotation and the instability patterns. In addition to matching the colour of the mode with the points in the central figure, the value of (α, q) is written inside each circle. With increasing α and decreasing q, the spiral patterns get more and more wound.

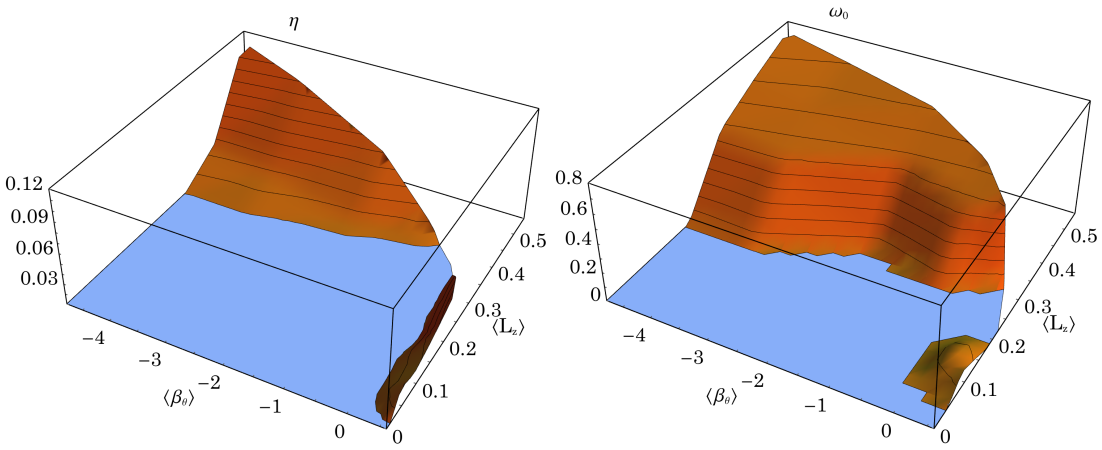

Figure 4.17: Illustration of the surfaces of instability in the $(\langle\beta_\theta\rangle, \langle L_z\rangle)$-space. This figure is to be compared to Fig. 4.9.

application of Lynden-Bell's demon, see also Appendix B). In Fig. 4.16, I also show the shape of the modes at different locations on the instability surface. The absence of any significant variation in the modes' shape suggests that the underlying instability mechanism remains the same.

4.5.5 Remapping the instability chart

In order to rephrase my results in a more general framework, I define macroscopic kinematic parameters of the sphere via the mass-weighted radial average of the polar anisotropy β_θ (see eq. (3.124)) and the angular momentum L_z. They read

$$\begin{aligned} \langle\beta_\theta\rangle &\equiv \frac{1}{M_{\rm tot}}\int \mathrm{d}r\, 4\pi r^2 \rho_0(r)\beta_\theta(r) = \frac{3}{10}\,q\,, \\ \langle L_z\rangle &= \alpha\sqrt{GM_{\rm tot}R_{\rm s}}\; l(q), \text{ with } l(q) \simeq \frac{3}{5} - \frac{10}{9}\left(\frac{69}{14} - q\right)^{-1}, \end{aligned} \tag{4.35}$$

where $l(q)$ is a good fit decreasing monotonically from 0.6 to 0.22 as q increases. From eq. (4.35), I note that to zeroth order, q and α are direct proxy for $\langle\beta_\theta\rangle$ and $\langle L_z\rangle$. Using this reparametrisation, I present in Fig. 4.17 a remapping of the stability manifolds in the $(\langle\beta_\theta\rangle, \langle L_z\rangle)$-space.

As expected, the qualitative differences between Figs. 4.9 and 4.17 are minor. The following simple fits represent the three manifolds

$$\boxed{\begin{array}{ll} \omega_0 = \frac{10L}{7} - \frac{\beta}{43} - \frac{1}{7}, & \eta = \frac{117L^2}{55} - \frac{\beta^2}{1623} - \frac{L\beta}{26} - \frac{141L}{89} + \frac{\beta}{107} + \frac{14}{47}, \\ \omega_0 = L, & \eta = \frac{11L}{21} - \frac{63L^2}{38} + \frac{2\beta}{17} - \frac{18L\beta}{37} - \frac{\beta^2}{20} - \frac{1}{28}, \\ \omega_0 = \frac{L}{3}, & \eta = \frac{L}{7} + \frac{\beta}{10} - \frac{1}{21}, \end{array}} \tag{4.36}$$

resp. for negative q, Fast-ROI, Slow-ROI, using the shortening notations $\beta = \langle\beta_\theta\rangle$ and $L = \langle L_z\rangle$. From eq. (4.36), the stability criteria from both Ostriker & Peebles (1973) and Polyachenko & Shukhman (1981) can be generalised by requesting that η is above a given threshold $\eta_{\rm crit}$. For instance, for the Slow-ROI, it reads

$$\boxed{\frac{\langle L_z\rangle}{7} + \frac{\langle\beta_\theta\rangle}{10} \geq \eta_{\rm crit} + \frac{1}{21}} \tag{4.37}$$

.

4.6 Destabilisation processes in radially anisotropic models

The results of the stability analysis reported in the previous sections give us insight on the specific processes which may destabilise rotating anisotropic clusters. While Chapter 5 discusses the case of tangentially anisotropic systems, I will discuss in the present section the destabilising processes in rotating radially anisotropic systems. I will confront the present results with a scenario by Palmer (1994), and propose a complementary scenario in light of my new results.

$\mathcal{I}$	$\eta(\alpha = 0.3)$	$\omega_0(\alpha = 0.3)$	$\eta(\alpha = 1)$	$\omega_0(\alpha = 1)$
Reference	0.033	0.081	0.040	0.066
$(-1, 2), (0, 0)$	0.024	0.073	0.040	0.060
$\mathcal{I}_0 \setminus (-1, 2)$	$< 10^{-4}$	-	$< 10^{-4}$	-
$\mathcal{I}_0 \setminus (0, 0)$	0.0090	0.012	0.015	0.024
$(-1, 2)$	0.0040	0.012	0.008	0.022
$(0, 0)$	$< 10^{-4}$	-	$< 10^{-4}$	-

Table 4.2: Values of the growth rate and pattern speed found through the truncated response matrix method applied to the $q = 2, \alpha = 0.3$ and 1 radially-biased system. In both cases, the main mode was considered, so that $\alpha = 0.3$ identifies a Fast-ROI mode, and $\alpha = 1$ identifies a Slow-ROI mode. With only the ILR and tumbling resonance, it is possible to recover the instability in both regimes. Removing either of them has however considerable consequences.

4.6.1 Restricted matrix in the radially anisotropic regime

In order to characterise the stability of radially anisotropic, rotating spheres in terms of resonant processes, I must rely again on the restricted matrix method. I recall that in Chapter 3, this method brought critical evidence to associate the instabilities detected in tangentially anisotropic clusters with the COI (see Section 3.4.3). For the COI, the process relied on the interaction of several resonances (the ILR to form a neutral mode, the other resonances to destabilise it) to produce instabilities. The ROI process is different, as the ILR alone is sufficient to destabilise the system. This suggests that the restricted matrix method should be adapted in this context. Instead of only successively *removing* individual resonances (in a kind of proof by negation), I will also build the instability by *keeping* only given resonances. I recall that the computation of reference should include all relevant resonance vectors with $|n_1|, |n_2| \leq 2$, corresponding to $\mathcal{I}_0 = \{(0, 0), (1, 0), (2, 0), (-2, 2), (-1, 2), (0, 2), (1, 2), (2, 2)\}$ (see Section 3.4.3).

Table 4.2 reports the values of the growth rate and oscillation frequency found by the restricted matrix method in the $q = 2$, $\alpha = 0.3$ and 1 systems, where combinations of resonance vectors are tested. In both cases, the main mode was considered, so that $\alpha = 0.3$ identifies a Fast-ROI mode, and $\alpha = 1$ identifies a Slow-ROI mode. The results are very similar in both regimes. It appears that turning off terms corresponding either to the ILR or to the tumbling process from the full matrix lowers the growth rate and modifies the oscillation frequency of the instability, while keeping only those two terms together preserves both its growth rate and its oscillation frequency. These results show that the destabilisation of radially anisotropic rotating systems is guaranteed through the interaction of the radial orbit and tumbling processes only. Therefore, a consistent framework for the description of destabilisation processes in radially anisotropic, rotating systems should involve the ILR and the tumbling resonances together. This is true in both the Fast- and Slow-ROI regimes.

4.6.2 Competition between radial orbit and tumbling processes

From the analytical characterisation of the ROI and the tumbling instabilities, Section 8.7 of Palmer (1994) presents a scenario regarding the relative roles of the radial orbit and tumbling instabilities in clusters with different degrees of radial anisotropy. The discussion is articulated around his Fig. 8.1, which I reproduced here in Fig. 4.18. This figure illustrates the following argument: since the tumbling instability requires the formation of a neutral bar (i.e. initially non-growing), its growth is slow, so in a system strongly biased towards radial orbits, the ROI dominates. In such a system, the angular momentum of the bar cannot be strong, as the angular momentum of quasi-radial orbits is low. As a consequence, ω_0 is low. This gives a point in the top left part of Fig. 4.18. From that point, consider a system with smaller radial anisotropy. The ROI grows at a slower pace, and the angular momentum of the bar increases because that of the orbits does too. Hence the line on Fig. 4.18 has a negative slope in the top left region. When the radial bias is further decreased, the ROI decays, and eventually gets dominated by the tumbling mode. This mode grows slowly, but has a larger oscillation frequency, because the angular momentum of the orbits is larger. In Fig. 4.18, it is assumed that, when the radial bias is even more decreased, the lack of radial orbits has a negative influence on the growth of the tumbling mode (there is not enough energy extracted by radial orbits from the neutral mode). Hence the negative slope of the curve in the bottom right part of the graph. Yet, the author does not conclude about the fate of the tumbling mode in this regime ("the growth rate is uncertain"). The curve may grow again when ω_0 increases.

The results of Section 4.5.3 allow me to fill this uncertainty with measurements from the matrix

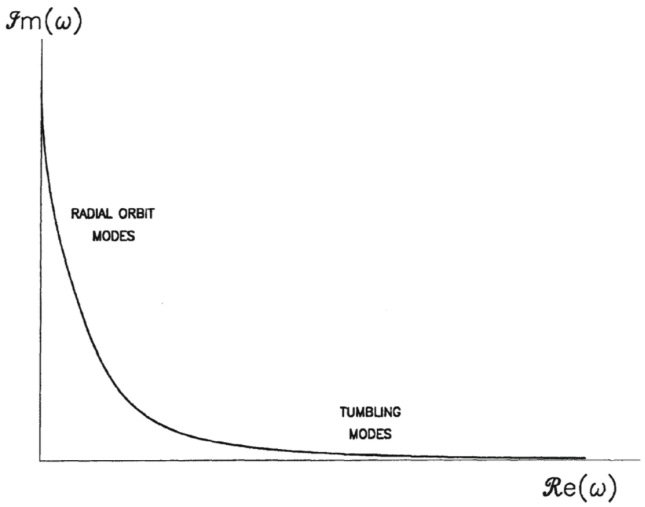

Figure 4.18: Reproduced from Palmer (1994), Fig. 8.1. The position of the instabilities is represented in the space of oscillation frequency (Re(ω)) and growth rate (Im(ω)). This curve represents the merging of the ROI (slow oscillations, fast growth) with the tumbling instability (fast oscillations, slow growth).

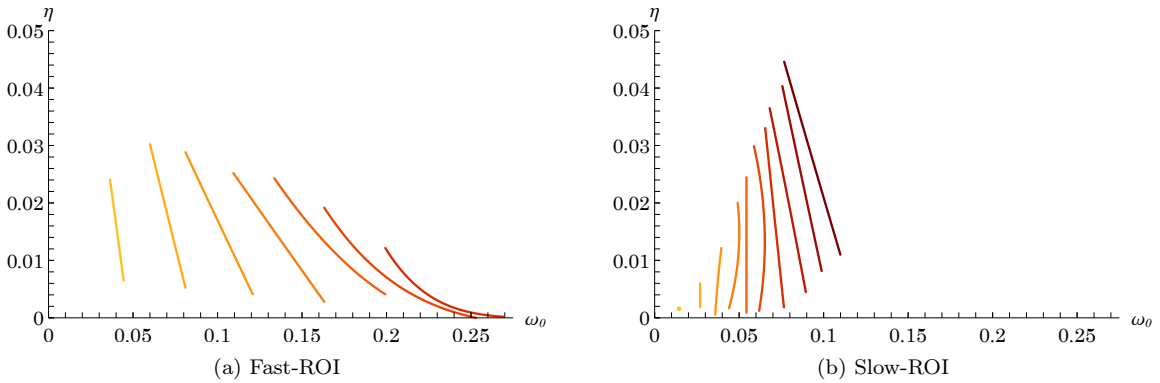

(a) Fast-ROI (b) Slow-ROI

Figure 4.19: Modes obtained by the matrix method (see Fig. 4.13) represented in (ω_0, η)-space for (a) the Fast-ROI and (b) the Slow-ROI. Lines of constant α and varying q are drawn, mimicking the procedure from Palmer (1994). In panel (a), α goes from 0.1 (yellow) to 0.7 (red) with steps of 0.1 (as shown by Fig. 4.13, the Fast-ROI disappears around $\alpha \simeq 0.8$). In panel (b), α goes from 0.1 (yellow) to 1 (dark red) with steps of 0.1. In both figures, it seems that all curves remain in the ROI branch of Fig. 4.18. Strikingly, when the Fast-ROI approaches the maximum of $\Omega_{\rm ILR}$ ($\omega_0 \simeq 0.26$), the instability disappears.

method, which are confirmed by N-body simulations as presented in Section 4.5.1. Figure 4.19a shows the corresponding lines on the Fast-ROI surface obtained by measuring frequencies at fixed values of α and varying q, while Fig. 4.19b is the corresponding figure for the Slow-ROI. In each case, the tip of the curve at high η corresponds to the edge of the permitted region $q \leq 2$ insuring a non-negative DF. I performed complementary tests on an Osipkov-Merritt DF (see Osipkov, 1979; Merritt, 1985, for the exact expression of this DF), which continuously extends the Dejonghe DF to more radially anisotropic clusters. In each case (Fast- and Slow-ROI, each α), the behaviour of the curves remains unchanged. On the low η side, each curve terminates because no instability was measured with $\eta > 10^{-4}$, with the parameters used for the runs presented in Section 4.5.1.

The Fast-ROI can be directly linked to the "true" ROI (i.e. ROI in the non-rotating case), because it appears in slowly rotating clusters. In that case, the behaviour of slowly rotating clusters ($\alpha \leq \frac{1}{2}$) does not seem to display any particular behaviour in the vicinity of the ROI's decay. At higher rotation, the steepness of the curves is lower, which may indicate some interaction with a tumbling mode, according to Palmer's predictions.

The results in the Slow-ROI regime are similar. The steepness of the curves seems to evolve with α (i.e. the yellow curve is steeper than the red one). Note that the inversion of the slope in some of the curves may be due to an insufficient precision of the matrix method in the frequency measurements at low η.

One particular point, which was not mentioned by Palmer, is the role of the maximum of Ω_{ILR} (which occurs around $\omega_0 = 0.26$, see Figs. 3.3 and 4.21). Indeed, it seems from Fig. 4.19a that the instabilities are depleted when they approach that oscillation frequency, and cannot exist above it. This observation highlights the role of resonant orbits at the ILR in the destabilisation process. The next section elaborates further on this observation.

4.6.3 A scenario for a rotating ROI

In the radially anisotropic region, the matrix method and angle-action variables allow me to emphasise the role played by orbits around specific resonances (ILR, corotation resonance (CR) and outer Lindblad resonance (OLR) for bi-symmetric instabilities) in driving the instability. It provides a mathematical framework to study the tumbling instability scenario brought forward by Lynden-Bell (1979) for discs, but which also applies to spheres dominated by quasi-radial orbits. Note that here, the term tumbling refers to the orbits' apsidal precession within the orbital plane, while the same term is unfortunately used in the previous sections and in Allen et al. (1992) to refer to the precession and oscillations of the orbital planes themselves. Under the assumption of the toy model presented in Pichon & Lynden-Bell (1993), which only focuses on the ILR, and assumes all orbits are identical with positive effective orbital moment of inertia[4] (Earn & Lynden-Bell, 1996), the instability criterion becomes the azimuthal analogue of Jeans' (Penrose, 1960). The distribution of tumbling orbits has to be narrow enough around a given maximum to allow their relative torque to overcome their spread in azimuthal tumbling rates (azimuthal pressure), which otherwise phase mixes any disturbance. The standard (non-rotating) ROI seems in most cases to qualitatively correspond to such a scenario (Polyachenko & Shukhman, 2015), so long as the adiabaticity of the fast action $J_{\mathrm{f}} = J_r + \frac{1}{2}L$ allows us to pin down the ILR as the unique relevant resonance (but see Polyachenko & Shukhman, 2015, for a discussion of counter examples with fast growing modes).

Indeed, Fig. 4.20 shows that most orbits have $\zeta_{\mathrm{ILR}} > 0$, with ζ_{ILR} the cooperation parameter at the ILR, defined by

$$\zeta_{\mathrm{ILR}} = \left.\frac{\partial \Omega_{\mathrm{ILR}}}{\partial L}\right|_{J_{\mathrm{f}}}. \tag{4.38}$$

Hence, the system is likely to support a tumbling instability (in the sense of Lynden-Bell), provided the resonance frequency distribution is sufficiently narrow (Lynden-Bell, 1979). This is illustrated in Fig. 4.21, where the probability distribution function (PDF) of the tumbling frequency Ω_{ILR} is represented for various values of $q \geq 0$ and α. As highlighted in these figures, the effect of increasing q is both to concentrate the orbits in regions of high cooperation parameter and to lower the spread in azimuthal precession rates. Rotation also narrows the spread in azimuthal precession rates, which favours the development of instabilities. In order to take into account the direction of rotation of the orbits and make this reasoning slightly more quantitative, I classified orbits by the sign of L_z[5], mapping them

[4] Note that the role played by the moment of inertia is implicit in eq. (2.20) via the integral over $\mathbf{J}$ which can be rewritten as an integral over, say, Ω_{ILR} via the corresponding moment of inertia.

[5] In such a system, all orbits precess in the same direction as they revolve.

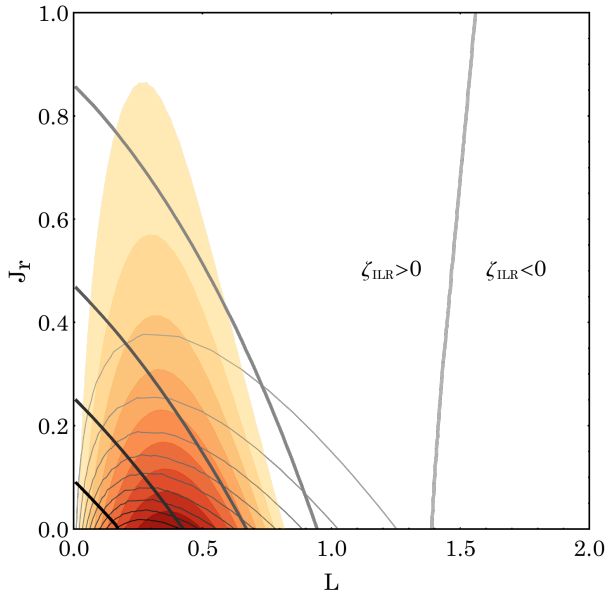

Figure 4.20: Superimposed isocontours of phase space DFs (eq. (3.121)) and cooperation parameter $\zeta_{\rm ILR}$ (eq. (4.38)) in (J_r, L) space. *Filled contours:* phase space DF of the $q = 2$ system. The coloured regions are linearly spaced from 10% (yellow) to 90% (red) of the maximum value. *Thin contours:* phase space DF of the $q = 0$ system. The contours are linearly spaced from 10% (grey) to 90% (black) of the maximum value. *Thick contours:* Cooperative parameter $\zeta_{\rm ILR}$. The contours are linearly spaced from 0% (grey) to 80% (black) of the maximum value. The large amount of radial cooperative orbits seems to be responsible for the instability of the $q = 2$ systems.

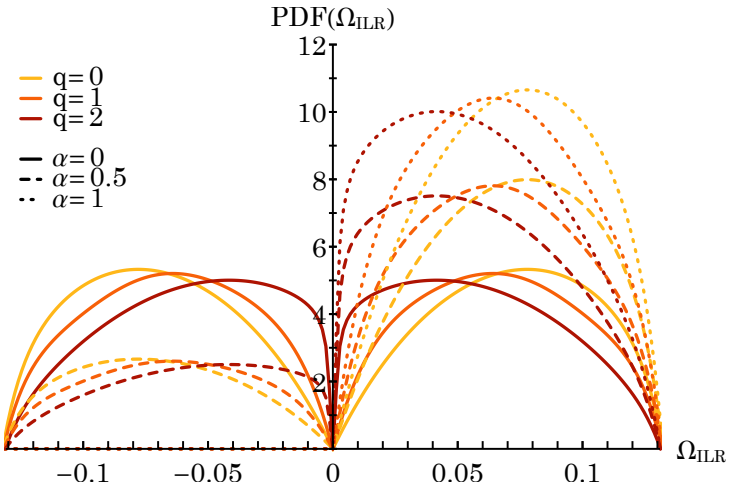

Figure 4.21: PDF of the tumbling frequency $\Omega_{\rm ILR}$ for various values of $q \geq 0$ and α. When q increases, the PDF symmetrically concentrates around $\Omega_{\rm ILR} = 0$. When α increases, some of the left hill is transferred into the right hill, concentrating the PDF around positive values of $\Omega_{\rm ILR}$. As α grows, the effective frequency PDF can become narrow enough to drive a tumbling instability.

into DF($\Omega_{\rm ILR}\,{\rm Sign}(L_z)$). Without rotation ($\alpha = 0$), the DF is symmetric, since the phase space DF is independent of L_z. In this case, increasing q concentrates the DF in the regions of low (absolute) frequency, consequently decreasing the overall spread. When $\alpha > 0$, the left bump of PDF($\Omega_{\rm ILR}$) will be multiplied by $1-\alpha$ and the right bump by $1+\alpha$. This rotation-induced tilting therefore also decreases the spread in $\Omega_{\rm ILR}$.

Increasing q increases the amount of radial and cooperating orbits, decreases the spread in precession rates, and makes the system more unstable. However, the evolution of the growth rate with α is more complicated. For $\alpha>0$, rotation provides a reservoir of rotational kinetic energy to feed possible unstable modes (Binney & Tremaine, 2008). A naive expectation would be that, as one introduces positive α the instability gets stronger and rotates more (while preserving adiabaticity), which it does on the Slow-ROI manifold. However, for $\alpha > 0.2$, the Fast-ROI pattern is spinning too fast to carry a large amount of orbits, which in turn lowers the destabilising power of this process. When the pattern speed reaches the edge of the $\Omega_{\rm ILR}$ distribution ($\alpha \simeq 0.8$ in the $q = 2$ case, where $\omega_0/m \simeq 0.11$ while $\omega_{\rm I}/m = 0.13$), no more orbits can contribute to the instability and it vanishes.

Orbital torquing between the CR and OLR, where orbits typically have negative moment of inertia, may also make the sphere unstable, if the spread in azimuthal tumbling rates is centred on a given narrow minimum (the galactic analogue of the two-stream instability in plasma physics, see Penrose, 1960). In practice, the exact condition from eq. (2.28) is more complex than Lynden-Bell's criterion since in eq. (2.20), $\widehat{\mathbf{M}}(\omega)$ involves all couplings simultaneously. The influence of these other resonances may be the reason why the growth rate and oscillation frequency of the Slow-ROI are affected when going from the first to the second line of Table 4.2.

Let me finally highlight the seemingly linear growth of the oscillation frequency with α in both the Slow- and the Fast-ROI regimes, as seen from Fig. 4.12. One may try to associate this growth with the tilting in the distribution of $\Omega_{\rm ILR}$ induced by rotation (see Fig. 4.21). However, such an explanation would fail at producing pattern speeds up to the boundary of the $\Omega_{\rm ILR}$ distribution, because the bulk of it is still located at lower values of $\Omega_{\rm ILR}$. The behaviour of the Slow-ROI around $\alpha = 0.7$ may therefore not be explained in this way. It is more likely that this linear relation is a sign of the interaction between the ILR and the tumbling resonance, as discussed in Section 4.6.1. From eq. (4.16), we know that such a linear relation between ω_0 and α is expected from a tumbling mode. Hence, a global picture of this instability may involve the tumbling resonance to fix the pattern speed of the instability, while the growth rate follows the subsequent ROI process (i.e. the clustering of elongated orbits) at that pattern speed.

In the end, my results share similarities with the predictions of Palmer. In particular, *the tumbling instability (in the sense of Palmer) and the ROI seem indeed to merge and to cooperate in a single line of instability.* Yet, these results also underline the fact that the ROI persists in the high-ω_0 regime, which reduces the region where the tumbling process dominates to nothing, because the resonance with orbits at the ILR cannot exist above the maximum of $\Omega_{\rm ILR}$. In this scenario, there is no fundamental difference between the formation processes of the Fast- and Slow-ROI. The Slow-ROI may be the second mode of the ROI, and only appears at large rotation because the first mode (the Fast-ROI) has started to decay due to a too high pattern speed. This observation is backed by the shape of the mode (see Fig. 4.13). The Slow-ROI mode has two lobes, hence one more node than the Fast-ROI mode. This is generically expected from the sub-dominant mode of a self-gravitating system (see, e.g., Toomre, 1981). It may be possible to detect the Slow-ROI mode in systems where the ROI is particularly violent, so that this second mode could be enhanced. Some studies with the response matrix already reported the detection of sub-dominant modes in radially anisotropic systems (see, e.g., Saha, 1991).

4.7 Conclusions

Since the argument by Allen et al. (1992) in favour of a tumbling instability specific to rotating spheroidal systems, studies of their linear stability have mainly relied on N-body approaches (Kuijken & Dubinski, 1994; van der Marel et al., 1997; Sellwood & Valluri, 1997; Alimi et al., 1999; Meza, 2002). Here, I revisited the stability of anisotropic, rotating stellar spheres using analytical methods, the results of which were again comforted by matching N-body simulations.

In this chapter, I first reproduced the argument from Allen et al. (1992) for the existence of a series of neutral modes related to the tumbling process, in rotating systems where it is assumed that no stars are resonating with the pattern. I then discussed the effect of resonant stars on the tumbling neutral mode, which seems less conclusive than for the neutral mode of the COI. In particular, the role of stars at the inner Lindblad resonance seems to depend on their eccentricity, which implies that the

destabilisation of the tumbling mode depends on the anisotropy in the cluster. In order to draw more definite conclusions, I therefore relied instead on the response matrix for rotating spheres, and applied it to find dynamical instabilities in a series of Plummer spheres with various degrees of anisotropy and global angular momentum. Complementary N-body simulations were also performed, which confirmed the stability results from the matrix method. Three regimes of instability were detected. On the one hand, tangentially anisotropic, rotating spheres develop relatively violent instabilities, which rotate at a fast pace (always larger than the maximum of the ILR frequency, $\Omega_{\rm ILR}$). For this regime, I presented phenomenological stability criteria in terms of the rotation (α) and anisotropy (q) parameters, and in terms of global physical quantities representing anisotropy and global angular momentum, $\langle\beta_\theta\rangle$ and $\langle L_z\rangle$. On the other hand, the radially anisotropic regime is occupied by two kinds of instabilities. At low global angular momentum, an extension of the classical ROI leads to instabilities with mild growth rates, and a pattern speed which quickly reaches the maximum of $\Omega_{\rm ILR}$ with increasing α. Due to the relatively larger pattern speed, this regime was coined Fast-ROI. At large global angular momentum, this instability is replaced by a slowly growing, slowly rotating instability, which I therefore coined Slow-ROI. I presented a unifying framework for both of these instabilities, which involves the merging of the ROI and tumbling modes. In this framework, the Fast- and Slow-ROI are the two main modes of a single process, which corresponds to the generalisation of the ROI to rotating systems. The Slow-ROI dominates at high global angular momentum, only because the tumbling mode has pushed the Fast-ROI to a rotation so fast that there are no more stars at the ILR.

Technically, my study involved a large parameter space exploration with the matrix method, with thousands of points on the (α, q) plane to build Figs. 4.13 and 4.16. The numerical improvements to the computation of the matrix I developed (see Section 2.4) proved critical.

The results of this study demonstrate that *an important part of the parameter space is occupied by unstable systems.* The unstable portion is actually larger than what Fig. 4.9 suggests. Indeed, I fixed a conservative threshold in growth rate of $\eta = 0.01$ for considering a system as unstable. This threshold allows me to consistently compare the results of the matrix method with those of N-body simulations, and to avoid a region where the Nyquist contours may have an intricate behaviour and lead to uncertain mode detections. The results of Chapter 3 indeed show that the line $\alpha = 0, q < -11$ is populated with slowly growing instabilities. Bridging the gap between both regions, it is probable that, provided that the tangential anisotropy is sufficient, the full rotating range is unstable. This particular point is confirmed in the next chapter, also with N-body simulations and the matrix method.

Let me insist on the particular role of the inner Lindblad resonance. From the pattern speed measurements in all anisotropic regimes, it seems that *the maximum of the ILR frequency* $\Omega_{\rm ILR}$ *is critical for both radial and tangential regimes of instability.* In the radial regime, I highlighted in Section 4.6 the role of $\omega_{\rm I}$ as a barrier to maintain the instability. When the oscillation frequency gets close to this value, the instability's growth rate is damped, and when $\omega > \omega_{\rm I}$, the Fast-ROI does not exist anymore. Instead, the Slow-ROI dominates, with a pattern speed still in the authorised range. In the tangential regime, $\omega_{\rm I}$ acts as a lower bound for the oscillation frequency. Indeed, all instabilities at large α develop with $\omega > \omega_{\rm I}$, and the same goes from the COI in Chapter 3. The next chapter elaborates on these instabilities, searching for the process for their destabilisation, as well as a universal stability criterion for it.

The scenario I developed in the radially anisotropic regime relies on a fusion between the ROI and the tumbling modes. As such, it seems that *there is no radially anisotropic rotating system where the tumbling process alone is at the source of a linear instability.* This fact also extends to the isotropic rotating sphere, where no instability was detected (at least at the level of the present threshold). The latter phenomenon had already been observed with numerical simulations by Meza (2002).

4.8 Prospects

Let me now highlight future works which may complement and improve the results of this chapter.

First, I discussed a particular scenario for the ROI, which does not seem to encompass all instabilities in radially anisotropic systems (Polyachenko & Shukhman, 2015). The role of the maximum of $\Omega_{\rm ILR}$ in the decay of the Fast-ROI around $\alpha = 0.7$ gives weight to a scenario for the ROI which involves stars at the ILR. I therefore developed a scenario based on the "orbital approach", which considers the ROI as the spherical counterpart of the tumbling instability in disks (Lynden-Bell, 1979). The modes I identified are indeed slow modes, i.e. modes with pattern speeds smaller than the characteristic orbital frequencies in the system. It would be interesting to investigate the behaviour of fast rotating instabilities, which may instead be due to a local Jeans process (i.e. where the dynamical pressure is directly related

to the tangential velocity dispersion), when rotation is added to the system (e.g., in the models from Polyachenko & Shukhman, 2015). The necessary material for such a study already exists: the code with which I studied the Plummer sphere can be straightforwardly adapted to the models of Polyachenko & Shukhman (2015). The detection of modes would however involve higher harmonics ℓ in the basis expansions. It is likely that net angular momentum also enhances these fast rotating instabilities, because rotation further reduces the dispersion in tangential velocities.

The rotation profiles I probed can also be made more realistic to reflect the observed kinematic diversity in data and cosmological simulations. Indeed, for now, as highlighted by the rotation curves of Fig. 4.3a, I considered clusters with a smooth rotation profile, corresponding to Lynden-Bell's demon. It would however be interesting to investigate the properties of rotating equilibria where the rotation curve is less smooth, with e.g. oscillations or counter-rotating regions. This is partly addressed in the next chapter. There, I will also investigate via analytical and numerical methods the stability of models where rotation depends on the inclination w.r.t. the equatorial plane, and the one of models with a counter-rotating core. Studying the stability of more complicated models may inform us on the fate of dips in the rotation curve, or in the anisotropy profile. This kind of irregular features may appear in star clusters, e.g. from the accretion of a small stellar cluster. Such a feature was observed in the Milky Way's stellar halo (Kafle et al., 2012; King et al., 2015), and it is still unclear whether it is transient or stable and long-lived.

This last point raises the question of the interaction of the cluster with its environment. As I mentioned earlier, it is likely that dynamical instabilities operate during large potential fluctuations, such as those of satellite accretion or important mergers. At these times, it is possible that the radial anisotropy of the main cluster increases, because the accreted body may be placed on a radially elongated orbit. If the radial anisotropy increases enough, that cluster can develop an instability. Then, the cluster's angular momentum may decrease, and its shape may change. This scenario can be explored using N-body simulations, by studying the endstates of mergers with different initial setups. Starting from a radially anisotropic cluster in a stable equilibrium, with different levels of net initial angular momentum, one can throw a small satellite at the cluster on a radially elongated orbit. If the cluster was initially rotating, it is possible that the increase in radial anisotropy will destabilise it. If the cluster was initially non-rotating, the satellite will likely be absorbed without destabilisation.

Another prospect concerns structures with significantly different potentials. In particular, nuclear star clusters are dominated by their central black hole, which strongly modifies the frequency structure of the system. As they are also fast rotators, it is important to study the linear stability of the models produced by Schwarzschild or Jeans modelling (see Section 1.2). Furthermore, a stability study of rotating structures with a central massive object may help constraining the formation scenario of NSCs. Indeed, scenarios based on the accretion of star clusters may significantly impact the shape of the NSC, which could be studied by analysing its linear response.

A similar study should be made on large DM halos, which are thought to have a cuspy central profile (Navarro et al., 1997). This particular shape also influences the system's frequency structure, and therefore the linear stability of DM halos. Since the halos are believed to be embedded in a rich cosmological environment, with which they interact a lot, DM halos are likely to explore many different dynamical states throughout their lifetime. This includes intricate kinematic features, such as anisotropy and rotation. Hence, studying the linear stability of DM halos may inform us on the subset of allowed dynamical states which they can explore, and on possible attractors within it, where DM halos find themselves with largest probability.

Finally, the scenario I propose for the destabilisation of radially anisotropic rotating spheres is based on the fusion of the tumbling and ROI modes. However, I did not give a definitive proof of this scenario, rather a plausible explanation for the accumulated data. Giving such a demonstration will likely involve further developments of the linear response theory, taking full account of the presence of two modes in the system. This treatment may proceed by considering the coupling of the tumbling and ROI modes, in a non-linear framework.

Chapter 5

Systems with multiple components

5.1 Introduction

In Chapter 4, while studying the stability of rotating, anisotropic spheres, I showed that a large part of the parameter space is occupied by unstable systems. In particular, Section 4.5.5 provided stability criteria in the different regimes of instability given by eq. (4.36), which set constraints on the global observables of the system (here, the global angular momentum and the mean anisotropy) warranting that the system is stable. Although useful in practice, these stability criteria may not represent rotating spherical systems in their full generality. Indeed, they are based on results on the stability of spheres with a given choice of potential, DF and procedure to inject rotation. In particular, I chose spheres with smooth distributions of the anisotropy and rotation in the cluster. As such, the subsequent stability criteria may be insufficient when considering systems with more complex kinematics which arise in nature and cosmological simulations. The goal of the present chapter is a first attempt at constructing generic stability criteria.

Indeed, in Section 1.1, I discussed recent observational results pointing towards systems with structure in their phase space distribution. In dark matter halos, past interaction with the environment (mergers, tidal torquing by the large scale structures) will influence their kinematics in the outskirts, whereas baryonic processes in the centre (such as stellar disc reformation) may also influence the inner kinematics independently. Similarly, depending on their past accretion history, elliptical galaxies integrate a variety of complex kinematics, such as a rotation axis misaligned with the isophotes, increasing and decreasing profiles for the velocity anisotropy (Emsellem et al., 2011), a counter-rotating centre w.r.t. the outer parts (Emsellem et al., 2007, see Fig. 5.1), or even shells with different rotation axes (Davies et al., 2001, see also Fig. 5.1). Finally, in globular clusters, astrometry shows that a single cluster can have varying flavours of anisotropy, and various rotational directions at different radii (Jindal et al., 2019). These measurements can also be matched to multiple stellar populations with different kinematics (Cordoni et al., 2020). It is therefore timely to try and exhibit stability criteria which also account for such complex features, in order to constrain their modelling.

To produce a more robust criterion, it is important to understand the physical processes leading to the destabilisation of rotating spheres. Only then will it become possible to naturally identify the most relevant observables which critically separate stable from unstable systems, with a variety in their phase space structure. In Sections 1.4, 3.2 and 4.2, I presented particular processes, namely the radial orbit (ROI), circular orbit (COI) and tumbling (TI) instabilities, which are possible candidates for sourcing instabilities in systems with given anisotropy and rotation (resp. radially anisotropic, tangentially anisotropic and rotating systems). In radially anisotropic rotating spheres, I discussed the interplay between the ROI and the TI, leading to the formation of rotating bars (see Section 4.6). The fact that the ILR and the tumbling resonances dominate over all other resonances make it possible to robustly connect the instabilities to this interplay. Understanding these physical processes lead to conclusions which go beyond the particular case of the systems probed in Section 4.5, and can also describe the stability of more complex systems. For example, the fact that the pattern speed of this instability cannot exceed $\omega_{\mathrm{I}}/2$ also applies to systems with a more complex radial anisotropy and rotation profile.

For tangentially anisotropic systems, however, I showed in Section 3.4 that the COI usually involves more resonances. Furthermore, I discussed in Section 4.2.4 the possibility that the tumbling mode gets damped in tangentially anisotropic clusters, because of its resonant interaction with quasi-circular orbits at the ILR. Yet, Section 4.5 presents a robust detection of fast growing modes in tangentially anisotropic

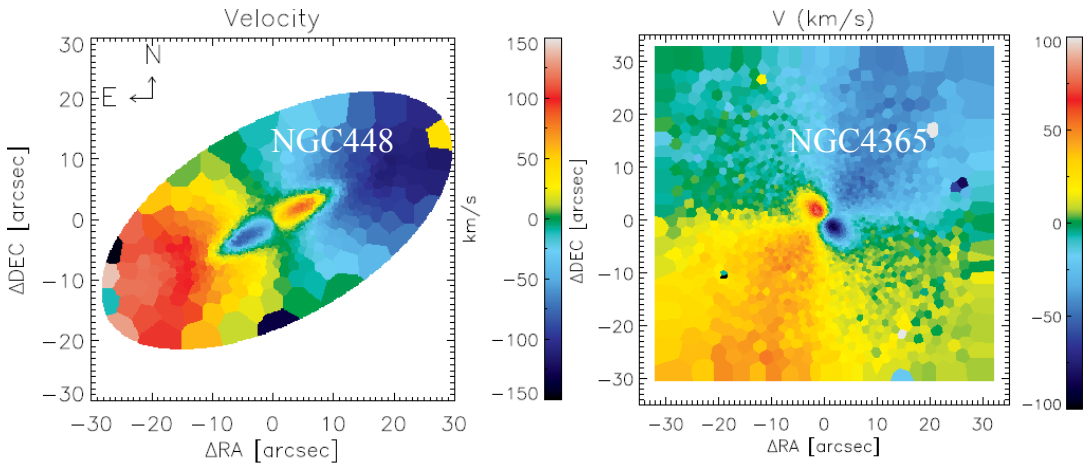

Figure 5.1: From Nedelchev et al. (2019). The line-of-sight velocity field of NGC 448 and NGC 4365 measured by MUSE. The fields of view span resp. ~ 10 kpc and ~ 6 kpc at the centre of the galaxies. Both galaxies present two kinematically distinct parts: a prograde core and a retrograde halo for NGC 448, while NGC 4365 has a core and a halo rotating around orthogonal axes.

rotating systems.

In the present chapter, I will focus on this regime, trying to identify the relevant processes leading to these instabilities. This chapter is mainly based on the results of Breen et al. (2020), which I co-authored and is being published by MNRAS. First, in Section 5.2, I will use the response matrix with a more complex injection of rotation than that studied in Section 4.5. This will allow me to measure the locations (more precisely the latitude) in the cluster where the destabilising process takes place. In order to study more precisely the role of stars at different locations in the cluster, I will then present in Section 5.3 a series of N-body simulations, focusing on the detection of linear instabilities in the form of rotating bars. Various setups for the initial conditions are designed, so that one can relate the growth rates of the instabilities with particular regions (i.e. particular radii and inclinations) in the cluster. In Section 5.4, I will develop a complementary approach, based on orbital resonances, both using the restricted matrix method, and N-body evidence for variations of the distribution of orbital frequencies in clusters where an instability is growing. From these complementary results, I will discuss a new stability criterion for tangentially anisotropic spheres with an arbitrary distribution of the global angular momentum within the system.

5.2 Matrix results with inclination-dependent rotation

Let me first focus on identifying locations in the cluster where rotation is the most important to the destabilisation of the system. In this section and the next, I will present stability measurements from the matrix method and from N-body simulations, in systems where I tune the locations where rotation is introduced. Here, I will derive the response matrix for spheres in which rotation depends on the inclination in the cluster. I will finally present the stability results of this series of models.

5.2.1 Deriving the response matrix

Equation (4.1) gives the general form of a DF for a spherical rotating system where rotation does not depend on the particular shape of the orbit (i.e. (J_r, L)). Let me spell out the response matrix for a system with the DF given by eq. (4.1), which is the generalisation of the matrix with Lynden-Bell's rotation, derived in Section 4.3.2. With that DF, eq. (2.20) becomes

$$\widehat{M}_{pq}(\alpha,\omega) = (2\pi)^3 \sum_{\mathbf{n}} \int \mathrm{d}\mathbf{J}\, \frac{\mathbf{n}\cdot\partial(F_0 + \alpha\, F_0\, g(L_z/L))/\partial \boldsymbol{J}}{\omega - \mathbf{n}\cdot\boldsymbol{\Omega}}\, \psi^{(p)*}_{\mathbf{n}}(\mathbf{J})\, \psi^{(q)}_{\mathbf{n}}(\mathbf{J}). \tag{5.1}$$

As in Section 4.3.2, the matrix can be decomposed as

$$\widehat{\mathbf{M}}(\alpha,\omega) = \widehat{\mathbf{M}}_0(\omega) + \alpha\, \widehat{\mathbf{M}}_1(\omega), \tag{5.2}$$

where $\widehat{\mathbf{M}}_0$ and $\widehat{\mathbf{M}}_1$ are defined as

$$\widehat{M}^0_{pq}(\omega) = (2\pi)^3 \sum_{\mathbf{n}} \int \mathrm{d}\mathbf{J}\, \frac{\mathbf{n}\cdot\partial F_0/\partial \mathbf{J}}{\omega - \mathbf{n}\cdot\mathbf{\Omega}(\mathbf{J})}\, \psi^{(p)*}_{\mathbf{n}}(\mathbf{J})\, \psi^{(q)}_{\mathbf{n}}(\mathbf{J}), \tag{5.3}$$

$$\widehat{M}^1_{pq}(\omega) = (2\pi)^3 \sum_{\mathbf{n}} \int \mathrm{d}\mathbf{J}\, \frac{\mathbf{n}\cdot\partial (F_0\, g(L_z/L))/\partial \mathbf{J}}{\omega - \mathbf{n}\cdot\mathbf{\Omega}(\mathbf{J})}\, \psi^{(p)*}_{\mathbf{n}}(\mathbf{J})\, \psi^{(q)}_{\mathbf{n}}(\mathbf{J}). \tag{5.4}$$

Using the DF gradient computed in eq. (4.3), $\widehat{M}^1_{pq}$ can be rewritten as

$$\widehat{M}^1_{pq}(\omega) = \delta^{m^q}_{m^p} \sum_{\tilde{\mathbf{n}}} \left\{ P^{\tilde{\mathbf{n}}}_{\ell^p n^p \ell^q n^q}(\omega)\, I^{\ell^p \ell^q}_{n_2 m^p} + Q^{\tilde{\mathbf{n}}}_{\ell^p n^p \ell^q n^q}(\omega)\, J^{\ell^p \ell^q}_{n_2 m^p} \right\}, \tag{5.5}$$

where P and Q are defined in eqs. (2.42) and (4.26), and the coefficients are now defined as

$$I^{\ell^p \ell^q}_{n_2 m^p} = (2\pi)^3\, Y^{n_2}_{\ell^p}\, Y^{n_2}_{\ell^q} \int_0^\pi \mathrm{d}i\, \sin(i)\, g(\cos(i))\, R^{\ell^p}_{n_2 m^p}(i)\, R^{\ell^q}_{n_2 m^p}(i), \tag{5.6}$$

$$\begin{aligned} J^{\ell^p \ell^q}_{n_2 m^p} = (2\pi)^3\, Y^{n_2}_{\ell^p}\, Y^{n_2}_{\ell^q} \Bigg[& - n_2 \int_0^\pi \mathrm{d}i\, \sin(i)\, \cos(i)\, g'(\cos(i))\, R^{\ell^p}_{n_2 m^p}(i)\, R^{\ell^q}_{n_2 m^p}(i) \\ & + m^p \int_0^\pi \mathrm{d}i\, \sin(i)\, g'(\cos(i))\, R^{\ell^p}_{n_2 m^p}(i)\, R^{\ell^q}_{n_2 m^p}(i) \Bigg], \end{aligned} \tag{5.7}$$

with g' the derivative of g w.r.t. its argument[1].

Using these expressions, it is now possible to study the linear stability of a sphere where the angular momentum is non-trivially distributed w.r.t. the orbits' inclinations. Let me focus on two straightforward choices for the function g, which I denote g_3 and g_4[2]. These are defined by

$$\begin{aligned} g_3(x) &= \Theta\big[x - \cos(i_3)\big] - \Theta\big[-x - \cos(i_3)\big], \\ g_4(x) &= \Theta\big[x\big] H\big[-x + \cos(i_4)\big] - \Theta\big[-x\big] H\big[x + \cos(i_4)\big], \end{aligned} \tag{5.8}$$

where Θ is the Heaviside step function. The first function g_3 is parametrised by an angle i_3, and corresponds to applying Lynden-Bell's demon only to the orbits with inclination i so that $|\frac{\pi}{2} - i| > \frac{\pi}{2} - i_3$[3], i.e. to the low-inclination orbits, which are close to the equatorial plane. The second function g_4 is parametrised by an angle i_4, and corresponds to applying Lynden-Bell's demon only to the orbits with inclination $|\pi/2 - i| < \pi/2 - i_4$, i.e. to the high-inclination orbits, which are closest to the poles. Let me normalise the angles i_3 and i_4 with the parameters $0 \leq \gamma_3 \leq 1$ and $0 \leq \gamma_4 \leq 1$, so that

$$i_3 = \frac{\pi}{2}\,\gamma_3 \quad ; \quad i_4 = \frac{\pi}{2}\,\gamma_4. \tag{5.9}$$

Figure 5.2 shows the graphs of g_3 and g_4. Both functions match all the requirements discussed in Section 4.2.1. Indeed, they are odd functions of their argument, and $\max(|g_3|) = \max(|g_4|) = 1$. Using these functions, I am now in position to investigate which inclinations of orbits are responsible for the onset of the instability.

5.2.2 Evolution of the growth rate with the size of the rotating cone

Using the numerical methods presented in Chapter 2, I first perform a stability analysis of Plummer spheres (eq. (3.119)) with the Dejonghe DF (eq. (3.121)), in a series of tangentially anisotropic clusters with inclination-dependent rotation. The results are presented in Fig. 5.3a. This figure shows the growth rate of the main $\ell = 2$ instability as a function of either γ_3 or γ_4, which control the fraction of the orbits that rotate. All computations are done for $\alpha = 1$. Therefore, in the γ_3 series, all low-inclination orbits with $|\frac{\pi}{2} - i| > \frac{\pi}{2}(1 - \gamma_3)$ rotate in the same direction, while high-inclination orbits are symmetrically distributed. When γ_3 increases, more and more inclinations are set to rotation so that for $\gamma_3 = 1$, the full cluster rotates. The picture is the opposite in the γ_4 series. All high-inclination orbits with $|\frac{\pi}{2} - i| < \frac{\pi}{2}(1 - \gamma_4)$ rotate in the same direction, while low-inclination orbits are symmetrically distributed. When γ_4 increases, the cone of rotation narrows around the poles, so that less and less inclinations are rotating. Hence, for $\gamma_4 = 0$, the full cluster rotates, while for $\gamma_4 = 1$, the cluster is non-rotating.

[1] Note that when g is replaced by Sign, one recovers the coefficients defined by eqs. (4.24) and (4.25).
[2] The subscripts 3 and 4 are chosen for consistency with Breen et al. (2020).
[3] This condition encompasses both prograde low-inclination orbits, with $i < i_3$, and retrograde ones, with $i > \pi - i_3$.

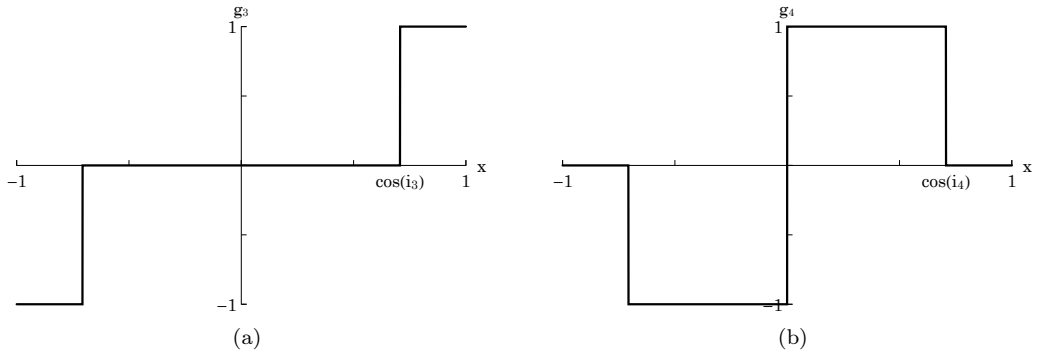

(a) (b)

Figure 5.2: Graphs of (a) $g_3(x)$ and (b) $g_4(x)$, with values of $\gamma_3 = \gamma_4 = 0.5$. Both functions are odd, and $\max(|g_3|) = \max(|g_4|) = 1$. Here, g_3 is responsible for the rotation of low-inclination orbits (i.e. high x), while g_4 makes high-inclination orbits (low x) rotate.

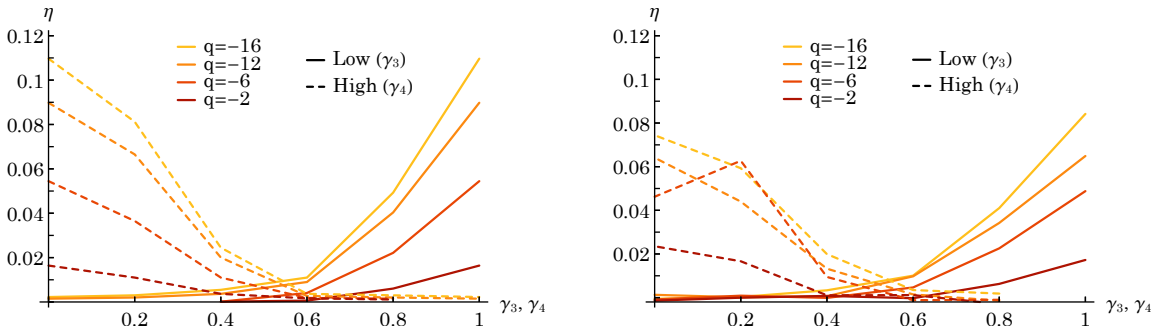

(a) Matrix results (b) N-body results

Figure 5.3: Growth rates measured with (a) the matrix method, and (b) N-body simulations, in series of Plummer spheres with different tangential anisotropies and inclination-dependent rotation. The γ_3 series has rotation in the low-inclination orbits only. Therefore, $\gamma_3 = 0$ is the non-rotating sphere, while the sphere with $\gamma_3 = 1$ fully rotates. The γ_4 series has rotation in the high-inclination orbits only. Therefore, $\gamma_4 = 0$ is the fully rotating sphere, while for $\gamma_4 = 1$, the cluster is non-rotating. Note that both methods identify similar trends of $\eta(\gamma, q)$. The small discrepancy in the amplitude may be attributed to systematic errors in the measurements.

Since the $\gamma_3 = 1$ and $\gamma_4 = 0$ cases both correspond to the same fully rotating sphere, it is no surprise that the measured growth rates are identical. As expected, in all series the growth rate is generically an increasing function of the global angular momentum in the system. Interestingly enough, it appears that the growth rate decreases as soon as a portion of the cluster does not rotate, whether it is in the polar (compare $\gamma_3 = 0.8$ with $\gamma_3 = 1$) or in the equatorial region (compare $\gamma_4 = 0.2$ with $\gamma_4 = 0$). This shows that both polar and equatorial orbits are relevant to the destabilisation process in the cluster, i.e. all inclinations plays a role. As γ_3 decreases from 1 to about 0.8, the growth rate drops by about a factor of 2, showing that stars with inclination above about 70° are very important in the instability. A complementary conclusion is drawn from the high-inclination models, whose growth rate drops by a comparable factor if γ_4 increases from 0 to about 0.3, i.e. if one excludes orbits with inclination less than about 30°. Thus *the presence of both high- and low-inclination stars is necessary for rapid growth, but neither group by itself is sufficient.*

5.3 A series of N-body simulations

In order to confirm and complement the results of the response matrix of Section 5.2, and to better identify the locations in the cluster where the destabilising processes take place, I now present N-body simulations of series of systems with complex rotation patterns. These include the clusters with inclination-dependent rotation (Section 5.3.1), and a new setup where rotation is added to parts of the cluster depending on the energy of the orbits (Section 5.3.2). This threshold energy is used here as a proxy for radius in tangentially anisotropic systems. I finally present refined numerical stability results in the slowly rotating regime, which help bridging the gap between high- and low-rotation in tangentially anisotropic clusters (Section 5.3.3).

5.3.1 Spheres with inclination-dependent rotation

The spheres with inclination-dependent rotation are generated with the initial conditions corresponding to eq. (4.1), where g is either g_3 or g_4 for the low- or high-inclination models (see eq. (5.8)). The generation of the initial conditions builds upon the one of the non-rotating DF (see Section 4.4.2), and flips the orbits according to their inclination. As in Section 4.4, the initial conditions were generated using the code `PlummerPlus`. Let me first describe the rotation curves in these models, as I am trying to analyse the destabilisation of the system w.r.t. places where the rotation is important.

There are several ways in which the rotation of these models can be measured. The first is a rotation profile, which can also be defined in different ways, e.g. in spherical or cylindrical geometry. Here, I chose to represent a cylindrical mean velocity. Note that this is not the convention I used for Fig. 4.3a, and this leads to differences in the subsequent rotation profile. The mean cylindrical velocity is easily calculated from any model by calculating the average rotation speed $\langle v_\phi \rangle(R)$ as the average azimuthal velocity in a cylindrical shell of cylindrical radius R, and a thickness of the shell chosen as a compromise between sufficient spatial resolution and sufficient statistical reliability. From an N-body simulation the corresponding quantity is easy to compute on a grid of R. The resulting rotation curves in the low- and high-inclination series are given in Fig. 5.4.

Let me first focus on the low-inclination series, i.e. the models characterised by γ_3. At small cylindrical radius this procedure greatly reduces the amount of rotation as compared to a fully rotating cluster, since most stars at small cylindrical radius must lie on high-inclination orbits. The effect at large radius is much smaller, unless the critical value γ_3 is very small. The opposite can be said of the high-inclination series described by γ_4. It is only at high γ_4 that the region of low cylindrical radius stops rotating. The effect at large radius is smaller, unless γ_4 is very high.

The simulations were integrated using the tree code `gyrfalcON` (Dehnen, 2002). From the time evolution of the simulations, I described in Section 4.4.3 how one can extract an instability's growth rate. I show the growth rates of the maximally rotating (i.e. for $\alpha = 1$) low- and high-inclination models in Fig. 5.3b.

The overall tendency of the curves, as well as their behaviour with q, are similar to the results of the matrix method (Section 5.2). The interpretation of Fig. 5.3a is therefore comforted by the simulations. One should however notice the $\sim 30\%$ difference in the amplitude of the measured growth rates between the simulations and the matrix method. This may be due to both systematic underestimate from the growth rate measurement, and systematic overestimate by the matrix method. Indeed, the overall similarities between Figs. 5.3a and 5.3b point towards systematic errors. The fact that only $\ell = 2$ terms were included in the matrix measurements may also impact the result. However, the overall agreement

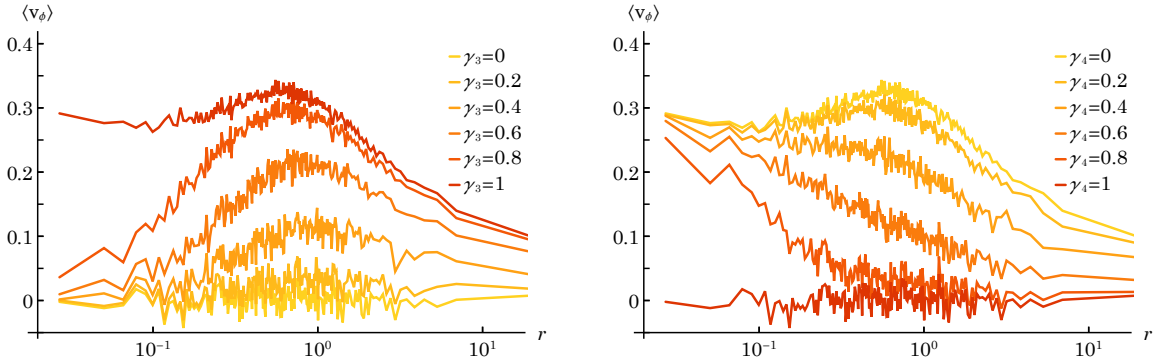

(a) Low-inclination series

(b) High-inclination series

Figure 5.4: Rotation curves of (a) six low-inclination models and (b) six high-inclination models with $q = -6, \alpha = 1$. As described in the text, Lynden-Bell's demon is applied only to low-inclination (resp. high-inclination) orbits whose inclination is less than $\gamma_3\,\pi/2$ (resp. more than $\gamma_4\,\pi/2$). The ordinate is the mean azimuthal velocity in a cylindrical shell of radius R (the abscissa). Each of the 200 shells contains 500 particles. All plots correspond to applications of Lynden-Bell's demon (with various values of γ_3, γ_4) to the same realisation of a Plummer-Dejonghe model; therefore the fluctuations in successive models are correlated.

means that there is little to no interaction with higher ℓ harmonics. Finally, the simulation at $q = -6$, $\gamma_4 = 0.2$ seems to stand out. This may be due to a particularity in the initial conditions, since we did not average over different realisations of the same model.

5.3.2 Spheres with energy-dependent rotation

Now that the impact of the inclination of the rotating orbits is characterised, let me now present a series of simulations where the rotation depends on the energy of the orbits. These are designed to study the influence on the instability of the injection of rotation in different radial shells. Indeed, in tangentially anisotropic clusters, most orbits are close to circular, hence the radius and the energy are tightly related. Two categories of initial conditions are built, with a prograde centre, and an either non-rotating (γ_1 series) or counter-rotating (γ_2 series) outer part. Studying these setups also informs us on the role of shear (i.e. large differential rotation) in the instabilities. The initial conditions are sampled as follows.

In the first series of models, Lynden-Bell's demon is applied only to a certain fraction of the mass ($0 \leq \gamma_1 \leq 1$) when the particles are ordered by energy. Thus $\gamma_1 = 0.2$ means that Lynden-Bell's demon works on the 20% most bound particles; $\gamma_1 = 0$ gives a Plummer-Dejonghe model, while when $\gamma_1 = 1$ and $\alpha = 1$, all particles are given prograde rotation. These models are intended to give insight into the range of radii which are active in the instabilities observed in them.

In the second series of models, the above procedure is applied to all particles (or rather to a fraction α of them) in the most bound fraction γ_2, but in the rest, i.e. the least bound fraction $1 - \gamma_2$ of them, Lynden-Bell's demon acts in reverse, reversing the orbit for all prograde stars (or a fraction α of them). These models are intended to maximise the shear in the rotation profile, as this may be a factor in the existence of instabilities.

Here, the stability of these models is only studied using N-body simulations. Indeed, the response matrix is not yet available for systems having an energy-dependent level of rotation. Such an extension would eventually provide a complementary tool to study sheared systems, and better span parameter space (see Section 5.6).

Note that both models represent systems where the rotation profile is strongly varying. The models with non-rotating outskirts (identified with γ_1) will be called mild-shear models. The models with counter-rotating parts (identified with γ_2) will be coined high-shear models.

Figure 5.5a illustrates various rotation curves for the set of mild-shear models. In this figure the uppermost curve shows the rotation curve of a model where Lynden-Bell's demon is applied to all stars, whereas the lowest one shows the rotation curve of the original Plummer model (anisotropy in all the models being modified by setting $q = -6$), and this slightly oscillates around zero only because the profile has been determined from an N-body model. The $\gamma_1 = 0.2$ curve, shows the result when the demon is applied only to the 20% most bound particles, affecting therefore only the most inner regions of the cluster. Other choices of α simply alter the ordinate in proportion to α. Note that the $\gamma_1 = 1$ rotation

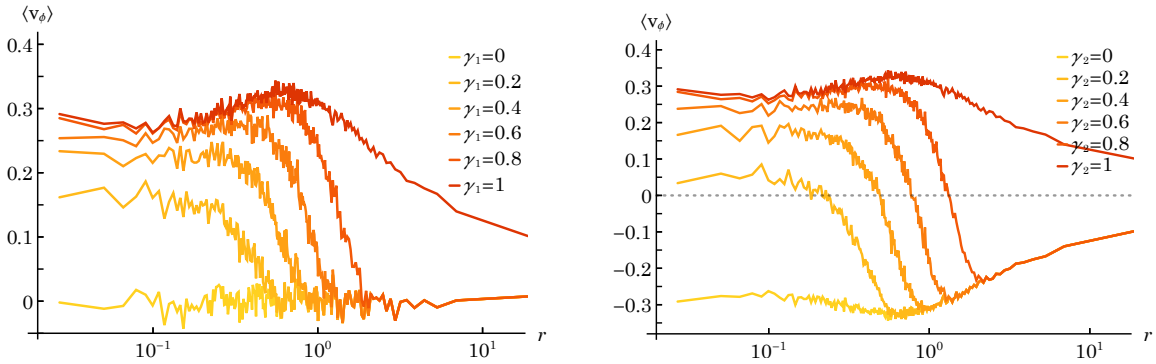

(a) Mild-shear models (b) High-shear models

Figure 5.5: Rotation curves of (a) six mild-shear models and (b) six high-shear models with $q = -6, \alpha = 1$. In (a), γ_1 is the fraction of stars, ordered by energy, below which Lynden-Bell's demon is applied. In (b), γ_2 is the fraction of stars, ordered by energy, below which Lynden-Bell's demon is applied in the sense of prograde rotation, while above that energy it is applied to give retrograde rotation.

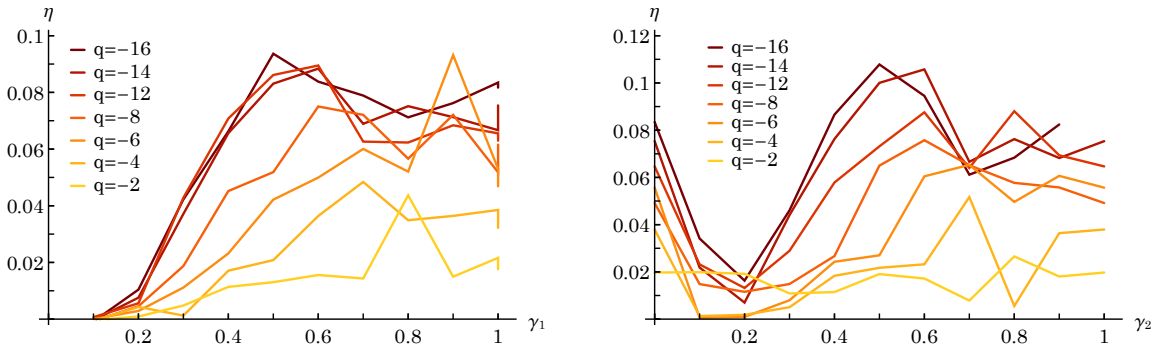

(a) Mild-shear models (b) High-shear models

Figure 5.6: (a) Growth rate for the maximally rotating model ($\alpha = 1$) at each γ_1, for several values of q. The isotropic case $q = 0$ was avoided, as I have shown (see Fig. 4.14) that if instabilities exist here, they may belong to a different family from those at smaller (more negative) values of q (i.e. to the ROI-type). The result of two independent simulations is given for $\gamma_1 = 1$, explaining the small vertical bars there. (b) Growth rate for the maximally rotating (and counter-rotating) model at each γ_2, for several values of q. For the reason stated in the text, the results for $\gamma_2 = 1$ have been duplicated for $\gamma_2 = 0$ (though new realisations would have led to slightly different results).

curve can be compared to the $(\alpha, q) = (1, -6)$ curve in Fig. 4.3a, although the average is spherical there, while it is cylindrical here.

Figure 5.5b gives similar illustrations for the high-shear (counter-rotating) models, in which γ_2 is the fraction of stars, ordered by energy, below which Lynden-Bell's demon is applied to give prograde rotation, while it is applied to the less bound stars to give counter-rotation. Qualitatively the rotation curves look very similar, but the difference between the maximum and minimum (largest retrograde) velocities are about twice as large.

Let me now present the stability results of these different models, as evaluated using N-body simulations, and analyse them w.r.t. the position of the rotating orbits. The results from the mild-shear models with maximal rotation ($\alpha = 1$) are shown in Fig. 5.6a. The growth rates of two models are given at $\gamma_1 = 1$ (hence the small vertical bars), to give an impression of the variability of the results for independent initial conditions. Even the large fluctuations (such as the maximum at $\gamma_1 = 0.8$ in the lowest curve) may be explained in terms of the choice of initial conditions, but trends in the data cannot be so discounted. The qualitative point that one may take from this plot is the fact that the growth rate does not keep increasing as the fraction γ_1 increases. Rather, the growth rate saturates when roughly the inner half of the system (ordered by energy) has been set to rotate in one sense[4]. As a result, I may conclude that the inner particles are the main contributors to the onset of the instability in these

[4]Actually there is some evidence from this figure that the saturation level is a little lower than the peak level, as one notices particularly for the most negative values of q. This could be investigated in detail using future developments of the matrix method.

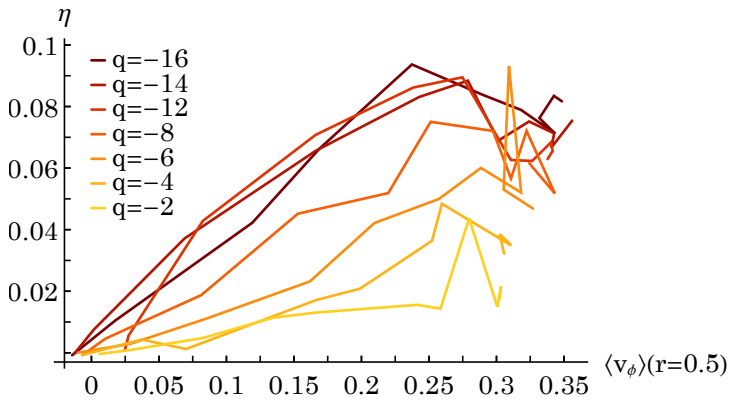

Figure 5.7: Growth rate for the maximally rotating model at each γ_1, for several values of q, plotted against the value of the rotation speed at radius $R = R_\mathrm{v}/2$.

rotating clusters.

The growth rate of maximally rotating ($\alpha = 1$), high-shear models (characterised by γ_2) is shown in Fig. 5.6b. Qualitatively the results show similarity with those for the mild-shear models. For $0.2 \leq \gamma_2 \leq 0.5$, the growth rate increases with γ_2, up to a plateau maintained over the range $\gamma_2 \geq 0.5$. Only at low γ_2 is the behaviour different from the γ_1 series (with non-rotating outskirts). Indeed, the $\gamma_2 = 0$ sphere is fully counter-rotating, hence self-consistency imposes that the growth rate there is the same as for $\gamma_2 = 1$. In order to be more quantitative, and relate these stability results to regions of the cluster, let me read these stability results together with the rotation curves of Fig. 5.5.

Looking at the mild-shear models, in particular for $\gamma_1 \geq 0.6$, the large differences in the rotation curves, which are particularly evident outside $r \sim 0.8$, make little difference to the growth rate, since they correspond to the flat part of Fig. 5.6a. By contrast, the rotation curves for $\gamma_1 = 0.2$ and 0.4 change dramatically inside $r \sim 0.8$, as do the growth rates (leftmost part of Fig. 5.6a). This, then, appears to be the region within which one must seek the mechanism for the instability, and any quantitative phenomenological model for it.

To make this discussion more quantitative, Fig. 5.7 shows how the growth rate (as plotted in Fig. 5.6a) varies with the value $\langle v_\phi \rangle (R_\mathrm{v}/2)$, where R_v is the virial radius of the Plummer sphere[5]. Note that this particular radius of $R_\mathrm{v}/2$ was chosen because it was readily available from data outputs, and very close to the region of interest. The value of $\langle v_\phi \rangle (R_\mathrm{v}/2)$ appears to be a roughly linear predictor of the growth rate, though for very negative values of q it does not predict well the saturation of the growth rate at the largest values of $\langle v_\phi \rangle (R_\mathrm{v}/2)$. Note that values at other neighbouring radii might well be equally useful, as I will illustrate in Section 5.6.

Let me now compare the maximum growth rates of the high-shear models (Fig. 5.6b) to those of the mild-shear models (Fig. 5.6a). In both γ_2 and γ_1 (resp. high- and mild-shear) series, these occur for models with smaller, i.e. more negative, values of q, and then at intermediate values of $\gamma \simeq 0.5$. One sees that these maxima are similar, say at the 10% level. This is indicative of the fact that the shear (i.e. the gradient of the rotation curve) is not by itself responsible for the destabilisation of the system. Otherwise, the high-shear models would have significantly larger growth rates than the mild-shear ones, owing to gradients about twice as large in the rotation curves (see Fig. 5.5). In the high-shear case, one notices more strongly that the maximum growth rate occurs at intermediate values of γ_2 (cf. footnote 4). Furthermore, the growth rate there is still slightly larger than in Fig. 5.6a. These remarks suggest that the maximum growth rate depends on the rotation of the outer (least bound) parts of the system. Indeed, when γ_1 is maximal, the outer parts of the cluster are non-rotating, while when γ_2 is maximal, they are counter-rotating. This shows that the growth rate of an otherwise identical system is larger when its outer parts counter-rotate. It is furthermore consistent with the behaviour of the growth rate at larger values of γ_1 and γ_2. Indeed, when γ_1 and γ_2 increase, more and more outer orbits are flipped towards prograde rotation, and this in both mild- and high-shear models. The fact that the growth rates in both setups gets slightly depleted in that region indicates that the system is more unstable when the outer parts are counter-rotating w.r.t. the centre. However, this is not a requirement for instability, as fully prograde systems are still unstable.

In Fig. 5.6b there are significant changes in the growth rate on the left, around $\gamma_2 = 0.2$, where the

[5] In the Plummer sphere, $R_\mathrm{v} \simeq 1.70 R_\mathrm{s}$.

values of η have a very pronounced minimum, increasing again as γ_2 decreases further. In fact for $\gamma_2 = 0$ the growth rates must be the same (within the error of the estimates) as for $\gamma_2 = 1$, as these two cases have the same rotation curve except for the sense of rotation.

While the previous discussion focused on the growth rate, it is also interesting to measure the pattern speed in relation to the coexistence of pro- and counter-rotation at different radii. For that purpose, let me focus on the $q = -16$ case. The model with $\gamma_2 = 0$ is completely counter-rotating (Fig. 5.5b), and the pattern speed is also negative: $\Omega_\mathrm{b} \simeq -0.32$[6]. The pattern speed reduces in magnitude to -0.23 at $\gamma_2 = 0.1$, which indicates that it corresponds to the destabilisation of the outer part of the cluster, since it rotates at a negative velocity. The pattern speed turns to about +0.32 (i.e. prograde) throughout the range $0.3 \leq \gamma_2 \leq 1$, meaning that it originates from the prograde inner part of the cluster. At $\gamma_2 = 0.2$ the instability is complicated, and no pattern speed could be measured confidently: up until $t \simeq 90$ a weak bar grows with a fast pattern speed around $\Omega_\mathrm{b} = -0.77$, but this gives way by $t \simeq 130$ to a bar with faster growth and $\Omega_\mathrm{b} \simeq -0.18$. This behaviour seems indicative of a non-linear coupling of the instabilities in the inner and outer parts of the cluster.

5.3.3 Slowly rotating clusters

The numerical results presented in the previous sections focused on the $\alpha = 1$ case, where some regions of the cluster are populated by orbits which all rotate in the same direction. Let me now present two particular numerical results at low rotation. The first one proves that clusters with $\alpha = 1$ can reasonably be taken as the most violently unstable ones of each series. The second result explores the regime of very low growth rate with a tailor-made measurement method, which allows me to bridge the gap between instabilities in non-rotating and fast-rotating tangentially anisotropic spheres.

5.3.3.1 Empirical scaling between rotation and instability

From numerical simulations of flattened stellar systems embedded in a spheroidal background, Ostriker & Peebles (1973) identified a stability criterion for stellar systems w.r.t. the formation of a bar (see Section 4.1 for further background). This stability criterion involves the mean global kinetic energy in ordered motions, T, and the gravitational potential energy of the cluster, W. The Ostriker-Peebles criterion states that a necessary condition for stability is $T/|W| < 0.14 \pm 0.02$. In a Plummer sphere, the gravitational energy is given by (Binney & Tremaine, 2008)

$$W = -\frac{3\pi G M_\mathrm{tot}^2}{32 R_\mathrm{s}}. \tag{5.10}$$

The rotational kinetic energy is computed by the following analysis. The average rotation speed on a circular ring of given R and z is defined, with, again, a suitably chosen bin size. Then the rotational kinetic energy is defined to be

$$T = \frac{1}{2}\int 2\pi R \,\mathrm{d}R \,\mathrm{d}z \,\rho(R,z)\langle v_\phi\rangle^2(R,z), \tag{5.11}$$

the integral being evaluated in practice by summing over the chosen grid. For the present purpose a fixed grid in R with 100 bins, and a grid in z adapted to contain approximately equal numbers of particles, was adopted.

Figure 5.8 shows the growth rate η as a function of the Ostriker-Peebles parameter $T/|W|$. Note that results for $\gamma_1 = 0$ are omitted, as I have shown in Section 3.4.4 that these models are stable (see Fig. 3.9 in particular). Results for $\gamma_1 = 1$ are duplicated, i.e. two independent realisations are shown for each value of α, to give an indication of the numerical uncertainty in the measured growth rate. Each colour corresponds to a given value of γ_1, and one moves to the right within a given sequence as α increases. This increase is well fitted by a cubic curve, i.e.

$$\eta(q,\gamma_1,\alpha) = \eta_0(q,\gamma_1)\left(\frac{T(q,\gamma_1,\alpha)}{|W|}\right)^3. \tag{5.12}$$

[6]Measurements reported in this paragraph were taken in a time interval around $15 < t < 46$, from the time of the clear emergence of the bar up to a time which is about half of the time when it reaches its maximum amplitude. The values are thought to be accurate to better than 10%.

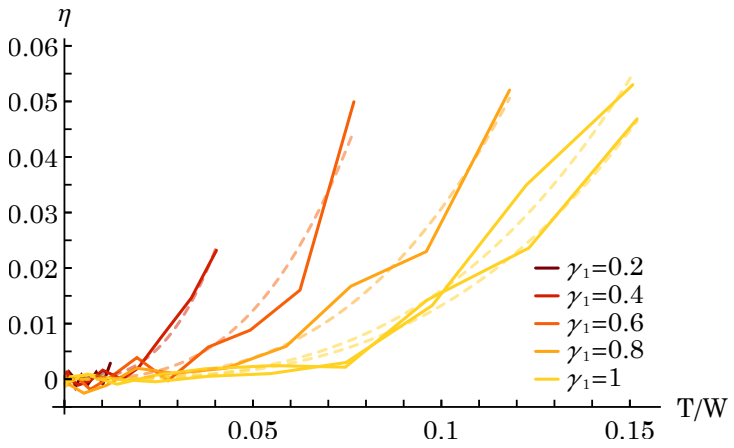

Figure 5.8: Growth rate versus Ostriker-Peebles parameter for six sets of models with $q = -6, 0 \leq \alpha \leq 1$ and various γ_1. Note that two realisations have been computed for the case $\gamma_1 = 1$, which gives an impression of the accuracy with which the growth rate has been estimated. The best cubic fit is represented with dashed curves, for each sequence.

This is a remarkably steep dependence, incidentally, being equivalent to the 6^{th} power of the rotation speed[7]. This monotonous (increasing) relation between the growth rate and the level of rotation (through either α or $T/|W|$) justifies the fact that the results in Sections 5.3.1 and 5.3.2 were systematically presented for maximal rotation, i.e. $\alpha = 1$. Results for lower α may generally be recovered by a suitable scaling.

This empirical relation has another interesting implication for the stability of slowly rotating spheres. Recall that the results of Section 4.5 gave an upper bound on the growth rate of instabilities in the regime of slowly rotating, tangentially anisotropic systems. However, since the effort was devoted to mapping the (α, q)-plane, a conservative threshold for instability of $\eta = 0.01$ was chosen, to mitigate measurement errors with both the matrix method and N-body simulations. If the scaling relation (5.12) is true, it means that the regime of slowly rotating, tangentially anisotropic clusters also sits in the unstable region of Fig. 4.9. Let me further explore this regime with a series of tailor-made simulations in the next section.

5.3.3.2 Joining slow- and fast-rotating clusters

The results that follow are based on a dedicated and distinct set of direct N-body models using `NBODY6`, with $N = 2^{15}$ particles and anisotropy parameter $q = -16$. They are fully rotating models of the type discussed and probed in Chapter 4, i.e. Lynden-Bell's demon is applied everywhere. The aim is to discuss the dependence of the complex frequency of the bar instability on the rotation parameter α, with a view to exploring the regime of low-rotation and low-growth rate, below the threshold of Fig. 4.9. Detailed discussions of the methods of analysing the runs are given in Breen et al. (2020). The resulting growth rates and pattern speeds are given in Fig. 5.9.

While detailed analyses and interpretations of this plot are given in later sections, an explanation is already required here for the fact that any pattern speed at all has been measured for the non-rotating case $\alpha = 0$. While the question of the stability of a non-rotating model with tangentially very biased velocity anisotropy is still controversial[8], no growth could be measured with confidence (the error bar on that growth rate extends to negative values). The corresponding point in Fig. 5.9 should therefore be considered as an upper limit. But the refined analysis of the $m = 2$ Fourier coefficient C_2 (see eq. (4.31)) clearly demonstrated the presence of oscillation with the stated pattern speed. Figure 5.9 therefore supports the view that the bar instability in models with $\alpha > 0$ connects continuously with the dynamical behaviour of the non-rotating model.

These results give me two important pieces of information. First, *the region of high tangential anisotropy and low rotation, which was below the growth rate threshold for the analysis of Section 4.5, seems to be filled with slowly growing instabilities.* Second, because the growth rate and more importantly the pattern speed seem to continuously evolve from $\alpha = 0$ to 1, it is probable that *the mechanism for the violent destabilisation of fast rotating, tangentially anisotropic spheres involves the same process as*

[7] Note that this scaling of the growth rate with α should not be mistaken for that of the pattern speed, which is expected to be proportional to α if the tumbling instability plays a role (see Section 4.2).

[8] As discussed in Section 3.6, because the COI has such a low growth rate in that case, N-body realisations are probably affected by secular diffusion before the mode can reach significant growth.

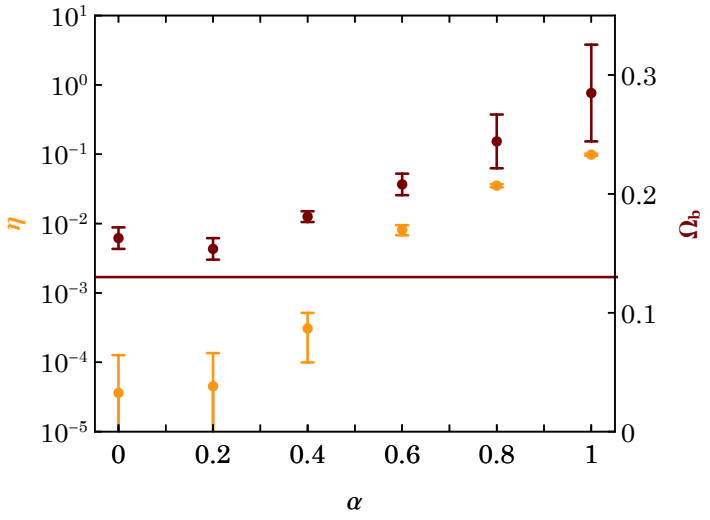

Figure 5.9: Growth rate and pattern speed of direct N-body models with $N = 2^{15}, q = -16$ for various values of α. For $\alpha = 0$ the confidence interval on the growth rate extends to negative values. Also shown, to relate these measurements to the circular orbit instability in non-rotating clusters, is the maximum of $\Omega_2 - \Omega_1/2$ for nearly circular orbits, which is the ILR frequency.

that which mildly destabilises the non-rotating sphere, i.e. the circular orbit instability. A model for the instabilities in tangentially anisotropic, fast rotators must therefore involve the COI. This leads me to consider the role of resonances in the destabilisation of rotating tangentially anisotropic systems.

5.4 Identifying destabilising processes

In order to identify the processes at the source of the instability, I now present complementary results from three types of sources, all focusing on orbital resonances. I will first derive the potential perturbation at any point in the system from a simple model of a weak rotating bar in a sphere. This derivation identifies the role of the different resonances in the orbits' perturbation, in relation to the inclination angle of the orbits. Then, I will show the results of a stability study based on restricted matrices (see Section 3.4.3), which will help me disentangle the specific role of each resonance in setting the instabilities. Finally, I will report on the evolution of the frequency distribution in an N-body unstable model, with a focus on how resonances may impact this distribution.

5.4.1 Resonances in tangentially biased systems

The role of resonances in driving bar instabilities in disks is sufficiently well known to be textbook material (e.g., Binney & Tremaine, 2008). The specific importance of corotation and Lindblad resonances is well known. However, less attention, has been paid to their role in spherical systems. In this section I focus on (very) tangentially anisotropic systems, where the radial motions are small, so that I can employ the epicyclic approximation. The main resonances can then be identified by a quite elementary calculation (Appendix C), leading to Table 5.1, which I now explain.

Let me assume there is a bar perturbation, whose pattern rotates with angular speed Ω_b. Then the familiar corotation resonance (line 2) is given by $\Omega_b = \Omega$, where Ω is the circular angular velocity. Similarly the inner and outer Lindblad resonances (ILR, line 3; OLR, line 4) are defined by $\Omega_b = \Omega \mp \kappa/2$, where κ is the epicyclic frequency. What is more unfamiliar is their inclination-dependence. What was termed *reverse* resonances would be the normal corotation and Lindblad resonances for a bar with retrograde pattern speed, as one can see from the $i \to \pi - i$ antisymmetry. Finally, I defined here the *epicyclic* and tumbling resonances, which are strongest at high inclinations (near $\pi/2$).

In a more general setting (Section 5.4.2), these resonance relations are written as $2\Omega_b = n_1\Omega_1 + n_2\Omega_2$, where n_1, n_2 are integers, Ω_1 is the frequency of radial motions, and Ω_2 is the mean longitudinal frequency,

Ω_b	i-dependence	Name	$\widetilde{\mathbf{n}} = (n_1, n_2)$
0	$\sin^2 i$	tumbling	(0,0)
Ω	$(1+\cos i)^2$	corotation	$(0, 2)$
$\Omega - \kappa/2$	$(1+\cos i)^2$	ILR	$(-1, 2)$
$\Omega + \kappa/2$	$(1+\cos i)^2$	OLR	$(1, 2)$
$\pm\kappa/2$	$\sin^2 i$	*epicyclic*	$(\pm 1, 0)$
$-\Omega$	$(1-\cos i)^2$	*reverse corotation*	$(0, -2)$
$-\Omega + \kappa/2$	$(1-\cos i)^2$	*reverse ILR*	$(1, -2)$
$-\Omega - \kappa/2$	$(1-\cos i)^2$	*reverse OLR*	$(-1, -2)$

Table 5.1: Resonances in the leading-order perturbations of epicyclic motions in a rotating spherical model. The method to obtain these dependencies is developed in Appendix C. Names which are not in common use are given in italic.

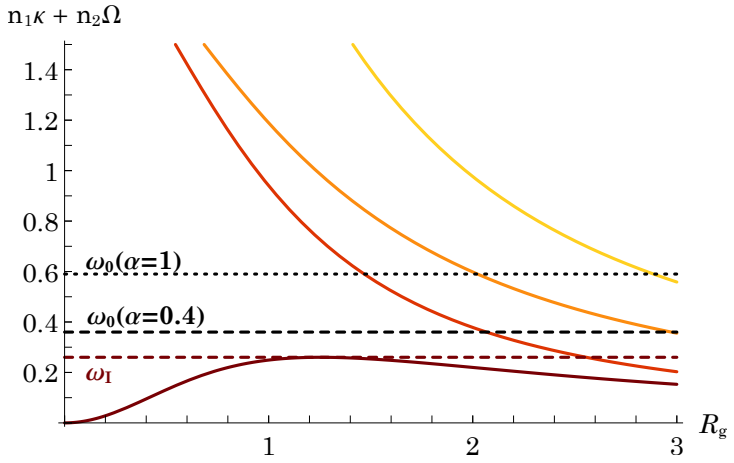

Figure 5.10: Zoomed-in version of Fig. 3.3. For combinations of epicyclic frequencies are represented, from bottom to top: ILR, ER (epicyclic resonance), CR and OLR frequencies. Also shown is the approximate oscillation frequency of the bars generated by the instability, as measured in a rotating model with $q = -16, \alpha = 0.4$ and 1. Note that, since all models of this chapter are built from the same potential, the orbital frequencies are the same.

which are equal to κ and Ω in the epicyclic approximation. These number pairs are included in the last column of the table.

Figure 5.10 reproduces the orbital resonance profiles of Fig. 3.3, with the addition of the observed oscillation frequencies (Section 5.3.3.2) found for the models with $q = -16$ and $\alpha = 0.4, 1$. Here, the anisotropy is sufficiently tangentially biased so that the epicyclic approximation is representative. The oscillation frequency of the $\alpha = 0.4$ model verifies $\omega_0 \gtrsim \omega_\mathrm{I}$, where ω_I is the maximum of $2\Omega_\mathrm{ILR} = 2\Omega - \kappa$. That of the $\alpha = 1$ model is further above.

In a later section (Section 5.4.3), I will present some evidence on the influence of resonances on the behaviour of particles in N-body models. For now, in Fig. 5.11, I simply present for one model the distribution of particles in the space of the frequencies Ω_1, Ω_2, where their proximity to the various resonances can be appreciated visually. It represents the initial conditions of a fully rotating model with $N = 2^{15}$ particles, $q = -16$ and $\alpha = 1$.

The distribution of orbits is narrow because the anisotropy is quite extreme ($q = -16$) (in the limit $q \to -\infty$ the distribution would have been one-dimensional). The inner Lindblad resonance and its reverse counterpart appear to involve no particles, but I will show (Section 5.4.2) that, somewhat counter-intuitively, the former still appears to play a central role in the dynamics. There are, however, particles lying close to the other three resonances (OLR, CR, ER), and empirical evidence for their influence is studied in Section 5.4.3. One can see immediately, however, that these particles are confined to the low-frequency part of the distribution, and this means that they affect stars at relatively large radius. With the exception of the tumbling resonance, the remaining resonances in Table 5.1 appear to play no role.

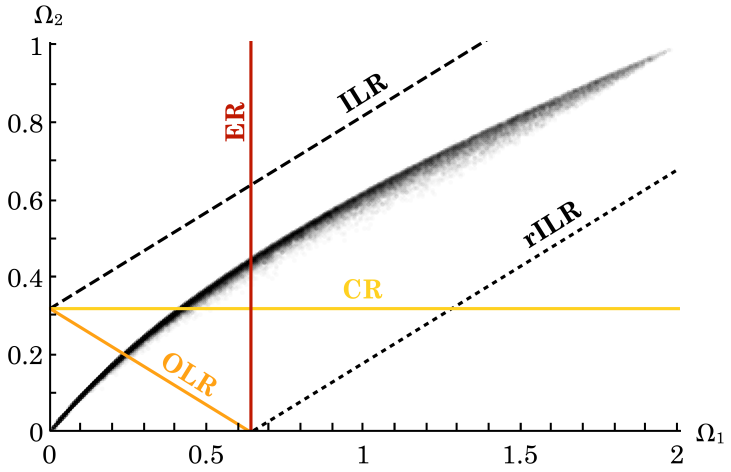

Figure 5.11: Distribution of initial frequencies Ω_1, Ω_2 in an N-body model with $N = 2^{15}, q = -16, \alpha = 1, \gamma_1 = 1$, along with the loci of four resonances (see Table 5.1). The model goes on to grow a bar (Section 5.4.3), and the pattern speed was determined in its early growth phase. This measured pattern speed was then used to trace the resonant lines. OLR/ILR: outer/inner Lindblad resonance, CR: corotation resonance, ER: epicyclic resonance, rILR: reverse ILR.

5.4.2 Identifying resonances with the restricted matrix

In Sections 3.2 and 4.2, I reproduced the arguments of Palmer et al. (1989) and Allen et al. (1992) for the existence of the circular orbit instability in tangentially anisotropic systems, and the tumbling instability in rotating systems. Using restricted matrices, where only a number of resonance vectors are kept in the angular Fourier decomposition of the perturbations, I was able to characterise instabilities found in non-rotating tangentially anisotropic systems. I confirmed in Section 3.4.3 that these clusters were indeed subject to the COI.

The purpose of this section is to reproduce a similar analysis using the restricted matrix, this time focusing on tangentially anisotropic, rotating clusters. In that case, I draw attention to the fact that a major difference between rotating and non-rotating systems emerges for $\tilde{\mathbf{n}} = (0, 0)$. The corresponding term in the response matrix (see eq. (4.26)) is directly related to the L_z-gradient of the DF, and is independent of the orbital frequencies. As I already discussed in Section 4.2.3, this resonance vector is related to the tumbling instability, as it is responsible for the existence of neutral modes, should there be no stars at any resonance with the mode. As a consequence, the reference case is now defined by the list $\mathcal{I}_0 = \{(0,0), (0,2), (-1,2), (1,0), (1,2), (-2,2), (2,0), (2,2)\}$ (see also Section 3.4.3).

The argument is similar to that used in Section 3.4.3. In order to identify which resonances are the most critical to the instabilities, I compared the results of the full matrix with results when a single resonance is removed. The importance of the removed resonance in the instability is then estimated through the change in growth rate and oscillation frequency of the instabilities found with and without the resonant term.

I focus on a frankly tangentially anisotropic system, with $q = -16$ (which was also the object of Table 3.1, in a non-rotating case), and perform the analysis on two values of α: $\alpha = 0.4$ and $\alpha = 1$. Table 5.2 shows the values of the growth rates and pattern speeds that were obtained by the restricted matrix method in these two cases, alternatively removing each of the resonant terms which are present in the matrix of reference. Notice that the values of the growth rate and pattern speed of reference are not exactly those corresponding to Rozier et al. (2019) (see also Fig. 4.9). Indeed, for the sake of numerical efficiency, I opted for fewer radial basis functions, making the mode reconstruction less accurate. However, the present reference case identifies the same instability, and I ensured the self-consistency of the present method by performing matrix calculations with constant parameters, in particular the nature and number of radial basis functions. Similarly, the slight discrepancy in the measured growth rate of the $\alpha = 0.4$ cluster between the simulations (see Fig. 5.9) and the matrix method is probably due to the relatively low number of basis functions used.

Let me first focus on the $\alpha = 0.4$ case. Some resonances have little influence on both the growth rate and on the pattern speed of the mode: removing either of $(-2, 2)$, $(2, 2)$ or $(2, 0)$ does not impact the frequencies by more than 20%[9]. Some resonances have a more significant impact on the instability

[9]These terms are actually smaller than the others by a factor of the order of the epicyclic amplitude, which is small in these tangentially anisotropic models. This can be shown by performing the development summed up in Appendix C.

$\mathcal{I}_0 \setminus \mathcal{I}$ (removed)		$\eta(\alpha = 0.4)$	$\Omega_\mathrm{b}(\alpha = 0.4)$	$\eta(\alpha = 1)$	$\Omega_\mathrm{b}(\alpha = 1)$
$\varnothing$	Reference	0.0055	0.17	0.11	0.30
$(-1, 2)$	ILR	0.0001	0.06	0.0030	0.15
$(1, 2)$		0.0037	0.15	0.040	0.28
$(0, 2)$		0.0018	0.14	0.010	0.23
$(0, 0)$	Tumbling	0.0033	0.15	0.020	0.18
$(1, 0)$		0.0020	0.17	0.09	0.30
$(-2, 2)$		0.0045	0.17	0.10	0.30
$(2, 2)$		0.0045	0.15	0.09	0.30
$(2, 0)$		0.0049	0.17	0.11	0.30

Table 5.2: Values of the growth rate and pattern speed found through the restricted response matrix method applied to the $(q, \alpha) = (-16, 0.4)$ and $(q, \alpha) = (-16, 1)$ tangentially-biased systems: comparison between the matrix of reference (complete) and the series of matrices obtained by removing a single resonance. Two particular lines are highlighted, corresponding to the removal of the ILR and the tumbling terms.

growth rate: removing a term among $\{(1, 2), (0, 2), (0, 0), (1, 0)\}$ decreases the growth rate by at least 30%, and up to 70%. The pattern speed, however, is barely impacted by the removal of any of these terms. It appears that the contribution to the instability from the resonances in these groups can be interpreted as follows: none of them has a fundamental role in the formation of the instability, however they all contribute more or less to it by increasing its growth rate. Their behaviour is therefore consistent with that of destabilising resonances in the TI and COI scenarios from Palmer (1994). They are not at the source of a mode, however their interaction with an existing one further destabilises it. This analysis does not apply to the ILR term $(-1, 2)$: when it is removed, the remaining instability has a growth rate about 50 times smaller than the reference one, while its pattern speed is decreased by about a factor of 3. This indicates that the instability identified in the absence of the ILR term is of a different nature from the one identified in all the other cases. Finally, the value of the pattern speed is above, but still close to, the maximum of Ω_ILR. This accumulated evidence shows that this instability can be attributed to the COI.

The maximally rotating, $\alpha = 1$, cluster seems to present a more subtle behaviour. One can still identify a group of resonances that have little significance to the instability: $\{(1, 0), (-2, 2), (2, 2), (2, 0)\}$. The group of resonances that influence the growth rate but not the pattern speed is now reduced to one element: the removal of the OLR term results in the depletion of the growth rate by a factor 3 and of the pattern speed by about 10%. A new category emerges: the tumbling and corotation terms are now associated to decreases of a factor resp. about 5 and 10 in the growth rate, and of resp. about 40% and 25% in the pattern speed. Finally, the ILR term is still bearing the most importance in the instability, as its removal leads to a decrease of a factor about 40 in the growth rate, and about 2 in the pattern speed.

The most important process that leads to instability seems, in both $\alpha = 0.4$ and $\alpha = 1$ cases, to emerge from the ILR term in the matrix. This is indicative of a similarity between the instabilities in both cases. However, the behaviour of the other terms changes when rotation increases: the importance of the $(-2, 2)$, $(2, 2)$, $(2, 0)$ and especially $(1, 0)$ terms is lower at higher rotation, while corotation, the OLR and the tumbling terms gain importance with rotation. The tumbling term seems to gain a particular role in setting the high pattern speed of the instability at high α.

As a consequence, the $\alpha = 1$ instability seems to have a composite nature. Some evidence points towards the COI, such as the importance of the ILR and the continuity with systems with slower rotation. However, the fact that the pattern speed is now far from the maximum of Ω_ILR makes it harder to rely on this process only. Some other evidence points towards the TI, such as the importance of the tumbling term, and the (approximate) proportionality between the pattern speed and α. However, in a tangentially anisotropic system, the role of the ILR would a priori be to damp such a tumbling mode, as discussed in Sections 3.2.3 and 4.2.4. Therefore, *it seems that a model for these instabilities should incorporate both the COI and the TI.*

It is finally worth mentioning that I have focused here on the most rapidly growing mode. For a broad range of values of large α and negative q (in models where Lynden-Bell's demon is applied everywhere), it coexists with a second mode which has smaller growth rate and pattern speed (by factors of order five and two, resp.). The ability to detect such modes is one of the major interests of using the response matrix. Indeed, detecting sub-dominant modes in an N-body simulations can be very hard, and sometimes nearly

impossible. This is due to the fact that the main mode quickly modifies the structure of the system, so that the initial potential is never maintained for long enough to allow for the growth of sub-dominant modes. One can try to artificially excite such sub-dominant instabilities in the initial conditions, however this may only work in a system where the growth rate of the second mode is not too small w.r.t. that of the main mode. The existence of several modes in the present clusters is consistent with the series of modes produced by both the COI and the TI (see Sections 3.2.2.3 and 4.2.3).

5.4.3 Resonances within an N-body model

Let me finally return to N-body modelling to examine evidence for resonant behaviour. In particular, I will discuss direct N-body simulations of basic models with $\gamma_1 = 1$ (i.e. Lynden-Bell's demon is applied everywhere), especially the case of extreme tangential anisotropy ($q = -16$) and maximal rotation ($\alpha = 1$). A simulation with $N = 2^{15}$ particles was integrated. This model exhibits a rapidly growing bar which reaches maximum amplitude at about $t = 66$, but its growth is clearly nonlinear by $t = 33$. During this shorter interval the pattern speed Ω_b decreases from 0.33 to 0.27.

The initial conditions and relevant resonances are shown in Fig. 5.11, and Fig. 5.12 shows the evolution of the distribution of the azimuthal frequency Ω_2 during the period of roughly linear behaviour ($t < 33$). In most cases it is difficult to distinguish features from sampling fluctuations, but in view of the large numbers of particles per bin (Poisson fluctuations are of order 2% in the highest bins), it is hard to dispute that there is a significant ridge around $\Omega_2 = 0.3$ and an equally significant groove around 0.48. It is tempting to link the first of these with corotation. Again tentatively, the second could be associated with the "epicyclic" resonance. Indeed, in Fig. 5.11 the corresponding line crosses the upper margin of the distribution of points, where they are concentrated, at a frequency $\Omega_2 \simeq 0.41$. Actually, this resonant frequency is somewhat too small, as shown by the shift between the groove and the grey rectangle marked ER. In this respect a better interpretation is offered by considering the ILR, the importance of which has already been established in Section 5.4.2. It is found that Ω_ILR reaches its maximum value at a radius where $\Omega_2 = 0.49$ (see Fig. 5.10). It may be surprising to see the ILR play a role here, because, as shown by Fig. 5.11, the particles are relatively far from that resonance. However, Section 5.3.3.2 showed that there is a continuity between the COI (in non-rotating systems) and the instabilities in fast rotators, so that the latter should also involve the ILR. Furthermore, the results of Section 5.4.2 show that it is fundamental to the instability, even though there are no resonant stars at the ILR. Its importance is emphasised again in Section 5.5. The epicyclic resonance, however, is closer to a smaller groove around $\Omega_2 = 0.39$, and may therefore be related to it.

Another ridge at a lower frequency, about $\Omega_2 = 0.18$, could very well correspond to the outer Lindblad resonance, as can be seen from Fig. 5.11. Other features at high frequency, if regarded as significant, correspond to none of the resonances listed in Table 5.1.

It is worth examining the distribution of the stars which contribute most to the evolution of the distribution of Ω_2. In this fully rotating system, the orbits were therefore subdivided w.r.t. the inclination of their orbital plane. Figure 5.13 shows two plots, corresponding to low and high inclination. The red curve, for instance, shows the change from $t = 0$ to $t = 33$ in the number of particles in a bin (centred at the indicated values of Ω_2), counting only the orbits of inclination $i < 60°$ or $i > 120°$. The bin size is half that of Fig. 5.12, and therefore the sum for both curves over two adjacent bins gives the total change which can be inferred from Fig. 5.11. In the features at $\Omega_2 \simeq 0.18$ and 0.3 the change is predominantly due to particles of low inclination, but the opposite is true of the feature at $\Omega_2 \simeq 0.5$. Bearing in mind the inclination-dependence noted in Table 5.1, these results lend weight to the interpretations as behaviour at the OLR, CR and ER, resp.. Indeed, the results from Table 5.1 favour a larger interaction at the OLR and the CR from low-inclination orbits, while interaction at the ER is larger for high-inclination orbits.

The interpretation that the groove around $\omega_2 = 0.45$ could be related to the ER is contradictory with it being closer to the maximum of Ω_ILR. As I will discuss later, this groove, as well as other features at larger frequencies, may be impacted by the tumbling resonance, which has a larger impact on high-inclination orbits.

What has been learned from studying the evolution of the distribution of Ω_2 can also be attempted with the distribution of Ω_1, in connection to the epicyclic resonance. This would, in all generality, give us extra information on the resonant processes at play, by giving the possibility to combine these frequencies into any kind of resonance (this analysis results in frequency mapping, see, e.g., Valluri & Merritt, 1998). However, a tangentially anisotropic system is essentially described by a single degree of freedom, which is either one or the other of the two resonances. This can be seen, e.g., in the narrowness of the distribution of the two basic frequencies in Fig. 5.11, or in the fact that resonances of epicyclic

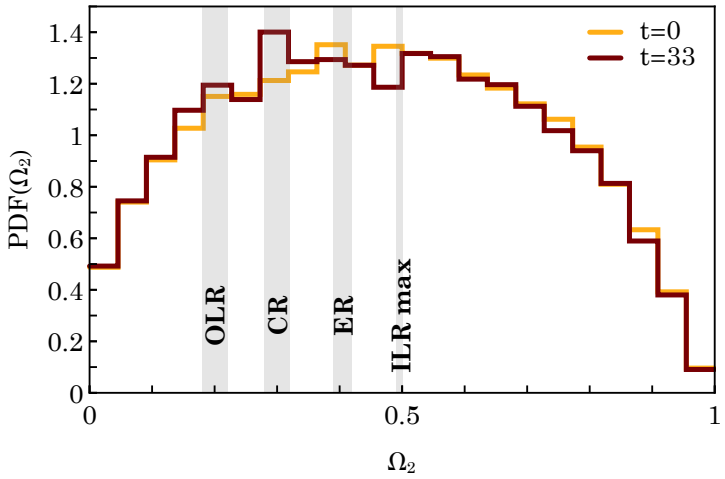

Figure 5.12: Evolution of the distribution of Ω_2 during the early growth of a bar in an N-body model with $N = 2^{15}$ particles, $q = -16$ and $\alpha = 1$. The orange line represents the initial distribution, the red one is measured by the end of the bar's linear growth. The grey rectangle marked CR shows the variation of Ω_b (which decreases slightly) during the same interval of time. The other rectangles show the ranges of the epicyclic (ER) and outer Lindblad (OLR) resonances. For those resonances the breadth of frequencies is mainly due to the width of the distribution of frequencies in the initial conditions (Fig. 5.11). The position of the maximum of Ω_{ILR} is also marked (ILR max), and depends neither on the pattern speed nor on the distribution of orbits. It seems that the grooves and ridges in the Ω_2 distribution can be related to the main characteristic resonances of the system and of the bar. The ER and maximum of Ω_{ILR} seem related to the formation of grooves, while the CR and the OLR seem related to the formation of ridges.

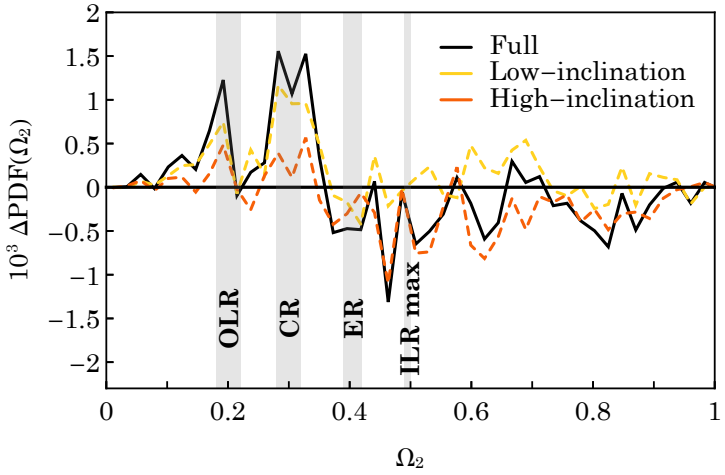

Figure 5.13: Change in the distribution of Ω_2 between $t = 0$ and $t = 33$, given separately for particles of high ($120° > i > 60°$; orange) and low inclination (yellow); the thick black line gives the sum, i.e. all inclinations. The grey rectangles have the same meaning as in Fig. 5.12. The binwidth is half that of Fig. 5.12.

orbits are functions of the sole guiding radius (see Fig. 5.10). The fact that the distribution of Ω_2 can give insight on the distribution of other resonances is already a consequence of that property. Still, the distribution is not infinitely thin, and studying the second degree of freedom may indeed contain some information. However, the variation in the pattern speed from simulation to simulation, and over the course of a single simulation, both blur the identification of single resonances. It is likely that these issues definitively forbid the existence of extra information in other resonances' distributions. Such an investigation is therefore not presented here.

5.5 Relating empirical evidence to destabilisation processes

In the previous sections, I presented complementary evidence from both N-body simulations and the matrix method, which relate instabilities to resonances and regions within the cluster. Let me now discuss these results together, in the framework of the destabilisation processes presented in the previous chapters. Let me first recall the main characteristics awaited from circular orbit and tumbling modes, and then propose a discussion of the empirical results, in order to identify a destabilisation process in tangentially anisotropic, rotating spheres.

5.5.1 A theoretical framework for bar formation

The previous sections presented a diversity of empirical information on bar formation in a tangentially anisotropic, rotating spherical system. To tie everything together, let me refer to the destabilising processes of Chapters 3 and 4, namely the circular orbit and the tumbling instability, which may both be relevant in tangentially anisotropic, rotating systems. First, I recall the main characteristics for these processes expected from the derivations of Palmer et al. (1989) and Palmer (1994), which I reproduced in Sections 3.2 and 4.2.

For the circular orbit process, the characteristics of the instability are the following:

- The ILR is at the source of the neutral mode, hence it is the fundamental cause of the instability.
- The mode rotates at a pattern speed larger than (but close to) the maximum value of the ILR frequency, defined by
$$\Omega_{\mathrm{ILR}} = \Omega - \frac{1}{2}\kappa. \tag{5.13}$$
Figure 5.10 shows this frequency in the present clusters as a function of radius.
- Destabilisation is ensured by other resonances, at the oscillation frequency of the mode.

A similar list of characteristics can be given for the tumbling instability:

- The tumbling process (corresponding to the $(0,0)$ resonance vector) is at the source of the neutral mode.
- The pattern speed is nearly proportional to the rotation parameter α. This is given by eq. (4.16). Note that the amplitude of this proportionality is a priori unknown, and was discussed in Section 4.2.3.
- Destabilisation is ensured by other resonances, at the oscillation frequency of the mode[10].

Before discussing empirical evidence on the mechanisms of bar formation, let me mention here one factor which supports the framework of the above theory: the presence of a second mode (as discussed in the last paragraph of Section 5.4.2). Both destabilisation processes produce a series of neutral modes, and the second mode detected with the matrix method could be an instance of one of these series.

[10] I assume here that the mode is destabilised, in order to describe the process. I already discussed the possible stabilising influence of other resonances, the ILR in particular.

5.5.2 The role of tumbling and resonances: empirical evidence

The series of experiments using the restricted matrix method that I reported in Section 5.4.2 helps in associating the instabilities I found in N-body experiments (mainly in Section 5.3) with the processes of tumbling and circular orbit instability. I will begin with the matrix results, and then I will move on to an interpretation of the N-body data.

The $(q, \alpha) = (-16, 0.4)$ case is particularly enlightening. It is obvious (from Table 5.2) that the instability mostly depends on the ILR. Indeed, the pattern speed of the mode lies just above the maximum of $\Omega_{\rm ILR}$ (see Fig. 5.10). In addition, the role of other resonances seems to be to increase the growth rate. These three characteristics were already found in the non-rotating cluster (see Section 3.4.3), and allowed me to identify the COI. The $(q, \alpha) = (-16, 1)$ case seems to follow a similar trend, yet less nicely matching the characteristics of the COI. It appears that the ILR term still bears most of the instability. Yet, the pattern speed is now twice as high as the maximum of $\Omega_{\rm ILR}$. Furthermore, some other terms play an important role, in particular that associated with the tumbling process.

In contrast with the conclusions of Allen et al. (1992), it seems that *the instabilities in the present tangentially anisotropic, rotating systems cannot be attributed to the tumbling instability alone.* Perhaps the high values of the pattern speed and the growth rate may diminish the accuracy of their perturbative approach. The question of the destabilisation of the neutral mode by resonant interactions should also be raised, as was already discussed in Section 4.2.4. The results of Table 5.2 rather point to a mixing of the circular orbit and the tumbling processes, the ILR still being the most important resonance to ensure the system's destabilisation. This indicates a similar role played by rotation in tangentially anisotropic clusters as in radially anisotropic ones (see the scenario of Section 4.6). *The fact that the system rotates does not create an instability, but rather enhances the destabilisation of anisotropic systems.*

It may however appear paradoxical to assert that the ILR is central to the observed instabilities, when Fig. 5.11 shows that particles in the models lie so far from that resonance. However, the restricted matrix method (Table 5.2) shows that, even if the pattern speed is far away from any value $\Omega_{\rm ILR}$ can take in the system (more than twice its maximum value), the ILR is fundamental to the development of the instability in the system. Furthermore, there are also indications in the N-body models that the ILR is playing a vital role. Indeed, the frequency measurements presented in Figs. 5.12 and 5.13 show strong activity in particles for which $\Omega_2 \lesssim 0.48$, which corresponds closely to the value of Ω_2 at which $\Omega_{\rm ILR}$ takes its maximum value ($\Omega_{\rm ILR} = 0.13$). Finally on this point, I recall Fig. 5.9, which illustrates the "floor" reached by the pattern speed as the rotation parameter α decreases. Indeed, this floor is near the maximum of $\Omega_{\rm ILR}$, as expected in the composite scenario outlined in the previous paragraph. The explanation for the shift between the maximum of $\Omega_{\rm ILR}$ and the measured pattern speed can also be found in the somewhat abusive denomination of "resonance" in a system where the growth rate is non-vanishing. Indeed, as highlighted by Jalali & Hunter (2005), exact resonances can only occur if the (complex) frequency is *equal* to the orbital frequency, and therefore ω must be real. If the instability grows, then the integral term corresponding to a combination of frequencies should rather be viewed as a certain Fourier component in the angular decomposition of the system's response. Formally, the growth rate blurs resonances when it becomes significant, and allows for apparent interaction far from resonance.

In Fig. 5.13, it appears that the inner region, corresponding to high frequency $\Omega_2 > 0.5$, also undergoes variations in the Ω_2 distribution, in particular among high-inclination orbits. Yet, in this region, the orbits do not resonate with the pattern at any of the usual low order resonances. Therefore, I interpret the activity here as being due to the tumbling process, because of its inclination-dependence. Table 5.1 indeed shows that the tumbling resonance is amplified at high inclination. This feature may also impact the groove at the maximum of $\Omega_{\rm ILR}$. As I have noticed, interaction at the ILR should mostly affect low-inclination orbits, while that groove is mostly visible in high-inclination ones. It is therefore possible that this groove is composite, corresponding to an interaction between apsidal precession and tumbling of high-inclination orbits.

The results of Section 5.3.2 show the importance of the inner orbits. From the high-shear models, flipping the orbits at $R < 0.7$ is enough to nearly suppress the instability. Conversely, building a larger and larger rotating core of radius $0.7 < R < 1.3$ increases the growth rate of the instability in the inner system up to its maximum value. By contrast, the results of these two sections also show that what happens at larger radii ($R > 1.3$, say) hardly matters. This region may rotate, counter-rotate, or not rotate at all, leaving the unstable mode mostly unaffected. The importance of the most central orbits is also supported by the shapes of the modes, as shown by Fig. 4.16. The modes seem indeed to be confined to the inner part of the cluster, since by about $R = 0.75$, the density has dropped to 10% of its maximum value. All this evidence supports the view that *the tumbling process, while not dominant in*

the generation of instability, is an important component of the mechanism which creates it.

It should be noted that the foregoing discussion refers to the cylindrical radius R. For high-inclination orbits, such as those most affected by the tumbling and epicyclic resonances, the spherical radius is significantly larger. Still, Fig. 5.13 shows that there is also some activity in the low inclination orbits in the inner region.

Low inclination orbits have a particularly important role in the regions of the OLR and corotation (around $\Omega_2 = 0.18$ and 0.3, resp.); these are orbits at relatively large radius. The matrix results however show that the role of these resonances is less important than those of the tumbling or the ILR. This is consistent with the stability results of Section 5.2.2: both high and low inclination orbits matter, but the high inclination ones are more important than the low inclination ones.

A final factor which hints at the significance of the tumbling resonance at high α is the theoretical result that the pattern speed of the relevant neutral mode is proportional to α. This suggests an explanation for the rising pattern speed for $\alpha \gtrsim 0.5$ in Fig. 5.9. However, this could not continue for small α, as then the damping effect of the ILR would come into play (see Section 4.2.4). It is interesting to note also, from Table 5.2 in the case $\alpha = 1$, that removal of the $(0, 0)$ term reduces Ω_b to a value quite similar to the reference result for the case $\alpha = 0.4$ which, I have argued, is constrained by the maximum of Ω_ILR.

To sum up, the present investigation points to the following scenario for the formation of instabilities in tangentially anisotropic, rotating systems. In the inner region of the cluster, the tumbling of orbital planes (especially for high-inclination orbits) and the drift in apsidal precession far from ILR (COI process) cooperate for the formation of an unstable bar. The growth rate of this pattern is enhanced by resonances with outer orbits at the epicyclic resonance and (most noticeably) the corotation and the OLR, in particular with the low-inclination orbits. Thus there is a kind of cross talk between all the resonances, which diminishes high-inclination orbits in the inner regions, and enhances those of low inclination at larger radii.

5.6 Going beyond the Ostriker-Peebles criterion

The discussion of the previous section highlights the fact that rotation in the central part of the cluster is decisive for the formation of fast-growing instabilities. This characteristic is important for the derivation of a new stability criterion for tangentially anisotropic, rotating systems. Let me therefore present a heuristic empirical attempt to complement the existing Ostriker-Peebles criterion with this piece of evidence.

5.6.1 General results

Using the N-body results of Section 5.3, the entire dataset of the mild-shear series (all values of $q \leq 0, \alpha$ and γ_1) can be aggregated in Fig. 5.14 through the following procedure. The axes correspond to the Ostriker-Peebles stability parameter $T/|W|$ (see eqs. (5.10) and (5.11)) and the azimuthal streaming speed at the virial radius $R_\mathrm{v} = 1.7R_\mathrm{s}$. Both the size and the colour of the symbol encode the growth rate of the bar. The region of the diagram containing the fastest growth rate is particularly interesting. Although the classical Ostriker-Peebles criterion (for *flattened* systems) $T/|W| \gtrsim 0.14$ corresponds rather well with the boundary of this region when $\langle v_\phi \rangle (R_\mathrm{v})$ is large, strongly unstable models are now present when $T/|W|$ is much smaller, provided that $\langle v_\phi \rangle (R_\mathrm{v})$ is small. These are models in which γ_1 is sufficiently small (i.e. only the most bound regions rotate) that the azimuthal speed has dropped almost to zero by the virial radius (cf. Fig. 5.5a). In fact the obvious, roughly horizontal groupings in this diagram correspond to the two or three highest values of γ_1 included in the numerical survey.

Figure 5.15a shows all results for the high-shear models (γ_2 series, with counter-rotating outskirts), except that now the ordinate is the absolute value of $\langle v_\phi \rangle (R_\mathrm{v})$. The result is qualitatively similar to that for the prograde models, but more noticeable here is the fact that there are some very rapidly rotating models (high $T/|W|$ and $|\langle v_\phi \rangle (R_\mathrm{v})|$) with relatively low growth rates. Let me now investigate the rotation curves of such models to try to identify distinctive features of their rotation curves.

In fact the models with low growth rate, high $T/|W|$ and high $|\langle v_\phi \rangle (R_\mathrm{v})|$ tend to have small (very negative) q and $\gamma_2 \sim 0.2$. Such models are also very distinctive in Fig. 5.6b, as discussed above. What distinguishes the rotation curve for these models, as can be seen in Fig. 5.5a, is that the interior radii of a $\gamma_2 = 0.2$ model are hardly rotating, at least by comparison with radii above about 0.85. This is therefore consistent with a correlation between the growth rate and the rotation velocity in the inner parts, as discussed in Section 5.5. Therefore, to separate such models better than in Fig. 5.15a, the abscissa is

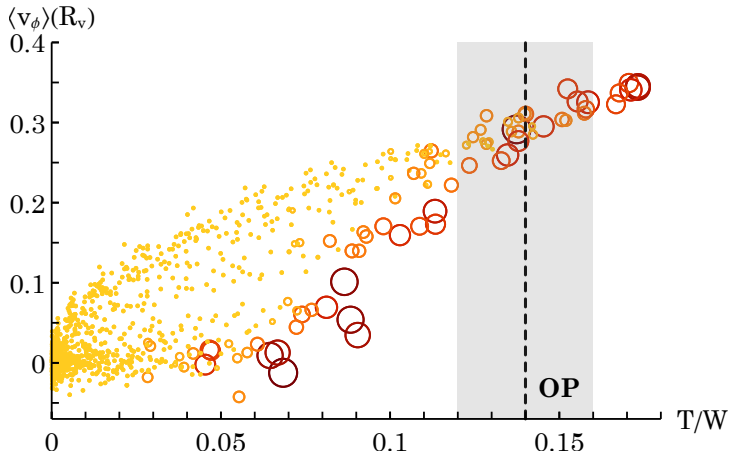

Figure 5.14: Scatterplot of all N-body results of the mild-shear series in the plane of $T/|W|, \langle v_\phi \rangle (R_\mathrm{v})$, i.e. the Ostriker-Peebles parameter and the azimuthal speed at the virial radius. The growth rate is coded in the size (as well as the colour) of the plotted points; the smallest symbols indicate growth rates less than 0.025. The vertical dashed line indicates the Ostriker-Peebles (OP) criterion, with the uncertainty represented as the grey rectangle. Clearly, this criterion does not separate well the stable and unstable configurations.

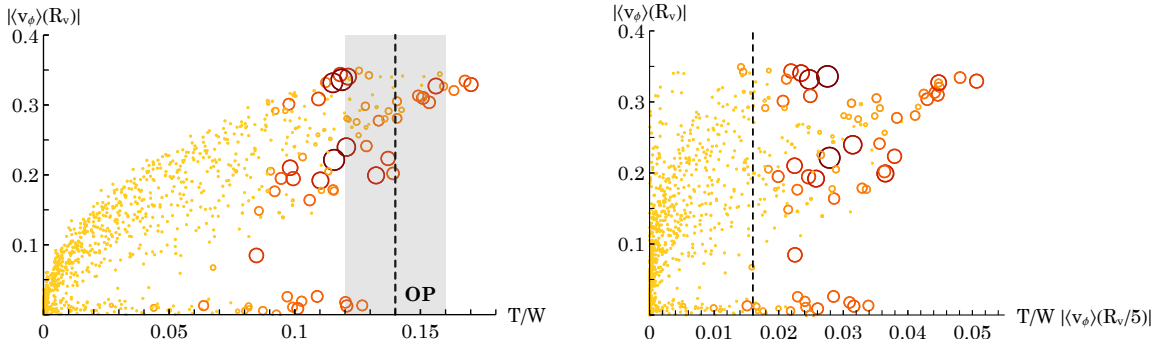

(a) Classical criterion $T/|W|$

(b) New criterion $T/|W|\,|\langle v_\phi \rangle (R_\mathrm{v}/5)|$

Figure 5.15: Scatterplots of all N-body results on models with high shear. (a) Plot in the plane of $T/|W|, |\langle v_\phi \rangle (R_\mathrm{v})|$, i.e. the Ostriker-Peebles parameter and the *absolute value* of azimuthal speed at the virial radius. (b) Same plot, but with $T/|W|\,|\langle v_\phi \rangle (R_\mathrm{v}/5)|$ in abscissa. The growth rate is coded in the size and colour of the plotted points; the smallest symbols indicate growth rates less than 0.025. In (a), the vertical dashed line indicates the Ostriker-Peebles (OP) criterion, with the uncertainty represented as the grey rectangle. Again, this criterion does not separate well the stable and unstable configurations. In (b), there is a clearer vertical separation between fast growing instabilities and systems below the threshold. The vertical line at $T/|W|\,|\langle v_\phi \rangle (R_\mathrm{v}/5)| = 0.016$ indicates where a better criterion could be placed. Note that this study did not exclude instability in any of the smallest dots.

simply multiplied by $|\langle v_\phi \rangle (R_\mathrm{v}/5)|$, where $R_\mathrm{v}/5 = 0.34 R_\mathrm{s}$ was among the easily accessible data in the simulations' outputs. The result is shown in Fig. 5.15b. There is now a better separation of slowly and rapidly growing modes, and this choice of parameters has comparable success in the mild-shear models. A stability criterion for this large series of models is therefore given by

$$\boxed{\frac{T}{|W|}\left|\langle v_\phi \rangle \left(0.2 R_\mathrm{v}\right)\right| = 0.016 \sqrt{\frac{G\,M_\mathrm{tot}}{R_\mathrm{s}}}.} \tag{5.14}$$

These results confirm the finding of Section 5.5 that the kinematics of the region inside $R \simeq 0.8$ is of particular importance for the presence of instability. They also confirm that a finer stability criterion is obtained by including in the criterion the rotation velocity in the inner parts of the cluster.

5.6.2 Towards a general stability criterion

In their classic study, Ostriker & Peebles (1973) stated that disks become "approximately stable" when $T/|W|$ falls to a value of 0.14 ± 0.02. The wording shows just how difficult it is to establish stability through numerical methods, and the same problem arises in the present work. Furthermore, the emphasis in their work was on disks (with or without halos), whereas here, I mainly focused on spherical models which rotate globally. Nevertheless, let me take the Ostriker-Peebles criterion as a starting point in this discussion.

Figures 5.14, 5.15a and 5.15b summarise the results of the mild- and high-shear numerical surveys, placing them in the space of growth rate, $T/|W|$ and peculiar circular velocities in the cluster. Even if there seems to be a trend towards more rapid instability with increasing $T/|W|$, an important fraction of the parameter space does not satisfy the Ostriker-Peebles criterion. These results simply add to the number of published deviations from this law (e.g., see Zang & Hohl, 1978; Berman & Mark, 1979; Aoki et al., 1979; Efstathiou et al., 1982; Evans & Read, 1998b; Athanassoula, 2008), and yet are among the few that exhibit such deviations in purely spherical clusters.

As a consequence, it appears that the linear stability of spherical systems cannot be uniquely determined by the ratio between global kinetic energy in rotating motion and global gravitational potential energy. First, the simulations of clusters with counter-rotating components (high-shear models) display the presence of fast growing instabilities in clusters with arbitrarily low global angular momentum (when the angular momentum of the inner prograde and outer retrograde parts of the cluster compensate). Second, there is evidence of unstable behaviour in purely *non-rotating*, tangentially anisotropic clusters under the effect of the circular orbit instability. The results of Chapter 3, based on the matrix method, are indeed complemented by a careful numerical analysis of the non-rotating cluster ($\alpha = 0$) in Fig. 5.9. A consequence of this finding is that sufficiently tangentially anisotropic clusters seem to display an unstable behaviour, *whatever their degree of rotation or shear*.

An important reservation should be made at this point, concerning the presence of instabilities with low growth rates. On the one hand, in terms of measurements by analytical means (i.e. the response matrix in the present case), recall that the behaviour of the analytical indicators at low growth rate gets very intricate (see, e.g., Merritt, 1999; Rozier et al., 2019), which makes it complicated to measure growth rates accurately. On the other hand, the measurement of slowly growing instabilities in numerical simulations also presents a number of technical difficulties. In particular, measuring the growth of very weak instabilities above the background noise requires sufficient integration time and number of particles, and in N-body simulations as well as in actual physical systems, the time scale required for the growth of such instabilities can overlap with the secular time scale of two-body relaxation in the cluster. As a consequence, one might miss the growth of an instability, because the system has already secularly evolved to another quasi-stable configuration.

Yet, even if I only focus on reasonably large growth rates (say $\eta > 0.025$), the results of Fig. 5.15a show that the stability of spherical clusters has at least one additional degree of freedom compared to the single one used in Ostriker & Peebles (1973). As discussed in Section 5.5.2, rotation in the innermost part of the cluster seems to have a critical influence on the increase in growth rate, compared to the non-rotating case. Figure 5.15b shows that a combination of $T/|W|$ and the mean azimuthal velocity at $R = 0.34$ makes a better stability criterion than the original $T/|W|$, even if the separation between stable and unstable systems (or, rather, slowly and rapidly growing instabilities) in that space is not yet perfect.

Let me remark in closing that the 2D space of global angular momentum (through $T/|W|$) and azimuthal velocity at a given radius can be mapped into the space of angular momentum and shear.

Indeed, a cluster with high $|\langle v_\phi \rangle(R_\mathrm{v}/5)|$ displays low shear if $T/|W|$ is also high, and high shear if $T/|W|$ is low. Conversely, a cluster with low $|\langle v_\phi \rangle(R_\mathrm{v}/5)|$ displays high shear if $T/|W|$ is high, and low shear if $T/|W|$ is low. This new stability criterion therefore includes two large scale properties of the system, namely rotation and shear, via integrated quantities, and may therefore be tested against observational data.

5.7 Conclusions

In this chapter, I focused on tangentially anisotropic, rotating spherical clusters, where an instability regime was identified in Chapter 4. These instabilities required a more thorough study than their counterparts in radially anisotropic systems (Section 4.6), because of the scarce existing results on tangential anisotropy. My goal was to acquire insight on the destabilisation processes at play, in order to design a general stability stability criterion for such systems. For that purpose, I used complementary evidence from the response matrix and N-body simulations, considering the particles in the system alternatively in terms of their location (latitude and distance to the centre) and in terms of their orbital frequencies. These complementary approaches allowed me to relate the observed instabilities to the processes I presented in Chapters 3 and 4, resp. the circular orbit instability (COI) and the tumbling instability (TI). This study finally allowed me to pin down a stability criterion in these systems, improving upon that of Ostriker & Peebles (1973).

I first focused on identifying the locations in the cluster where rotation was important for the instability. This analysis was performed by setting up specific initial conditions for a stability analysis by the matrix method and N-body simulations. These included clusters in which rotation depends on the one hand on the latitude, and on the other on the distance to the centre. This study showed that both high- and low-inclination orbits are important to the instability, and that the destabilisation of the system is mostly determined by the rotation of its inner parts (i.e. inside its core). I then focused on identifying the resonant processes leading to the destabilisation of the cluster. This question was tackled by the complementary use of (i) an analytical model describing the dynamics of epicyclic orbits in a barred sphere, (ii) the restricted matrix method and (iii) measurements of the variation of the distribution of orbital frequencies in a system where an instability is developing. From this approach, I was able to show that both the COI and the TI seem to have specific roles in the destabilisation of tangentially anisotropic, rotating clusters. Brought together, the location-based and the resonance-based approaches provided important insight on the process of bar formation in tangentially anisotropic, rotating clusters. I finally used this insight to identify a new stability criterion for these structures, which better separated stable from unstable N-body setups.

I showed that a larger part of the parameter space than illustrated in Fig. 4.9 is occupied by unstable systems. This leaves even less room for anisotropic and rotating stable equilibria around the line of isotropic systems with rotation, in particular in the region of tangentially anisotropic, slow rotators. Our numerical results also confirmed that the COI in non-rotating clusters can be continuously matched to the violent instabilities measured in tangentially anisotropic, fast rotators. However, this continuity does not imply that the COI alone is responsible for these violent instabilities. Indeed, the analysis with the restricted matrix method showed that the tumbling resonance is also very active to destabilise the system. It therefore seems, as for radially anisotropic systems, that *the TI acts as a catalyser for bar formation through the COI.* This enhancement is even more pronounced in tangentially anisotropic systems than in radially anisotropic ones, since the growth rates of tangential systems reach values twice as large as the maximum growth rate of the radial regime (see Fig. 4.9). The interplay between COI and TI seems however different from that identified in radially anisotropic systems. In the latter, it seems that the TI is mainly responsible for shifting the instability's pattern speed, and the strength of the ROI is related to the number of orbits at the ILR with that pattern. In tangential clusters, the TI may also be responsible for imposing the pattern speed, as can be seen from the linear growth of ω_0 with α for $\alpha \geq 0.2$ (see Figs. 4.15b and 5.9). However, at such pattern speeds, the COI should be damped, because it requires a pattern speed close to the maximum of Ω_ILR. The TI therefore must also have an important influence on maintaining and enhancing the COI, apart from setting the pattern speed.

Let me insist on the surprising persistence of the COI at large pattern speeds. N-body measurements (Fig. 5.13) and the restricted matrix (Table 5.2) showed that unstable systems present an important activity at the ILR, in particular around the maximum of Ω_ILR. This indicates that the COI plays a role in the system's destabilisation. From the derivation of Section 3.2, the pattern speed should therefore develop in the vicinity of the maximum of Ω_ILR. However, both the matrix method and N-body simulations (Fig. 4.9) measured pattern speeds at values three times higher. This activity far from

resonance may be related to the breaking of the orbital hypothesis (see, e.g., Polyachenko & Shukhman, 2015). Indeed, these instabilities develop with high growth rates, of the order of the maximum of $\Omega_{\rm ILR}$ (yet still a fraction of Ω_1 and Ω_2). It is therefore possible that the orbits start to feel the potential change in the course of their orbital motion. This has the effect of blurring the resonances, and this blurring may be responsible for the interaction with the ILR far from resonance. Formally, the large growth rate is involved in the resonant denominator $\omega_0 + \mathrm{i}\eta - \widetilde{\mathbf{n}} \cdot \widetilde{\mathbf{\Omega}}$, which smooths the pole and blurs the resonance. Jalali & Hunter (2005) argue that a non-zero growth rate reveals the intrinsic nature of the corresponding integral, which is rather a Fourier component than a proper resonance.

Finally, a detailed study of the destabilising processes allowed me to identify a stability criterion which involves both rotation and shear, improving upon the classical $T/|W|$ criterion from Ostriker & Peebles (1973). Indeed, Figs. 5.15a and 5.14 showed that $T/|W|$ poorly separates stable from unstable systems in the series of N-body models with mild-shear (prograde core and non-rotating outskirts) and high-shear (prograde core and retrograde outskirts). The new criterion, in which $T/|W|$ is multiplied by the mean azimuthal velocity in the central part of the cluster ($|\langle v_\phi \rangle(R_{\rm v}/5)|$), much better separates stable from unstable tangential spheres with rotation and shear. This is shown by Fig. 5.15. Let me insist on the fact that Fig. 5.15 includes high-shear models varying along three parameters: the system's anisotropy (via q), its rotation and its shear (through the interplay between the fraction of orbits in the prograde core, γ_2, and the net angular momentum of each component, via α). In this criterion, $T/|W|$ represents the overall rotation of the cluster, while its multiplication with $|\langle v_\phi \rangle(R_{\rm v}/5)|$ also accounts for the shear in the system. The identification of this criterion was based on two observations. First, the complementary analysis of the role of frequencies from the restricted matrix and N-body simulations identified that *the tumbling resonance and the ILR are active around the centre of the cluster, and that they play an important role in the cluster's destabilisation.* This influence of the centre is confirmed by the stability results from N-body simulations. Second, the stability results from N-body simulations showed that *orbits at intermediate radius also enhance the instability's growth rate.* This may be due to the enhanced interaction with the tumbling resonance and the ILR, and may also be attributed to interactions with resonances located further away, such as the CR and the OLR. The role of these resonances is, again, deduced from the frequency analyses. In the end, it resulted that an efficient stability criterion should include both the global and the central rotation of the system.

5.8 Prospects

Let me now discuss some implications of these results, as well as still unanswered questions and possible future projects.

The validation of the new stability criterion for tangentially anisotropic spheres with rotation and shear uses stability results from N-body simulations with high shear (prograde core and counter-rotating outskirts), and a variety in the anisotropy, rotation, and shear. However, it may still be insufficient for comparison with observations. Indeed, some complex features observed in real clusters are more intricate than those probed here (Davies et al., 2001; Emsellem et al., 2007, 2011; Jindal et al., 2019; Cordoni et al., 2020, see also Fig. 5.1). In particular, the distribution of anisotropy in the cluster is still smooth (the whole cluster has the same flavour of anisotropy). As I have shown, rotating systems with radial and tangential anisotropy may both be unstable, and it would be interesting to study the possible development of instabilities in systems where the anisotropy displays different flavours at different distances from the centre. One can for example imagine that the mixing of anisotropies in the cluster further destabilises it. Such a phenomenon would be of great interest to the evolution of spheroidal clusters. Indeed, the interaction with the environment naturally produces such kinematic features, and if these systems are unstable, then it is probable that their kinematic structure reflects more the attractors in the space of stable equilibria than their past interaction with their environment. The same applies to systems displaying shells with different rotation axes.

To study systems with ever larger complexity in the kinematics, it will soon become hopeless to rely on N-body simulations alone, as these are too costly to be fit for parameter space exploration (here, we reached the boundary of such exploration). Such a study should therefore be performed with the matrix method, which is currently more efficient for stability studies. For now, only rotating DFs of the form of eq. (4.1) can be used, however efficient methods for more complex DFs could be (and should be) implemented. The analytical derivation already exists (see eq. 2.20), and it is merely a matter of implementation. In particular, I expect that the inclusion of shear should easily be made efficient.

In order to test whether or not the new stability criterion can apply to more general systems, it would be interesting to test it against observational data. One could therefore check for the location of the

clusters in the stable region of the parameter space, and perhaps for particular attractors on that line. A priori, observations of GCs and dwarf spheroidal galaxies should be best suited, since these systems both display rather smooth central profiles. However, the parameter was designed for tangentially anisotropic systems, and it seems that this flavour of anisotropy is under-represented in observations. Furthermore, the new criterion is not yet expressed directly in terms of observable quantities, but the translation should be relatively straightforward.

Let me underline a yet unexplained feature from the stability study of sheared models. In both series (mild- and high-shear), it seems that the growth rate reaches a maximum at intermediate values of γ ($\gamma_1, \gamma_2 \simeq 0.5$). This means that the outer parts have a larger destabilising influence if they are counter-rotating than if they are prograde. This behaviour is different from that at smaller γ, where the growth rate is an increasing function of γ. For now, there is no sufficient evidence to give a definite explanation for it, but there are hints of resonant activity in these regions (see Figs. 5.12 and 5.13, which show ridge formation at CR and OLR). Interestingly enough, the transition occurs around $R = 1.3$, which is very close to $R_\mathrm{I} = 1.25$, where Ω_ILR reaches its maximum. Going further requires a dedicated study of this specific region. In particular, the restricted matrix method can bring important information. Indeed, applying it to the series of sheared models will allow me to disentangle the role of different resonances in these regions, by comparing the results of models with different γ (i.e. different positions of the separation between the prograde core and the outskirts, either non-rotating or retrograde).

All in all, these results have important implications regarding the interaction between tangentially anisotropic, rotating systems and their environment. First, as hinted by Fig. 4.15a and later confirmed by Figs. 5.8 and 5.9, the decrease of the growth rate in systems with decreasing net angular momentum is very shallow. In particular, it seems that there is no net transition between stability and instability. This indicates that rotating tangentially anisotropic clusters, even close to isotropy, are likely to develop slowly growing instabilities, neutral modes, and weakly damped modes[11]. Such modes may have an important role in the secular evolution of these clusters. One the one hand, they can be regularly excited by the interaction with the environment. On the other, they can be the drivers of important diffusion in the cluster, leading to secular changes in its density structure and in its kinematics. A more detailed study of the slow growth regime in other parts of the blue region in Fig. 4.9 is therefore required. Weinberg (1994) and the present chapter showed that detecting resp. weakly damped and slowly growing modes is possible with the matrix method. Heggie et al. (2020) and the present chapter showed that it is also possible with N-body methods. Here, I proved that the analytical and numerical methods are complementary, and the study of such modes with both methods should help confirming and characterising them.

Another kind of numerical simulations may give us insight on the impacts of these instabilities on the secular evolution of spheroidal systems. This prospect was already highlighted in Section 4.8, and involves studying the possible development of instabilities during a merger. Starting from a tangentially anisotropic, rotating cluster in a stable equilibrium, one can throw a small satellite at the cluster with different initial velocities. A satellite with a prograde orbit will likely increase the rotation of the cluster, and may provoke its destabilisation. A satellite with a purely radial, or retrograde orbit will likely be absorbed without destabilising the cluster. Such experiments may provide us with interesting information about the endstates of a merger. For example, my results tend to indicate that a prograde merger (i.e. the satellite runs in the same direction as the cluster's rotation) would have a larger effect on the cluster's structure than a retrograde one.

[11] Note that slowly growing instabilities play a similar role as neutral and weakly damped modes in stellar systems. Indeed, if the timescale for secular evolution is smaller than the one of the instability, it may never develop as an instability, but have the same effects as low-amplitude modes. Similarly, if the system undergoes important external perturbations, the instability never has the time to develop.

Chapter 6

Conclusions

In the last 20 years, new evidence for various levels of kinematic richness in spheroidal stellar systems opened new venues in their theoretical study. For dark matter (DM) halos, the origin of rotation is now partially understood (Peebles, 1969; Vitvitska et al., 2002; Codis et al., 2012), and precisely characterised in cosmological simulations (Bullock et al., 2001; Aubert et al., 2004; Bett et al., 2007). These results revived the interest in the influence of rotation on the radial orbit instability, which is thought to play an important role for shaping DM halos at the time of their formation (Merritt & Aguilar, 1985). They also question its influence on the interaction between DM halos and their environment. For spheroidal galaxies, integral field spectroscopy now allows for a precise reconstruction, orbit per orbit, of their phase space structure (Bacon et al., 2001; Kuntschner et al., 2006; Cappellari et al., 2011; Emsellem et al., 2011; Wisnioski et al., 2015, 2019). These models present anisotropy and rotation, and it is important to guarantee that they are physical (i.e. leading to self-consistent distributions) and linearly stable. Furthermore, these kinematic features may reflect their past history. Recent astrometric data on galactic globular clusters unveiled the 6D phase space of such structures as never probed before, revealing that anisotropy and rotation are usually present at various degrees in GCs (Bianchini et al., 2018; Vasiliev, 2019; Sollima et al., 2019). Hence, they are becoming fantastic laboratories to study spherical systems with complex kinematics. These kinematic features may also inform us on the formation and evolution of GCs, in particular on their interaction with the external tidal field of their host galaxy. Finally, integral field spectroscopy also revealed the high degree of rotation (Seth et al., 2008; Feldmeier et al., 2014) of nuclear star clusters. These observations can be used to constrain formation scenarios for NSCs, in relation with the build-up of the angular momentum of super massive black holes .

The questions raised by the evidence for rotation in spheroidal systems are multiple: how are these features produced, and maintained? What is their role in the evolution of spheroidal systems when in isolation? What is their influence on the interaction of spheroidal systems with their environment? How can the consequences of rotation be traced in spheroidal systems, using existing and forthcoming data? To answer these questions, it was critical to analyse the production of spherical equilibria with some complexity in velocity space, and their subsequent evolution under the effect of internal and external perturbations. *This is the central role of linear response theory: starting with a given equilibrium, this strategy consists in the computation of the response of the system to any kind of potential perturbation, by solving the equations of motion at first order in the perturbing potential.*

Many phenomena can indeed be described by linear response theory. At the first level, one can compute the response of a system to a specific perturbation, i.e. follow the time evolution of the system under the effect of that perturbation. In a cold system, which strongly responds to a perturber, this can lead to strong amplified fluctuations in the system's potential, such as that involved in swing amplification in stellar disks (Toomre, 1981). Although not the central topic of the present manuscript, this use of linear response theory is also particularly timely for the study of the Milky Way, where signs of recent potential perturbations were observed in the stars' dynamics (see, e.g., Antoja et al., 2018). This first level gives access to two separate and connected uses of linear response theory. On the one hand, when one statistically averages the response to particular perturbers over the system's lifetime, it is possible to model the secular evolution of self-gravitating systems. This is the purpose of the gravitational quasi-linear formalism (Fokker-Planck, Balescu-Lenard), which has recently proved to be a powerful tool to describe the secular evolution of various astrophysical systems (see, e.g., Fouvry et al., 2015a; Hamilton et al., 2018). On the other hand, linear response theory can also identify particular perturbers which are self-sustained, in the sense that the response of the system maintains the perturbation for some time.

Some of these modes can decay in time (Weinberg, 1994), or grow at a very slow rate (Breen et al., 2020). In that case, although they do not importantly transform the system's structure on short time scales, they distribute heat globally within the system via resonances and will have a role in its secular evolution, if they do not decay too fast. Other modes can grow at a fast exponential rate (Rozier et al., 2019), so that they are able to step out of the linear regime, and significantly modify the structure of the system on a few dynamical times. This latter use of linear response theory was my focus for my thesis.

6.1 Overview

In this manuscript, I adapted analytical and numerical methods to the study of the linear stability of spherical systems with a cored potential and rich kinematic structures. First, in Chapter 2, I presented the matrix method, which is the main analytical tool I used in my stability analyses. *I also developed new numerical methods which led to a considerable improvement in the computational efficiency of the matrix calculation.* These improvements bring the matrix method at a stage where it can be more efficient than N-body simulations to detect instabilities. I also adapted similar methods to the computation of different versions of the response matrix, e.g. its Lagrangian formulation (Appendix A), its form for the singular case of the Einstein sphere (Section 3.5), and more importantly the response matrix for rotating spheres (Sections 4.3 and 5.2), which given their lower symmetry involve more numerous matrix elements. I intend to distribute the code and make it available to the community.

In Chapter 3, I focused on the scarcely studied case of spherical clusters with tangential anisotropy. Revisiting a demonstration by Palmer et al. (1989) of the existence of a circular orbit instability (COI) in such systems, I performed a thorough study of their linear stability. After excluding tightly-wound waves as the source of the instability, *I was able to detect slowly growing large scale modes with the matrix method.* I performed a parameter exploration of this instability along the line of increasing tangential anisotropy, and found the point of marginal stability on that line. I also developed a new technique based on the matrix method, which I coined the restricted matrix method, which confirmed that the modes I detected are indeed of the COI type. I finally presented preliminary results on the stability of the Einstein sphere, where the tangentiality is maximal, i.e. all orbits are circular. These results confirm the expectation from Palmer et al. (1989) that this sphere is stable, which would imply that the instability of tangentially anisotropic systems is non-monotonic when the tangential anisotropy is further increased.

In Chapter 4, I considered the case of spheres with anisotropy and rotation. I first revisited the argument from Allen et al. (1992) in favour of a tumbling instability (TI) in rotating systems, and discussed its existence in light of later results from the literature. I then simplified the response matrix for rotating spheres, and used the matrix method to evaluate the stability of spheres with various degrees of anisotropy and rotation. In order to confirm the robustness of the matrix results, I compared these with dedicated N-body simulations, and showed that the matrix achieves results of similar accuracy, with smaller computation time. *I exhibited two regimes of fast growing overstabilities in anisotropic, rotating spheres, one for radially anisotropic systems and one for tangentially anisotropic systems.* I further showed that the radial regime is subdivided in two parts, the Fast-ROI with large pattern speeds and the Slow-ROI with low pattern speeds. I proposed that these instabilities are two modes of the same ROI process, the main mode decaying at large rotation because its pattern speed is too high for any radial orbit to follow its rotation. In that picture, the tumbling process (à la Allen et al. (1992)) is mainly responsible for the rotation of the pattern, and the destabilisation is ensured by the spherical counterpart of the tumbling instability in disks (à la Lynden-Bell (1979)).

In Chapter 5, I dissected the stability of tangentially anisotropic, rotating spheres. Indeed, it seems that the instabilities in such systems are significantly more complicated than those of the ROI type. This study was based on complementary experiments using the matrix method and N-body simulations. I analysed the destabilising processes on two fronts. First, I used stability results from the matrix method and the simulations to identify the locations in the cluster, in terms of inclination and of radius, where rotation was the most critical to the instability. Second, I presented results from the restricted matrix, as well as frequency measurements in simulations, and a theoretical model for the dynamics of orbits in a weakly barred potential. I used this evidence to relate instabilities to the orbital resonances at play. These combined results put the central part of the cluster as the main driver of the instabilities. I therefore designed a stability criterion for tangentially anisotropic spheres with rotation and shear, improving upon the classical Ostriker & Peebles (1973) criterion. It states that *a necessary condition for instability is given by* $T/|W||\langle v_\phi \rangle(R_\mathrm{v})| > 0.016$, and involves both the global angular momentum and the shear in the system.

Anisotropy	Rotation	Section	Instability	Process
Radial	×	2.3	✓	ROI
Tangential - WKB	×	3.3	∼ ×	
Tangential	×	3.4	✓	COI
Einstein	×	3.5	∼ ×	
Radial	✓ (low)	4.5.3	✓	ROI + TI (Fast-ROI)
Radial	✓ (high)	4.5.3	✓	ROI + TI (Slow-ROI)
Tangential	✓	4.5.4	✓	COI + TI
Tangential	✓ (inclination-dependent)	5.2 & 5.3.1	✓	COI + TI
Tangential	✓ (sheared)	5.3.2	✓	COI + TI

Table 6.1: Summary of the stability results of my thesis. The columns are: the anisotropy in the system, the specification for rotation (rotation or not, and some more details), the section in the manuscript where the results are presented, whether or not an instability is detected, and what process was identified. For the tangential spheres with WKB basis elements, an $\ell = 2$ instability was not fully excluded, but only that it may be due to the COI (see Polyachenko, 1987, for a characterisation of this specific case). For the Einstein sphere, results are preliminary. In the radially anisotropic rotating sphere, two regimes were identified: the Fast-ROI for systems with relatively low net angular momentum, and the Slow-ROI for fast rotators. The denomination is related to the pattern speed.

Table 6.1 summarises the various stability results I obtained, using mainly the response matrix and sometimes N-body simulations.

6.2 Highlights

Let me here highlight some of the key results of my thesis work, from the possibilities offered by analytical methods to new insight on star cluster dynamics.

First, let me insist again on the efficiency of the response matrix computation. As I have shown, this method is now fit for parameter space exploration in a variety of setups. In my thesis, I have used this possibility to study the stability of spheres in the non-rotating, radially (Chapter 2) and tangentially anisotropic regimes (Chapter 3), in the rotating, radially and tangentially anisotropic regimes (Chapter 4), as well as in a tangential regime where rotation depends on the inclination (Chapter 5). I have also applied the restricted matrix method to non-rotating tangentially anisotropic spheres (Chapter 3), and to rotating spheres with radial (Chapter 4) and tangential (Chapter 5) anisotropy. However, my results only apply to the Plummer or the isochrone potentials, representing all cored potential, which have similar frequency structures. I have already highlighted some of the possibilities that this new efficiency opens in the future, among which the application of the method to (possibly rotating) cuspy spheres or quasi-Keplerian potentials, its adaptation to the Einstein sphere, a refined study in the low growth rate limit, the study of neutral and weakly damped modes, as well as parameters explorations in systems with more refined kinematic structures. Some adaptations will however still be required to study triaxial systems, and models produced from observations of star clusters (see Section 1.2).

Using the matrix method, I analysed the stability of rotating, anisotropic stellar spheres and identified three types of destabilising processes, which (sometimes collaboratively) lead to $\ell = 2$ instabilities. These processes are the radial orbit instability (ROI), the circular orbit instability (COI) and the tumbling instability (TI). I studied the stability of rotating and non-rotating systems with radial and tangential anisotropy, and refined setups such as the Einstein sphere, systems with shear or inclination-dependent rotation, as well as the stability of the non-rotating tangential sphere to WKB-like perturbations (see Table 6.1). I detected instabilities in all cases except the WKB and Einstein tangential cases, and characterised the destabilising processes in each case. *Radially anisotropic systems are unstable to the ROI when non-rotating, and to the collaboration between the ROI and the TI when rotating. Tangentially anisotropic systems are unstable to the COI when non-rotating, and to the collaboration between the COI and the TI when rotating.*

My results prove that a large fraction of anisotropic, rotating spheres are unstable. This means that, around the isotropic, non-rotating sphere (which is stable by the Antonov and Doremus-Feix-Baumann theorems, assuming $\mathrm{d}F/\mathrm{d}E < 0$), *the region of stability is relatively narrow, both in the direction of increasing anisotropy and increasing rotation.* This has two important consequences for star cluster science. First, when modelling an observed cluster, configurations with large anisotropy or rotation are

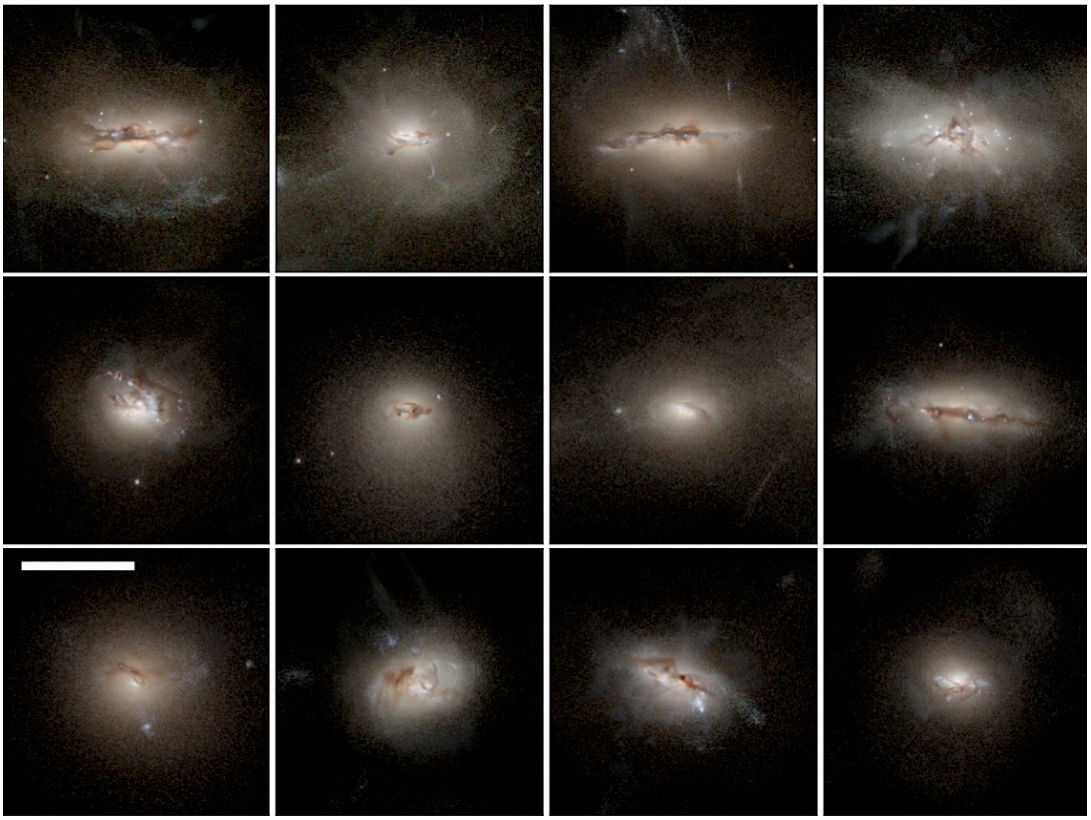

Figure 6.1: Galaxy snapshots from the NewHorizon simulations (Park et al., 2019). All these galaxies are perturbed, and most of them seem to undergo a filamentary inflow of gas.

dynamically excluded. Second, over its lifetime, linear instabilities prevent a star cluster from exploring configurations with large anisotropy and net angular momentum. Identifying a simple stability criterion helps building linearly stable models for spheroidal star clusters (e.g. by testing the model a posteriori against the criterion, or by including the criterion a priori in the modelling algorithm), and identifying the regions of marginal stability to which the systems may be attracted along their secular evolution.

Indeed, my results show that any injection from the environment (infall, merger, etc.) which increases the system's anisotropy and/or net angular momentum pushes the system towards thermodynamically less probable states, and closer to a stability boundary. If the process is a violent event (such as a merger), violent relaxation will likely put the system in a state of relatively low anisotropy and net angular momentum. However, if the system undergoes steady consistent perturbations (e.g., infall of baryons along preferred directions with advection of angular momentum, see Fig. 6.1), it will eventually reach marginal stability. From that point, linear instabilities develop, putting the system back in a region of higher entropy. In that process, a bar may radiate part of the central energy and angular momentum away, and modify the phase space structure of the system. Its density structure may change by either modifying the radial distribution of stars, or increasing its triaxiality. To find this stability boundary, a simple stability criterion will undoubtedly be an efficient tool.

However, identifying the ultimate stability criterion may prove difficult, since I have shown that the stability boundary can have an intricate shape. For example, my preliminary results on the Einstein sphere tend to show that the growth rate of the COI along the line of increasing tangential anisotropy is not monotonic. Furthermore, in the radially anisotropic regime, the growth rate is not a strictly increasing function of the net angular momentum, since it decreases at the transition between the Fast- and the Slow-ROI (consider, e.g., the $q = 0.2$ line in Fig. 4.13, where the system is unstable for $0.15 \lesssim \alpha \lesssim 0.6$, and stable otherwise). First, it seems that stability criteria should be different, when the associated destabilising processes are different. As such, *efficient stability criteria should incorporate the nature of the anisotropy in the system.* This raises issues when considering systems with both flavours of anisotropy in different regions, but as I underlined earlier, the stability of such systems is yet largely unexplored. In Chapter 5, I identified a specific stability criterion for tangentially anisotropic systems with rotation and shear. It would be useful to compare it with observational data.

Before discussing some possible future improvements, let me finally underline the crucial influence of

the apsidal precession of orbits in all the systems which I studied in my thesis. In radially anisotropic systems, the possible role of the ILR in the ROI had been identified for a while (see Palmer & Papaloizou, 1987). Indeed, the instability stems from the alignment of highly elongated orbits precessing at the same rate. I have shown that in radially anisotropic, rotating systems too, this process is at the source of instabilities in both slow rotators (Fast-ROI) and fast rotators (Slow-ROI). In that picture, the TI mainly accounts for the pattern speed of the instability, while the ROI develops through its regular process at that pattern speed. The growth rate is enhanced, as soon as the density of orbits is larger around a non-zero pattern speed. Similarly, in tangentially anisotropic systems, the COI is also closely related to the ILR. Indeed, in the epicyclic approximation, the ILR is the only (low-order) resonance to have an extremum inside the populated region of the system. This is a critical characteristic: it implies that the ILR separates two regions of the sphere, and defines a characteristic radius and frequency at that maximum. Furthermore, it induces the coalescence of two resonant points below the characteristic frequency, allowing for the formation of neutral modes, later destabilised by other resonances. When rotation is introduced, it seems that the same process applies. Only at high rotation does the pattern speed depart from the maximum of $\Omega_{\rm ILR}$, starting to blur the resonance. From that picture in radially and tangentially anisotropic systems, it seems that *the characteristic frequency given by the ILR clearly separates the instabilities between both regimes of anisotropy.* Indeed, the ROI develops with $\omega_0 < \omega_{\rm I}$, while the COI has $\omega_0 > \omega_{\rm I}$. This separation was found true for all of the instabilities I measured in my thesis.

6.3 Prospects

I already mentioned potential prospects related to the specific content of each chapter. Let me nonetheless finally highlight a few specific prospects that are triggered by my global results.

In the previous section, I underlined the role of the pattern speed in the destabilisation of anisotropic, rotating systems. For the ROI, the pattern speed determines the regions where orbits interact at the ILR. It is therefore determinant in setting the growth rate of the Fast-ROI, as well as in the transition from the Fast- to the Slow-ROI. For the COI, the growth of the pattern speeds at high net angular momentum is related to an important increase of the growth rate. However, the question of how precisely the pattern speed is determined remains unanswered. In both regimes of anisotropy, I identified the TI as the process by which the pattern speed is set. Yet, we still need more work to precisely characterise the interplay between the ROI/COI and the TI, in order to be able to predict the precise value of the pattern speed at a given net angular momentum. Such a characterisation may rely on N-body simulations. For example, in the same fashion as Allen et al. (1992), one could measure the possible precession and oscillation of the orbital planes during the growth of the instability. In parallel, analytical work on the tumbling term in the response matrix may help identifying the relevant characteristics of the system which source the pattern speed. A first step on this path may be given by the following result. In the fully rotating, tangentially anisotropic sphere with $(\alpha, q) = (1, -16)$, the matrix method and N-body simulations both detect an instability with growth rate and oscillation frequency $(\eta, \omega_0) \simeq (0.11, 0.74)$. From the neutral mode scenario, the pattern speed should be set by the real part of the response matrix, while the growth rate should be fixed by its imaginary part (see, e.g., Section 3.2). However, it relies on the hypothesis that η can be considered as a perturbation to ω_0, which is not exactly true here. To test for this scenario, I did a full mode search with a response matrix where the imaginary part of the matrix is continuously turned on from 0 to its total value. In other words, I performed a series of mode searches for (fictitious) response matrices, where $\widehat{\mathbf{M}}$ is replaced by $\mathrm{Re}(\widehat{\mathbf{M}}) + \epsilon\,\mathrm{Im}(\widehat{\mathbf{M}})$, and ϵ is varied from 1 to 0. The results of this exploration show that, whatever the value of ϵ, *an instability is always detected for similar values of* (η, ω_0)[1]. A first step to a precise characterisation of the pattern speed could therefore proceed by a careful analysis of different resonant terms in $\mathrm{Re}(\widehat{\mathbf{M}})$.

The numerical methods I designed can also be used in other versions of the response matrix. For example, they could be used to compute the temporal response of a given equilibrium to a given time-varying perturbation. Using the conventions of Chapter 2, the time variation of the system's response

[1] Note that this is not a general property of complex matrices (i.e. a non-invertible complex matrix may have an invertible real part). Indeed, a counter-example is given by

$$\begin{pmatrix} 1 & \mathrm{i} \\ -\mathrm{i} & 1 \end{pmatrix} = \begin{pmatrix} 1 & 0 \\ 0 & 1 \end{pmatrix} + \begin{pmatrix} 0 & \mathrm{i} \\ -\mathrm{i} & 0 \end{pmatrix}. \tag{6.1}$$

can be straightforwardly computed from the linearised collisionless Boltzmann – Poisson system, giving

$$\mathbf{a}(t) = \int_{-\infty}^{t} \mathrm{d}t' \, \mathbf{M}(t'-t) \cdot (\mathbf{a}(t') + \mathbf{b}(t')). \tag{6.2}$$

Here, recall that $\mathbf{a}$ is the vector corresponding to the response of the system, projected on the bi-orthogonal basis, while $\mathbf{b}$ corresponds to the external perturbation. The time-varying response matrix is given by

$$\mathbf{M}_{pq}(t) = (2\pi)^3 \sum_{\mathbf{n}} \int \mathrm{d}\mathbf{J} \, \mathrm{i}\,\mathbf{n} \cdot \frac{\partial F}{\partial \mathbf{J}} \, \psi_{\mathbf{n}}^{(p)*}(\mathbf{J}) \, \psi_{\mathbf{n}}^{(q)}(\mathbf{J}) \, \mathrm{e}^{\mathrm{i}\,\mathbf{n}\cdot\mathbf{\Omega}\,t}. \tag{6.3}$$

In spherically symmetric systems, all of my numerical methods can straightforwardly apply to the computation of this matrix. Indeed, it involves (i) integration over action space, (ii) the (fast) computation of the Fourier-transformed basis elements $W^{\widetilde{\mathbf{n}}}_{\ell^p n^p}(\widetilde{\mathbf{J}})$ (in order to evaluate $\psi^{(p)}_{\mathbf{n}}(\mathbf{J})$), and (iii) the precise computation of the resonant exponential $\mathrm{e}^{\mathrm{i}\,\mathbf{n}\cdot\mathbf{\Omega}\,t}$. This form of the response matrix can have three types of direct applications. First, one can compute the system's response to any kind of external perturber $\mathbf{b}(t)$. For instance, in the context of the stellar disk of the Milky Way, Monari et al. (2017) recently used this method to evaluate the local response of stars in the Sun's vicinity to the rotating bar of the Milky Way (which was therefore considered as an external perturber to the disk). However, their method did not consider the self-gravity of the disk, while a direct implementation of eq. (6.2) would consider it. In the context of star clusters, the response of a dark matter halo to the formation of a baryonic component (elliptical or disk galaxy) at the centre can also be a topic of interest. Then, this formalism can in principle be inverted up to some fairly limited past horizon, in order to infer the past state of an equilibrium from a given measurement of its perturbations. The key ingredient is to formulate the inverse problem in the eigen-frame of the response matrix of the underlying system, so as to decouple the time evolution of each mode. Leverage is provided by the measured spectrum of angular frequencies, which encode differentially past tides. I started implementing such a method in the context of galactic archeology, to infer the perturber from the observed phase space perturbations in the Milky Way, as observed by Gaia (see Antoja et al., 2018). The third use of the time-dependent response is to evaluate the dynamical friction applied to a body embedded in a stellar system (see, e.g., Tremaine & Weinberg, 1984). This can help characterise the sinking of super massive black holes towards the centre of galaxies, the dynamics of globular clusters in dwarfs galaxies (in order to constrain the shape of their DM halos), or the dynamical slow down of a galactic bar from its interaction with the halo. In all these cases, a detailed estimation of the amplitude of the cluster's self-gravitating response is paramount to precisely describe these processes.

Finally, let me briefly consider the implications of my results for the topical question of secular evolution. Over their lifetime, star clusters will be able to build up new components from their interaction with their environment, and therefore explore many kinematic states. These new components may increase their anisotropy, increase their rotation, or both. I have shown that systems with anisotropy and rotation can respond strongly to potential perturbations, and sometimes develop slowly growing instabilities, neutral modes or weakly damped modes. I have also discussed the possibility of being attracted to a stability boundary, because of self-regulated fine-tuning between dynamical cooling from externally injected components and dynamical heating by linear instabilities. But even far from the stability boundary, the linear response of a star cluster will significantly impact its secular evolution, since it determines how it reacts to both external and internal perturbations. Therefore, anisotropy and rotation can significantly impact its secular evolution. Some recent results tend to corroborate this statement. From N-body simulations of anisotropic star clusters in isolation, Breen et al. (2017) showed that tangentially anisotropic clusters tend to evolve faster than their isotropic counterparts, while radially anisotropic systems tend to evolve slower. Using similar methods, Szölgyén et al. (2019) showed that rotating star clusters were subject to anisotropic mass segregation, leading massive particles to aggregate around the equatorial plane, while lighter particles are kicked to high inclinations. There is therefore no doubt that the details of the kinematic structure of a cluster can have drastic imprints on the efficiency of its long-term evolution.

The secular evolution of star clusters can also be tackled by using an analytical formalism, the gravitational quasi-linear formalism, which captures self-consistently some level of non-linearities while assuming time decoupling. In this framework, two master equations were derived, disentangling the competition between nature and nurture in driving the secular evolution of self-gravitating systems. On the one hand, the dressed Fokker-Planck equation (Binney & Lacey, 1988; Weinberg, 2001; Pichon & Aubert, 2006) describes the secular evolution of a system driven by external perturbations amplified by

the system's self-gravity. It reads

$$\frac{\partial F(\mathbf{J},t)}{\partial t} = \frac{\partial}{\partial \mathbf{J}} \cdot \left[\sum_{\mathbf{n}} \mathbf{n}\, D_{\mathbf{n}}(\mathbf{J},t)\, \mathbf{n} \cdot \frac{\partial F}{\partial \mathbf{J}} \right], \tag{6.4}$$

where the diffusion coefficients are given by

$$D_{\mathbf{n}}(\mathbf{J},t) = \frac{1}{2} \sum_{p,q} \psi_{\mathbf{n}}^{(p)}(\mathbf{J})\, \psi_{\mathbf{n}}^{(q)*}(\mathbf{J}) \left[\left[\mathbf{I} - \widehat{\mathbf{M}} \right]^{-1} \cdot \widehat{\mathbf{C}} \cdot \left[\mathbf{I} - \widehat{\mathbf{M}} \right]^{-1} \right]_{pq} (\omega = \mathbf{n} \cdot \mathbf{\Omega}). \tag{6.5}$$

In that expression, the DF is now a function of time, precisely because it describes the long-term evolution of the DF along a line of quasi-equilibria. Furthermore, $\widehat{\mathbf{C}} \propto \langle \mathbf{b}_p \mathbf{b}_q \rangle$ is the time auto-correlation of the external perturbation projected onto the bi-orthogonal basis. Once this auto-correlation is known, the computation of the dressed Fokker-Planck equation critically relies on the response matrix $\widehat{\mathbf{M}}$. Indeed, the diffusion coefficients in action space not only depend on the perturber, but also on the response of the system to the external perturbation. On the other hand, the inhomogeneous Balescu-Lenard equation (Heyvaerts, 2010; Chavanis, 2012) describes the secular evolution of an isolated system under the self-amplified noise generated by its finite number of particles. It reads

$$\frac{\partial F(\mathbf{J},t)}{\partial t} = \pi (2\pi)^3 \frac{M_{\rm tot}}{N} \frac{\partial}{\partial \mathbf{J}} \cdot \left[\sum_{\mathbf{n},\mathbf{n}'} \mathbf{n} \int \mathrm{d}\mathbf{J}' \frac{\delta(\mathbf{n}\cdot\mathbf{\Omega} - \mathbf{n}'\cdot\mathbf{\Omega}')}{\left| \mathcal{D}_{\mathbf{n},\mathbf{n}'}(\mathbf{J},\mathbf{J}',\mathbf{n}\cdot\mathbf{\Omega}) \right|^2} \left(\mathbf{n} \cdot \frac{\partial}{\partial \mathbf{J}} - \mathbf{n}' \cdot \frac{\partial}{\partial \mathbf{J}'} \right) F(\mathbf{J},t) F(\mathbf{J}',t) \right], \tag{6.6}$$

where the dressed susceptibility coefficients are given by

$$\frac{1}{\mathcal{D}_{\mathbf{n},\mathbf{n}'}(\mathbf{J},\mathbf{J}',\omega)} = \sum_{p,q} \psi_{\mathbf{n}}^{(p)}(\mathbf{J}) \left[\mathbf{I} - \widehat{\mathbf{M}}(\omega) \right]^{-1}_{pq} \psi_{\mathbf{n}'}^{(q)*}(\mathbf{J}'). \tag{6.7}$$

Similarly, the Balescu-Lenard equation critically involves the system's response matrix, which determines how the shot noise coming from the finite number of particles (the stars themselves, giant molecular clouds, etc.) is amplified by the system's self-gravity. Both of these equations can be implemented using the numerical methods I have developed during my thesis: integrals over action space, treatment of resonant terms, sum over resonance numbers, computation of the response matrix, as well as efficient Fourier transforms in angle space. Of all of these, the computation of the response matrix is clearly the most time demanding, since it requires the careful computation of an integral with a resonant denominator. My numerical methods should therefore bring more efficiency to this process. For example, the Balescu-Lenard equation was recently implemented for isotropic and radially anisotropic star clusters (Hamilton et al., 2018), in order to compute the secular evolution of a star cluster in isolation. However, the results are still hard to compare to N-body simulations of star clusters (see, e.g., Lau & Binney, 2019). The formalism of Hamilton et al. (2018) may straightforwardly be adapted to anisotropic, rotating spheres, using my developments of the matrix method to account for the linear response of rotating clusters. Furthermore, the quasi-linear formalism should better describe systems where resonances have an important role, which I showed is the case of anisotropic, rotating ones. One may first try, as in Fouvry et al. (2015b), to work with tangentially anisotropic systems and the WKB approximation, which simplifies a lot the formalism. However, I have shown that for spheres, WKB waves do not allow for an accurate representation of the resonant processes at play. One can further show that, in this approximation, the tumbling term of the matrix vanishes. A consistent treatment of the secular evolution of anisotropic, rotating spheres should therefore use the full matrix formalism (in the spirit of Fouvry et al., 2015a).

A critical role in the secular evolution of star clusters appears to be played by neutral and weakly damped modes. In a stable system, these modes are the longest-lived remnants of every perturbations. Indeed, when the system undergoes a perturbation, most of the energy of the perturber is quickly absorbed by the star cluster, through dynamical friction and phase mixing. If the perturber excites a neutral or a weakly damped mode, then the mode drives non local exchanges of energy and angular momentum between the particles in the system. The importance of these modes implies that the linear and secular formalisms should be improved on two parallel fronts. On the one hand, one can rely on the possibility to finely sample the complex frequency space in order to build an accurate analytical prolongation of the response matrix in the lower-half plane, i.e. in the frequency space of damped modes. On the other, the numerical tools I developed can be used to efficiently compute orbital diffusion in the quasi-linear formalism. Such improvements may allow us to precisely characterise long-term dynamical

phenomena in spheroidal star clusters. At a time when ab initio cosmological simulations of large volume of our universe reach sufficient resolution to characterise the intricate resonant dynamics of stellar clusters, the linear response theory presented in this thesis, together with its quasi-linear counterpart, should prove enlightening to best make sense of how populations of self-gravitating systems evolve over a Hubble time.

Appendix A

The Lagrangian form of the response matrix

A.1 Relating the Eulerian and Lagrangian formulations

The response matrix of eq. (2.20) does not actually correspond to the original one from Kalnajs (1977). While I focused on a Eulerian description, considering perturbations in the DF, potential and density at fixed positions of phase space or configuration space, Kalnajs originally took the path of a Lagrangian description, following the perturbations to the individual particles' positions in phase space. The outcome of the original demonstration is the following form of the response matrix

$$\widehat{M}^{\mathrm{Lag}}_{pq}(\omega) = -(2\pi)^3 \sum_{\mathbf{n}} \int \mathrm{d}\mathbf{J}\, F(\mathbf{J})\, \mathbf{n} \cdot \frac{\partial}{\partial \mathbf{J}} \left(\frac{\psi^{(p)*}_{\mathbf{n}}(\mathbf{J})\, \psi^{(q)}_{\mathbf{n}}(\mathbf{J})}{\omega - \mathbf{n}\cdot\boldsymbol{\Omega}(\mathbf{J})} \right). \tag{A.1}$$

In order to relate this form to that proposed in eq. (2.20), I apply the divergence theorem

$$\int \mathrm{d}\mathbf{J}\, \frac{\partial}{\partial \mathbf{J}} \cdot \left(F(\mathbf{J})\, \frac{\psi^{(p)*}_{\mathbf{n}}(\mathbf{J})\, \psi^{(q)}_{\mathbf{n}}(\mathbf{J})}{\omega - \mathbf{n}\cdot\boldsymbol{\Omega}(\mathbf{J})}\, \mathbf{n} \right) = \int \mathrm{d}S \left(F(\mathbf{J})\, \frac{\psi^{(p)*}_{\mathbf{n}}(\mathbf{J})\, \psi^{(q)}_{\mathbf{n}}(\mathbf{J})}{\omega - \mathbf{n}\cdot\boldsymbol{\Omega}(\mathbf{J})} \right) (\mathbf{n}\cdot\mathbf{j}), \tag{A.2}$$

where $\mathrm{d}S$ is the surface element on the boundary of the 3D action space, and $\mathbf{j}$ is the unitary vector orthogonal to the surface and pointing outwards. The right-hand side is what is called the boundary term, and the left-hand side can be decomposed as

$$\begin{aligned} \int \mathrm{d}\mathbf{J}\, \frac{\partial}{\partial \mathbf{J}} \cdot \left(F(\mathbf{J})\, \frac{\psi^{(p)*}_{\mathbf{n}}(\mathbf{J})\, \psi^{(q)}_{\mathbf{n}}(\mathbf{J})}{\omega - \mathbf{n}\cdot\boldsymbol{\Omega}(\mathbf{J})}\, \mathbf{n} \right) &= \int \mathrm{d}\mathbf{J}\, \mathbf{n}\cdot\frac{\partial F}{\partial \mathbf{J}}\, \frac{\psi^{(p)*}_{\mathbf{n}}(\mathbf{J})\, \psi^{(q)}_{\mathbf{n}}(\mathbf{J})}{\omega - \mathbf{n}\cdot\boldsymbol{\Omega}(\mathbf{J})} \\ &\quad + \int \mathrm{d}\mathbf{J}\, F(\mathbf{J})\, \mathbf{n}\cdot\frac{\partial}{\partial \mathbf{J}} \left(\frac{\psi^{(p)*}_{\mathbf{n}}(\mathbf{J})\, \psi^{(q)}_{\mathbf{n}}(\mathbf{J})}{\omega - \mathbf{n}\cdot\boldsymbol{\Omega}(\mathbf{J})} \right). \end{aligned} \tag{A.3}$$

Adding all resonance vectors $\mathbf{n}$ and multiplying by $(2\pi)^3$, I get

$$\widehat{M}^{\mathrm{Lag}}_{pq}(\omega) = \widehat{M}_{pq}(\omega) - (2\pi)^3 \sum_{\mathbf{n}} \int \mathrm{d}S\, F(\mathbf{J})\, \frac{\psi^{(p)*}_{\mathbf{n}}(\mathbf{J})\, \psi^{(q)}_{\mathbf{n}}(\mathbf{J})}{\omega - \mathbf{n}\cdot\boldsymbol{\Omega}(\mathbf{J})}\, (\mathbf{n}\cdot\mathbf{j}), \tag{A.4}$$

where $\widehat{\mathbf{M}}$ is the Eulerian matrix. Jalali & Hunter (2005) argue that the Lagrangian form takes into account the orbital perturbations at the boundary of the integration space, while the Eulerian form misses the boundary term. The authors show that for disk systems with 2D DFs, by multiplying the DF by Heaviside functions at the boundaries, the edge term can be recovered. I show here that, in 3D systems too, this replacement recovers the missing term in eq. (A.4). Applying such a replacement amounts to adding to each term in the sum over resonance vectors the expression

$$\int \mathrm{d}\mathbf{J}\, F(\mathbf{J})\, \mathbf{n}\cdot\frac{\partial \big(H(J_r) H(L - |L_z|) \big)}{\partial \mathbf{J}}\, \frac{\psi^{(p)*}_{\mathbf{n}}(\mathbf{J})\, \psi^{(q)}_{\mathbf{n}}(\mathbf{J})}{\omega - \mathbf{n}\cdot\boldsymbol{\Omega}(\mathbf{J})}, \tag{A.5}$$

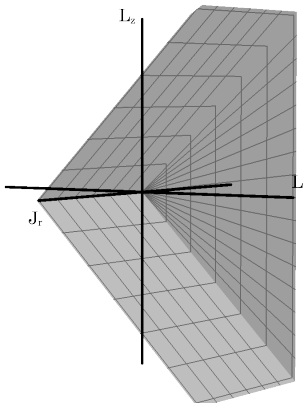

Figure A.1: Surface of the 3D action space where the orbits are physically allowed.

where a superfluous $H(L)$ term was omitted, since it is redundant with $H(L-|L_z|)$.

Let me relate the three additive terms in the scalar product $\mathbf{n}\cdot\partial/\partial\mathbf{J}$ of eq. (A.5) to parts of the surface integral in eq. (A.4). That surface integral can be decomposed into several surfaces: those that are at infinity give no contribution to the integral, as the DF is 0 at infinity; the surface $J_r=0$, delimited by the lines $L_z=\pm L$; the surface $L_z=L$, with $J_r>0$; the surface $L_z=-L$, with $J_r>0$. These surfaces are represented in Fig. A.1. On the surface $J_r=0$, the surface elements is $\mathrm{d}S=\mathrm{d}L\,\mathrm{d}L_z$ and the normal vector is $\mathbf{j}=-\mathbf{e}_1$, where $(\mathbf{e}_1,\mathbf{e}_2,\mathbf{e}_3)$ is the basis of space. As a consequence, the resulting surface integral is

$$-n_1\int\mathrm{d}L\,\mathrm{d}L_z\,F(0,L,L_z)\,\frac{\psi_{\mathbf{n}}^{(p)*}(0,L,L_z)\,\psi_{\mathbf{n}}^{(q)}(0,L,L_z)}{\omega-\mathbf{n}\cdot\boldsymbol{\Omega}(0,L,L_z)}. \tag{A.6}$$

Considering the minus sign in eq. (A.4), this term corresponds to the term $\partial/\partial J_r$ in eq. (A.5). On the surface $L_z=L$, I have $\mathrm{d}S=\mathrm{d}J_r\,(\sqrt{2}\,\mathrm{d}L)$, and $\mathbf{j}=(-\mathbf{e}_2+\mathbf{e}_3)/\sqrt{2}$, so the resulting surface integral is

$$(-n_2+n_3)\int\mathrm{d}J_r\,\mathrm{d}L\,F(J_r,L,L)\,\frac{\psi_{\mathbf{n}}^{(p)*}(J_r,L,L)\,\psi_{\mathbf{n}}^{(q)}(J_r,L,L)}{\omega-\mathbf{n}\cdot\boldsymbol{\Omega}(J_r,L,L)}. \tag{A.7}$$

Finally, on the surface $L_z=-L$, the surface integral is

$$(-n_2-n_3)\int\mathrm{d}J_r\,\mathrm{d}L\,F(J_r,L,-L)\,\frac{\psi_{\mathbf{n}}^{(p)*}(J_r,L,-L)\,\psi_{\mathbf{n}}^{(q)}(J_r,L,-L)}{\omega-\mathbf{n}\cdot\boldsymbol{\Omega}(J_r,L,-L)}. \tag{A.8}$$

On the other hand, I have

$$\frac{\partial H(L-|L_z|)}{\partial L}=\delta(L-|L_z|)\;\;;\;\;\frac{\partial H(L-|L_z|)}{\partial L_z}=-\delta(L-L_z)+\delta(L+L_z), \tag{A.9}$$

so the corresponding terms in eq. (A.5) are, for $\partial/\partial L$,

$$\begin{aligned}n_2\Bigg[&\int\mathrm{d}J_r\,\mathrm{d}L\,F(J_r,L,L)\,\frac{\psi_{\mathbf{n}}^{(p)*}(J_r,L,L)\,\psi_{\mathbf{n}}^{(q)}(J_r,L,L)}{\omega-\mathbf{n}\cdot\boldsymbol{\Omega}(J_r,L,L)}\\&+\int\mathrm{d}J_r\,\mathrm{d}L\,F(J_r,L,-L)\,\frac{\psi_{\mathbf{n}}^{(p)*}(J_r,L,-L)\,\psi_{\mathbf{n}}^{(q)}(J_r,L,-L)}{\omega-\mathbf{n}\cdot\boldsymbol{\Omega}(J_r,L,-L)}\Bigg],\end{aligned} \tag{A.10}$$

and for $\partial/\partial L_z$,

$$\begin{aligned}n_3\Bigg[&-\int\mathrm{d}J_r\,\mathrm{d}L\,F(J_r,L,L)\,\frac{\psi_{\mathbf{n}}^{(p)*}(J_r,L,L)\,\psi_{\mathbf{n}}^{(q)}(J_r,L,L)}{\omega-\mathbf{n}\cdot\boldsymbol{\Omega}(J_r,L,L)}\\&+\int\mathrm{d}J_r\,\mathrm{d}L\,F(J_r,L,-L)\,\frac{\psi_{\mathbf{n}}^{(p)*}(J_r,L,-L)\,\psi_{\mathbf{n}}^{(q)}(J_r,L,-L)}{\omega-\mathbf{n}\cdot\boldsymbol{\Omega}(J_r,L,-L)}\Bigg].\end{aligned} \tag{A.11}$$

This proves that in 3D integrable systems, multiplying the DF by edge Heaviside functions recovers all of the boundary terms.

While the boundary terms are sometimes important for 2D systems, as is discussed by Jalali & Hunter (2005), especially for radial orbits at the boundary $L = 0$, 3D systems are quite different. Indeed, the radial orbits now represent only a line in the permitted region of 3D action space, so that the corresponding boundary term must be singular to make a difference. In other words, as soon as the system does not involve a macroscopic amount of purely radial orbits, which is excluded for density distributions that are smooth in the centre, the corresponding boundary term can be neglected. On the other hand, new boundary terms appear at $L = |L_z|$, corresponding to perturbations in the inclination of orbits in the equatorial plane that could make their inclination even smaller. As this type of perturbations seems unphysical, it can be shown, using the properties of the basis elements $\psi^{(p)}_{\mathbf{n}}$, that the corresponding boundary term actually vanishes in all 3D cases. For the boundary term corresponding to $L_z = L$, eq. (A.7), developing the Fourier-transformed basis elements following eq. (2.33) gives

$$(-n_2+n_3)\int \mathrm{d}J_r\,\mathrm{d}L\,F(J_r,L,L)\,\frac{\delta^{n_3}_{m^p}\delta^{n_3}_{m^q}Y^{n_2}_{\ell^p}Y^{n_2}_{\ell^q}R^{\ell^p}_{n_2m^p}(0)R^{\ell^q}_{n_2m^q}(0)\,W^{\tilde{\mathbf{n}}}_{\ell^pn^p}(\widetilde{\mathbf{J}})W^{\tilde{\mathbf{n}}}_{\ell^qn^q}(\widetilde{\mathbf{J}})}{\omega-\mathbf{n}\cdot\boldsymbol{\Omega}(J_r,L,L)}. \tag{A.12}$$

Now, the rotation matrix $R^{\ell^p}_{n_2m^p}(0)$ is equal to $\delta^{m^p}_{n_2}$, so the resulting integral is proportional to $\delta^{n_3}_{n_2}$, which multiplied by $(-n_2+n_3)$ gives 0. The same occurs with the edge term $L_z = -L$, with $R^{\ell^p}_{n_2m^p}(\pi)$ being equal to $\delta^{-m^p}_{n_2}$, which is sufficient to justify that the whole term vanishes. Finally, the boundary term on the surface $J_r = 0$ follows the same fate as is discussed in Jalali & Hunter (2005) for disks: whenever $n_1 \neq 0$, the Fourier-transformed elements of the basis $\psi^{(p)}_{\mathbf{n}}(0,L,L_z)$ vanish, so the product of eq. (A.7) vanishes whatever n_1. A detailed proof of the vanishing of the basis elements at $J_r = 0$ will be given in Section 3.5.

All in all, I proved that in most 3D cases, the Eulerian and the Lagrangian form of the response matrix are equivalent. Note that such a demonstration was already produced in Polyachenko & Shukhman (2015). This justifies that throughout the manuscript, I alternatively pick the formulation that seems most handy. Section A.2 details the expression of the Lagrangian matrix for non-rotating spheres, exhibiting terms that require a numerical treatment which slightly differs from that used in the computation of the Eulerian matrix, especially concerning the action space integration. The way the integration is dealt with is detailed in Section A.3.2.

A.2 The case of non-rotating spheres

In order to compute the Lagrangian version of the response matrix in cases where it is more handy, I simplify here the expression of the response matrix in the case of a non-rotating sphere. Starting with eq. (A.1), one can essentially follow the same steps that led to the simplification of the Eulerian matrix. Using eq. (2.33) for the basis elements, one gets

$$\widehat{M}^{\mathrm{Lag}}_{pq}(\omega) = -(2\pi)^3\delta^{m^q}_{m^p}\sum_{\mathbf{n}}Y^{n_2}_{\ell^p}Y^{n_2}_{\ell^q}\int\mathrm{d}\mathbf{J}\,F_0(\widetilde{\mathbf{J}})\,\mathbf{n}\cdot\frac{\partial}{\partial\mathbf{J}}\left(\frac{R^{\ell^p}_{n_2m^p}(i)\,W^{\tilde{\mathbf{n}}}_{\ell^pn^p}(\widetilde{\mathbf{J}})\,R^{\ell^q}_{n_2m^q}(i)\,W^{\tilde{\mathbf{n}}}_{\ell^qn^q}(\widetilde{\mathbf{J}})}{\omega-\tilde{\mathbf{n}}\cdot\widetilde{\boldsymbol{\Omega}}(\widetilde{\mathbf{J}})}\right). \tag{A.13}$$

Separating the divergence term in the integrand, the matrix can be expressed as

$$\widehat{M}^{\mathrm{Lag}}_{pq}(\omega) = N_{pq}(\omega) + O_{pq}(\omega), \tag{A.14}$$

where

$$N_{pq}(\omega) = -(2\pi)^3\delta^{m^q}_{m^p}\sum_{\mathbf{n}}\delta^{m^p}_{n_3}Y^{n_2}_{\ell^p}Y^{n_2}_{\ell^q}\int\mathrm{d}\mathbf{J}\,F_0(\widetilde{\mathbf{J}})\,\mathbf{n}\cdot\frac{\partial}{\partial\mathbf{J}}\left(R^{\ell^p}_{n_2m^p}(i)\,R^{\ell^q}_{n_2m^q}(i)\right)\frac{W^{\tilde{\mathbf{n}}}_{\ell^pn^p}(\widetilde{\mathbf{J}})\,W^{\tilde{\mathbf{n}}}_{\ell^qn^q}(\widetilde{\mathbf{J}})}{\omega-\tilde{\mathbf{n}}\cdot\widetilde{\boldsymbol{\Omega}}(\widetilde{\mathbf{J}})} \tag{A.15}$$

$$O_{pq}(\omega) = -(2\pi)^3\delta^{m^q}_{m^p}\sum_{\tilde{\mathbf{n}}}Y^{n_2}_{\ell^p}Y^{n_2}_{\ell^q}\int\mathrm{d}\mathbf{J}\,F_0(\widetilde{\mathbf{J}})\,\tilde{\mathbf{n}}\cdot\frac{\partial}{\partial\widetilde{\mathbf{J}}}\left(\frac{W^{\tilde{\mathbf{n}}}_{\ell^pn^p}(\widetilde{\mathbf{J}})\,W^{\tilde{\mathbf{n}}}_{\ell^qn^q}(\widetilde{\mathbf{J}})}{\omega-\tilde{\mathbf{n}}\cdot\widetilde{\boldsymbol{\Omega}}(\widetilde{\mathbf{J}})}\right)R^{\ell^p}_{n_2m^p}(i)\,R^{\ell^q}_{n_2m^q}(i). \tag{A.16}$$

Let me focus on the simplification of N, and consider the fact that

$$\mathbf{n}\cdot\frac{\partial}{\partial\mathbf{J}}\left(R^{\ell^p}_{n_2m^p}(i)\,R^{\ell^q}_{n_2m^q}(i)\right) = \left(\frac{n_2}{L\tan i}-\frac{n_3}{L\sin i}\right)\frac{\partial(R^{\ell^p}_{n_2m^p}(i)\,R^{\ell^q}_{n_2m^q}(i))}{\partial i}. \tag{A.17}$$

Changing integration variables from L_z to i, I have

$$\begin{aligned}\int_{-L}^{L}\mathrm{d}L_z\,\mathbf{n}\cdot\frac{\partial}{\partial\mathbf{J}}\left(R^{\ell^p}_{n_2m^p}(i)\,R^{\ell^q}_{n_2m^q}(i)\right) &= \int_0^\pi \mathrm{d}i\,(n_2\cos i - n_3)\,\frac{\partial(R^{\ell^p}_{n_2m^p}(i)\,R^{\ell^q}_{n_2m^q}(i))}{\partial i}\\ &= n_2\left(\left[R^{\ell^p}_{n_2m^p}(i)\,R^{\ell^q}_{n_2m^q}(i)\,\cos i\right]_0^\pi + \int_0^\pi \mathrm{d}i\,\sin i\,R^{\ell^p}_{n_2m^p}(i)\,R^{\ell^q}_{n_2m^q}(i)\right)\\ &\quad - n_3\left[R^{\ell^p}_{n_2m^p}(i)\,R^{\ell^q}_{n_2m^q}(i)\right]_0^\pi\\ &= -(n_2+n_3)\,\delta^{-m^p}_{n_2}\,\delta^{-m^q}_{n_2} + (n_3-n_2)\,\delta^{m^p}_{n_2}\,\delta^{m^q}_{n_2} + n_2\frac{2\delta^{\ell^q}_{\ell^p}}{2\ell^p+1},\end{aligned} \tag{A.18}$$

where the orthogonality relation (2.38) was used, as well as the values of the rotation matrix at 0 and π. At this stage, N can be simplified as

$$N_{pq}(\omega) = -\delta^{m^q}_{m^p}\delta^{\ell^q}_{\ell^p}\sum_{\widetilde{\mathbf{n}}} C^{n_2}_{\ell^p}\int\mathrm{d}\widetilde{\mathbf{J}}\,F_0(\widetilde{\mathbf{J}})n_2\frac{W^{\widetilde{\mathbf{n}}}_{\ell^pn^p}(\widetilde{\mathbf{J}})\,W^{\widetilde{\mathbf{n}}}_{\ell^qn^q}(\widetilde{\mathbf{J}})}{\omega-\widetilde{\mathbf{n}}\cdot\widetilde{\mathbf{\Omega}}(\widetilde{\mathbf{J}})}, \tag{A.19}$$

where C^n_ℓ is defined in the same way as eq. (2.41).

The simplification of O is more straightforward, as the integral over L_z can be readily computed, giving

$$O_{pq}(\omega) = -\delta^{m^q}_{m^p}\,\delta^{\ell^q}_{\ell^p}\sum_{\widetilde{\mathbf{n}}} C^{n_2}_{\ell^p}\int\mathrm{d}\widetilde{\mathbf{J}}\,F_0(\widetilde{\mathbf{J}})\,L\,\widetilde{\mathbf{n}}\cdot\frac{\partial}{\partial\widetilde{\mathbf{J}}}\left(\frac{W^{\widetilde{\mathbf{n}}}_{\ell^pn^p}(\widetilde{\mathbf{J}})\,W^{\widetilde{\mathbf{n}}}_{\ell^qn^q}(\widetilde{\mathbf{J}})}{\omega-\widetilde{\mathbf{n}}\cdot\widetilde{\mathbf{\Omega}}(\widetilde{\mathbf{J}})}\right). \tag{A.20}$$

Noticing that for any function $f(\widetilde{\mathbf{J}})$,

$$L\,\widetilde{\mathbf{n}}\cdot\frac{\partial f(\widetilde{\mathbf{J}})}{\partial\widetilde{\mathbf{J}}} + n_2\,f(\widetilde{\mathbf{J}}) = \widetilde{\mathbf{n}}\cdot\frac{\partial[L\,f(\widetilde{\mathbf{J}})]}{\partial\widetilde{\mathbf{J}}}, \tag{A.21}$$

N and O can be added to give

$$\boxed{\widehat{M}^{\mathrm{Lag}}_{pq}(\omega) = \delta^{m^q}_{m^p}\,\delta^{\ell^q}_{\ell^p}\sum_{\widetilde{\mathbf{n}}} C^{n_2}_{\ell^p}\,P^{\widetilde{\mathbf{n}},\mathrm{Lag}}_{\ell^pn^p\ell^qn^q}(\omega),} \tag{A.22}$$

where I defined the new term

$$\boxed{P^{\widetilde{\mathbf{n}},\mathrm{Lag}}_{\ell^pn^p\ell^qn^q}(\omega) = -\int\mathrm{d}\widetilde{\mathbf{J}}\,F_0(\widetilde{\mathbf{J}})\,\widetilde{\mathbf{n}}\cdot\frac{\partial}{\partial\widetilde{\mathbf{J}}}\left(\frac{L\,W^{\widetilde{\mathbf{n}}}_{\ell^pn^p}(\widetilde{\mathbf{J}})\,W^{\widetilde{\mathbf{n}}}_{\ell^qn^q}(\widetilde{\mathbf{J}})}{\omega-\widetilde{\mathbf{n}}\cdot\widetilde{\mathbf{\Omega}}(\widetilde{\mathbf{J}})}\right).} \tag{A.23}$$

At that point, one can notice that the same result could be obtained by applying the divergence theorem to eq. (2.42), given that the edge terms are vanishing.

A.3 Computing the Lagrangian matrix

Let me now give some details about the developments required to efficiently compute the Lagrangian matrix, as given by the expression from eq. (A.23). First, I present how partial derivatives of the functions in the integrand are computed, then I detail the specific functions for the sub-region integration in the Lagrangian case.

A.3.1 Partial derivatives

In practice, the computation of the Lagrangian matrix requires developing the divergence in $P^{\widetilde{\mathbf{n}},\mathrm{Lag}}_{\ell^pn^p\ell^qn^q}(\omega)$. As explained in Section 2.4.1, the variables used for the computation of all the functions depending on action space coordinates are $(r_\mathrm{p}, r_\mathrm{a})$. Additionally, the development of the divergence leads to

$$\widetilde{\mathbf{n}}\cdot\frac{\partial}{\partial\widetilde{\mathbf{J}}}\left(\frac{L\,W^{\widetilde{\mathbf{n}}}_{\ell^pn^p}(\widetilde{\mathbf{J}})W^{\widetilde{\mathbf{n}}}_{\ell^qn^q}(\widetilde{\mathbf{J}})}{\omega-\widetilde{\mathbf{n}}\cdot\widetilde{\mathbf{\Omega}}(\widetilde{\mathbf{J}})}\right) = \frac{\widetilde{\mathbf{n}}\cdot\frac{\partial}{\partial\widetilde{\mathbf{J}}}[L\,W^{\widetilde{\mathbf{n}}}_{\ell^pn^p}(\widetilde{\mathbf{J}})W^{\widetilde{\mathbf{n}}}_{\ell^qn^q}(\widetilde{\mathbf{J}})]}{\omega-\widetilde{\mathbf{n}}\cdot\widetilde{\mathbf{\Omega}}(\widetilde{\mathbf{J}})} + \frac{L\,W^{\widetilde{\mathbf{n}}}_{\ell^pn^p}(\widetilde{\mathbf{J}})W^{\widetilde{\mathbf{n}}}_{\ell^qn^q}(\widetilde{\mathbf{J}})}{(\omega-\widetilde{\mathbf{n}}\cdot\widetilde{\mathbf{\Omega}}(\widetilde{\mathbf{J}}))^2}\,\widetilde{\mathbf{n}}\cdot\frac{\partial}{\partial\widetilde{\mathbf{J}}}[\widetilde{\mathbf{n}}\cdot\widetilde{\mathbf{\Omega}}(\widetilde{\mathbf{J}})], \tag{A.24}$$

so that the resonant denominator does not have the same behaviour as in the case of the Eulerian matrix. The algorithm for sub-region integration of the Lagrangian matrix is detailed Section A.3.2, here I give some elements of the computation of the relevant functions in $(r_\mathrm{p}, r_\mathrm{a})$ variables.

First, let me focus on the last term of eq. (A.24), which is the simplest. Section 2.4.1 already shows how to express L, $\widetilde{\mathbf{\Omega}}$ and W as a function of $r_\mathrm{p}, r_\mathrm{a}$, the remaining complexity resides in the derivative. Using successive changes of variables from (J_r, L) through (E, L) to $(r_\mathrm{p}, r_\mathrm{a})$, together with the right formulae for changes of variables in partial derivatives, one gets for any function $f(\widetilde{\mathbf{J}})$

$$\widetilde{\mathbf{n}} \cdot \frac{\partial f}{\partial \widetilde{\mathbf{J}}} = \frac{1}{\frac{\partial J_2}{\partial r_\mathrm{a}}\frac{\partial E}{\partial r_\mathrm{p}} - \frac{\partial J_2}{\partial r_\mathrm{p}}\frac{\partial E}{\partial r_\mathrm{a}}} \left[\widetilde{\mathbf{n}} \cdot \widetilde{\mathbf{\Omega}} \left(\frac{\partial f}{\partial r_\mathrm{p}}\frac{\partial J_2}{\partial r_\mathrm{a}} - \frac{\partial f}{\partial r_\mathrm{a}}\frac{\partial J_2}{\partial r_\mathrm{p}} \right) - n_2 \left(\frac{\partial f}{\partial r_\mathrm{p}}\frac{\partial E}{\partial r_\mathrm{a}} - \frac{\partial f}{\partial r_\mathrm{a}}\frac{\partial E}{\partial r_\mathrm{p}} \right) \right]. \tag{A.25}$$

Hence, the problem is now reduced to the computation of derivatives w.r.t. r_p and r_a. For the frequencies, the derivatives are easily computed when one regularises the edge divergence in the integrals of eq. (2.59) with the change of variables defined by eq. (2.63), giving

$$\begin{aligned}
\Omega_1 &= \frac{1}{\pi}\int_{-1}^{1} \mathrm{d}u\, \Delta\, f'(u)\, [2(E - \psi(r(u))) - L^2/r(u)^2]^{-1/2} \\
\Omega_2 &= \frac{\Omega_1}{\pi}\int_{-1}^{1} \mathrm{d}u\, \Delta\, f'(u)\, \frac{L}{r(u)^2}\, [2(E - \psi(r(u))) - L^2/r(u)^2]^{-1/2}.
\end{aligned} \tag{A.26}$$

Considering Δ, E, $r(u)$ and L as functions of r_p and r_a, I can now straightforwardly carry out the derivatives of the frequencies w.r.t. r_p and r_a.

Now, focusing on the first term in the right hand side of eq. (A.24), the divergence in the numerator needs to be developed. Again, the problem of the computation of the numerator amounts to computing derivatives of L and W w.r.t. r_p and r_a. While eq. (2.57) allows for the computation of the derivatives of L, eqs. (2.64) and (2.65) allow for the computation of the derivatives of the angles w.r.t. r_p and r_a, which in turns allows for the derivation of W by deriving inside the integral. In practice, the treatment of the nested integrals in the computation of $\partial W/\partial r_\mathrm{p}$ and $\partial W/\partial r_\mathrm{a}$ can be straightforwardly adapted from the one developed in Section 2.4.2 for the computation of W.

A.3.2 Sub-region integration

As I showed in this appendix, and in particular eq. (A.24), a second type of integral is required to compute the Lagrangian response matrix, namely

$$\int \mathrm{d}r_\mathrm{p}\, \mathrm{d}r_\mathrm{a}\, \frac{g^{\widetilde{\mathbf{n}}}_{\ell^p n^p \ell^q n^q}(r_\mathrm{p}, r_\mathrm{a})}{\left[\omega - h^{\widetilde{\mathbf{n}}}(r_\mathrm{p}, r_\mathrm{a})\right]^2}. \tag{A.27}$$

Following Section 2.4.3, I implemented the integral as the sum over small squares of approximate analytical expressions, computed by taking first order developments of g and h around the centre of the square. On a single square, the integral is now equal to

$$\aleph^2(a_g, b_g, c_g, a_h, b_h, c_h, \Delta r, \eta) = \int_{-\frac{\Delta r}{2}}^{\frac{\Delta r}{2}} \mathrm{d}x_\mathrm{p} \int_{-\frac{\Delta r}{2}}^{\frac{\Delta r}{2}} \mathrm{d}x_\mathrm{a}\, \frac{a_g + b_g x_\mathrm{p} + c_g x_\mathrm{a}}{\left[a_h + b_h x_\mathrm{p} + c_h x_\mathrm{a} + \mathrm{i}\,\eta\right]^2}. \tag{A.28}$$

Assuming that $a_g, a_h \neq 0$ and using the change of variables $x = x_p/\Delta r$ and $y = x_a/\Delta r$, one can simplify this integral as

$$\aleph^2(a_g, b_g, c_g, a_h, b_h, c_h, \Delta r, \eta) = \frac{a_g}{a_h^2}\Delta r^2 \aleph^2_\mathrm{D}\left(\frac{b_g\Delta r}{a_g}, \frac{c_g\Delta r}{a_g}, \frac{b_h\Delta r}{a_h}, \frac{c_h\Delta r}{a_h}, \frac{\eta}{a_h}\right), \tag{A.29}$$

with the dimensionless integral

$$\aleph^2_\mathrm{D}(b, c, e, f, \eta) = \int_{-\frac{1}{2}}^{\frac{1}{2}} \int_{-\frac{1}{2}}^{\frac{1}{2}} \mathrm{d}x\mathrm{d}y\, \frac{1 + bx + cy}{\left[1 + ex + fy + \mathrm{i}\eta\right]^2}. \tag{A.30}$$

An antiderivative to the integrand is given by

$$\begin{aligned}
H(x, y) = &-\frac{1}{2\,d^2\,e^2}\,\mathrm{i}\left[e\,(b\,e\,y + \mathrm{i}\,b\,\eta + b - d) + c\,d\,(d\,x + \mathrm{i}\,\eta + 1)\right] \\
&\times \left\{ 2\cot^{-1}\left(\frac{\eta}{d\,x + e\,y + 1}\right) + \mathrm{i}\log\left[4\left((d\,x + e\,y + 1)^2 + \eta^2\right)\right] \right\}.
\end{aligned} \tag{A.31}$$

Interestingly enough, this antiderivative has a much simpler form than that for the Eulerian matrix in eq. (2.77). This simplicity can be related to the fact that the integrand in eq. (A.30) is closer to an f'/f form than that of eq. (2.76).

Appendix B

Influence of the discontinuity of Lynden-Bell's demon on instabilities

The analytical and numerical results of Section 4.5 detect instabilities in a variety of rotating star clusters. In this study, the DF relies on Lynden-Bell's demon (see eq. (4.17)) and therefore has a discontinuity in the velocity space, as illustrated by Fig. 4.4. Later, in Section 5.2, I develop the response matrix for smoother distributions of the angular momentum in the system, and show that this treatment is reliable by comparing the results to N-body simulations (see Section 5.3.1). Let me use a similar setup to show that the unstable behaviour detected in these studies cannot be solely attributed to the DF's discontinuity.

In order to tackle this question, I used the response matrix of eq. (4.1) with a series of choices for the function g which continuously connect a smooth DF to the discontinuous one. For that purpose, I used the parametrisation

$$g_a(x) = \frac{\mathrm{erf}(ax)}{\mathrm{erf}(a)}, \tag{B.1}$$

where erf is the error function. When the parameter a is varied, the profiles for g_a are given by Fig. B.1a. The functions all match the requirements for g, i.e. they are odd and their maximum amplitude is 1. For $a \ll 1$, g_a approaches the identity, and is therefore maximally smooth (given the constraint that its maximum should be 1). When a is increased, g_a gradually increases its gradient near $x = 0$, until it reaches the Sign(x) function when $a \to \infty$.

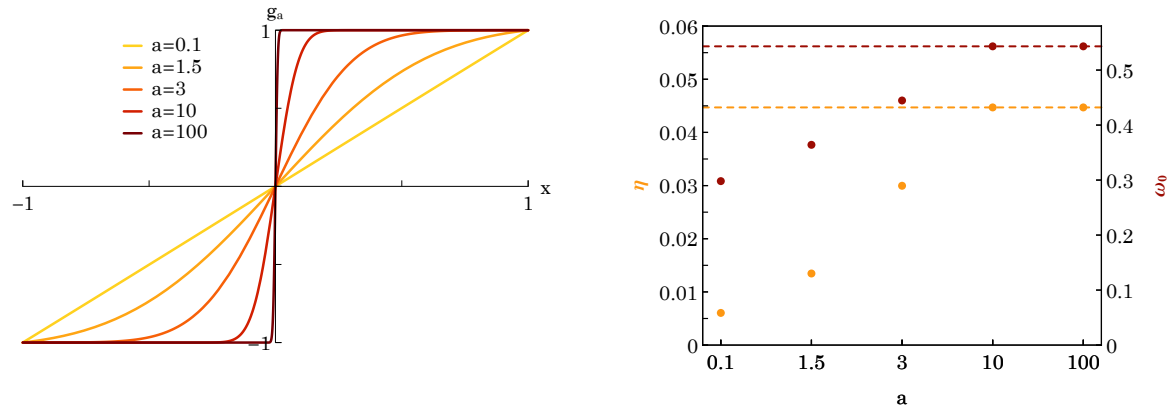

(a) g_a profiles

(b) Stability measurements

Figure B.1: (a) Profiles of the function g_a for different values of a. When $a \ll 1$, g_a approaches the identity. When $a \gg 1$, g_a approaches the Sign function. (b) Growth rates (η) and oscillation frequencies (ω_0) measured from the matrix method. The setup is identical to the standard case of the convergence study in Section 4.5.2.1 (see Table 4.1). The horizontal, dashed lines indicate the results found with the Sign function, corresponding to the discontinuous case. Clearly, there is a continuous transition both in η and ω_0 from the sharp to the smooth DF.

I detected modes in such systems using the matrix method, with the same setup as the standard case

of the convergence study in Section 4.5.2.1 ($q = -6$, $\alpha = 1$, same numerical parameters). The measured growth rates and pattern speeds are represented in Fig. B.1b. In the smoothest $a = 0.1$ case, an instability was detected with sensibly lower growth rate and oscillation frequency. When a is increased, η and ω continuously increase towards a value identical to that obtained with the discontinuous DF. This is solid evidence that the instabilities found with the discontinuous DF cannot be attributed to the discontinuity.

Appendix C

Resonances in inclined epicyclic motions perturbed by a rotating bar

In the context of disk dynamics, Binney & Tremaine (2008, Section 3.3.3) use the expression $\psi(R,\phi) = \psi_{\rm b}(R)\cos[2(\phi-\Omega_{\rm b}t)]$ as a model for the potential of a planar bar, where R,ϕ are plane polar coordinates in the orbital plane, $\Omega_{\rm b}$ is the pattern speed, and $\psi_{\rm b}$ specifies the radial dependence of the potential. The obvious extension to three dimensions is $\psi(r,\theta,\phi) = \psi_{\rm b}(r)\,\sin^2\theta\,\cos[2(\phi-\Omega_{\rm b}t)]$ in spherical coordinates, since the angle-dependence is that of an $\ell = 2$ spherical harmonic.

Let me consider the first-order perturbing potential of a particle which, at lowest order, is in epicyclic motion on a plane inclined at inclination i to the x,y plane ($\theta = \pi/2$), and passes its ascending node at longitude Ω at time $t = 0$[1]. In cylindrical polar coordinates (R,ϕ,z) based on the orbital plane, with the angular coordinate $\phi = 0$ at the node, it is easy (but a bit tedious) to show that

$$\psi_1(R,\phi,z=0) = \frac{1}{4}\psi_{\rm b}(R)\big\{2\sin^2 i\,\cos[2(\Omega-\Omega_{\rm b}t)] + (1+\cos i)^2\cos[2(\Omega-\Omega_{\rm b}t+\phi)] + (1-\cos i)^2\cos[2(\Omega-\Omega_{\rm b}t-\phi)]\big\}. \tag{C.1}$$

Now I make use of the epicyclic approximation, by which (see eq. (3.31))

$$\begin{aligned} R &= R_{\rm g} - A_R\cos\theta_1, \\ \phi &= \theta_2 + \frac{2\Omega}{\kappa}\frac{A_R}{R_{\rm g}}\sin\theta_1. \end{aligned} \tag{C.2}$$

Substituting eqs. (C.2) into eq. (C.1) and expanding to lowest order in A_R, one can readily locate all trigonometrical terms of the form

$$\left\{\begin{array}{c}\cos\\ \sin\end{array}\right\}\big[2(\Omega-\Omega_{\rm b}t) + n_1\theta_1 + n_2\theta_2\big], \tag{C.3}$$

where n_1, n_2 are (small) integers. This includes the pair (0,0), which arises from the first term in eq. (C.1). Using the fact that $\dot\theta_{1,2} = \Omega_{1,2}$ (the radial and azimuthal frequencies), these terms yield the resonances listed in Table 5.1, including the stated i-dependence and the values in the last column.

[1] Here, Ω should not be confused with the circular angular velocity, used elsewhere in the rest of the manuscript.

Bibliography

Alimi, J.-M., Perez, J., & Serna, A. 1999, MNRAS, 305, 859
Allen, A. J., Palmer, P. L., & Papaloizou, J. C. B. 1992, MNRAS, 256, 695
An, J. H., & Evans, N. W. 2006, AJ, 131, 782
Anderson, J., & King, I. R. 2003, AJ, 126, 772
Antoja, T., Helmi, A., Romero-Gómez, M., et al. 2018, Nature, 561, 360
Antonini, F., Capuzzo-Dolcetta, R., & Merritt, D. 2009, MNRAS, 399, 671
Antonov, V. A. 1961, Soviet Ast., 4, 859
Antonov, V. A. 1973, in Dynamics of Galaxies and Star Clusters, 139–143
Aoki, S., Noguchi, M., & Iye, M. 1979, PASJ, 31, 737
Athanassoula, E. 2008, MNRAS, 390, L69
Aubert, D., Pichon, C., & Colombi, S. 2004, MNRAS, 352, 376
Bacon, R., Copin, Y., Monnet, G., et al. 2001, MNRAS, 326, 23
Baes, M., & van Hese, E. 2007, A&A, 471, 419
Ballone, A., Mapelli, M., Di Carlo, U. N., et al. 2020, MNRAS, 496, 49
Barazza, F. D., Jogee, S., & Marinova, I. 2008, ApJ, 675, 1194
Barnes, J., Goodman, J., & Hut, P. 1986, ApJ, 300, 112
Baumgardt, H., & Makino, J. 2003, MNRAS, 340, 227
Bellini, A., Libralato, M., Bedin, L. R., et al. 2018, ApJ, 853, 86
Berman, R. H., & Mark, J. W. K. 1979, A&A, 77, 31
Bertin, G., Pegoraro, F., Rubini, F., & Vesperini, E. 1994, ApJ, 434, 94
Bett, P., Eke, V., Frenk, C. S., et al. 2007, MNRAS, 376, 215
Bianchini, P., Sills, A., & Miholics, M. 2017, MNRAS, 471, 1181
Bianchini, P., van der Marel, R. P., del Pino, A., et al. 2018, MNRAS, 481, 2125
Binney, J., & Lacey, C. 1988, MNRAS, 230, 597
Binney, J., & Tremaine, S. 2008, Galactic Dynamics: Second Edition (Princeton University Press)
Blumenthal, G. R., Faber, S. M., Primack, J. R., & Rees, M. J. 1984, Nature, 311, 517
Bonnivard, V., Combet, C., Maurin, D., & Walker, M. G. 2015, MNRAS, 446, 3002
Borzyszkowski, M., Porciani, C., Romano-Díaz, E., & Garaldi, E. 2017, MNRAS, 469, 594
Breen, P. G., Rozier, S., Varri, A. L., & Heggie, D. C. 2020, MNRAS, submitted
Breen, P. G., Varri, A. L., & Heggie, D. C. 2017, MNRAS, 471, 2778
Bryan, S. E., Kay, S. T., Duffy, A. R., et al. 2013, MNRAS, 429, 3316
Bullock, J. S., Dekel, A., Kolatt, T. S., et al. 2001, ApJ, 555, 240
Cappellari, M. 2008, MNRAS, 390, 71
Cappellari, M., Emsellem, E., Krajnović, D., et al. 2011, MNRAS, 413, 813
Carretta, E., Bragaglia, A., Gratton, R. G., et al. 2009, A&A, 505, 117
Chandrasekhar, S. 1942, Principles of Stellar Dynamics (University of Chicago Press)
Chandrasekhar, S. 1943a, ApJ, 97, 255
—. 1943b, ApJ, 97, 263
—. 1949, Rev. Mod. Phys., 21, 383
Chavanis, P.-H. 2012, Physica A, 391, 3680
Choi, H., Yi, S. K., Dubois, Y., et al. 2018, ApJ, 856, 114
Clutton-Brock, M. 1972, Ap&SS, 16, 101
—. 1973, Ap&SS, 23, 55
Codis, S., Pichon, C., Devriendt, J., et al. 2012, MNRAS, 427, 3320
Codis, S., Pichon, C., & Pogosyan, D. 2015, MNRAS, 452, 3369
Cordoni, G., Milone, A. P., Mastrobuono-Battisti, A., et al. 2020, ApJ, 889, 18
Davies, R. L., Kuntschner, H., Emsellem, E., et al. 2001, ApJ, 548, L33
De Lorenzi, F., Hartmann, M., Debattista, V. P., Seth, A. C., & Gerhard, O. 2013, MNRAS, 429, 2974
De Rijcke, S., Fouvry, J.-B., & Dehnen, W. 2019a, MNRAS, 485, 150
De Rijcke, S., Fouvry, J.-B., & Pichon, C. 2019b, MNRAS, 484, 3198
De Rijcke, S., & Voulis, I. 2016, MNRAS, 456, 2024
de Zeeuw, T. 1985, MNRAS, 216, 273
Dehnen, W. 2001, MNRAS, 324, 273
—. 2002, J. Comput. Phys., 179, 27
Dejonghe, H. 1987, MNRAS, 224, 13
Do, T., Ghez, A., Becklin, E., et al. 2019, BAAS, 51, 530
Doremus, J. P., Feix, M. R., & Baumann, G. 1971, Phys. Rev. Lett., 26, 725
Doroshkevich, A. G. 1970, Astrofizika, 6, 581
Dubois, Y., Pichon, C., Welker, C., et al. 2014, MNRAS, 444, 1453
Dury, V., de Rijcke, S., Debattista, V. P., & Dejonghe, H. 2008, MNRAS, 387, 2
Earn, D. J. D., & Lynden-Bell, D. 1996, MNRAS, 278, 395
Eddington, A. S. 1916, MNRAS, 76, 572
Efstathiou, G., Lake, G., & Negroponte, J. 1982, MNRAS, 199, 1069
Emsellem, E., Cappellari, M., Krajnović, D., et al. 2007, MNRAS, 379, 401
—. 2011, MNRAS, 414, 888
Evans, N. W., Hafner, R. M., & de Zeeuw, P. T. 1997, MNRAS, 286, 315
Evans, N. W., & Read, J. C. A. 1998a, MNRAS, 300, 83
—. 1998b, MNRAS, 300, 106
Feldmeier, A., Neumayer, N., Seth, A., et al. 2014, A&A, 570, A2
Feldmeier-Krause, A., Zhu, L., Neumayer, N., et al. 2017, MNRAS, 466, 4040
Ferraro, F. R., Mucciarelli, A., Lanzoni, B., et al. 2018, ApJ, 860, 50
Fouvry, J.-B. 2016, Thèse, Université Pierre et Marie Curie - Paris VI
Fouvry, J.-B., Pichon, C., Magorrian, J., & Chavanis, P.-H. 2015a, A&A, 584, A129
Fouvry, J.-B., Pichon, C., & Prunet, S. 2015b, MNRAS, 449, 1967
Fridman, A. M., Polyachenko, V. L., Aries, A. B., & Poliakoff, I. N. 1984a, Physics of gravitating systems. I.
—. 1984b, Physics of gravitating systems. II.
Genzel, R., Eisenhauer, F., & Gillessen, S. 2010, Rev. Mod. Phys., 82, 3121
Giersz, M., & Heggie, D. C. 1994, MNRAS, 268, 257
—. 1997, MNRAS, 286, 709
Gillon, D. 1980, Académie des Sciences Paris Comptes Rendus Série B Sciences Physiques, 290, 545
Gradshteyn, I. S., & Ryzhik, I. M. 2007, Table of integrals, series, and products (Elsevier Academic Press)
Hamilton, C., Fouvry, J.-B., Binney, J., & Pichon, C. 2018, MNRAS, 481, 2041
Hansen, S. H. 2009, ApJ, 694, 1250
Hansen, S. H., & Moore, B. 2006, New A, 11, 333
Heggie, D. C., Breen, P. G., & Varri, A. L. 2020, MNRAS, 492, 6019
Hénault-Brunet, V., Gieles, M., Evans, C. J., et al. 2012, A&A, 545, L1
Henon, M. 1959, Annales d'Astrophysique, 22, 126
—. 1971, Ap&SS, 14, 151
—. 1973, A&A, 24, 229
Hernquist, L., & Ostriker, J. P. 1992, ApJ, 386, 375
Heyvaerts, J. 2010, MNRAS, 407, 355
Hohl, F. 1971, ApJ, 168, 343
—. 1976, AJ, 81, 30
Host, O., Hansen, S. H., Piffaretti, R., et al. 2009, ApJ, 690, 358
Hunter, C. 2002, in Astronomical Society of the Pacific Conference Series, Vol. 275, Disks of Galaxies: Kinematics, Dynamics and Peturbations, ed. E. Athanassoula, A. Bosma, & R. Mujica, 293–300

Hurley, J. R., & Shara, M. M. 2012, MNRAS, 425, 2872
Husemann, B., Jahnke, K., Sánchez, S. F., et al. 2013, A&A, 549, A87
Ideta, M. 2002, ApJ, 568, 190
Jalali, M. A. 2007, ApJ, 669, 218
—. 2008, ApJ, 689, 134
Jalali, M. A., & Hunter, C. 2005, ApJ, 630, 804
Jeans, J. H. 1915, MNRAS, 76, 70
—. 1919, Philosophical Transactions of the Royal Society of London Series A, 218, 157
Jeans, J. H. 1929, Astronomy and Cosmogony (Cambridge University Press)
Jeeson-Daniel, A., Dalla Vecchia, C., Haas, M. R., & Schaye, J. 2011, MNRAS, 415, L69
Jindal, A., Webb, J. J., & Bovy, J. 2019, MNRAS, 487, 3693
Kafle, P. R., Sharma, S., Lewis, G. F., & Bland -Hawthorn, J. 2012, ApJ, 761, 98
Kalnajs, A. J. 1965, PhD thesis, Harvard University.
—. 1972, ApJ, 175, 63
—. 1976, ApJ, 205, 745
—. 1977, ApJ, 212, 637
Kalnajs, A. J. 1978, in IAU Symposium, Vol. 77, Structure and Properties of Nearby Galaxies, ed. E. M. Berkhuijsen & R. Wielebinski, 113
Kamann, S., Dalessandro, E., Bastian, N., et al. 2020, MNRAS, 492, 966
Kandrup, H. E., & Sygnet, J. F. 1985, ApJ, 298, 27
King, Charles, I., Brown, W. R., Geller, M. J., & Kenyon, S. J. 2015, ApJ, 813, 89
Krajnović, D., Bacon, R., Cappellari, M., et al. 2008, MNRAS, 390, 93
Kuijken, K., & Dubinski, J. 1994, MNRAS, 269, 13
—. 1995, MNRAS, 277, 1341
Kuntschner, H., Emsellem, E., Bacon, R., et al. 2006, MNRAS, 369, 497
Lacroix, T., Stref, M., & Lavalle, J. 2018, J. Cosm. Astropart. Phys., 2018, 040
Lau, J. Y., & Binney, J. 2019, MNRAS, 490, 478
Lemze, D., Wagner, R., Rephaeli, Y., et al. 2012, ApJ, 752, 141
Lilley, E. J., Sanders, J. L., & Evans, N. W. 2018, MNRAS, 478, 1281
Lin, C. C., & Shu, F. H. 1966, Proc. Natl. Acad. Sci. USA, 55, 229
Loose, H. H., Kruegel, E., & Tutukov, A. 1982, A&A, 105, 342
Lynden-Bell, D. 1960, MNRAS, 120, 204
—. 1967, MNRAS, 136, 101
—. 1979, MNRAS, 187, 101
Lynden-Bell, D., & Kalnajs, A. J. 1972, MNRAS, 157, 1
Lynden-Bell, D., & Wood, R. 1968, MNRAS, 138, 495
Magorrian, J. 1995, MNRAS, 277, 1185
Mapelli, M. 2017, MNRAS, 467, 3255
Maréchal, L., & Perez, J. 2011, Transport Theor. Stat. Phys., 40, 425
Mark, J. W. K. 1971, Proc. Nat. Acad. Sci., 68, 2095
Mark, J. W. K. 1974, ApJ, 193, 539
Massari, D., Breddels, M. A., Helmi, A., et al. 2018, Nature Ast., 2, 156
Massari, D., & Helmi, A. 2018, A&A, 620, A155
Massari, D., Helmi, A., Mucciarelli, A., et al. 2020, A&A, 633, A36
Merritt, D. 1985, AJ, 90, 1027
Merritt, D. 1987, in IAU Symposium, Vol. 127, Structure and Dynamics of Elliptical Galaxies, ed. P. T. de Zeeuw, 315–329
—. 1999, PASP, 111, 129
Merritt, D., & Aguilar, L. A. 1985, MNRAS, 217, 787
Meylan, G., & Mayor, M. 1986, A&A, 166, 122
Meza, A. 2002, A&A, 395, 25
Mikhailovskiĭ, A. B., Fridman, A. M., & Epel'Baum, Y. G. 1971, Soviet J. Exp. Theor. Phys., 32, 878
Milone, A. P., Marino, A. F., Mastrobuono-Battisti, A., & Lagioia, E. P. 2018, MNRAS, 479, 5005
Milosavljević, M. 2004, ApJ, 605, L13
Monari, G., Famaey, B., Siebert, A., et al. 2017, MNRAS, 465, 1443
Navarro, J. F., Frenk, C. S., & White, S. D. M. 1997, ApJ, 490, 493
Nedelchev, B., Coccato, L., Corsini, E. M., et al. 2019, A&A, 623, A87
Nitadori, K., & Aarseth, S. J. 2012, MNRAS, 424, 545
Osipkov, L. P. 1979, Soviet Ast. Lett., 5, 42
Ostriker, J. P., & Peebles, P. J. E. 1973, ApJ, 186, 467
Palmer, P. 1994, Stability of Collisionless Stellar Systems (Springer Netherlands)
Palmer, P. L., & Papaloizou, J. 1987, MNRAS, 224, 1043
—. 1988, MNRAS, 231, 935
—. 1990, MNRAS, 243, 263
Palmer, P. L., Papaloizou, J., & Allen, A. J. 1989, MNRAS, 238, 1281
—. 1990, MNRAS, 243, 282
Park, M.-J., Yi, S. K., Dubois, Y., et al. 2019, ApJ, 883, 25
Peebles, P. J. E. 1969, ApJ, 155, 393
Penrose, O. 1960, The Physics of Fluids, 3, 258
Perez, J., & Aly, J.-J. 1996, MNRAS, 280, 689
Pichon, C., & Aubert, D. 2006, MNRAS, 368, 1657
Pichon, C., & Cannon, R. C. 1997, MNRAS, 291, 616
Pichon, C., & Lynden-Bell, D. 1993, in Statistical Description of Transport in Plasma, Astro- and Nuclear Physics, ed. J. Misquich, G. Pelletier, & P. Schuck, 261
Plummer, H. C. 1911, MNRAS, 71, 460
Polyachenko, E. V., & Just, A. 2015, MNRAS, 446, 1203
Polyachenko, E. V., Polyachenko, V. L., & Shukhman, I. G. 2008, MNRAS, 386, 1966
Polyachenko, E. V., & Shukhman, I. G. 2015, MNRAS, 451, 601
—. 2017, MNRAS, 470, 2190
—. 2019, MNRAS, 483, 692
Polyachenko, V. L. 1987, Astrophysics, 27, 512
Polyachenko, V. L., Polyachenko, E. V., & Shukhman, I. G. 2012, Soviet J. Exp. Theor. Phys., 114, 596
Polyachenko, V. L., & Shukhman, I. G. 1981, Soviet Ast., 25, 533
Press, W., et al. 2007, Numerical Recipes 3rd Edition (Cambridge University Press)
Rahmati, A., & Jalali, M. A. 2009, MNRAS, 393, 1459
Read, J. I., Walker, M. G., & Steger, P. 2018, MNRAS, 481, 860
Robijn, F. H. A. 1995, PhD thesis, Leiden Observatory
Romeo, A. B., & Falstad, N. 2013, MNRAS, 433, 1389
Rozier, S., Fouvry, J.-B., Breen, P. G., et al. 2019, MNRAS, 487, 711
Saha, P. 1991, MNRAS, 248, 494
Sawamura, M. 1988, PASJ, 40, 279
Schödel, R., Merritt, D., & Eckart, A. 2009, A&A, 502, 91
Schwarzschild, M. 1979, ApJ, 232, 236
Sellwood, J. A. 1981, A&A, 99, 362
Sellwood, J. A., & Evans, N. W. 2001, ApJ, 546, 176
Sellwood, J. A., & Valluri, M. 1997, MNRAS, 287, 124
Seth, A. C., Blum, R. D., Bastian, N., Caldwell, N., & Debattista, V. P. 2008, ApJ, 687, 997
Sollima, A., Baumgardt, H., & Hilker, M. 2019, MNRAS, 485, 1460
Syer, D., & Tremaine, S. 1996, MNRAS, 282, 223
Synakh, V. S., Fridman, A. M., & Shukhman, I. G. 1971, Akademiia Nauk SSSR Doklady, 201, 827
Szölgyén, Á., Meiron, Y., & Kocsis, B. 2019, ApJ, 887, 123
Takahashi, K., Lee, H. M., & Inagaki, S. 1997, MNRAS, 292, 331
Tanner, A., Figer, D. F., Najarro, F., et al. 2006, ApJ, 641, 891
Taylor, J. E., & Navarro, J. F. 2001, ApJ, 563, 483
Tiongco, M. A., Vesperini, E., & Varri, A. L. 2016a, MNRAS, 461, 402
—. 2016b, MNRAS, 455, 3693
—. 2018, MNRAS, 475, L86
Toomre, A. 1964, ApJ, 139, 1217
Toomre, A. 1981, in Structure and Evolution of Normal Galaxies, 111–136
Tremaine, S. 2005, ApJ, 625, 143
Tremaine, S., & Weinberg, M. D. 1984, MNRAS, 209, 729
Tremaine, S. D., Ostriker, J. P., & Spitzer, L., J. 1975, ApJ, 196, 407
Tsatsi, A., Mastrobuono-Battisti, A., van de Ven, G., et al. 2017, MNRAS, 464, 3720
Valluri, M., & Merritt, D. 1998, ApJ, 506, 686
van Albada, T. S. 1982, MNRAS, 201, 939
van der Marel, R. P., Sigurdsson, S., & Hernquist, L. 1997, ApJ, 487, 153
van Leeuwen, F., Le Poole, R. S., Reijns, R. A., Freeman, K. C., & de Zeeuw, P. T. 2000, A&A, 360, 472
Vandervoort, P. O. 1970, ApJ, 161, 87
—. 1980, ApJ, 240, 478
—. 1982, ApJ, 256, L41
Varri, A. L. 2012, PhD thesis, Università degli Studi di Milano
Vasiliev, E. 2018, MNRAS, 481, L100
—. 2019, MNRAS, 489, 623
Vasiliev, E., & Athanassoula, E. 2015, MNRAS, 450, 2842
Vauterin, P., & Dejonghe, H. 1996, A&A, 313, 465
Vesperini, E., Varri, A. L., McMillan, S. L. W., & Zepf, S. E. 2014, MNRAS, 443, L79
Vesperini, E., & Weinberg, M. D. 2000, ApJ, 534, 598
Vitvitska, M., Klypin, A. A., Kravtsov, A. V., et al. 2002, ApJ, 581, 799
Wang, L., Spurzem, R., Aarseth, S., et al. 2016, MNRAS, 458, 1450
Watkins, L. L., van der Marel, R. P., Bellini, A., & Anderson, J. 2015, ApJ, 803, 29

Weinberg, M. D. 1989, MNRAS, 239, 549
—. 1991a, ApJ, 368, 66
—. 1991b, ApJ, 373, 391
—. 1994, ApJ, 421, 481
—. 1998, MNRAS, 299, 499
—. 1999, AJ, 117, 629
—. 2001, MNRAS, 328, 311
Welker, C., Devriendt, J., Dubois, Y., Pichon, C., & Peirani, S. 2014, MNRAS, 445, L46
White, S. D. M. 1984, ApJ, 286, 38
Wisnioski, E., Förster Schreiber, N. M., Wuyts, S., et al. 2015, ApJ, 799, 209
Wisnioski, E., Förster Schreiber, N. M., Fossati, M., et al. 2019, ApJ, 886, 124
Wojtak, R., Gottlöber, S., & Klypin, A. 2013, MNRAS, 434, 1576
Zang, T. A. 1976, PhD thesis, Massachussets Inst. Tech.
Zang, T. A., & Hohl, F. 1978, ApJ, 226, 521
Zhao, H. 1996, MNRAS, 278, 488
Zjupa, J., & Springel, V. 2017, MNRAS, 466, 1625